Molten Metal Oscillatory Behaviour in Advanced Fusion-based Manufacturing Processes

Ebrahimi, Amin

DOI
10.4233/uuid:06ff0b5e-d5da-4149-a90f-62064c29f238

Publication date
2022

Document Version
Final published version

Citation (APA)
Ebrahimi, A. (2022). *Molten Metal Oscillatory Behaviour in Advanced Fusion-based Manufacturing Processes*. [Dissertation (TU Delft), Delft University of Technology]. https://doi.org/10.4233/uuid:06ff0b5e-d5da-4149-a90f-62064c29f238

Important note
To cite this publication, please use the final published version (if applicable).
Please check the document version above.

Molten Metal Oscillatory Behaviour

in Advanced Fusion-based Manufacturing Processes

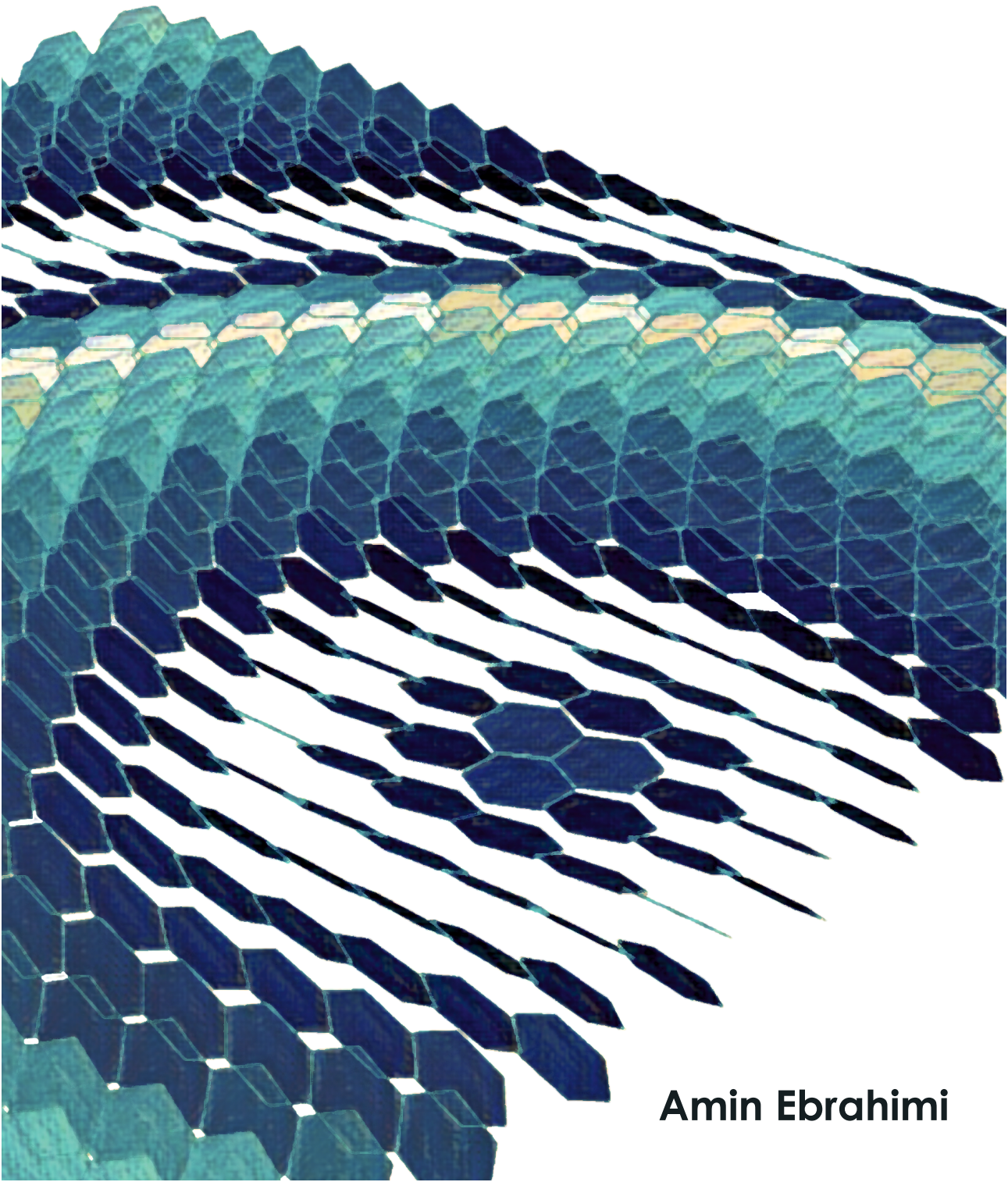

Amin Ebrahimi

Molten Metal Oscillatory Behaviour

in Advanced Fusion-based Manufacturing Processes

Molten Metal Oscillatory Behaviour

in Advanced Fusion-based Manufacturing Processes

Dissertation

for the purpose of obtaining the degree of doctor
at Delft University of Technology,
by the authority of the Rector Magnificus Prof.dr.ir. T.H.J.J. van der Hagen,
chair of the Board for Doctorates,
to be defended publicly on Wednesday 30 March 2022 at 10:00 a.m.

by

Amin EBRAHIMI

Master of Science in Aerospace Engineering,
Ferdowsi University of Mashhad, Iran,
born in Tehran, Iran.

This dissertation has been approved by the promotors.

Composition of the doctoral committee:

Rector Magnificus,	Chairperson
Prof.dr. I.M. Richardson,	Delft University of Technology, promotor
Prof.dr.ir. C.R. Kleijn,	Delft University of Technology, promotor
Independent members:	
Prof.dr.ir. F. van Keulen,	Delft University of Technology
Prof.dr. S. Kenjereš,	Delft University of Technology
Dr.ir. M.J.M. Hermans,	Delft University of Technology
Prof.dr.ir. G.R.B.E. Römer,	University of Twente
Prof.dr.Dipl.-Ing. N. Enzinger,	Graz University of Technology

This research was carried out under the project number F31.7.13504 in the framework of the Partnership Program of the Materials innovation institute M2i (www.m2i.nl) and the Foundation for Fundamental Research on Matter (FOM) (www.fom.nl), which is part of the Netherlands Organisation for Scientific Research (www.nwo.nl).

Keywords: Materials processing; Fusion welding and additive manufacturing; Process design and optimisation; Melt pool behaviour; Computational modelling.

E-mail: ebrahimi.amin@gmail.com | a.ebrahimi@tudelft.nl
https://orcid.org/0000-0002-4912-2549

ISBN 978-94-6423-741-2

An electronic version of this dissertation is available at
http://repository.tudelft.nl/

Contents

Summary

The growing demand for manufactured products with complex geometries requiring advanced fusion-based manufacturing techniques emphasises the importance of process development and optimisation to reduce the risk of adverse outcomes, which is currently impeded with traditional approaches (trial and error experiments). Development, optimisation and qualification of such procedures are often expensive and time-consuming, particularly when new materials or new material combinations are involved. Process stability is intrinsically linked to the stability of the molten metal melt-pool, which ideally should solidify in a smooth and continuous manner to produce a consistent product, free of undesirable geometric and metallurgical defects. The influence of material properties and process conditions on melt-pool stability are generally difficult to derive from experimental observations; hence process optimisation is often reliant on a trial-and-error approach, mitigated to a large extent by a considerable body of industrial experience.

The challenge addressed in this research is to develop a simulation-based approach to assess the stability of oscillating melt-pools in fusion welding and additive manufacturing, to minimise the number of trial-and-error experiments required for process development and optimisation, which ultimately will lead to shortening the time between design and production. The computational model developed in the present work has a generic construction with specific process influences addressed through appropriate boundary conditions, avoiding the necessity to integrate melt pool and detailed process descriptions in a single simulation. The model is therefore capable of representing a wide range of welding and additive manufacturing technologies through selection of appropriate material properties and boundary conditions. The robustness of the present computational model in predicting the melt-pool behaviour is demonstrated by comparing the numerical predictions with experimental, analytical and numerical data.

Focusing on numerical simulations of solidification and melting using the enthalpy-porosity method, the influence of the permeability coefficient (also known as the mushy-zone constant) on the numerical predictions, which is employed to dampen fluid velocities in the mushy zone and suppress them in solid regions, is systematically analysed for both isothermal and non-isothermal phase-change problems. For isothermal phase-change problems, reducing the cell size diminishes the influence of the mushy-zone constant on the results and the solution becomes independent of the mushy-zone constant for fine enough meshes. Numerical predictions of non-isothermal phase-change problems are inherently dependent on the mushy-zone constant. A method is proposed, based on a Péclet number, to predict and evaluate the influence of the permeability coefficient on numerical predictions of solidification and melting problems.

In many numerical studies in the literature, the transport coefficients of the material, specifically thermal conductivity and viscosity, are artificially increased by a so-called 'enhancement factor' to achieve agreement between experiments and numerically predicted melt-pool sizes and solidification rates. However, the use of an enhancement

factor has little physical meaning, does not represent the physics of complex transport phenomena and can significantly affect the numerical predictions. The effects of using enhancement factors on the numerical predictions of melt-pool behaviour in fusion welding and additive manufacturing are studied in detail. Moreover, the effects of employing temperature-dependent material properties on the numerical predictions are discussed in the present thesis.

Melt pools in fusion welding and additive manufacturing exhibit highly non-linear responses to variations of process parameters and are very sensitive to imposed boundary conditions. Temporal and spatial variations in the energy-flux distribution, which are often neglected in numerical simulations, are taken into account in the present work. It is shown how deformations of the melt-pool surface, due to fluid motion as well as changes in the system orientation, affect the numerical predictions of thermal and fluid flow fields. The effects of joint shape design on melt-pool behaviour during fusion welding is also studied in the present work.

Changes in power-density and force distributions affect the thermal and fluid flow fields on the melt-pool surface, which in turn can influence the pool shape. Oscillations strongly relate to shape and size of the melt-pool and the surface tension distribution on the molten material surface. Using the simulation-based approach developed in the present work, the frequency and amplitude of melt-pool oscillations and changes in the oscillation modes are predicted, which are not accessible using published analytical models and are generally difficult to measure experimentally. Additionally, using the proposed simulation-based approach, the need for triggering of the melt-pool oscillations is obviated, since even small surface displacements are detectable, which are not sensible to the current measurement devices employed in experiments.

The dynamic features of the oscillation signals cannot easily be derived employing conventional Fourier transform (FT) analysis since the oscillation signals are assumed to be stationary (*i.e.* the behaviour of the system is linear and time-invariant), which is often not the case in fusion welding and additive manufacturing. The continuous wavelet transform (CWT) has been employed in the present work to overcome the shortcomings of the conventional fast Fourier transform (FFT) analysis in characterising the non-stationary features of the surface oscillation signals received from the melt pool. Employing the continuous wavelet transform, the time-resolved melt-pool surface oscillation signals obtained from the numerical simulations can be decomposed into time and frequency spaces simultaneously.

The simulation-based approach developed in the present work addresses some of the significant challenges involved in assessing the melt-pool stability for process development and optimisation. The numerical predictions of the present computational model enhances the current understanding of the process behaviour, which is often very challenging to achieve from experiments alone. Moreover, the present simulation-based approach can be employed to explore the design space and reduce the costs associated with process development and optimisation.

Samenvatting

De groeiende vraag naar gefabriceerde producten met complexe geometrieën die geavanceerde, op smelten en stollen gebaseerde productietechnieken vereisen, benadrukt het belang van procesontwikkeling en -optimalisatie om het risico op ongunstige uitkomsten bij vervaardiging te verminderen. Een snelle ontwikkel- en optimalisatieproces wordt momenteel bemoeilijkt door een traditionele 'trial-and-error'-benaderingen. Het ontwikkelen, optimaliseren en kwalificeren van dergelijke op experimenten gebaseerde procedures is vaak duur en tijdrovend, vooral als het om nieuwe materialen of nieuwe materiaalcombinaties gaat. Processtabiliteit is intrinsiek verbonden met de stabiliteit van het smeltbad. Om een consistent product te vervaardigen, vrij van ongewenste geometrische en metallurgische defecten, is een onverstoorde en continue manier van stolling idealiter gewenst. De invloed van materiaaleigenschappen en procesomstandigheden op de stabiliteit van het smeltbad is over het algemeen moeilijk af te leiden uit experimentele waarnemingen. Alhoewel procesoptimalisatie vaak afhankelijk is van een 'trial-and-error'-benadering, kan het putten uit de aanzienlijke hoeveelheid industriële ervaring.

De uitdaging die in dit onderzoek aan de orde komt, is het ontwikkelen van een op simulatie gebaseerde benadering om de stabiliteit van oscillerende smeltbaden bij smeltlassen en additive manufacturing te beoordelen. Door middel van deze simulaties is het mogelijk het aantal 'trial-and-error'-experimenten, nodig voor procesontwikkeling en -optimalisatie, te minimaliseren. Dit zal uiteindelijk leiden tot een verkorting van de tijd tussen ontwerp en productie. Het numerieke model dat in het huidige werk is ontwikkeld, heeft een generieke constructie, waarbij de specifieke procesinvloedsfactoren worden ingebracht door het opstellen van geschikte randvoorwaarden. Hierdoor wordt ook de noodzaak vermeden om smeltbad- en gedetailleerde proceskarakteristieken in één enkele simulatie te integreren. Het model is daarom in staat een breed scala aan las- en additive manufacturing technologieën te representeren door selectie van geschikte materiaaleigenschappen en randvoorwaarden. De robuustheid van het huidige numerieke model voor het voorspellen van het smeltbadgedrag wordt aangetoond door de uitkomsten te vergelijken met experimentele, analytische en numerieke gegevens.

In de numerieke simulaties ligt de nadruk op smelten en stollen met behulp van de enthalpie-porositeitsmethode. Deze methode maakt gebruik van de permeabiliteitscoëfficiënt (ook bekend als de 'mushy-zone' constante), die in de numerieke voorspellingen vloeistofsnelheden in de 'mushy-zone' dempt en in de vast stof onderdrukt. De invloed van deze coëfficiënt is op systematisch geanalyseerd voor zowel isotherme als niet-isotherme faseveranderingsproblemen. Voor isotherme faseveranderingsproblemen vermindert het verkleinen van de mesh-grootte de invloed van de 'mushy-zone' constante op de resultaten en wordt de oplossing onafhankelijk van de 'mushy-zone' constante als de mesh-grootte klein genoeg is. Numerieke voorspellingen van niet-isotherme faseveranderingsproblemen zijn inherent afhankelijk van de 'mushy-zone' constante. Er wordt

een methode voorgesteld, gebaseerd op een Pecletgetal, om de invloed van de permeabiliteitscoëfficiënt op numerieke voorspellingen van smelt- en stollingsproblemen te voorspellen en te evalueren.

In veel numerieke studies in de literatuur worden de transportcoëfficiënten van het materiaal, met name thermische geleidbaarheid en viscositeit, kunstmatig verhoogd met een (zogenaamde) 'versterkingsfactor', om overeenstemming te bereiken tussen experimenten en numeriek voorspelde smeltbadgroottes en stolsnelheden. Het gebruik van een versterkingsfactor heeft echter weinig fysieke betekenis, vertegenwoordigt niet de fysica van complexe transportverschijnselen en kan de numerieke voorspellingen aanzienlijk beïnvloeden. De effecten van het gebruik van versterkingsfactoren op de numerieke voorspellingen van smeltbadgedrag bij smeltlassen en 'additive manufacturing' zijn in detail bestudeerd. Bovendien worden de effecten van het gebruik van temperatuurafhankelijke materiaaleigenschappen op de numerieke voorspellingen in dit proefschrift besproken.

Smeltbaden bij smeltlassen en 'additive manufacturing' vertonen een niet-lineaire respons op variaties in procesparameters en zijn erg gevoelig voor opgelegde randvoorwaarden. In dit werk wordt rekening gehouden met temporele en ruimtelijke variaties in de energieflux-verdeling, die vaak worden verwaarloosd in numerieke simulaties. Er wordt aangetoond hoe vervormingen van het smeltbadoppervlak, als gevolg van vloeistofbeweging en veranderingen in de systeemoriëntatie, de numerieke voorspellingen van thermische en vloeistofstroomvelden beïnvloeden. De effecten van het ontwerp van de naadvorm op het gedrag van lasbaden tijdens smeltlassen zijn ook bestudeerd in deze studie.

Veranderingen in vermogensdichtheid en krachtverdelingen beïnvloeden de thermische en vloeistofstroomvelden aan het smeltbadoppervlak, wat op zijn beurt de vorm van het smeltbad kan beïnvloeden. Oscillaties hangen sterk samen met de vorm en grootte van het smeltbad en de oppervlaktespanningsverdeling aan het gesmolten materiaaloppervlak. Met behulp van de op simulatie gebaseerde benadering, die in deze studie is ontwikkeld, worden de frequentie en amplitude van smeltbadoscillaties en veranderingen in de oscillatiemode voorspeld. Deze informatie wordt niet verkregen met behulp van gepubliceerde analytische modellen en is over het algemeen moeilijk experimenteel te meten. Bovendien is de noodzaak om smeltbad-oscillaties te triggeren, met behulp van de voorgestelde op simulatie gebaseerde benadering niet nodig, aangezien zelfs kleine oppervlakteverplaatsingen detecteerbaar zijn. De huidige meetapparatuur die bij experimenten wordt gebruikt is ongevoelig voor het meten van deze kleine verplaatsingen.

De dynamische kenmerken van de oscillatiesignalen kunnen niet eenvoudig worden afgeleid met behulp van conventionele Fourier-transformatie (FT) -analyse. Bij de conventionele analyse wordt aangenomen dat de oscillatiesignalen stationair zijn (met andere woorden het gedrag van het systeem is lineair en tijdinvariant), wat vaak niet het geval is bij smeltlassen en 'additive manufacturing'. In de huidige studie is de continue wavelet-transformatie (CWT) gebruikt om de tekortkomingen van de conventionele snelle Fourier-transformatie (FFT)-analyse te verhelpen bij het karakteriseren van de niet-stationaire kenmerken van de oppervlakteoscillatiesignalen gegenereerd door het smeltbad. Door gebruik te maken van de continue wavelet-transformatie, kunnen de in de tijd opgeloste oscillatiesignalen van het smeltbadoppervlak die zijn verkregen uit de numerieke simulaties, tegelijkertijd worden ontleed naar tijd- en frequentiedomein.

De op simulatie gebaseerde benadering die in het huidige werk is ontwikkeld, adresseert enkele van de belangrijke uitdagingen bij het beoordelen van de smeltbadstabiliteit voor procesontwikkeling en -optimalisatie. De numerieke voorspellingen van het ontwikkelde model verbeteren het huidige begrip van het procesgedrag, hetgeen moeilijk te verkrijgen is met alleen experimenten. Bovendien kan de huidige op simulatie gebaseerde benadering worden gebruikt om de ontwerpruimte te verkennen en de kosten die gepaard gaan met procesontwikkeling en -optimalisatie te verminderen.

1

Introduction

1

1.1. Background and motivation

Fusion-based manufacturing processes, such as welding and additive manufacturing (also known as 3D-printing), play an essential role in manufacturing parts and structures in many industries including, but not limited to, aerospace, maritime and automotive. Development, optimisation and qualification of such procedures are often expensive and time-consuming, particularly when new materials or new material combinations are involved [1]. Process stability is intrinsically linked to the stability of the molten metal melt-pool, which ideally should solidify in a smooth and continuous manner to produce a consistent product, free of undesirable geometric and metallurgical defects [2, 3]. The influence of material properties and process conditions on melt-pool stability are generally difficult to derive from experimental observations; hence process optimisation is often reliant on a trial-and-error approach, mitigated to a large extent by a considerable body of industrial experience. In recent years, the development of advanced fusion-based manufacturing processes has received increasing attention; however, the industrial uptake is limited, in large part due to the complexity of process optimisation. To enhance the successful adoption of such technologies, developing a scientific understanding of the process is indispensable [4].

A major challenge associated with the development and optimisation of welding and additive manufacturing is that the melt-pool behaviour in these processes is characterised by highly non-linear responses to input parameters and boundary conditions. The practical consequences of such non-linearity are that welding and additive manufacturing cannot be considered turn-key operations, for which all influencing parameters are uniquely defined, but must be regarded as procedure driven. Moreover, process optimisation requires tolerance to parameter ranges, within which the resultant product integrity must be fit for the intended purpose, irrespective of the particular parameter combinations within the defined procedural range. Developing improved techniques for the assessment of parameter combinations is essential, not only to reduce the costs of process development and optimisation but also to improve the current understanding of process behaviour. Recent advances in available computational resources along with enhanced modelling tools offer a unique opportunity to explore the design space and foster the current understanding of internal molten metal flow in welding and additive manufacturing using numerical simulations. Such numerical simulations can be utilised to determine the stability or lack of stability of a process from the relevant material data and processing conditions, so that inappropriate combinations can be excluded and experimental optimisation can be focused exclusively on the range of valid parameter combinations. The challenge addressed in the present work is to construct a simulation-based approach to study molten metal oscillatory behaviour in advanced fusion-based manufacturing processes.

The ability to make products using advanced fusion-based manufacturing techniques depends critically upon the dynamic melt-pool stability [5]. High-energy-density heat distributions, a range of driving forces (such as Marangoni forces, electromagnetic forces, thermal buoyancy and gas pressures and shear stresses) and solid-liquid-solid phase transformations, are crucial elements that affect the complex flows induced inside molten metal melt-pools. Flow in the melt-pool can result in free surface deformation and oscillation. Depending on the chosen process parameters, boundary conditions and material

properties, the melt-pool can become unstable, eventually leading to process failure. Additionally, multi-scale spatio-temporal transport phenomena (heat and mass) determine the quality, structure and properties of joints (in fusion welding) or deposits (in additive manufacturing) used in a wide range of industrial applications [6]. A better understanding of the complex melt-pool behaviour is vital to control composition, structure and properties of new materials and to fully unlock the utility of novel manufacturing processes which can enhance the production rate and quality.

1.2. Goal of the study

The aim of the present study is to develop a simulation-based approach to assess the stability of oscillating melt-pools to minimise the volume of trial-and-error experimenting required for welding and additive manufacturing process development and optimisation, which ultimately will lead to shortening the time between design and production. The approach has a generic structure and is applicable to any fusion-based manufacturing process and material, and represents a major advance in the optimisation of such processes and in particular, for fusion-based manufacturing processes subject to a large number of operating variables. Of particular interest is the influence of gravity as a function of system orientation. Stability of fusion-based manufacturing processes will influence the power dissipation and forces applied to the melt-pool, which are described here in terms of initial and boundary conditions as well as material properties. Variations in boundary conditions on the support geometry of the melt-pool as well as the power-density distribution have also been taken into account.

1.3. Outline of the thesis

The key concepts related to internal flow behaviour in fusion welding and additive manufacturing are comprehensively summarised in **chapter 2**, covering the underlying physical processes, flow patterns in the pool, and the state-of-the-art in the computational modelling of heat and fluid flow in melt-pools and associated surface oscillations. Moreover, limitations of the available models and challenges involved in numerical simulations of complex thermal and fluid flow fields in fusion welding and additive manufacturing are discussed. An introduction is provided for each chapter, supplying further details to the reader.

In **chapter 3**, the details of the computational model and the assumptions made to develop the present model are described. Additionally, the laser absorptivity model, surface tension model and the continuous wavelet transform (CWT) employed in the present work are elaborated. Reliability and validity of the proposed model in predicting the fundamental aspects of fusion welding and additive manufacturing are also discussed focusing on various benchmark problems.

The influence of the permeability coefficient (also known as the mushy-zone constant, which is employed to dampen fluid velocities in the mushy zone and suppress them in solid regions), on the numerical predictions of solidification and melting problems using the enthalpy-porosity method is systematically analysed and the results are discussed in **chapter 4**. The sensitivity of numerical predictions to the value of the permeability coefficient for both isothermal and non-isothermal phase-change problems are explained.

Based on the results obtained from the numerical simulations, a method is proposed to predict and evaluate the influence of the permeability coefficient on numerical predictions of solidification and melting problems. The general applicability of the proposed method is examined for a simulation of a laser spot melting process.

In **chapter 5**, the effect of assuming a flat non-deformable gas-metal interface on the numerical predictions of melt pool behaviour are explained focusing on conduction mode laser spot melting, and the results are compared with those obtained using a deformable gas-metal interface. Temporal and spatial variations in the energy-flux distribution, which are often neglected in numerical simulations of melt pool behaviour, are taken into account. The influence on melt-pool oscillatory behaviour of dynamically adjusted energy flux distribution as well as changing thermo-physical material properties to achieve agreement between predicted melt-pool shape and experimental post solidification macrographs, commonly described in terms of enhancement factors, which are widely employed in published melt-pool flow models, is discussed in detail. Moreover, the effects of employing temperature-dependent material properties on numerical predictions of thermal and flow fields as well as the melt-pool shape are described.

In **chapter 6**, an enhanced absorption model that takes into account the effects of laser characteristics, incident angle, surface temperature, and material composition is employed to predict internal heat and fluid flow in laser melting. High-fidelity three-dimensional numerical simulations were performed using both variable and constant absorptivity models and the predictions compared with experimental data. Moreover, the difference between melt-pool shapes obtained using fibre and CO_2 laser sources are explained, and factors affecting the local energy absorption are discussed.

In **chapter 7**, the complex molten metal flow in melt pools and associated melt-pool surface oscillations during both steady-current and pulsed-current stationary gas tungsten arc welding (GTAW) are described. The computational model employed takes into account the effects of surface deformation on arc power-density and force distributions, as described in chapter 3. These factors are often neglected in numerical simulations of arc welding and additive manufacturing. An analysis based on a wavelet transform is performed to extract the time-frequency component of the displacement signals obtained from numerical simulations, and the results are compared with published analytical and experimental data. It is also demonstrated that using the proposed simulation-based approach, the need of triggering the melt-pool oscillations is obviated since even small surface displacements are detectable, which are not sensible to the current measurement devices employed in experiments.

Utilising the simulation-based approach developed in chapter 7, the effects of changing the welding orientation, material composition and travel speed on melt-pool oscillatory behaviour in gas tungsten arc welding (GTAW) are described in **chapter 8**. It is shown that changes in the surface morphology of the pool resulting from a change in welding position alter the spatial distribution of arc forces and power-density applied to the molten material, and in turn affect flow patterns in the pool. It is also explained how changing the sulphur concentration affects the Marangoni flow pattern, and increasing the travel speed affects the flow structures (vortex formation) on the surface and the resulting melt-pool shape.

Focusing on understanding the melt-pool behaviour during root pass gas metal

arc welding (GMAW), a systematic numerical study is described in **chapter 9**. Three-dimensional calculations are performed to simulate the dynamics of heat and molten metal flow in GMAW for various groove shapes. Additionally, experiments are performed to validate the numerical predictions.

Finally, in **chapter 10**, the contributions of the present work are summarised, conclusions are drawn and an outlook for future applications and developments of the present simulation-based approach for the development and optimisation of fusion welding and additive manufacturing processes is presented.

References

[1] Pollock, T. M. Alloy design for aircraft engines. *Nature Materials*, 15(8):809–815, 2016. doi:10.1038/nmat4709.

[2] DebRoy, T. and David, S. A. Physical processes in fusion welding. *Reviews of Modern Physics*, 67 (1):85–112, 1995. doi:10.1103/revmodphys.67.85.

[3] DebRoy, T., Wei, H. L., Zuback, J. S., Mukherjee, T., Elmer, J. W., Milewski, J. O., Beese, A. M., Wilson-Heid, A., De, A., and Zhang, W. Additive manufacturing of metallic components – Process, structure and properties. *Progress in Materials Science*, 92:112–224, 2018. doi:10.1016/j.pmatsci.2017.10.001.

[4] Roca, J. B., Vaishnav, P., Fuchs, E. R. H., and Morgan, M. G. Policy needed for additive manufacturing. *Nature Materials*, 15(8):815–818, 2016. doi:10.1038/nmat4658.

[5] Tapia, G. and Elwany, A. A review on process monitoring and control in metal-based additive manufacturing. *Journal of Manufacturing Science and Engineering*, 136(6), 2014. doi:10.1115/1.4028540.

[6] Lancaster, J. F., editor. *The Physics of Welding*. International series on materials science of technology. Pergamon Press, Oxford, UK, 2nd edition, 1986. ISBN 0080340768.

2

Fundamentals, Recent Developments and Challenges

2.1. Introduction

The practice of joining metallic parts using fusion-based techniques such as soldering and brazing can be traced back to ancient times with the earliest examples coming from several thousand years ago [1]. Figure 2.1 shows an example of a historical female figurine made of hammered metal sheets (approximate composition: 52% silver and 44% gold) joined through soldering [2]. Modern fusion-based manufacturing technologies began to develop in the late 19th century, mainly after the use of electricity to provide the heat required to melt materials. Since then, various welding and additive manufacturing processes have been developed and employed in many industries, such as construction, aerospace, maritime, automotive, energy, and electronics. Parts manufactured using fusion-based techniques vary in length from micrometres to several meters and can be produced in timescales ranging from fractions of a second to several days [3], during which a variety of natural phenomena take place. The advancement of fusion-based manufacturing technologies relies, to a great extent, on the interdisciplinary knowledge developed over the past decades; however, the full potential is not yet fully realised.

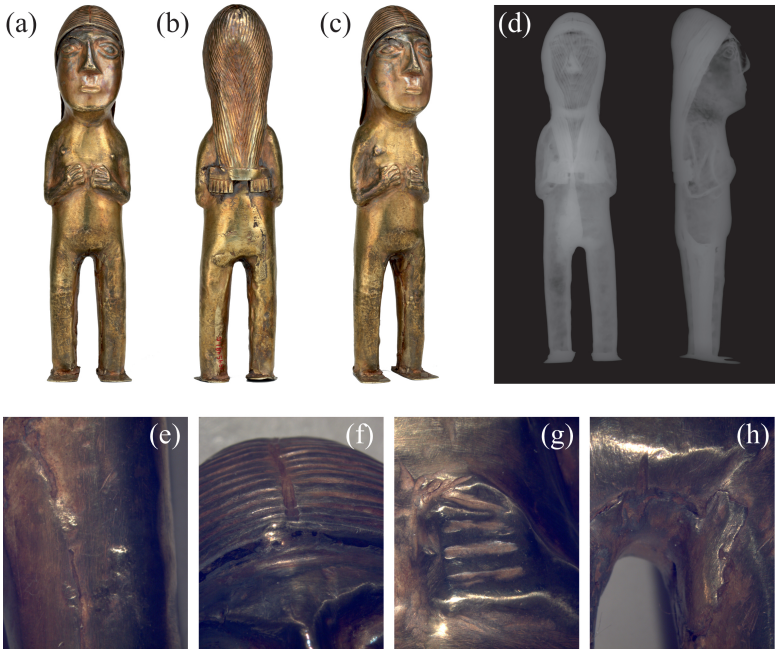

Figure 2.1: An example of using fusion-based techniques (soldering) to join metallic parts to produce a female figurine. The figurine has been made in A.D. 1400–1600 and is currently at The Metropolitan Museum of Art in New York City, USA. (a–c) different views of the figurine, (d) X-ray profiles of the figurine indicating its hollow structure, (e–h) zoomed views of the figurine showing the joints [2].

In fusion welding and additive manufacturing, various physical processes such as solid-liquid phase transformation, heat and fluid flow, interfacial transport phenomena, and vaporisation take place. The interaction of the localised heat input and the material

leads to rapid heating and successive solid-liquid phase transformations, resulting in the formation of a melt-pool. The melt-pool then cools down, solidifies and forms a joint (in welding) or a deposit (in additive manufacturing). Heat and fluid flow in the melt-pool affect geometrical evolution of the pool, homogeneity of material composition and thermal cycles that the material experience, and thus determine the structure and properties of the product [4]. Moreover, realising stability of the molten metal flow in fusion welding and additive manufacturing is crucial for control of the process, to reduce the number of failures in production. Correct control of flow dynamics in melt-pools is therefore essential to achieve desired properties in fusion-based manufacturing. Fundamentals and recent advances in understanding internal flow behaviour in fusion welding and additive manufacturing are discussed in this chapter.

2.2. Internal flow behaviour in melt pools

A melt-pool forms soon after applying a localised heat input to the material in fusion welding and additive manufacturing. The molten material in the melt-pool often undergoes complex recirculating motion [5], affecting the energy transfer not only inside the pool but also to the surrounding material and hence influencing the melt-pool shape [6, 7]. Various driving and dissipation mechanisms such as surface tension and electromagnetic effects, buoyancy, vaporisation recoil pressure, arc pressure, and plasma shear force have already been identified as governing factors for molten metal flow in melt-pools; these are primarily influenced by process parameters, boundary conditions and material properties. The interplay between the driving forces coupled with non-linearly varying material properties determine the fluid flow in a melt-pool and can generate complex unsteady flow patterns [8–10]. Process stability is intrinsically linked to the stability of the melt-pool, which ideally should solidify in a smooth and continuous manner to produce a consistent product, free of undesirable geometric and metallurgical defects [11, 12]. For instance, fluid flow in melt-pools can result in self-excited oscillations of the pool surface that may occur in various modes depending on pool shape and size as well as on the surface tension of the molten material [13–16]. Surface oscillations in fusion welding and additive manufacturing have been employed for nonintrusive estimation of melt-pool penetration and geometry during the process [17–20]. Melt-pool oscillations can also be utilised to monitor process stability based on whether the amplitude of oscillations grow or decay over time. Hence, efforts have been made to understanding internal flow behaviour in fusion welding and additive manufacturing melt-pools in the past decades, which are briefly reviewed here.

2.2.1. Forces acting on a melt-pool

Four fluid flow mechanisms are often introduced to describe complex molten metal flow in melting pools as shown schematically in figure 2.2 [21]. The degree of contribution of these forces in melt-pool behaviour varies depending on the operating parameters [5, 22, 23]. Flow instabilities and interactions between the melt-pool and the plasma make this fluidic system even more complex [24–27].

The buoyancy effects originate from variations in the local density of the molten metal, mainly due to the changes in temperature and weakly because of changes in local

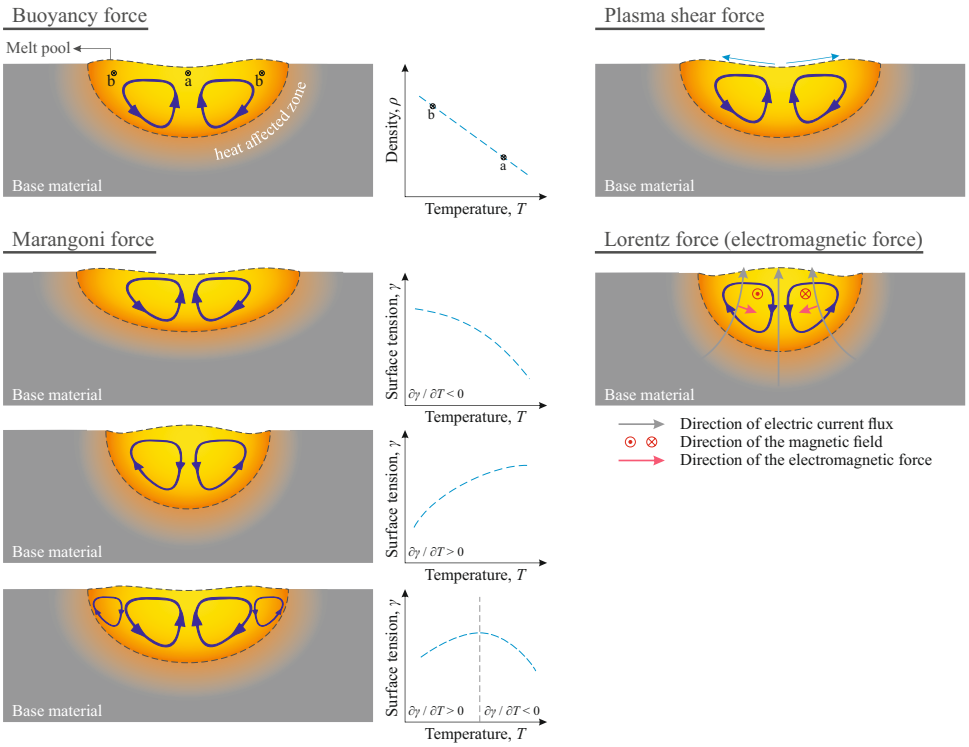

Figure 2.2: Major forces that drive fluid flow in melt-pools in fusion welding and additive manufacturing [21].

composition [28]. The effect of buoyancy force on melt-pool behaviour is suggested to be insignificant if the pool depth is less than one centimetre [6]. Woods and Milner [29] demonstrated that buoyancy force is negligible compared to Lorentz force in arc welding. Interactions between electric and magnetic fields during arc welding generate Lorentz force that drives the flow of conducting fluids from regions of high to regions of low current density [29]. Woods and Milner [29] observed a double circulation flow pattern in the pool by applying a symmetrical current flow, but one-half of this double circulation starts to dominate the other when the current flow was asymmetric. They also reported that the speed of molten metal flow in the pool is higher for materials with higher melting temperatures (such as steels) than materials with lower melting temperatures (such as silver, copper and aluminium). This observation was attributed to the higher degree of constriction of current at the arc root in the melting of high melting-temperature materials. To understand the effects of the buoyancy force on the size of the fusion zone, gas tungsten arc welding has been performed in a centrifuge [30–34], indicating that the fusion zone becomes shallower and wider as the acceleration, synonymous with gravity, increases. However, it should be noted that investigation of the effect of the Coriolis force on the fluid flow in melt-pools was absent in those studies.

Changes in chemical composition of metallic alloys can affect weldability and melt-

pool shape [35–42]. This observation was attributed to changes in the arc characteristics [36] and the interfacial tension of molten metal [37]. Later, an experimental study of Heiple *et al.* [39] indicated that changing the chemical composition of steels can affect the melt-pool shape during laser and electron beam welding. Since arcs are not involved in laser and electron beam welding processes, Heiple *et al.* [39] confirmed that the influence of the chemical composition of steels on melt-pool shape could not be described solely by the alterations to the arc characteristics. Therefore, variable melt-pool penetration, which is not governed by thermal conduction in ferrous alloys [38], could be related to the flow direction at the surfaces. It was known that surface flows mainly arise from surface tension gradients along the liquid-gas interface [43–45]. Molecules that are present at the surface, the electrical condition at the surface, and the temperature of the surface are known as parameters that can affect surface tension of liquids [46–49]. Heiple and Roper [38] proposed that the surface flows of melt-pools are driven primarily by surface tension gradients arising from the temperature gradient at the melt-pool surface. Subsequently, attention has been turned to the surface properties of the molten metal in melt-pools [6, 41, 42, 50, 51]. Previous studies have demonstrated that implementation of the Marangoni force in a fluid flow model can influence the flow pattern in melt-pools and the final pool shape and characteristics (see for instance, [27, 52, 53]). Nowadays, it is widely acknowledged that the Marangoni force is a major driving force for fluid flow in melt-pools [51], particularly for steels.

Marangoni-driven flows are influenced both by temperature gradients (thermocapillary effect) [54] and by the presence of surface-active elements (surfactants) [39, 55, 56]. Surface tension of molten pure metals decreases linearly with increasing temperature [57]. Surfactants change the surface tension of liquids and can induce a solutocapillary effect when distributed inhomogeneously over the surface. Moreover, surfactants affect variation of surface tension with temperature (*i.e.* $\partial\gamma/\partial T$, where γ is the surface tension, and T the temperature) [58]. Phosphorus, sulphur, oxygen, selenium and tellurium are examples of surface-active elements in many inorganic liquids such as molten iron, cooper, silver, chromium, nickel and cobalt [59]. Other elements such as aluminium, calcium, silicon and manganese can also affect the surface tension of molten material through, for instance, reacting with the molten material [60]. The estimated values of surface tension for binary Fe–S and Fe–O alloys [59] are depicted in figure 2.3, assuming that surface active elements (here oxygen and sulphur) are distributed homogeneously over the surface. The temperature coefficient of surface tension ($\partial\gamma/\partial T$) changes from positive to negative at high oxygen or sulphur concentrations, which corresponds to the reduction in oxygen or sulphur solubility at high temperatures [38, 61, 62]. Although the interfacial transport phenomena are of interests in materials processing at elevated temperatures, experimental data refer to a limited set of metals and there is a need for further study in this field [56, 63].

In arc welding and additive manufacturing the plasma jet exerts a shear force on the melt-pool surface, which can play a quite complex role because of the coupling of the melt-pool with the welding arc [52]. The effect of plasma jet shear force is usually ignored in the literature (see for example, [64–70]) since the momentum transferred to the melt-pool by the plasma jet was assumed to be negligible because of the relatively low viscosity of plasma compared with that of the molten metal. However, the effect of

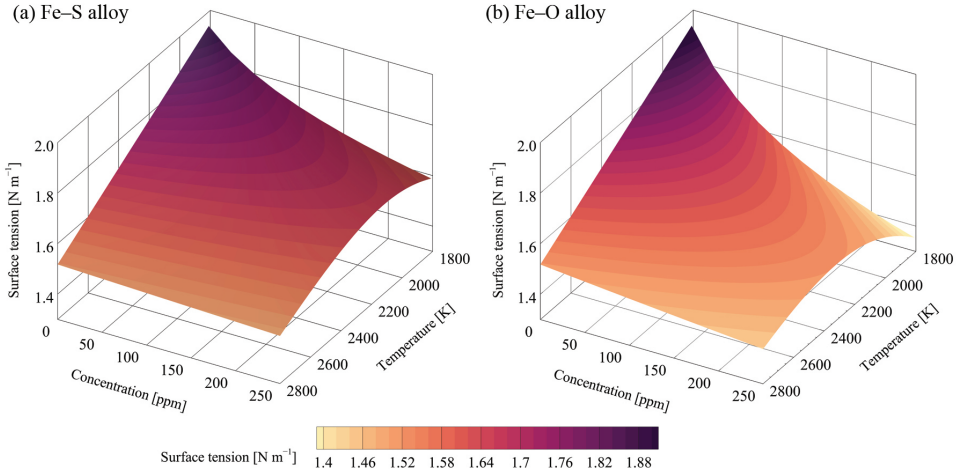

Figure 2.3: The approximated surface tension of (a) Fe-S and (b) Fe-O alloys for different temperatures and concentrations of surface-active elements. Values are calculated using the model proposed by Sahoo *et al.* [59].

plasma jet shear force can become important when the magnitude approaches that of the surface tension shear force. Since the viscosities of the plasma jet and molten metal are different and there is a mismatch in velocities at the interface, surface instabilities (such as Kelvin–Helmholtz hydrodynamic instability [71, 72]) can form [73–76]. Therefore, there is a possibility to generate waves that either grow and cause defects or damp out and result in surface oscillations [15, 77]. Lin and Eagar [78] stated that the effects of arc shear force are suspected to be responsible for the onset of deep penetrations found in high-current welding. Choo and Szekely [79] performed numerical simulations to understand the effects of plasma jet shear force on melt-pool size as well as the surface temperature and velocity. They examined the effects of plasma jet shear force for welding currents between 100 A and 300 A assuming a flat non-deformable melt-pool surface; and concluded that shear force exerted by the plasma jet has little effect in low current welding operations but its effect tends to be pronounced in high current operations. They argued that for deformed surfaces, the surface temperature profile will not be as simple as that of a planar surface and fluctuations in the free-surface shape can affect the heat flux and temperature distribution. Additionally, the surface curvature may change the arc pressure and shear force distributions over the melt-pool surface.

Burleigh and Eagar [80] made measurements of the arc force exerted on the melt-pool during gas tungsten arc welding using a torsion balance apparatus in order to investigate the effects of welding currents on pool shape. They stated that for welding currents higher than approximately 200 A, the arc force might play an important role in producing a significant surface depression and the final melt-pool shape. Based on the results, they argued that the arc force is proportional to the square of the welding current; this argument is consistent with theory [81] and other experiments [25, 82], and contradicts previous measurements [83] that reported a linear relationship between arc force and

welding current. It was also confirmed that the large differences in weld penetration caused by changing the chemical composition of a material cannot be described solely by variations in the arc force. Lin and Eagar [84] proposed a theoretical model (based on a compound vortex) to explain melt-pool surface depression at welding currents higher than 300 A and distinguished three different current ranges. Based on this model, surface depression does not influence the pool shape for welding currents lower than 200 A. For currents between 300 A and 500 A, surface depression influences the pool shape and a circumferential vortex flow was introduced to explain melt-pool surface depression. The shape of the pool may only be influenced by the arc force at currents more than 500 A. This classification agrees with experimental observations of Chihoski [85]. Later, Rokhlin and Guu [25] performed an experimental investigation to establish a relationship between weld penetration and melt-pool surface depression using an integrated system of force sensors and real-time radiography. They found a linear relationship between the arc force and melt-pool depression at welding currents above 200 A. They also noticed that the arc force is about 20% of the sum of the gravitational and surface tension forces.

When a high energy-density beam (*i.e.* electron or laser beam) is employed as the heat source in fusion welding or additive manufacturing, a deep cavity may form in the melt-pool due to the recoil pressure produced by material evaporation [86]. Molten material is removed from the workpiece both in liquid and vapour forms [87, 88]. Liquid ejection from the keyhole is driven by the recoil pressure and the Marangoni force [89, 90]. The keyhole is often unstable and instabilities are known to significantly increase the risk of porosity formation [91, 92]. Since studying keyhole formation is outside the scope of the present work, the readers are referred to previous studies [10, 93–98] for further reading about the reasons of porosity formation.

2.2.2. Flow patterns in melt pools

The interplay between the driving forces introduced in section 2.2.1 can lead to complex unsteady flow patterns. Performing high-resolution measurements of molten metal flow in melt-pools with a reasonable level of accuracy is challenging, mainly due to the opacity of molten metal, small dimensions of the pool ($\mathcal{O}(10^{-5})$–$\mathcal{O}(10^{-3})$) m), high fluid temperatures ($\mathcal{O}(10^{3})$ K) and velocities ($\mathcal{O}(1)\,\mathrm{m\,s^{-1}}$). Hence, experimental measurements of molten metal flow in melt-pools are, to a great extent, limited to visualisation of surface flow patterns. On the basis of experimental measurement of surface-temperature profiles, Kraus [50] categorised the flow patterns into three distinct groups, as shown schematically in figure 2.4. For a negative temperature coefficient of surface tension ($\partial\gamma/\partial T$) the surface flow moves outward resulting in a shallow and wide pool when the electromagnetic forces are relatively small. In contrast, the pool is deep and narrow for positive temperature coefficients of surface tension, and for the cases with relatively large electromagnetic forces the pool becomes deeper. For the cases that the electromagnetic forces are relatively large and the temperature coefficient of surface tension is negative, a double circulation flow pattern was observed; the electromagnetic force is dominant in the inner region and the Marangoni-driven flow is dominant in the outer region. For high current welds (currents higher than 200 A), a multi-cellular flow pattern may form in the pool. Kraus [50] discussed that this observation is similar to Rayleigh–Bénard cellular convection [99, 100], but driven by a different combination of forces. Bénard cells are mainly driven by surface

tension and buoyancy forces, whereas the convection cells in the melt-pool, are driven by surface tension and electromagnetic forces, although they may also be driven by buoyancy forces as well when dealing with high welding currents and large pools. Some of these experiments have been verified later by Zacharia *et al.* [101].

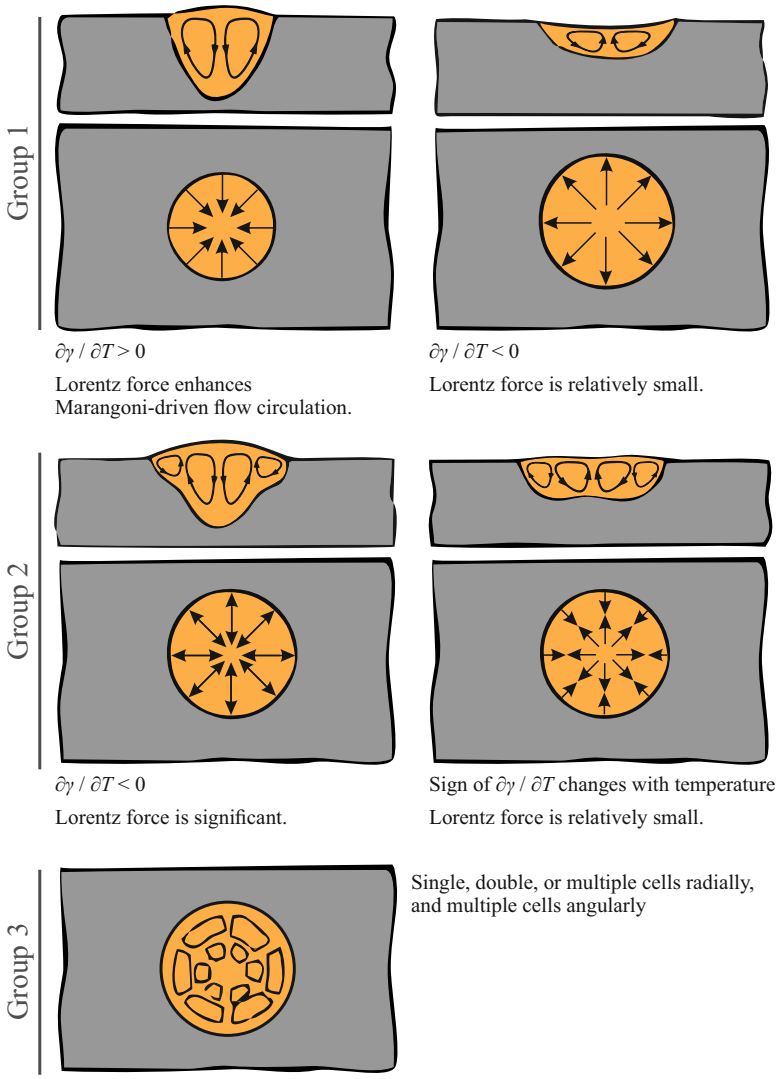

Figure 2.4: Flow patterns in melt-pools categorised by Kraus [50] based on the surface-temperature profiles observed in stationary gas tungsten arc welding.

Applying the particle image velocimetry (PIV) technique, Zhao *et al.* [102] visualised the velocity field on a melt-pool surface during non-stationary gas tungsten arc welding. They observed asymmetrical flow patterns on the surface that oscillated around the melt-

pool centreline, forming vortex structures. Later, the experimental data reported by Zhao *et al.* [62] revealed a transition in fluid flow direction from outward to inward flow during laser spot melting of stainless steel exposed to an oxidising atmosphere. They argued that the transition is related to the temporal variation of the amount of oxygen dissolved in the melt-pool and the laser exposure time that affects the surface temperature. Moreover, an asymmetrical rotational flow pattern in the pool was observed using high-speed videos taken from the surface while the pool seems axisymmetric; this observation has been described through statistical averaging of heat and fluid flow in the pool during the process.

Limmaneevichitr and Kou [103, 104, 105] conducted experiments using a transparent system (*i.e.* sodium nitrate $NaNO_3$) to simulate internal flow behaviour in melt-pools and employed alumina as tracer particles to visualise molten metal flow. Although such experimental simulations offer opportunities to study melt-pool like behaviour, they are often insufficient for detailed analysis of internal flow, due to the imperfect analogy between such systems and real molten metal melt-pools (for instance, differences in Prandtl number, which reflects the ratio of momentum diffusivity to thermal diffusivity). Utilisation of high-energy X-rays has opened up new routes to study internal flow behaviour in melt-pools in fusion welding and additive manufacturing. X-ray transmission real-time imaging has been employed to describe molten metal flow, variable melt-pool penetration and porosity formation in fusion welding [8, 106–112] and additive manufacturing [112–115]. To date, experimental data obtained using *in-situ* X-ray radiography are exclusively limited to two-dimensional radiographic projections, which is often insufficient to fully realise the internal flow behaviour in melt-pools that appears to be inherently three-dimensional. However, such *in-situ* X-ray radiography experiments provide valuable information for model validation that currently relies on comparing numerical predictions with post-solidification pool shapes.

2.3. Numerical simulations of melt-pool behaviour

Numerical simulations of fluid flow in liquid metal melt-pools have been under investigation since the early 1980s and published papers number in the low hundreds (Web of Science search), covering different processes, boundary conditions, materials and geometries (see for example [5, 116–120]). A variety of numerical simulations have been developed to predict and describe various aspects of welding and additive manufacturing across different length and time scales, which are comprehensively reviewed by King *et al.* [121], Francois *et al.* [122] and Wei *et al.* [123], and thus are not repeated here. Such numerical simulations can provide a quantitative physical understanding of welding and additive manufacturing processes, which is essential for realising sensitivities to process parameters, performance margins and control of the process [121]. Here, the focus is primarily on numerical simulation of melt-pool behaviour during fusion welding and additive manufacturing.

Due to the complexity of the multi-scale physical processes involved in fusion welding and additive manufacturing as well as the limitations in available computational capabilities, it is not yet feasible (if not impossible) to perform numerical simulations based on complete descriptions of the physics involved. The combined process–melt-pool models that have been constructed [24, 27, 124–131] are not yet fast enough or reliable

enough to explore the design space for process optimisation. One approach often adopted when simulating aspects of welding and additive manufacturing processes, melt-pools or material response is to decouple the arc from the melt-pool, or the melt-pool from the solidified material and to treat each regime separately under the assumption that boundary conditions between regimes can be approximated with sufficient accuracy. This permits a focus on the regime of interest whilst avoiding excessive simulation complexity and execution time. The disadvantage of this approach is that interesting physics at the regime boundaries and beyond is inevitably ignored in favour of simplifying approximations.

2.3.1. Heat transfer in melt-pools

A critical aspect of modelling fusion welding and additive manufacturing is the description of the energy absorption by the base material that affects the thermal field in the melt-pool and the surrounding material, and hence the structure and properties of the product. The net energy transferred to the workpiece is the sum of all heating and cooling contributions, which may include the energy absorbed from the heat source (arc, laser, electron beam *etc.*) and energy transferred by filler metal droplets and energy lost (or gained) by radiation, convection and vaporisation. The total energy supplied by the power source is not absorbable by the workpiece due to the losses in the process, but the fraction of the total energy absorbed should be sufficient to form a liquid pool. The ratio of the energy required for melting the material to the total energy supplied by the power source (known as 'melting efficiency' [132]) is directly proportional to the energy density, which is a function of operating parameters and equipment characteristics (*e.g.* electrode tip shape, arc length and beam shape). The higher the energy density the faster the material is heated and the lower the amount of the total energy lost by heat conduction in the material [133, 134]. The amount of energy transferred to the workpiece is influenced by the process and depends on the material and the type of the power source [135–137].

Accurately estimating the amount of energy absorbed by the workpiece as well as the energy-density distribution from theoretical calculations is still challenging and therefore experimental studies have been undertaken to determine the efficiency of energy absorption and energy-flux distribution in welding and additive manufacturing [11, 121, 138, 139]. For example, a challenge in determining energy-density distribution is related to its variations with surface deformations during the process [67]. Generally, the models based on experimental observations are the most accurate, but the costs for developing these models are considerable and they are often not suitable for predictive purposes. Various models have been developed to describe heat input to the base material when simulating fusion welding or additive manufacturing; these are summarised by Wei *et al.* [123]. Theoretical models are useful for the cases that experimental data are not available although they have not yet reached sufficient maturity to predict accurate values. Choosing an appropriate approach depends on the purpose of modelling, the required accuracy, available information, the assumptions that are made for specifying the energy-density distribution, the degree of the model complexity and available computational resources.

Depending on how the feeding material is added to the melt-pool, it can add a certain amount of energy to the pool or take some away, changing the thermal field in the pool that in turn can affect the pool penetration. To study the effect of the feeding material

on welding and additive manufacturing processes, two different methods are considered in numerical simulations. One is to simulate the metal transfer explicitly [69, 140–143], the other is to model metal transfer by adding source terms to the governing equations [65, 144, 145]. Modelling droplet transfer by adding source terms to the governing equations is not an option for simulating the start of a process since the melt-pool has not been formed and the droplets do not penetrate in the base material; therefore, the volumetric heat source model with a fixed shape may not be able to model this process accurately. Moreover, mixing in the melt-pool due to the successive droplet impacts is ignored in the implicit approach, which may affect the heat transfer in melt-pool. For gas metal arc welding and wire-arc additive manufacturing processes, the frequency of droplet transfer and the droplet size depends on the operating parameters such as current and shielding gas [146–149]. Deciding between modelling metal transfer explicitly or implicitly depends on the operating parameters and the main interest of a study. Generally, it can be argued that for some conditions, the frequency of droplet transfer is high enough (generally higher than 150 Hz) to assume that the melt-pool response, in terms of molten metal displacement, is small and negligible. Under this condition, the implicit method can be employed to describe material addition to the pool.

A primary mechanism for energy transfer in fusion welding and additive manufacturing is through heat conduction from the melt-pool to the surrounding material [11, 121]. The cooling rate of the pool is influenced by dimensions of the workpiece and thermal conductivity of the surrounding material, which can affect the structure and properties of the product. Heat conduction to the surrounding material is computed during numerical simulations. In computational models, a boundary condition is often set at the outer boundaries of the base material to approximate convective and radiative heat losses, which permits a reduction in the size of the computational domain and thus the calculation time. It is noteworthy that the input parameters to model convective and radiative heat losses (such as the heat transfer coefficient and the radiation emissivity) are often not reported in the published literature.

2.3.2. Fluid dynamics in melt-pools

A complex set of interacting physical mechanisms governs internal flow behaviour in melt-pools during fusion-based manufacturing processes such as solid-liquid phase transformations, heat and mass transfer, free surface deformation and oscillation, and chemical reactions at the surfaces. Fluid flow in the pool often dominates energy transfer in fusion welding and additive manufacturing, which is evident from experimental observations as well as relatively large values of Péclet number ($\mathcal{O}(10^2)$) [11], which indicates the ratio of advective to diffusive heat transfer. Moreover, fluid flow in melt-pools is generally acknowledged as an important factor affecting ripple formation, some sorts of defects (*e.g.* porosity formation, humping, and burn-through), and material homogeneity [11, 21, 121, 150].

Numerical simulations with various levels of complexity have been developed to comprehend the effects of parameters on internal flow behaviour in melt-pools. Complexities in such numerical simulations generally depend on the simplifying assumptions that are made to develop the computational models, which often covers dimensionality (two-dimensional versus three-dimensional), free-surface modelling (non-deformable versus

deformable), molten metal flow regimes (laminar versus turbulent) and modelling surface chemistry. Obviously, some of these assumptions have notable effects on numerical predictions and some of them have negligible effects. For instance, previous experimental and numerical studies have shown that the fluid flow in melt-pools is inherently three-dimensional in most cases [11, 50, 121, 151]; therefore, reducing the dimensionality of the computational models in simulations of melt-pool behaviour is a questionable assumption. Deciding on the level of model sophistication depends on the goals of the study, availability of computational resources and limitations of the theoretical models.

The modelling of internal flow behaviour in melt-pools usually requires extensive knowledge of the thermophysical data of the materials as a function of temperature, particularly at elevated temperatures above the melting point. Unfortunately, a reliable database of temperature-dependent properties for common materials employed in fusion welding and additive manufacturing (*e.g.* steel alloys) is scarce in the literature. Further studies are essential to enhance the accuracy of calculation and measurement of temperature-dependent material properties.

2.3.3. Melt-pool oscillations in welding and additive manufacturing

Melt-pool surface oscillations occur during fusion welding and additive manufacturing due either to fluid motion in the pool that can result in self-excited oscillations or exposing the melt-pool to time-varying external loadings such as welding current pulsation and filler droplet impingement [13–16]. The results reported by Choo *et al.* [24] suggest that changes in free-surface profile and variations in power-density distribution can affect molten metal flow in melt-pools and its stability. Comparing the melt-pool shapes predicted using both deformable and non-deformable surface assumptions, Ha and Kim [152] stated that free-surface oscillations can enhance convection in the pool and influence the pool shape. Different schemes have been proposed to monitor the position of the liquid-gas interface in numerical simulations of fusion welding and additive manufacturing such as interface-tracking methods (often based on the Lagrangian approach), interface-capturing methods (based on the Eulerian approach) and free-surface energy minimisation.

When accounting for surface deformations, the volume-of-fluid (VOF) method developed by Hirt and Nichols [153], based on a Eulerian formulation, is the most common method for modelling the melt-pool behaviour [121, 123, 154]. The volume-of-fluid method employs a fixed grid and is based on the computing the values of a scalar function describing different phases. The scalar function is a step function equal to one if a grid cell is full of the primary phase and zero if the cell contains the secondary fluid phase(s). Accordingly, the interface of different phases is located in grid cells where the value of the scalar function is between zero and one. The boundary conditions at the melt-pool surface (such as interfacial forces and energy fluxes) are defined through volumetric source terms in the surface region. Another Eulerian approach to track the interface is the level-set (LS) method. The advantage of the level-set method over the volume-of-fluid method is in its capability to predict interface sharpness more accurately compared with the smeared interface predicted by the volume-of-fluid method. However, the volume-of-fluid method is superior to the level-set method in that it can guarantee a much better mass conservation.

Another approach for tracking the position of the melt-pool surface is the arbitrary Lagrangian–Eulerian method[155], which is based on aligning a boundary of the computational grid with the interface between two phases and has been employed in simulations of melt-pool behaviour [156–158]. This method results in a sharp interface and allows for the implementation of exact boundary conditions at the interface. When the flow field changes in time, the grid points on the boundary will be updated accordingly and then the interior grid points will be adjusted based on the free-surface profile. Applications of this method for highly-deformed surfaces may cause some stability issues in numerical simulations and increases the errors due to the reduction of mesh quality. A re-meshing process could be interesting to avoid too high distortions but it increases the computational costs as well.

2.4. Summary and conclusions

In the past few decades, significant progress has been made in understanding melt-pool behaviour in fusion welding and additive manufacturing processes. However, further developments are still required to resolve the remaining key problems and issues related to the accuracy and predictability of melt-pool behaviour. The main difficulties in the quantitative analysis of the molten metal flow are the complexity of the physical processes involved, the highly non-linear responses to the process parameters and the rarity of relevant data for material properties at elevated temperatures. Making a balance between the computational costs and the capability of the numerical model to predict the transport phenomena in fusion welding and additive manufacturing is indeed a challenging task. Most of the current models make a lot of non-physical assumptions and are not adequately verified. Furthermore, there is no comprehensive guideline for making simplifying assumptions that retain the physical sense of the problem. Reliable, physically-based correlations between the transport phenomena and properties of the welds or deposits are essential for the development of new numerical models with enhanced capabilities.

The key concepts related to molten metal melt-pool behaviour in fusion welding and additive manufacturing have been briefly discussed in this chapter. Each individual chapter contains an introduction providing further details to the reader.

References

[1] Cornu, J. Historical development of welding. In *Fundamentals of Fusion Welding Technology*, pages 1–9. Springer Berlin Heidelberg, 1988. doi:10.1007/978-3-662-11049-2_1.

[2] Cockrell, B., Edelstein, B., Howe, E., and Mahony, C. Female figurine | Inca | The Metropolitan Museum of Art, 2021. URL: `https://www.metmuseum.org/art/collection/search/317753`.

[3] David, S. A. and DebRoy, T. Current issues and problems in welding science. *Science*, 257 (5069):497–502, 1992. doi:10.1126/science.257.5069.497.

[4] David, S. A. and Vitek, J. M. Correlation between solidification parameters and weld microstructures. *International Materials Reviews*, 34(1):213–245, 1989. doi:10.1179/imr.1989.34.1.213.

[5] Oreper, G. M. and Szekely, J. Heat- and fluid-flow phenomena in weld pools. *Journal of Fluid Mechanics*, 147(-1):53, 1984. doi:10.1017/s0022112084001981.

[6] Mills, K. C. and Keene, B. J. Factors affecting variable weld penetration. *International Materials Reviews*, 35(1):185–216, 1990. doi:10.1179/095066090790323966.

[7] David, S. A., DebRoy, T., and Vitek, J. M. Phenomenological modeling of fusion welding processes. *MRS Bulletin*, 19(1):29–35, 1994. doi:10.1557/s0883769400038835.

[8] Aucott, L., Dong, H., Mirihanage, W., Atwood, R., Kidess, A., Gao, S., Wen, S., Marsden, J., Feng, S., Tong, M., Connolley, T., Drakopoulos, M., Kleijn, C. R., Richardson, I. M., Browne, D. J., Mathiesen, R. H., and Atkinson, H. V. Revealing internal flow behaviour in arc welding and additive manufacturing of metals. *Nature Communications*, 9(1), 2018. doi:10.1038/s41467-018-07900-9.

[9] Khairallah, S. A., Anderson, A. T., Rubenchik, A., and King, W. E. Laser powder-bed fusion additive manufacturing: Physics of complex melt flow and formation mechanisms of pores, spatter, and denudation zones. *Acta Materialia*, 108:36–45, 2016. doi:10.1016/j.actamat.2016.02.014.

[10] Zhao, C., Parab, N. D., Li, X., Fezzaa, K., Tan, W., Rollett, A. D., and Sun, T. Critical instability at moving keyhole tip generates porosity in laser melting. *Science*, 370(6520):1080–1086, 2020. doi:10.1126/science.abd1587.

[11] DebRoy, T. and David, S. A. Physical processes in fusion welding. *Reviews of Modern Physics*, 67(1):85–112, 1995. doi:10.1103/revmodphys.67.85.

[12] DebRoy, T., Wei, H. L., Zuback, J. S., Mukherjee, T., Elmer, J. W., Milewski, J. O., Beese, A. M., Wilson-Heid, A., De, A., and Zhang, W. Additive manufacturing of metallic components – Process, structure and properties. *Progress in Materials Science*, 92:112–224, 2018. doi:10.1016/j.pmatsci.2017.10.001.

[13] Zacksenhouse, M. and Hardt, D. E. Weld pool impedance identification for size measurement and control. *Journal of Dynamic Systems, Measurement, and Control*, 105(3):179–184, 1983. doi:10.1115/1.3140652.

[14] Renwick, R. J. and Richardson, R. W. Experimental investigation of GTA weld pool oscillations. *Welding Journal*, 62(2):29s–35s, 1983. URL: `https://app.aws.org/wj/supplement/WJ_1983_02_s29.pdf`.

[15] Sorensen, C. D. and Eagar, T. W. Modeling of oscillations in partially penetrated weld pools. *Journal of Dynamic Systems, Measurement, and Control*, 112(3):469–474, 1990. doi:10.1115/1.2896166.

[16] Morvan, D. and Bournot, P. Oscillatory flow convection in a melted pool. *International Journal of Numerical Methods for Heat & Fluid Flow*, 6(1):13–20, 1996. doi:10.1108/eum0000000004128.

[17] Xiao, Y. H. and den Ouden, G. A study of GTA weld pool oscillation. *Welding Journal*, 69(8):289s–293s, 1990. URL: `http://files.aws.org/wj/supplement/WJ_1990_08_s289.pdf`.

[18] Xiao, Y. H. and den Ouden, G. Weld pool oscillation during GTA welding of mild steel. *Welding Journal*, 72(8):428s–434s, 1993. URL: `http://files.aws.org/wj/supplement/WJ_1993_08_s428.pdf`.

[19] Yudodibroto, Y. B. *Liquid metal oscillations and arc behaviour during welding*. PhD dissertation, Delft University of Technology, 2010. URL: http://resolver.tudelft.nl/uuid:dcae1f78-9186-4161-ad88-711f27781335.

[20] Caprio, L., Demir, A. G., and Previtali, B. Observing molten pool surface oscillations during keyhole processing in laser powder bed fusion as a novel method to estimate the penetration depth. *Additive Manufacturing*, 36:101470, 2020. doi:10.1016/j.addma.2020.101470.

[21] Kou, S. *Welding Metallurgy*. John Wiley & Sons, Inc., 2002. doi:10.1002/0471434027.

[22] Kim, W.-H., Fan, H. G., and Na, S.-J. Effect of various driving forces on heat and mass transfer in arc welding. *Numerical Heat Transfer, Part A: Applications*, 32(6):633–652, 1997. doi:10.1080/10407789708913910.

[23] Wu, F., Falch, K. V., Guo, D., English, P., Drakopoulos, M., and Mirihanage, W. Time evolved force domination in arc weld pools. *Materials & Design*, 190:108534, 2020. doi:10.1016/j.matdes.2020.108534.

[24] Choo, R. T. C., Szekely, J., and Westhoff, R. C. Modeling of high-current arcs with emphasis on free surface phenomena in the weld pool. *Welding Journal*, 69(9):346s–361s, 1990. URL: http://files.aws.org/wj/supplement/WJ_1990_09_s346.pdf.

[25] Rokhlin, S. I. and Guu, A. C. A study of arc force, pool depression, and weld penetration during gas tungsten arc welding. *Welding Journal*, 72(8):381s–390s, 1993. URL: https://app.aws.org/wj/supplement/WJ_1993_08_s381.pdf.

[26] Tanaka, M. and Lowke, J. J. Predictions of weld pool profiles using plasma physics. *Journal of Physics D: Applied Physics*, 40(1):R1–R23, 2006. doi:10.1088/0022-3727/40/1/r01.

[27] Mougenot, J., Gonzalez, J.-J., Freton, P., and Masquère, M. Plasma–weld pool interaction in tungsten inert-gas configuration. *Journal of Physics D: Applied Physics*, 46(13):135206, 2013. doi:10.1088/0022-3727/46/13/135206.

[28] Tsai, M. C. and Kou, S. Weld pool convection and expansion due to density variations. *Numerical Heat Transfer, Part A: Applications*, 17(1):73–89, 1990. doi:10.1080/10407789008944733.

[29] Woods, R. A. and Milner, D. R. Motion in the weld pool in arc welding. *Welding Journal*, 50(4):163s–173s, 1971. URL: http://files.aws.org/wj/supplement/WJ_1971_04_s163.pdf.

[30] Domey, J., Aidun, D. K., Ahmadi, G., Regel, L. L., and Wilcox, W. R. Numerical simulation of the effect of gravity on weld pool shape. In *Materials Processing in High Gravity*, pages 193–202. Springer US, 1994. doi:10.1007/978-1-4615-2520-2_20.

[31] Aidun, D. K. and Martin, S. A. Penetration in spot GTA welds during centrifugation. *Journal of Materials Engineering and Performance*, 7(5):597–600, 1998. doi:10.1361/105994998770347431.

[32] Aidun, D., Domey, J., and Ahmadi, G. Effect of high gravity on weld fusion zone shape. *Welding Journal*, 79(6):145s–150s, 2000. URL: https://app.aws.org/wj/supplement/WJ_2000_06_s145.pdf.

[33] Aidun, D. K. Influence of simulated high-G on the weld size of Al–Li alloy. *Acta Astronautica*, 48(2-3):153–156, 2001. doi:10.1016/s0094-5765(00)00151-x.

[34] Eisazadeh, H., Haines, D. J., and Torabizadeh, M. Effects of gravity on mechanical properties of GTA welded joints. *Journal of Materials Processing Technology*, 214(5):1136–1142, 2014. doi:10.1016/j.jmatprotec.2014.01.002.

[35] Glickstein, S. S. and Yeniscavich, W. *A Review of Minor Element Effects on the Welding Arc and Weld Penetration*. Welding Research Council bulletin: Welding Research Council. Welding Research Council bulletin, 1977. ISBN 9781581452259.

[36] Savage, W., Nippes, E., and Goodwin, G. Effect of minor elements on fusion zone dimensions of Inconel 600. *Welding Journal*, 56(4):126s–132s, 1977. URL: https://app.aws.org/wj/supplement/WJ_1977_04_s126.pdf.

[37] Roper, J. and Olson, D. Capillarity effects in the GTA weld penetration of 21-6-9 stainless steel. *Welding Journal*, 57(4):103s–108s, 1978. URL: https://app.aws.org/wj/supplement/WJ_1978_04_s103.pdf.

[38] Heiple, C. R. and Roper, J. R. Mechanism for minor element effect on GTA fusion zone geometry. *Welding Journal*, 61(4):97s–102s, 1982. URL: https://app.aws.org/wj/supplement/WJ_1982_04_s97.pdf.

[39] Heiple, C. R., Roper, J. R., Stagner, R. T., and Aden, R. J. Surface active element effects on the shape of GTA, laser, and electron beam welds. *Welding Journal*, 62(3):72s–77s, 1983. URL: http://files.aws.org/wj/supplement/WJ_1983_03_s72.pdf.

[40] Pollard, B. The effects of minor elements on the welding characteristics of stainless steel. *Welding Journal*, 67(9):202s–213s, 1988. URL: https://app.aws.org/wj/supplement/WJ_1988_09_s202.pdf.

[41] Shirali, A. A. and Mills, K. C. The effect of welding parameters on penetration in GTA welds. *Welding Journal*, 72(7):347s–353s, 1993. URL: https://app.aws.org/wj/supplement/WJ_1993_07_s347.pdf.

[42] Pierce, S. W., Burgardt, P., and Olson, D. L. Thermocapillary and arc phenomena in stainless steel welding. *Welding Journal*, 78(2):45s–52s, 1999. URL: https://app.aws.org/wj/supplement/Pierce/ARTICLE3.pdf.

[43] Levich, V. G. and Krylov, V. S. Surface-Tension-Driven Phenomena. *Annual Review of Fluid Mechanics*, 1(1):293–316, 1969. doi:10.1146/annurev.fl.01.010169.001453.

[44] Chang, C. E. and Wilcox, W. R. Analysis of surface tension driven flow in floating zone melting. *International Journal of Heat and Mass Transfer*, 19(4):355–366, 1976. doi:10.1016/0017-9310(76)90091-0.

[45] Schwabe, D., Scharmann, A., Preisser, F., and Oeder, R. Experiments on surface tension driven flow in floating zone melting. *Journal of Crystal Growth*, 43(3):305–312, 1978. doi:10.1016/0022-0248(78)90387-1.

[46] Defay, R., Prigogine, I., and Bellemans, A. *Surface Tension and Adsorption*. Longmans, London, 1966.

[47] Myers, D. *Surfaces, Interfaces, and Colloids*. John Wiley & Sons, Inc., New York, 1999. doi:10.1002/0471234990.

[48] Hartland, S., editor. *SURFACE AND INTERFACIAL TENSION: measurement, theory, and applications*, volume 119. CRC Press, New York, 2004. ISBN 9780367394493.

[49] Deyev, G. *Surface phenomena in fusion welding processes*. CRC Taylor & Francis, Boca Raton, FL, 2006. ISBN 1420036297.

[50] Kraus, H. Experimental measurement of stationary SS 304, SS 316 L and 8630 GTA weld pool surface temperatures. *Welding Journal*, 95(8):273s–279s, 1989. URL: `http://s3.amazonaws.com/WJ-www.aws.org/supplement/WJ_2016_08_s273.pdf`.

[51] Mills, K. C., Keene, B. J., Brooks, R. F., and Shirali, A. Marangoni effects in welding. *Philosophical Transactions of the Royal Society A: Mathematical, Physical and Engineering Sciences*, 356 (1739):911–925, 1998. doi:10.1098/rsta.1998.0196.

[52] Choo, R. T. C., Szekely, J., and Westhoff, R. C. On the calculation of the free surface temperature of gas-tungsten-arc weld pools from first principles: Part I. modeling the welding arc. *Metallurgical and Materials Transactions B*, 23(3):357–369, 1992. doi:10.1007/bf02656291.

[53] Traidia, A., Roger, F., Guyot, E., Schroeder, J., and Lubineau, G. Hybrid 2D–3D modelling of GTA welding with filler wire addition. *International Journal of Heat and Mass Transfer*, 55 (15-16):3946–3963, 2012. doi:10.1016/j.ijheatmasstransfer.2012.03.025.

[54] Egry, I., Lohoefer, G., and Jacobs, G. Surface tension of liquid metals: Results from measurements on ground and in space. *Physical Review Letters*, 75(22):4043–4046, 1995. doi:10.1103/physrevlett.75.4043.

[55] Lu, S., Fujii, H., and Nogi, K. Sensitivity of marangoni convection and weld shape variations to welding parameters in O_2–Ar shielded GTA welding. *Scripta Materialia*, 51(3):271–277, 2004. doi:10.1016/j.scriptamat.2004.03.004.

[56] Egry, I., Ricci, E., Novakovic, R., and Ozawa, S. Surface tension of liquid metals and alloys — recent developments. *Advances in Colloid and Interface Science*, 159(2):198–212, 2010. doi:10.1016/j.cis.2010.06.009.

[57] Keene, B. J. Review of data for the surface tension of pure metals. *International Materials Reviews*, 38(4):157–192, 1993. doi:10.1179/imr.1993.38.4.157.

[58] Paul, A. and DebRoy, T. Free surface flow and heat transfer in conduction mode laser welding. *Metallurgical Transactions B*, 19(6):851–858, 1988. doi:10.1007/bf02651409.

[59] Sahoo, P., Debroy, T., and McNallan, M. J. Surface tension of binary metal—surface active solute systems under conditions relevant to welding metallurgy. *Metallurgical Transactions B*, 19(3):483–491, 1988. doi:10.1007/bf02657748.

[60] Kidess, A. *Multiscale modeling of mesoscale phenomena in weld pools*. PhD dissertation, Delft University of Technology, Delft, The Netherlands, 2016.

[61] Keene, B. J., Mills, K. C., and Brooks, R. F. Surface properties of liquid metals and their effects on weldability. *Materials Science and Technology*, 1(7):559–567, 1985. doi:10.1179/mst.1985.1.7.559.

[62] Zhao, C. X., Kwakernaak, C., Pan, Y., Richardson, I. M., Saldi, Z., Kenjeres, S., and Kleijn, C. R. The effect of oxygen on transitional Marangoni flow in laser spot welding. *Acta Materialia*, 58 (19):6345–6357, 2010. doi:10.1016/j.actamat.2010.07.056.

[63] Brillo, J. *Thermophysical Properties of Multicomponent Liquid Alloys*. De Gruyter Oldenbourg, Berlin, Boston, 2016. doi:10.1515/9783110468991.

[64] Zhang, W., Kim, C.-H., and DebRoy, T. Heat and fluid flow in complex joints during gas metal arc welding—Part I: Numerical model of fillet welding. *Journal of Applied Physics*, 95(9): 5210–5219, 2004. doi:10.1063/1.1699485.

[65] Chen, J., Schwenk, C., Wu, C. S., and Rethmeier, M. Predicting the influence of groove angle on heat transfer and fluid flow for new gas metal arc welding processes. *International Journal of Heat and Mass Transfer*, 2011. doi:10.1016/j.ijheatmasstransfer.2011.08.046.

[66] Oreper, G. M. and Szekely, J. A comprehensive representation of transient. *Metallurgical Transactions A*, 18(7):1325–1332, 1987. doi:10.1007/bf02647202.

[67] Ko, S. H., Yoo, C. D., Farson, D. F., and Choi, S. K. Mathematical modeling of the dynamic behavior of gas tungsten arc weld pools. *Metallurgical and Materials Transactions B*, 31(6): 1465–1473, 2000. doi:10.1007/s11663-000-0031-1.

[68] Ko, S. H., Choi, S. K., and Yoo, C. D. Effects of surface depression on pool convection and geometry in stationary GTAW. *Welding Journal*, 80(2):39s–45s, 2001. URL: `https://app.aws.org/wj/supplement/Ko02-01.pdf`.

[69] Hu, J., Guo, H., and Tsai, H. L. Weld pool dynamics and the formation of ripples in 3D gas metal arc welding. *International Journal of Heat and Mass Transfer*, 51(9-10):2537–2552, 2008. doi:10.1016/j.ijheatmasstransfer.2007.07.042.

[70] Wu, D., Hua, X., Ye, D., and Li, F. Understanding of humping formation and suppression mechanisms using the numerical simulation. *International Journal of Heat and Mass Transfer*, 104:634–643, 2017. doi:10.1016/j.ijheatmasstransfer.2016.08.110.

[71] Drazin, P. G. *Hydrodynamic stability*. Cambridge University Press, Cambridge Cambridgeshire New York, 1981. ISBN 9780521227988.

[72] Charru, F. *Hydrodynamic instabilities*. Cambridge University Press, Cambridge New York, 2011. ISBN 9781139112673.

[73] Soderstrom, E. and Mendez, P. Humping mechanisms present in high speed welding. *Science and Technology of Welding and Joining*, 11(5):572–579, 2006. doi:10.1179/174329306x120787.

[74] Kumar, A. and Debroy, T. Toward a unified model to prevent humping defects in gas tungsten arc welding. *Welding Journal*, 85(12):292s–304s, 2006. ISSN 0043-2296. URL: `https://app.aws.org/wj/supplement/wj1206-292.pdf`.

[75] Wei, P. S. Thermal science of weld bead defects: A Review. *Journal of Heat Transfer*, 133(3), 2010. doi:10.1115/1.4002445.

[76] Meng, X., Qin, G., and Zou, Z. Investigation of humping defect in high speed gas tungsten arc welding by numerical modelling. *Materials & Design*, 94:69–78, 2016. doi:10.1016/j.matdes.2016.01.019.

[77] Sorensen, C. D. and Eagar, T. W. Measurement of oscillations in partially penetrated weld pools through spectral analysis. *Journal of Dynamic Systems, Measurement, and Control*, 112 (3):463–468, 1990. doi:10.1115/1.2896165.

[78] Lin, M. L. and Eagar, T. W. Influence of surface depression and convection on arc weld pool geometry. *Transport Phenomena in Materials Processing*, 10:63–69, 1983.

[79] Choo, R. and Szekely, J. The effect of gas shear stress on Marangoni flows in arc welding. *Welding Journal*, 70(9):223s–233s, 1991. URL: https://app.aws.org/wj/supplement/WJ_1991_09_s223.pdf.

[80] Burleigh, T. D. and Eagar, T. W. Measurement of the force exerted by a welding arc. *Metallurgical Transactions A*, 14(5):1223–1224, 1983. doi:10.1007/bf02659870.

[81] Converti, J. *Plasma-jets in arc welding*. PhD dissertation, Massachusetts Institute of Technology, Department of Mechanical Engineering, 1981. URL: http://dspace.mit.edu/handle/1721.1/7582.

[82] Adonyi, Y., Richardson, R. W., and Baeslack, W. A. I. I. I. Investigation of arc force effects in subsurface GTA welding. *Welding Journal*, 71(9):321s–330s, 1992. URL: http://files.aws.org/wj/supplement/WJ_1992_09_s321.pdf.

[83] Savage, W. F., Nippes, E. F., and Agusa, K. Effect of arc force on defect formation in GTA welding. *Welding Journal*, 58(7):212s–224s, 1979. URL: http://files.aws.org/wj/supplement/WJ_1979_07_s212.pdf.

[84] Lin, M. L. and Eagar, T. W. Influence of arc pressure on weld pool geometry. *Welding Journal*, 64(6):163s–169s, 1985. URL: http://files.aws.org/wj/supplement/WJ_1985_06_s163.pdf.

[85] Chihoski, R. A. The rationing of power between the gas tungsten arc and electrode. *Welding Journal*, 49(2):69s–82s, 1970. URL: https://app.aws.org/wj/supplement/WJ_1970_02_s69.pdf.

[86] Duley, W. W. *Laser Welding*. John Wiley & Sons, New York, 1998. ISBN 0471246794.

[87] Fabbro, R., Hamadou, M., and Coste, F. Metallic vapor ejection effect on melt pool dynamics in deep penetration laser welding. *Journal of Laser Applications*, 16(1):16–19, 2004. doi:10.2351/1.1642633.

[88] Fabbro, R., Slimani, S., Doudet, I., Coste, F., and Briand, F. Experimental study of the dynamical coupling between the induced vapour plume and the melt pool for Nd–Yag CW laser welding. *Journal of Physics D: Applied Physics*, 39(2):394–400, 2006. doi:10.1088/0022-3727/39/2/023.

[89] Semak, V. V., Hopkins, J. A., McCay, M. H., and McCay, T. D. Melt pool dynamics during laser welding. *Journal of Physics D: Applied Physics*, 28(12):2443–2450, 1995. doi:10.1088/0022-3727/28/12/008.

[90] Ki, H., Mohanty, P. S., and Mazumder, J. Modelling of high-density laser-material interaction using fast level set method. *Journal of Physics D: Applied Physics*, 34(3):364–372, 2001. doi:10.1088/0022-3727/34/3/320.

[91] Matsunawa, A., Kim, J.-D., Seto, N., Mizutani, M., and Katayama, S. Dynamics of keyhole and molten pool in laser welding. *Journal of Laser Applications*, 10(6):247–254, 1998. doi:10.2351/1.521858.

[92] Lee, J. Y., Ko, S. H., Farson, D. F., and Yoo, C. D. Mechanism of keyhole formation and stability in stationary laser welding. *Journal of Physics D: Applied Physics*, 35(13):1570–1576, 2002. doi:10.1088/0022-3727/35/13/320.

[93] Seto, N., Katayama, S., and Matsunawa, A. Porosity formation mechanism and suppression procedure in laser welding of aluminium alloys. *Welding International*, 15(3):191–202, 2001. doi:10.1080/09507110109549341.

[94] Matsunawa, A., Mizutani, M., Katayama, S., and Seto, N. Porosity formation mechanism and its prevention in laser welding. *Welding International*, 17(6):431–437, 2003. doi:10.1533/wint.2003.3138.

[95] Zhou, J. and Tsai, H.-L. Porosity formation and prevention in pulsed laser welding. *Journal of Heat Transfer*, 129(8):1014–1024, 2006. doi:10.1115/1.2724846.

[96] Meng, W., Li, Z., Lu, F., Wu, Y., Chen, J., and Katayama, S. Porosity formation mechanism and its prevention in laser lap welding for T-joints. *Journal of Materials Processing Technology*, 214(8):1658–1664, 2014. doi:10.1016/j.jmatprotec.2014.03.011.

[97] Hojjatzadeh, S. M. H., Parab, N. D., Yan, W., Guo, Q., Xiong, L., Zhao, C., Qu, M., Escano, L. I., Xiao, X., Fezzaa, K., Everhart, W., Sun, T., and Chen, L. Pore elimination mechanisms during 3D printing of metals. *Nature Communications*, 10(1), 2019. doi:10.1038/s41467-019-10973-9.

[98] Cunningham, R., Zhao, C., Parab, N., Kantzos, C., Pauza, J., Fezzaa, K., Sun, T., and Rollett, A. D. Keyhole threshold and morphology in laser melting revealed by ultrahigh-speed x-ray imaging. *Science*, 363(6429):849–852, 2019. doi:10.1126/science.aav4687.

[99] Koschmieder, E. L. *Bénard Cells and Taylor Vortices*. Cambridge monographs on mechanics and applied mathematics. Cambridge University Press, Cambridge, England, 1993. ISBN 0521402042. URL: `https://www.ebook.de/de/product/10947690/e_l_koschmieder_b_nard_cells_and_taylor_vortices.html`.

[100] Normand, C., Pomeau, Y., and Velarde, M. G. Convective instability: A physicist's approach. *Reviews of Modern Physics*, 49(3):581–624, 1977. doi:10.1103/revmodphys.49.581.

[101] Zacharia, T., David, S. A., Vitek, J. M., and Kraus, H. G. Computational modeling of stationary gastungsten-arc weld pools and comparison to stainless steel 304 experimental results. *Metallurgical Transactions B*, 22(2):243–257, 1991. doi:10.1007/bf02652489.

[102] Zhao, C. X., van Steijn, V., Richardson, I. M., Kleijn, C. R., Kenjeres, S., and Saldi, Z. Unsteady interfacial phenomena during inward weld pool flow with an active surface oxide. *Science and Technology of Welding and Joining*, 14(2):132–140, 2009. doi:10.1179/136217108x370281.

[103] Limmaneevichitr, C. and Kou, S. Visualization of Marangoni convection in simulated weld pools. *Welding Journal*, 79(5):126s–135s, 2000. URL: `https://app.aws.org/wj/supplement/05-2000-LIMMANEEVICHITR-s.pdf`.

[104] Limmaneevichitr, C. and Kou, S. Experiments to simulate effect of Marangoni convection on weld pool shape. *Welding Journal*, 79(8):231s–237s, 2000. URL: `https://app.aws.org/wj/supplement/WJ_2000_08_s231.pdf`.

[105] Limmaneevichitr, C. and Kou, S. Visualization of Marangoni convection in simulated weld pools containing a surface-active agent. *Welding Journal*, 79(11):324s–330s, 2000. URL: `https://app.aws.org/wj/supplement/11-2000-LIMMANEEVICHITR-s.pdf`.

[106] Naito, Y., Mizutani, M., and Katayama, S. Effect of oxygen in ambient atmosphere on penetration characteristics in single yttrium–aluminum–garnet laser and hybrid welding. *Journal of Laser Applications*, 18(1):21–27, 2006. doi:10.2351/1.2164484.

[107] Kawahito, Y., Mizutani, M., and Katayama, S. High quality welding of stainless steel with 10 kW high power fibre laser. *Science and Technology of Welding and Joining*, 14(4):288–294, 2009. doi:10.1179/136217108x372531.

[108] Gatzen, M., Tang, Z., Vollertsen, F., Mizutani, M., and Katayama, S. X-ray investigation of melt flow behavior under magnetic stirring regime in laser beam welding of aluminum. *Journal of Laser Applications*, 23(3):032002, 2011. doi:10.2351/1.3580552.

[109] Peng, J., Li, L., Lin, S., Zhang, F., Pan, Q., and Katayama, S. High-speed X-Ray transmission and numerical study of melt flows inside the molten pool during laser welding of aluminum alloy. *Mathematical Problems in Engineering*, 2016:1–13, 2016. doi:10.1155/2016/1409872.

[110] Gao, M., Kawahito, Y., and Kajii, S. Observation and understanding in laser welding of pure titanium at subatmospheric pressure. *Optics Express*, 25(12):13539, 2017. doi:10.1364/oe.25.013539.

[111] Börner, S., Dittrich, D., Mohlau, P., Leyens, C., García-Moreno, F., Kamm, P. H., Neu, T. R., and Schlepütz, C. M. In situ observation with x-ray for tentative exploration of laser beam welding processes for aluminum-based alloys. *Journal of Laser Applications*, 33(1):012026, 2021. doi:10.2351/7.0000315.

[112] Chen, Y., Clark, S. J., Huang, Y., Sinclair, L., Leung, C. L. A., Marussi, S., Connolley, T., Magdysyuk, O. V., Atwood, R. C., Baxter, G. J., Jones, M. A., Todd, I., and Lee, P. D. In situ X-ray quantification of melt pool behaviour during directed energy deposition additive manufacturing of stainless steel. *Materials Letters*, 286:129205, 2021. doi:10.1016/j.matlet.2020.129205.

[113] Leung, C. L. A., Marussi, S., Towrie, M., del Val Garcia, J., Atwood, R. C., Bodey, A. J., Jones, J. R., Withers, P. J., and Lee, P. D. Laser-matter interactions in additive manufacturing of stainless steel SS316l and 13-93 bioactive glass revealed by in situ X-ray imaging. *Additive Manufacturing*, 24:647–657, 2018. doi:10.1016/j.addma.2018.08.025.

[114] Leung, C. L. A., Marussi, S., Atwood, R. C., Towrie, M., Withers, P. J., and Lee, P. D. In situ X-ray imaging of defect and molten pool dynamics in laser additive manufacturing. *Nature Communications*, 9(1), 2018. doi:10.1038/s41467-018-03734-7.

[115] Wolff, S. J., Webster, S., Parab, N. D., Aronson, B., Gould, B., Greco, A., and Sun, T. In-situ observations of directed energy deposition additive manufacturing using high-speed X-ray imaging. *JOM*, 73(1):189–200, 2020. doi:10.1007/s11837-020-04469-x.

[116] Atthey, D. R. A mathematical model for fluid flow in a weld pool at high currents. *Journal of Fluid Mechanics*, 98(4):787–801, 1980. doi:10.1017/s0022112080000390.

[117] Kou, S. and Sun, D. K. Fluid flow and weld penetration in stationary arc welds. *Metallurgical Transactions A*, 16(1):203–213, 1985. doi:10.1007/bf02815302.

[118] Craine, R. E. On determining the shape of weld pools. *Applied Scientific Research*, 44(1-2): 261–275, 1987. doi:10.1007/bf00412017.

[119] McLay, R. and Carey, G. F. Coupled heat transfer and viscous flow, and magnetic effects in weld pool analysis. *International Journal for Numerical Methods in Fluids*, 9(6):713–730, 1989. doi:10.1002/fld.1650090605.

[120] Zacharia, T., Eraslan, A. H., Aidun, D. K., and David, S. A. Three-dimensional transient model for arc welding process. *Metallurgical Transactions B*, 20(5):645–659, 1989. doi:10.1007/bf02655921.

[121] King, W. E., Anderson, A. T., Ferencz, R. M., Hodge, N. E., Kamath, C., Khairallah, S. A., and Rubenchik, A. M. Laser powder bed fusion additive manufacturing of metals; physics, computational, and materials challenges. *Applied Physics Reviews*, 2(4):041304, 2015. doi:10.1063/1.4937809.

[122] Francois, M. M., Sun, A., King, W. E., Henson, N. J., Tourret, D., Bronkhorst, C. A., Carlson, N. N., Newman, C. K., Haut, T., Bakosi, J., Gibbs, J. W., Livescu, V., Wiel, S. A. V., Clarke, A. J., Schraad, M. W., Blacker, T., Lim, H., Rodgers, T., Owen, S., Abdeljawad, F., Madison, J., Anderson, A. T., Fattebert, J.-L., Ferencz, R. M., Hodge, N. E., Khairallah, S. A., and Walton, O. Modeling of additive manufacturing processes for metals: Challenges and opportunities. *Current Opinion in Solid State and Materials Science*, 21(4):198–206, 2017. doi:10.1016/j.cossms.2016.12.001.

[123] Wei, H. L., Mukherjee, T., Zhang, W., Zuback, J. S., Knapp, G. L., De, A., and DebRoy, T. Mechanistic models for additive manufacturing of metallic components. *Progress in Materials Science*, 116:100703, 2021. doi:10.1016/j.pmatsci.2020.100703.

[124] Kim, W. H., Fan, H. G., and Na, S. J. A mathematical model of gas tungsten arc welding considering the cathode and the free surface of the weld pool. *Metallurgical and Materials Transactions B*, 28(4):679–686, 1997. doi:10.1007/s11663-997-0042-2.

[125] Xu, G., Hu, J., and Tsai, H. L. Three-dimensional modeling of arc plasma and metal transfer in gas metal arc welding. *International Journal of Heat and Mass Transfer*, 52(7-8):1709–1724, 2009. doi:10.1016/j.ijheatmasstransfer.2008.09.018.

[126] Tanaka, M., Yamamoto, K., Tashiro, S., Nakata, K., Yamamoto, E., Yamazaki, K., Suzuki, K., Murphy, A. B., and Lowke, J. J. Time-dependent calculations of molten pool formation and thermal plasma with metal vapour in gas tungsten arc welding. *Journal of Physics D: Applied Physics*, 43(43):434009, 2010. doi:10.1088/0022-3727/43/43/434009.

[127] Murphy, A. B. A self-consistent three-dimensional model of the arc, electrode and weld pool in gas–metal arc welding. *Journal of Physics D: Applied Physics*, 44(19):194009, 2011. doi:10.1088/0022-3727/44/19/194009.

[128] Chen, X., Mu, Z., Hu, R., Liang, L., Murphy, A. B., and Pang, S. A unified model for coupling mesoscopic dynamics of keyhole, metal vapor, arc plasma, and weld pool in laser-arc hybrid welding. *Journal of Manufacturing Processes*, 41:119–134, 2019. doi:10.1016/j.jmapro.2019.03.034.

[129] Cadiou, S., Courtois, M., Carin, M., Berckmans, W., and masson, P. L. 3D heat transfer, fluid flow and electromagnetic model for cold metal transfer wire arc additive manufacturing (Cmt-Waam). *Additive Manufacturing*, 36:101541, 2020. doi:10.1016/j.addma.2020.101541.

[130] Wu, F., Flint, T. F., Falch, K. V., Smith, M. C., Drakopoulos, M., and Mirihanage, W. Mapping flow evolution in gas tungsten arc weld pools. *International Journal of Heat and Mass Transfer*, 179:121679, 2021. doi:10.1016/j.ijheatmasstransfer.2021.121679.

[131] Wang, D. and Lu, H. Numerical analysis of internal flow of molten pool in pulsed gas tungsten arc welding using a fully coupled model with free surface. *International Journal of Heat and Mass Transfer*, 165:120572, 2021. doi:10.1016/j.ijheatmasstransfer.2020.120572.

[132] Fuerschbach, P. W. and Knorovsky, G. A. A study of melting efficiency in plasma arc and gas tungsten arc welding. *Welding Journal*, 70(11):287s–297s, 1991. URL: https://app.aws.org/wj/supplement/WJ_1991_11_s287.pdf.

[133] Kou, S. and Le, Y. Three-dimensional heat flow and solidification during the autogenous GTA welding of aluminum plates. *Metallurgical Transactions A*, 14(11):2245–2253, 1983. doi:10.1007/bf02663298.

[134] DuPont, J. N. and Marder, A. R. Thermal efficiency of arc welding processes. *Welding Journal*, 74(12):406s–416s, 1995. URL: https://app.aws.org/wj/supplement/WJ_1995_12_s406.pdf.

[135] Kim, W.-H. and Na, S.-J. Heat and fluid flow in pulsed current GTA weld pool. *International Journal of Heat and Mass Transfer*, 41(21):3213–3227, 1998. doi:10.1016/s0017-9310(98)00052-0.

[136] Goodarzi, M., Choo, R., Takasu, T., and Toguri, J. M. The effect of the cathode tip angle on the gas tungsten arc welding arc and weld pool: II. the mathematical model for the weld pool. *Journal of Physics D: Applied Physics*, 31(5):569–583, 1998. doi:10.1088/0022-3727/31/5/014.

[137] Murphy, A. B., Tanaka, M., Tashiro, S., Sato, T., and Lowke, J. J. A computational investigation of the effectiveness of different shielding gas mixtures for arc welding. *Journal of Physics D: Applied Physics*, 42(11):115205, 2009. doi:10.1088/0022-3727/42/11/115205.

[138] Murphy, A. B. The effects of metal vapour in arc welding. *Journal of Physics D: Applied Physics*, 43(43):434001, 2010. doi:10.1088/0022-3727/43/43/434001.

[139] Ye, J., Khairallah, S. A., Rubenchik, A. M., Crumb, M. F., Guss, G., Belak, J., and Matthews, M. J. Energy coupling mechanisms and scaling behavior associated with laser powder bed fusion additive manufacturing. *Advanced Engineering Materials*, 21(7):1900185, 2019. doi:10.1002/adem.201900185.

[140] Fan, H. G. and Kovacevic, R. Three-dimensional model for gas tungsten arc welding with filler metal. *Proceedings of the Institution of Mechanical Engineers, Part B: Journal of Engineering Manufacture*, 220(7):1107–1115, 2006. doi:10.1243/09544054jem406.

[141] Cho, D.-W., Na, S.-J., Cho, M.-H., and Lee, J.-S. Simulations of weld pool dynamics in V-groove GTA and GMA welding. *Welding in the World*, 57(2):223–233, 2013. doi:10.1007/s40194-012-0017-z.

[142] Zhou, X., Zhang, H., Wang, G., and Bai, X. Three-dimensional numerical simulation of arc and metal transport in arc welding based additive manufacturing. *International Journal of Heat and Mass Transfer*, 103:521–537, 2016. doi:10.1016/j.ijheatmasstransfer.2016.06.084.

[143] Cheon, J., Kiran, D. V., and Na, S.-J. CFD based visualization of the finger shaped evolution in the gas metal arc welding process. *International Journal of Heat and Mass Transfer*, 97:1–14, 2016. doi:10.1016/j.ijheatmasstransfer.2016.01.067.

[144] Pan, J., Hu, S., Yang, L., and Wang, D. Investigation of molten pool behavior and weld bead formation in VP-GTAW by numerical modelling. *Materials & Design*, 111:600–607, 2016. doi:10.1016/j.matdes.2016.09.022.

[145] Bai, X., Colegrove, P., Ding, J., Zhou, X., Diao, C., Bridgeman, P., roman Hönnige, J., Zhang, H., and Williams, S. Numerical analysis of heat transfer and fluid flow in multilayer deposition of PAW-based wire and arc additive manufacturing. *International Journal of Heat and Mass Transfer*, 124:504–516, 2018. doi:10.1016/j.ijheatmasstransfer.2018.03.085.

[146] Liu, S. and Siewert, T. A. Metal transfer in gas metal arc welding: droplet rate. *Welding Journal*, 68(2):52s–58s, 1989. URL: `https://app.aws.org/wj/supplement/WJ_1989_02_s52.pdf`.

[147] Kim, Y. S. and Eagar, T. W. Analysis of metal transfer in gas metal arc welding. *Welding Journal*, 72(6):269s–278s, 1993. URL: `https://app.aws.org/wj/supplement/WJ_1993_06_s269.pdf`.

[148] Pires, I., Quintino, L., and Miranda, R. M. Analysis of the influence of shielding gas mixtures on the gas metal arc welding metal transfer modes and fume formation rate. *Materials & Design*, 28(5):1623–1631, 2007. doi:10.1016/j.matdes.2006.02.012.

[149] Scotti, A., Ponomarev, V., and Lucas, W. A scientific application oriented classification for metal transfer modes in GMA welding. *Journal of Materials Processing Technology*, 212(6): 1406–1413, 2012. doi:10.1016/j.jmatprotec.2012.01.021.

[150] Lancaster, J. F., editor. *The Physics of Welding*. International series on materials science of technology. Pergamon Press, Oxford, UK, 2nd edition, 1986. ISBN 0080340768.

[151] Kidess, A., Kenjereš, S., Righolt, B. W., and Kleijn, C. R. Marangoni driven turbulence in high energy surface melting processes. *International Journal of Thermal Sciences*, 104:412–422, 2016. doi:10.1016/j.ijthermalsci.2016.01.015.

[152] Ha, E.-J. and Kim, W.-S. A study of low-power density laser welding process with evolution of free surface. *International Journal of Heat and Fluid Flow*, 26(4):613–621, 2005. doi:10.1016/j.ijheatfluidflow.2005.03.009.

[153] Hirt, C. W. and Nichols, B. D. Volume of fluid (VOF) method for the dynamics of free boundaries. *Journal of Computational Physics*, 39(1):201–225, 1981. doi:10.1016/0021-9991(81)90145-5.

[154] Cook, P. S. and Murphy, A. B. Simulation of melt pool behaviour during additive manufacturing: Underlying physics and progress. *Additive Manufacturing*, 31:100909, 2020. doi:10.1016/j.addma.2019.100909.

[155] Hirt, C. W., Amsden, A. A., and Cook, J. L. An arbitrary Lagrangian-Eulerian computing method for all flow speeds. *Journal of Computational Physics*, 14(3):227–253, 1974. doi:10.1016/0021-9991(74)90051-5.

[156] Wirth, F. and Wegener, K. A physical modeling and predictive simulation of the laser cladding process. *Additive Manufacturing*, 22:307–319, 2018. doi:10.1016/j.addma.2018.05.017.

[157] Dal, M., Masson, P. L., and Carin, M. A model comparison to predict heat transfer during spot GTA welding. *International Journal of Thermal Sciences*, 75:54–64, 2014. doi:10.1016/j.ijthermalsci.2013.07.013.

[158] Hejripour, F., Valentine, D. T., and Aidun, D. K. Study of mass transport in cold wire deposition for wire arc additive manufacturing. *International Journal of Heat and Mass Transfer*, 125: 471–484, 2018. doi:10.1016/j.ijheatmasstransfer.2018.04.092.

3

Model Implementation and Verification

A generic three-dimensional multi-phase computational model based on the finite-volume method is developed in the present work to predict and study molten metal flow behaviour in fusion welding and associated free surface oscillations. The model employs the volume-of-fluid (VOF) method to capture the position of the melt-pool surface during the process. The effects of surface tension variations with temperature and surface-active elements (surfactants) are taken into account in the proposed model. Moreover, to characterise the melt-pool oscillatory behaviour, a wavelet transform is employed to extract the time-dependent frequency spectra of oscillation signals obtained from the numerical simulations. The details of the computational model and the assumptions made to develop the present model are described in this chapter. Reliability and validity of the proposed model are also verified focusing on various benchmark problems.

Parts of this chapter have been published in:
Energies, **2019**, *12*(22), 4360, DOI: 10.3390/en12224360,
J. Phys. D: Appl. Phys., **2021**, *54*(10), 105304, DOI: 10.1088/1361-6463/abca62,
Int. J. Heat Mass Transf., **2021**, *164*, 120535, DOI: 10.1016/j.ijheatmasstransfer.2020.120535,
J. Phys. D: Appl. Phys., **2021**, *54*(27), 275303, DOI: 10.1088/1361-6463/abf808,
Materials, **2021**, *14*(23), 7444, DOI: 10.3390/ma14237444,
and *Materials & Design*, **2022**, *214*, 110385, DOI: 10.1016/j.matdes.2022.110385.

3.1. Introduction

Fusion welding and additive manufacturing processes involve complex physical phenomena such as successive solid–liquid phase transformations, churning fluid motion in the melt pools, and moving boundaries at both solid–liquid and liquid–gas interfaces. These physical phenomena are coupled to one another, occur over various length and time scales, and respond non-linearly to changes in process parameters, material properties and operating conditions. In the present work, a computational model has been developed to enhance our understanding of the complex molten metal melt pool behaviour in fusion-based manufacturing processes, driven by various forces such as Marangoni, Lorentz, surface tension, arc pressure, drag and thermal buoyancy.

The computational model has been employed to study the effects of material properties as well as the process and operating conditions on complex molten metal flow and heat transfer in fusion-based manufacturing processes. The model is generic and can be utilised to numerically simulate various material compositions and fusion welding and additive manufacturing processes; obviously within the bounds of the assumptions made. The model is also able to represent different processes by changing the relevant boundary conditions and material properties. The general assumptions and governing equations are described in this chapter. SI units are employed to develop the present model unless explicitly otherwise stated.

3.2. Model formulation

A three-dimensional multiphase model is developed to predict molten metal flow, heat transfer and associated surface movements in fusion welding and additive manufacturing. In this model, the fluids are treated as Newtonian fluids and their densities are assumed to be pressure-independent. Assuming that the fluid flows under consideration are in the continuum regime, the dynamics of heat and fluid flow in melt pools and their surroundings are governed by the equations of motion given by the conservation equations for mass (also known as the continuity equation), momentum (also known as the Navier–Stokes equations) and energy. Accordingly, the unsteady governing equations are cast in conservative form as follow:

$$\frac{D\rho}{Dt} + \rho\left(\nabla\cdot\mathbf{u}\right) = S_{\mathrm{m}}, \tag{3.1}$$

$$\rho\frac{D\mathbf{u}}{Dt} = \mu\nabla^2\mathbf{u} - \nabla p + \mathbf{F}_{\mathrm{d}} + \mathbf{F}_{\mathrm{s}} + \mathbf{F}_{\mathrm{b}} + S_{\mathrm{m}}\left(\mathbf{u}_{\mathrm{s}} - \mathbf{u}\right), \tag{3.2}$$

$$\rho\frac{Dh}{Dt} = \frac{k}{c_{\mathrm{p}}}\nabla^2 h - \rho\frac{D\left(\psi\mathscr{L}_{\mathrm{f}}\right)}{Dt} + S_{\mathrm{q}} + S_{\mathrm{l}} + S_{\mathrm{m}}\left(\mathscr{L}_{\mathrm{fd}} + \int_{T_{\mathrm{i}}}^{T_{\mathrm{d}}} c_{\mathrm{p_d}}\,\mathrm{d}T\right), \tag{3.3}$$

where, ρ is the density, $\mathbf{u}$ the relative fluid-velocity vector, $\mathbf{u}_{\mathrm{s}}$ the fluid-velocity vector for the filler material, t the time, μ the dynamic viscosity, p the pressure, h the sensible heat, k the thermal conductivity, c_{p} the specific heat capacity at constant pressure, $\left(\psi\mathscr{L}_{\mathrm{f}}\right)$ the latent heat, and S_{m} the volumetric source term defined to model filler material addition [1]. The subscripts 'd' and 'i' indicate the filler material (*e.g.* filler metal droplets in gas metal

arc welding) and initial condition respectively. The total enthalpy of the material $\mathcal{H}$ is the sum of the latent heat $(\psi \mathscr{L}_\mathrm{f})$ and the sensible heat h and is defined as follows [2]:

$$\mathcal{H} = \left(h_\mathrm{r} + \int_{T_\mathrm{r}}^{T} c_\mathrm{p}\,\mathrm{d}T\right) + \psi \mathscr{L}_\mathrm{f}, \tag{3.4}$$

where, T is the temperature, ψ the local liquid volume-fraction, and $\mathscr{L}_\mathrm{f}$ the latent heat of fusion. The subscript 'r' indicates the reference condition. Assuming the liquid volume-fraction ψ to be a linear function of temperature [2], its value can be calculated as follows:

$$\psi = \frac{T - T_\mathrm{s}}{T_\mathrm{l} - T_\mathrm{s}}; \quad T_\mathrm{s} \leq T \leq T_\mathrm{l}, \tag{3.5}$$

where, T_l and T_s are the liquidus and solidus temperatures, respectively.

To capture the position of the gas-metal interface, the volume-of-fluid (VOF) method [3] is employed, where the scalar function ϕ indicates the local volume-fraction of a phase in a given computational cell. The value of ϕ varies from 0 in the gas phase to 1 in the metal phase, and cells with $0 < \phi < 1$ represent the gas-metal interface. The linear advection equation describes the advection of the scalar function ϕ as follows:

$$\frac{D\phi}{Dt} = \frac{S_\mathrm{m}}{\rho}. \tag{3.6}$$

Accordingly, the effective thermophysical properties of the material in each computational cell are determined as follows:

$$\xi = \phi\,\xi_\mathrm{m} + (1 - \phi)\,\xi_\mathrm{g}, \tag{3.7}$$

where, ξ corresponds to thermal conductivity k, specific heat capacity c_p, viscosity μ or density ρ, and subscripts 'g' and 'm' indicate gas or metal respectively.

Filler material addition during the process was modelled by adding a mass source term to the governing equations (*i.e.* equations (3.1) to (3.3) and (3.6)). Except for the simulations of gas metal arc welding, the value of S_m was set to 0 for all the simulations reported in the present work because no filler material addition was considered.

Solid–liquid phase transformation occurs in the temperature range between T_s and T_l in the so-called 'mushy zone'. To model the damping of liquid velocities in the mushy zone, and suppression of liquid velocities in solid regions, the sink term $\mathbf{F}_\mathrm{d}$ based on the enthalpy-porosity technique [4], is incorporated into the momentum equation and is defined as

$$\mathbf{F}_\mathrm{d} = -C\,\frac{(1-\psi)^2}{\psi^3 + \epsilon}\,\mathbf{u}, \tag{3.8}$$

where, C is the mushy-zone constant and ϵ is a constant, equal to 10^{-3}, employed to avoid division by zero. Depending on the melting temperature range as well as the imposed boundary conditions, the value of the mushy-zone constant can affect the numerical predictions of solidification and melting simulations. The value of the mushy-zone constant should be assigned appropriately to avoid numerical artefacts in simulations of solid–liquid phase transformations, which is discussed in detail in Chapter 4. In the present work, the value of the mushy-zone constant C was chosen to equal $10^7\,\mathrm{kg\,m^{-2}\,s^{-2}}$.

To model forces acting on the gas-metal interface such as surface tension, thermocapillary and arc plasma forces, the continuum surface force (CSF) model [5] is employed. In the CSF model, surface forces are considered as volumetric forces acting on the material contained in grid cells in the interface region. The source term $\mathbf{F}_s$ is included in equation (3.2) as follows:

$$\mathbf{F}_s = \mathbf{f}_s \|\nabla\phi\| \frac{2\rho}{\rho_m + \rho_g}, \tag{3.9}$$

where, subscripts 'g' and 'm' indicate gas or metal respectively. In equation (3.9), $\mathbf{f}_s$ is the surface force applied to a unit area, and is adjusted to represent different processes considered in the present work, as described later in this chapter. The term $2\rho/(\rho_m + \rho_g)$ is employed to abate the effect of the large metal-to-gas density ratio by redistributing the volumetric surface-forces towards the metal phase (*i.e.* the heavier phase). In addition to surface forces, body forces such as thermal buoyancy and electromagnetic forces are incorporated in the source term $\mathbf{F}_b$ in equation (3.2).

To model the thermal energy input to the material, the source S_q is included in equation (3.3). Moreover, heat losses from the workpiece surface due to convection, radiation and vaporisation are accounted for by including the sink term S_l in equation (3.3).

3.2.1. Laser melting

The source and sink terms incorporated in the governing equations were adjusted to numerically simulate the dynamics of molten metal flow in laser melting. The surface force applied to the gas-metal interface $\mathbf{f}_s$ is determined as follows:

$$\begin{aligned}\mathbf{f}_s &= \mathbf{f}_{\text{capillary}} + \mathbf{f}_{\text{Marangoni}} + \mathbf{f}_{P_{\text{recoil}}} \\ &= \gamma\kappa\hat{\mathbf{n}} + \frac{d\gamma}{dT}\left[\nabla T - \hat{\mathbf{n}}(\hat{\mathbf{n}}\cdot\nabla T)\right] + \left[0.54 \cdot p_0 \exp\left(\frac{\mathscr{L}_v M (T - T_b)}{R\, T\, T_b}\right)\right]\hat{\mathbf{n}}.\end{aligned} \tag{3.10}$$

where, γ is the surface tension, $\hat{\mathbf{n}}$ the surface unit normal vector ($\hat{\mathbf{n}} = \nabla\phi/\|\nabla\phi\|$), κ the surface curvature ($\kappa = \nabla\cdot\hat{\mathbf{n}}$), T the temperature, p_0 the ambient pressure, $\mathscr{L}_v$ the latent heat of vaporisation, M the molar mass of the material, T_b the boiling temperature, and R the universal gas constant. The third term on the right-hand side of equation (3.10), $\mathbf{f}_{P_{\text{recoil}}}$, is included to model the recoil pressure generated due to vaporisation of the molten metal [6–8].

The source term S_q and the sink term S_l are incorporated into equation (3.3) to model the laser heat input to the material and heat losses from the material due to convection, radiation and vaporisation [9] respectively, and are defined as follows:

$$S_q = \mathscr{F}_q \left[(a\, \mathscr{P}\mathscr{d}_f)\, \|\nabla\phi\| \frac{2\,\rho\, c_p}{(\rho\, c_p)_m + (\rho\, c_p)_g}\right], \tag{3.11}$$

$$S_l = -\left(S_{\text{convection}} + S_{\text{radiation}} + S_{\text{vaporisation}}\right) \|\nabla\phi\| \frac{2\,\rho\, c_p}{(\rho\, c_p)_m + (\rho\, c_p)_g}. \tag{3.12}$$

Here, a is the absorptivity the material, $\mathcal{P}$ the laser power, l_f the distribution function of laser power intensity, and

$$S_\mathrm{convection} = \hbar_\mathrm{c}\,(T - T_0)\,, \tag{3.13}$$

$$S_\mathrm{radiation} = \mathcal{K}_\mathrm{b}\mathcal{E}\left(T^4 - {T_0}^4\right), \tag{3.14}$$

$$S_\mathrm{vaporisation} = 0.82 \cdot \frac{\mathscr{L}_\mathrm{v} M}{\sqrt{2\pi M \mathrm{R} T}}\, p_0 \exp\left(\frac{\mathscr{L}_\mathrm{v} M\,(T - T_\mathrm{b})}{\mathrm{R}\,T\,T_\mathrm{b}}\right), \tag{3.15}$$

where, T_0 is the ambient temperature, $\mathcal{K}_\mathrm{b}$ the Stefan-Boltzmann constant, $\hbar_\mathrm{c}$ the heat transfer coefficient, and $\mathcal{E}$ the radiation emissivity. In the present work, the value of the heat transfer coefficient $\hbar_\mathrm{c}$, and the radiation emissivity $\mathcal{E}$ are assumed to remain constant and equal to $25\,\mathrm{W\,m^{-2}\,K^{-1}}$ [10] and 0.45 [11] respectively. It should be noted that the heat losses from the material due to convection and radiation are quite small compared to the total laser energy absorbed by the material; thus, the precise values of $\hbar_\mathrm{c}$ and $\mathcal{E}$ are not critical in the present simulations. The coefficient 0.82 in equation (3.15) is included based on Anisimov's theory [6] to account for the reduced cooling effect due to metal vapour condensation.

A temperature-dependent density model is employed in numerical simulations of laser melting presented in chapter 6. Accordingly, the source term for body forces $\mathbf{F}_\mathrm{b}$ is defined as follows:

$$\mathbf{F}_\mathrm{b} = \rho\mathbf{g}. \tag{3.16}$$

where, ρ is the density and $\mathbf{g}$ the gravitational acceleration vector.

In the VOF method, the energy fluxes applied to the material surface are included as volumetric source terms in the computational cells that encompass the melt-pool surface (*i.e.* cells with $0 < \phi < 1$). Hence, melt-pool surface deformations that occur during the process can result in an increase in the total heat input to the material [12]. $\mathcal{F}_\mathrm{q}$ in equation (3.11) is a dynamic adjustment factor introduced to abate artificial increase in energy absorption due to surface deformations and is defined as

$$\mathcal{F}_\mathrm{q} = \frac{1}{\iiint\limits_{\forall} \|\nabla\phi\| \frac{2\,\rho\,c_\mathrm{p}}{(\rho\,c_\mathrm{p})_\mathrm{m} + (\rho\,c_\mathrm{p})_\mathrm{g}}\,\mathrm{d}V}, \tag{3.17}$$

where, "$\forall$" indicates the computational domain. The effects of surface deformations on the total energy input to the material as well as the energy flux distribution over the melt-pool surface were considered in the present numerical simulations. The influence of utilising such an adjustment factor on numerical predictions of molten metal flow in laser melting is explained in Chapter 5.

Conduction-mode laser melting

Under certain circumstances, the laser melting model described in section 3.2.1 can be simplified. In conduction-mode laser-melting, the heat-source energy density is too low to cause significant vaporisation of the liquid metal [13], and the surface deformations are

too small to cause multiple reflections of the laser rays at the liquid surface [14]. The preliminary results for laser melting of stainless steel alloys in the conduction mode indicate that the maximum temperature of the melt pool is predominantly below 2700 K, significantly less than the boiling temperature of stainless steels, which is typically $\mathcal{O}(3100)$ K. Hence, multiple reflections and vaporisation can safely be ignored. With this, the surface force applied to the gas-metal interface $\mathbf{f}_s$ comprises surface tension and thermocapillary forces, defined as follows:

$$\mathbf{f}_s = \mathbf{f}_{\text{capillary}} + \mathbf{f}_{\text{Marangoni}} = \gamma\kappa\hat{\mathbf{n}} + \frac{\mathrm{d}\gamma}{\mathrm{d}T}\left[\nabla T - \hat{\mathbf{n}}\left(\hat{\mathbf{n}}\cdot\nabla T\right)\right], \tag{3.18}$$

where, γ is the surface tension, $\hat{\mathbf{n}}$ the surface unit normal vector ($\hat{\mathbf{n}} = \nabla\phi/\|\nabla\phi\|$), and κ the surface curvature ($\kappa = \nabla\cdot\hat{\mathbf{n}}$).

Arguably, thermal buoyancy forces are generally negligible compared to thermocapillary forces in conduction-mode laser melting [15], and thus can be ignored; accordingly, the source term for body forces $\mathbf{F}_b$ can be eliminated from equation (3.2).

The energy input supplied by the laser is modelled by adding a volumetric source term S_q to equation (3.3) in cells at the gas-metal interface; its general form can be defined as follows:

$$S_q = \bar{a}\, Q\, \delta_f \|\nabla\phi\| \frac{2\,\rho\, c_p}{(\rho\, c_p)_m + (\rho\, c_p)_g}, \tag{3.19}$$

where, $\bar{a}$ is the averaged laser absorptivity of the material surface, Q the laser beam power, δ_f the distribution function, and subscripts 'g' and 'm' indicate gas or metal respectively. Compared to the total laser energy absorbed by the material, the heat losses from the material due to convection and radiation are quite small and thus can be neglected in the simulations of conduction-mode laser melting.

This model is employed in chapter 5 to simulate the melt-pool behaviour in conduction-mode laser spot melting. It should be noted that further considerations will be required to develop the model for keyhole-mode welding, including the complex laser-matter interactions, changes in surface chemistry and consequent surface tension variations for non- or partially shielded welding conditions. However, the inclusion of such factors will increase the model complexity and computational costs and have not been considered here.

3.2.2. Gas tungsten arc welding

The surface force acting on the gas-metal interface $\mathbf{f}_s$ in gas tungsten arc welding includes a contribution from the arc plasma as well as surface tension and thermocapilary forces, and is defined as follows:

$$\mathbf{f}_s = \mathbf{f}_a + \gamma\kappa\hat{\mathbf{n}} + \frac{\mathrm{d}\gamma}{\mathrm{d}T}\left[\nabla T - \hat{\mathbf{n}}\left(\hat{\mathbf{n}}\cdot\nabla T\right)\right], \tag{3.20}$$

where, $\mathbf{f}_a$ is the force due to impingement of the arc plasma, γ the surface tension, $\hat{\mathbf{n}}$ the surface unit normal vector ($\hat{\mathbf{n}} = \nabla\phi/\|\nabla\phi\|$) and κ the surface curvature ($\kappa = \nabla\cdot\hat{\mathbf{n}}$).

The arc plasma force $\mathbf{f}_\mathrm{a}$ defined in equation (3.20) comprises the arc plasma shear stress $\mathbf{f}_\tau$ and arc pressure $\mathbf{f}_\mathrm{p}$,

$$\mathbf{f}_\mathrm{a} = \mathbf{f}_\tau + \mathbf{f}_\mathrm{p}. \tag{3.21}$$

The arc plasma shear stress $\mathbf{f}_\tau$, which acts at a tangent to the surface, is defined as follows [16]:

$$\mathbf{f}_\tau = \left[\tau_\mathrm{max}\, g_\tau\left(\mathcal{R}, \sigma_\tau\right)\right]\hat{\mathbf{t}}, \tag{3.22}$$

where, the maximum arc shear stress τ_max [17, 18], the arc shear stress distribution function g_τ [19] and the surface unit tangent vector $\hat{\mathbf{t}}$ [16] are defined as follows:

$$\tau_\mathrm{max} = 7\times10^{-2} I^{1.5} \exp\left(\frac{-2.5\times10^{4}\bar{\ell}}{I^{0.985}}\right), \tag{3.23}$$

$$g_\tau\left(\mathcal{R}, \sigma_\tau\right) = \sqrt{\frac{\mathcal{R}}{\sigma_\tau}} \exp\left(\frac{-\mathcal{R}^2}{{\sigma_\tau}^2}\right), \tag{3.24}$$

$$\hat{\mathbf{t}} = \frac{\mathbf{r} - \hat{\mathbf{n}}\left(\hat{\mathbf{n}}\cdot\mathbf{r}\right)}{\left\|\mathbf{r} - \hat{\mathbf{n}}\left(\hat{\mathbf{n}}\cdot\mathbf{r}\right)\right\|}. \tag{3.25}$$

Here, I is the welding current in Amperes, $\bar{\ell}$ the mean arc length, $\mathcal{R}$ the radius in x-y plane (*i.e.* $\mathcal{R} = \sqrt{x^2 + y^2}$), and $\mathbf{r}$ the position vector in the x-y plane. The distribution parameter σ_τ (in meters) is assumed to be a function of the mean arc length $\bar{\ell}$ and current I and is approximated on the basis of the data reported by Lee and Na [17]:

$$\sigma_\tau = 1.387\times10^{-3} + I^{-0.595}\bar{\ell}^{0.733}. \tag{3.26}$$

The arc pressure $\mathbf{f}_\mathrm{p}$ is determined as follows [20]:

$$\mathbf{f}_\mathrm{p} = \mathcal{J}_\mathrm{p}\left[\frac{\mu_0 I}{4\pi}\frac{I}{2\pi{\sigma_\mathrm{p}}^2}\exp\left(\frac{-\mathcal{R}^2}{2{\sigma_\mathrm{p}}^2}\right)\right]\hat{\mathbf{n}}, \tag{3.27}$$

where, I is the current, and μ_0 is the vacuum permeability equal to $4\pi\cdot10^{-7}\,\mathrm{H\,m^{-1}}$. The distribution parameter σ_p is determined using the experimental data reported by Tsai and Eagar [21] for an argon arc with an electrode tip angle of 75°:

$$\sigma_\mathrm{p} = 7.03\times10^{-2}\ell^{0.823} + 2.04\times10^{-4} I^{0.376}, \tag{3.28}$$

where, ℓ is the local arc length, and I the current. Hence, spatial and temporal variations of the arc pressure distribution resulting from changes in morphology of the melt-pool surface are taken into account. Changes in surface morphology can cause the total arc force applied to the melt-pool surface ($\iiint_{\forall}\|\mathbf{f}_\mathrm{p}\|\,\mathrm{d}V$) to differ from the expected arc force ($\mu_0 I^2/4\pi$) due to changes in $\|\nabla\phi\|$ [22, 23]. This numerical artefact is negated by incorporating $\mathcal{J}_\mathrm{p}$, which is defined as follows:

$$\mathcal{J}_\mathrm{p} = j\,\frac{\mu_0 I^2}{4\pi}\frac{1}{\iiint_{\forall}\|\mathbf{f}_\mathrm{p}\|\,\mathrm{d}V}. \tag{3.29}$$

The dimensionless factor j is employed, as suggested by Lin and Eagar [20] and Liu *et al.* [24], to match the theoretically determined arc pressure with experimentally measured values, and is calculated as follows:

$$j = 3 + 8 \times 10^{-3} I, \tag{3.30}$$

with I the welding current in Amperes.

$\mathbf{F}_\mathrm{b}$ in equation (3.2) is the body force, which comprises electromagnetic, gravity and thermal buoyancy forces. The electromagnetic force is computed using the model proposed by Tsao and Wu [25] transformed into a body-fitted coordinate system, and the thermal buoyancy force is modelled using the Boussinesq approximation [26]. Hence, the body forces are defined as follows:

$$\mathbf{f}_{\mathrm{b}x} = \frac{-\mu_0 I^2}{4\pi^2 {\sigma_\mathrm{e}}^2 \mathcal{R}} \exp\left(\frac{-\mathcal{R}^2}{2{\sigma_\mathrm{e}}^2}\right)\left[1 - \exp\left(\frac{-\mathcal{R}^2}{2{\sigma_\mathrm{e}}^2}\right)\right]\left(1 - \frac{z - z'}{H_\mathrm{m} - z'}\right)^2 \left(\frac{x}{\mathcal{R}}\right), \tag{3.31}$$

$$\mathbf{f}_{\mathrm{b}y} = \frac{-\mu_0 I^2}{4\pi^2 {\sigma_\mathrm{e}}^2 \mathcal{R}} \exp\left(\frac{-\mathcal{R}^2}{2{\sigma_\mathrm{e}}^2}\right)\left[1 - \exp\left(\frac{-\mathcal{R}^2}{2{\sigma_\mathrm{e}}^2}\right)\right]\left(1 - \frac{z - z'}{H_\mathrm{m} - z'}\right)^2 \left(\frac{y}{\mathcal{R}}\right), \tag{3.32}$$

$$\mathbf{f}_{\mathrm{b}z} = \frac{-\mu_0 I^2}{4\pi^2 \mathcal{R}^2 H_\mathrm{m}}\left[1 - \exp\left(\frac{-\mathcal{R}^2}{2{\sigma_\mathrm{e}}^2}\right)\right]^2 \left(1 - \frac{z - z'}{H_\mathrm{m} - z'}\right) + \rho \mathbf{g} - \rho\beta\,(T - T_\mathrm{l})\,\mathbf{g}. \tag{3.33}$$

Here, the distribution parameter for the electromagnetic force σ_e is the same as σ_p, according to Tsai and Eagar [21], z' is the position of the melt-pool surface in x-y plane at a given time t, β the thermal expansion coefficient, and $\mathbf{g}$ the gravitational acceleration vector.

The thermal energy provided by the arc is modelled by adding the source term S_q to the energy equation (equation (3.3)). S_q is defined as

$$S_\mathrm{q} = \mathcal{F}_\mathrm{q}\left[\frac{\eta I U}{2\pi {\sigma_\mathrm{q}}^2} \exp\left(\frac{-\mathcal{R}^2}{2{\sigma_\mathrm{q}}^2}\right) \|\nabla\phi\| \frac{2\,\rho\, c_\mathrm{p}}{(\rho\, c_\mathrm{p})_\mathrm{m} + (\rho\, c_\mathrm{p})_\mathrm{g}}\right], \tag{3.34}$$

where, the process efficiency η is considered to be a linear function of welding current, varying from 80% at 50 A to 70% at 300 A [27]. It should be noted that the source term S_q is only applied to the top surface of the workpiece. The arc voltage U depends on welding current and arc length, and is approximated as follows:

$$U = U_\mathrm{o} + U_\mathrm{I} I + U_\mathrm{e} \bar{\ell}, \tag{3.35}$$

where, U_o is the electrode fall voltage equal to 8 V [28], U_I the coefficient of variation of arc voltage with current equal to $1.3 \times 10^{-2}\,\mathrm{V A^{-1}}$ [29], and U_e the electric field strength equal to $7.5\,\mathrm{V cm^{-1}}$ [28]. Using the data reported by Tsai and Eagar [21], the distribution parameter σ_q (in meters) is determined as follows:

$$\sigma_\mathrm{q} = 1.61 \times 10^{-1}\,\ell^{0.976} + 2.23 \times 10^{-4}\, I^{0.395}, \tag{3.36}$$

with ℓ in meters and I in Amperes. The adjustment factor $\mathcal{F}_q$ used to negate changes in the total heat input due to surface deformations, is defined as follows:

$$\mathcal{F}_q = \frac{\eta I U}{\iiint\limits_{\forall} S_q \, dV}. \tag{3.37}$$

The sink term S_l is added to the energy equation to account for heat losses due to convection and radiation, is determined as follows:

$$S_l = -\left[h_c (T - T_0) + \mathcal{K}_b \mathcal{E} \left(T^4 - {T_0}^4\right)\right] \|\nabla \phi\| \frac{2 \rho c_p}{(\rho c_p)_m + (\rho c_p)_g}, \tag{3.38}$$

where, h_c is the heat transfer coefficient, $\mathcal{K}_b$ the Stefan–Boltzmann constant and $\mathcal{E}$ the radiation emissivity. In the present work, the value of the heat transfer coefficient h_c, and the radiation emissivity $\mathcal{E}$ are assumed to remain constant and equal to $25\,\mathrm{W\,m^{-2}\,K^{-1}}$ [10] and 0.45 [11] respectively. The heat losses from the material due to convection and radiation are quite small compared to the total heat input; thus, the precise values of h_c and $\mathcal{E}$ are not critical in the present simulations.

3.2.3. Gas metal arc welding

In gas metal arc welding, similar to gas tungsten arc welding, the surface force acting on the gas-metal interface $\mathbf{f}_s$ includes an arc plasma term, surface tension and thermocapillary forces, and is defined as follows:

$$\mathbf{f}_s = \mathbf{f}_a + \gamma \kappa \hat{\mathbf{n}} + \frac{d\gamma}{dT} \left[\nabla T - \hat{\mathbf{n}} (\hat{\mathbf{n}} \cdot \nabla T)\right], \tag{3.39}$$

where, $\mathbf{f}_a$ is arc plasma force, γ the surface tension, $\hat{\mathbf{n}}$ the surface unit normal vector ($\hat{\mathbf{n}} = \nabla\phi / \|\nabla\phi\|$) and κ the surface curvature ($\kappa = \nabla \cdot \hat{\mathbf{n}}$).

The arc plasma force $\mathbf{f}_a$ defined in equation (3.39) comprises arc plasma shear stress $\mathbf{f}_\tau$ and arc pressure $\mathbf{f}_p$,

$$\mathbf{f}_a = \mathbf{f}_\tau + \mathbf{f}_p. \tag{3.40}$$

Assuming that the arc plasma shear stress $\mathbf{f}_\tau$ in gas metal arc welding resembles that in gas tungsten arc welding, the arc plasma shear stress $\mathbf{f}_\tau$, which acts at a tangent to the surface, is defined as follows [16]:

$$\mathbf{f}_\tau = \left[\tau_{max} \, g_\tau (\mathcal{R}, \sigma_\tau)\right] \hat{\mathbf{t}}, \tag{3.41}$$

where, the maximum arc shear stress τ_{max} [17, 18], the arc shear stress distribution function g_τ [19] and the surface unit tangent vector $\hat{\mathbf{t}}$ [16] were defined as follows:

$$\tau_{max} = 7 \times 10^{-2} I^{1.5} \exp\left(\frac{-2.5 \times 10^4 \bar{\ell}}{I^{0.985}}\right), \tag{3.42}$$

$$g_\tau (\mathcal{R}, \sigma_\tau) = \sqrt{\frac{\mathcal{R}}{\sigma_\tau}} \exp\left(\frac{-\mathcal{R}^2}{{\sigma_\tau}^2}\right), \tag{3.43}$$

$$\hat{\mathbf{t}} = \frac{\mathbf{r} - \hat{\mathbf{n}}(\hat{\mathbf{n}} \cdot \mathbf{r})}{\|\mathbf{r} - \hat{\mathbf{n}}(\hat{\mathbf{n}} \cdot \mathbf{r})\|}. \tag{3.44}$$

Here, I is the welding current, $\bar{\ell}$ the mean arc length, $\mathcal{R}$ the radius in x-y plane (*i.e.* $\mathcal{R} = \sqrt{x^2 + y^2}$), and $\mathbf{r}$ the position vector in the x-y plane. The distribution parameter σ_τ (in meters) is assumed to be a function of the mean arc length $\bar{\ell}$ and current I and was approximated on the basis of the data reported by Lee and Na [17]:

$$\sigma_\tau = 1.387 \times 10^{-3} + I^{-0.595}\bar{\ell}^{0.733}. \tag{3.45}$$

The arc pressure $\mathbf{f}_\mathrm{p}$ is determined as follows [20]:

$$\mathbf{f}_\mathrm{p} = \mathcal{F}_\mathrm{p}\left[\frac{\mu_0 I}{4\pi}\frac{I}{2\pi{\sigma_\mathrm{p}}^2}\exp\left(\frac{-\mathcal{R}^2}{2{\sigma_\mathrm{p}}^2}\right)\right]\hat{\mathbf{n}}, \tag{3.46}$$

where, I is the current in Ampere, and μ_0 is the vacuum permeability equal to $4\pi \cdot 10^{-7}\,\mathrm{H\,m^{-1}}$. The distribution parameter σ_p (in metres) was determined using the experimental data reported by Tsai and Eagar [21] as follows:

$$\sigma_\mathrm{p} = 7.03 \times 10^{-2}\ell^{0.823} + 2.04 \times 10^{-4} I^{0.376}, \tag{3.47}$$

where, ℓ is the local arc length in meters, and I the current in Amperes. Changes in surface morphology can cause the total arc force applied to the melt-pool surface ($\iiint_\forall \|\mathbf{f}_\mathrm{p}\|\,\mathrm{d}V$) to differ from the expected arc force ($\mu_0 I^2/4\pi$) due to changes in $\|\nabla\phi\|$ [22, 23]. This numerical artefact is negated by incorporating $\mathcal{F}_\mathrm{p}$, defined as follows:

$$\mathcal{F}_\mathrm{p} = j\frac{\mu_0 I^2}{4\pi}\frac{1}{\iiint_\forall \|\mathbf{f}_\mathrm{p}\|\,\mathrm{d}V}. \tag{3.48}$$

The dimensionless factor j is employed, as suggested by Lin and Eagar [20] and Liu *et al.* [24], to match the theoretically determined arc pressure with experimentally measured values, and is calculated as follows:

$$j = 3 + 8 \times 10^{-3} I, \tag{3.49}$$

with I the welding current in Amperes.

$\mathbf{F}_\mathrm{b}$ in equation (3.2) is the body force, which comprises electromagnetic and gravity forces. The electromagnetic force was computed using the model proposed by Tsao and Wu [25] transformed into a body-fitted coordinate system. Hence, the body forces are defined as follows:

$$\mathbf{f}_{\mathrm{b}x} = \frac{-\mu_0 I^2}{4\pi^2{\sigma_\mathrm{e}}^2\mathcal{R}}\exp\left(\frac{-\mathcal{R}^2}{2{\sigma_\mathrm{e}}^2}\right)\left[1 - \exp\left(\frac{-\mathcal{R}^2}{2{\sigma_\mathrm{e}}^2}\right)\right]\left(1 - \frac{z - z'}{H_\mathrm{m} - z'}\right)^2\left(\frac{x}{\mathcal{R}}\right), \tag{3.50}$$

$$\mathbf{f}_{\mathrm{b}y} = \frac{-\mu_0 I^2}{4\pi^2{\sigma_\mathrm{e}}^2\mathcal{R}}\exp\left(\frac{-\mathcal{R}^2}{2{\sigma_\mathrm{e}}^2}\right)\left[1 - \exp\left(\frac{-\mathcal{R}^2}{2{\sigma_\mathrm{e}}^2}\right)\right]\left(1 - \frac{z - z'}{H_\mathrm{m} - z'}\right)^2\left(\frac{y}{\mathcal{R}}\right), \tag{3.51}$$

$$\mathbf{f}_{bz} = \frac{-\mu_0 I^2}{4\pi^2 \mathscr{R}^2 H_m}\left[1-\exp\left(\frac{-\mathscr{R}^2}{2{\sigma_e}^2}\right)\right]^2\left(1-\frac{z-z'}{H_m-z'}\right)+\rho\mathbf{g}. \tag{3.52}$$

Here, the distribution parameter for the electromagnetic force σ_e is the same as σ_p, according to Tsai and Eagar [21], z' is the position of the melt-pool surface in x-y plane at a given time t, and $\mathbf{g}$ the gravitational acceleration vector. It should be noted that the current-density profile is assumed to be Gaussian in the model proposed by Tsao and Wu [25] to compute the electromagnetic forces. Further studies are required to develop a generic model to approximate the evolution of current-density profile during gas metal arc welding [30–32].

The thermal energy provided by the arc was modelled by adding the source term S_q to the energy equation (equation (3.3)) and was defined as

$$S_q = \mathscr{F}_q\left[\frac{\eta_a IU}{2\pi{\sigma_q}^2}\exp\left(\frac{-\mathscr{R}^2}{2{\sigma_q}^2}\right)\|\nabla\phi\|\frac{2\,\rho\,c_p}{(\rho\,c_p)_m+(\rho\,c_p)_g}\right], \tag{3.53}$$

where, the arc efficiency η_a is defined as follows:

$$\eta_a = \eta_p - \eta_d. \tag{3.54}$$

Here, η_p is the process efficiency and is assumed to vary linearly with welding current from 77% at 200 A to 72% at 300 A [27], and η_d is the efficiency of thermal energy transfer by molten metal droplets, which is defined as follows:

$$\eta_d = \frac{q_d}{IU}, \tag{3.55}$$

with q_d the thermal energy content of the droplets that are assumed to be spherical. q_d is defined as follows:

$$q_d = \rho_d\frac{4}{3}\pi r_d^3\left(\mathscr{L}_{fd}+\int_{T_i}^{T_d} c_{pd}\,\mathrm{d}T\right)f_d, \tag{3.56}$$

where, subscript 'd' indicates droplet and r_d is the radius of molten metal droplet. In equation (3.56) f_d is the frequency of droplet detachment, and is defined as:

$$f_d = \frac{3u_w r_w^2}{4r_d^3}, \tag{3.57}$$

where, u_w is the wire feed rate and r_w is the radius of the welding wire. For metal transfer in the spray mode, the radius of the molten metal droplets and the welding wire are assumed to be the same. Accordingly, the magnitude of molten metal droplet velocity u_d just after detachment was approximated using the correlation proposed by Lin *et al.* [33]:

$$u_d = \frac{I}{2\pi r_d}\sqrt{\frac{3\mu_0}{\rho_d}}G, \tag{3.58}$$

where, I is the current, r_d the radius of the droplet in meters, μ_0 the vacuum permeability, ρ_d the density of the molten droplet, and G a dimensionless constant introduced to obtain agreement with experimental measurements, which is equal to 0.98 for steel electrodes.

The process voltage U was assumed to be a function of welding current and arc length [34–36], and was determined as follows:

$$U = U_{\mathrm{w}} + U_{\mathrm{o}} + U_{\mathrm{a}}. \tag{3.59}$$

Here, U_{w} is the wire voltage assumed to be constant and equal to 7 V [35], U_{o} the sum of the electrode fall voltages that is assumed to be a function of welding current I as follows:

$$U_{\mathrm{o}} = C_{\mathrm{I}} I + 10, \tag{3.60}$$

with I in Ampere and C_{I} the coefficient of variation of the electric fall voltage with current equal to $0.016\,\mathrm{V A^{-1}}$ [35, 36]. U_{a} in equation (3.59) is the arc column voltage determined as follows:

$$U_{\mathrm{a}} = C_{\mathrm{e}} \ell, \tag{3.61}$$

with ℓ in meters and C_{e} the electric field strength equal to $1.09\,\mathrm{V mm^{-1}}$ [35, 36]. Using the data reported by Tsai and Eagar [21], the distribution parameter σ_{q} (in meters) was determined as follows:

$$\sigma_{\mathrm{q}} = 1.61 \times 10^{-1} \ell^{0.976} + 2.23 \times 10^{-4} I^{0.395}. \tag{3.62}$$

The adjustment factor $\mathcal{F}_{\mathrm{q}}$ was used to negate changes in the total heat input due to surface deformations and is defined as follows:

$$\mathcal{F}_{\mathrm{q}} = \frac{\eta I U}{\iiint\limits_{\forall} S_{\mathrm{q}} \, \mathrm{d}V}. \tag{3.63}$$

It should be noted that the source term S_{q} is only applied to the top surface of the workpiece.

The sink term S_{l} was added to the energy equation to account for heat losses due to convection and radiation, and is determined as follows:

$$S_{\mathrm{l}} = -\left[\hbar_{\mathrm{c}} (T - T_0) + \mathcal{K}_{\mathrm{b}} \mathcal{E} \left(T^4 - {T_0}^4\right)\right] \|\nabla \phi\| \frac{2 \rho \, c_{\mathrm{p}}}{(\rho \, c_{\mathrm{p}})_{\mathrm{m}} + (\rho \, c_{\mathrm{p}})_{\mathrm{g}}}, \tag{3.64}$$

where, $\hbar_{\mathrm{c}}$ is the heat transfer coefficient, $\mathcal{K}_{\mathrm{b}}$ the Stefan–Boltzmann constant, and $\mathcal{E}$ the radiation emissivity. In the present work, the value of the heat transfer coefficient $\hbar_{\mathrm{c}}$, and the radiation emissivity $\mathcal{E}$ are assumed to remain constant and equal to $25\,\mathrm{W m^{-2} K^{-1}}$ [10] and 0.45 [11] respectively. The heat losses from the material due to convection and radiation are quite small compared to the total heat input; thus, the precise values of $\hbar_{\mathrm{c}}$ and $\mathcal{E}$ are not critical in the present simulations.

3.3. Absorptivity model

When a laser beam with total energy of $\mathcal{P}$ interacts with material part of its energy is absorbed by the material for a fraction equal to its absorptivity (a). Numerical simulations developed for laser welding and additive manufacturing commonly assume the absorptivity to be constant [37], which is physically unrealistic, and its value is often

regarded as a calibration parameter [38]. The absorptivity should be considered as a system parameter and not a calibration parameter [38]. In the present work, the amount of laser energy absorbed by the material was described by the absorptivity model proposed by Yang *et al.* [38] and Mahrle and Beyer [39], which takes into account the effects of laser characteristics, laser-ray incident angle, surface temperature and base-material composition. Accordingly, the absorptivity a for circularly polarised or un-polarised laser radiation was approximated as follows:

$$a = 1 - \frac{R_s + R_p}{2}, \tag{3.65}$$

where, according to the Fresnel's reflection equations, R_s and R_p are the reflectance for parallel and perpendicularly polarised light defined as

$$R_s = \frac{\alpha^2 + \beta^2 - 2\alpha\cos(\theta) + \cos^2(\theta)}{\alpha^2 + \beta^2 + 2\alpha\cos(\theta) + \cos^2(\theta)}, \tag{3.66}$$

$$R_p = R_s\left(\frac{\alpha^2 + \beta^2 - 2\alpha\sin(\theta)\tan(\theta) + \sin^2(\theta)\tan^2(\theta)}{\alpha^2 + \beta^2 + 2\alpha\sin(\theta)\tan(\theta) + \sin^2(\theta)\tan^2(\theta)}\right). \tag{3.67}$$

Here, θ is the incident angle of the laser beam, and α and β are functions of the refractive index n and the extinction coefficient k of the irradiated material. The values of α, β, n and k were determined as follows:

$$\alpha = \left(\frac{\sqrt{\left(n^2 - k^2 - \sin^2(\theta)\right)^2 + 4n^2k^2} + n^2 - k^2 - \sin^2(\theta)}{2}\right)^{\frac{1}{2}}, \tag{3.68}$$

$$\beta = \left(\frac{\sqrt{\left(n^2 - k^2 - \sin^2(\theta)\right)^2 + 4n^2k^2} - n^2 + k^2 + \sin^2(\theta)}{2}\right)^{\frac{1}{2}}, \tag{3.69}$$

$$n = \left(\frac{\sqrt{e_r^2 + e_i^2} + e_r}{2}\right)^{\frac{1}{2}}, \tag{3.70}$$

$$k = \left(\frac{\sqrt{e_r^2 + e_i^2} - e_r}{2}\right)^{\frac{1}{2}}, \tag{3.71}$$

where, e_r and e_i are the real and imaginary parts of the relative electric permittivity $\tilde{e}$ respectively, defined as

$$e_r = 1 - \frac{\omega_p^2}{f^2 + \delta^2}, \tag{3.72}$$

$$e_i = \frac{\delta}{f}\frac{\omega_p^2}{f^2 + \delta^2}. \tag{3.73}$$

Here, ω_p, f and δ are the plasma frequency, laser frequency and damping frequency respectively, defined as follows:

$$\omega_p = \sqrt{\frac{N_e q_e^2}{M_e v_0}}, \tag{3.74}$$

$$f = \frac{2\pi c}{\lambda}, \tag{3.75}$$

$$\delta = \omega_p^2 v_0 \mathscr{R}_T, \tag{3.76}$$

where, N_e is the mean number density of free electrons (the value of which approximately equals to $5.83 \times 10^{29}\,m^{-3}$ for stainless steel 316L [38]), q_e the elementary electric charge, M_e the electron rest mass, v_0 the electric constant, c the speed of light in vacuum, λ the emission wavelength of the laser, and $\mathscr{R}_T$ the temperature-dependent electrical resistivity. The values approximated using the present absorptivity model for stainless steel 316L are presented in figure 3.1, showing the influence of laser emission wavelength, incident angle and temperature on the absorptivity. The data shown in figure 3.1 suggest that the incident angle of the laser beam θ negligibly affects the absorptivity up to 40° but its effect becomes significant for larger incident angles (for instance, in cases where a keyhole is formed). Additionally, changes in the temperature notably affect absorptivity, making the assumption of constant absorptivity inappropriate.

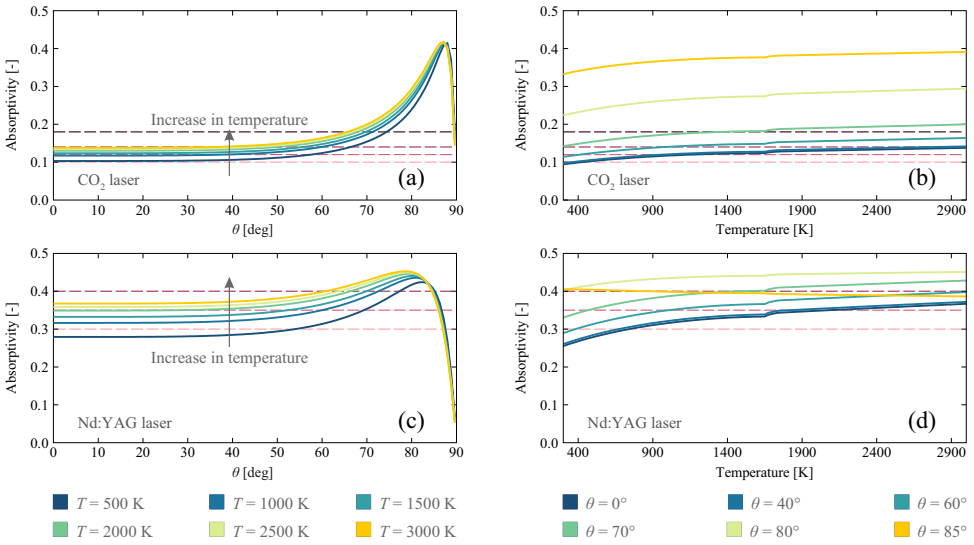

Figure 3.1: The effects of laser emission wavelength λ, temperature and incident angle of the laser beam θ on the absorptivity of stainless steel 316L. Values are obtained from the absorptivity model described in section 3.3. (a and b) CO_2 laser with $\lambda = 1.060 \times 10^{-5}$ m and (c and d) Nd:YAG laser with $\lambda = 1.064 \times 10^{-6}$ m. Dashed lines indicate the constant absorptivities studied in chapter 6 of the present work.

3.4. Surface tension model

The temperature dependence of the surface tension of a liquid solution with a low concentration of surfactant that is distributed homogeneously over the surface can be approximated using a theoretical correlation derived on the basis of the combination of Gibbs and Langmuir adsorption isotherms as follows [40, 41]:

$$\gamma = \gamma^{\circ} - \mathrm{R}\,T\,\Gamma_{\mathrm{s}}\ln(1 + K a_{\mathrm{s}}), \tag{3.77}$$

where, γ is the surface tension of the solution, γ° the pure solvent surface tension, R the gas constant, Γ_{s} the adsorption at saturation, K the adsorption coefficient, and a_{s} the activity of the solute. From this, Sahoo *et al.* [42] derived a correlation for binary molten metal–surfactant systems, including binary Fe–S systems:

$$\gamma = \gamma^{\circ}_{\mathrm{m}} + \left(\frac{\partial\gamma}{\partial T}\right)^{\circ}(T - T_{\mathrm{m}}) - \mathrm{R}\,T\,\Gamma_{\mathrm{s}}\ln\left[1 + \mathcal{S}\,a_{\mathrm{s}}\exp\left(\frac{-\Delta H^{\circ}}{\mathrm{R}T}\right)\right], \tag{3.78}$$

where, $\gamma^{\circ}_{\mathrm{m}}$ is the surface tension of pure molten-metal at the melting temperature T_{m}, $\mathcal{S}$ an entropy factor, ΔH° the standard heat of adsorption, and $\left(\partial\gamma/\partial T\right)^{\circ}$ the temperature coefficient of the surface tension of the pure molten-metal. Values of the properties used in equation (3.78) to calculate the temperature dependence of the surface tension of the molten Fe–S alloy are presented in table 3.1. Variations of the surface tension and its temperature coefficient with temperature are shown in figure 3.2 for Fe–S alloys with different sulphur concentrations.

Table 3.1: The values used to calculate the surface tension of molten Fe–S alloy [42].

Property	Value	Unit
$\gamma^{\circ}_{\mathrm{m}}$	1.943	$\mathrm{N\,m^{-1}}$
$\left(\partial\gamma/\partial T\right)^{\circ}$	-4.3×10^{-4}	$\mathrm{N\,m^{-1}\,K^{-1}}$
Γ_{s}	1.3×10^{-5}	$\mathrm{mol\,m^{-2}}$
$\mathcal{S}$	3.18×10^{-3}	–
ΔH°	-166.2×10^{5}	$\mathrm{J\,mol^{-1}}$

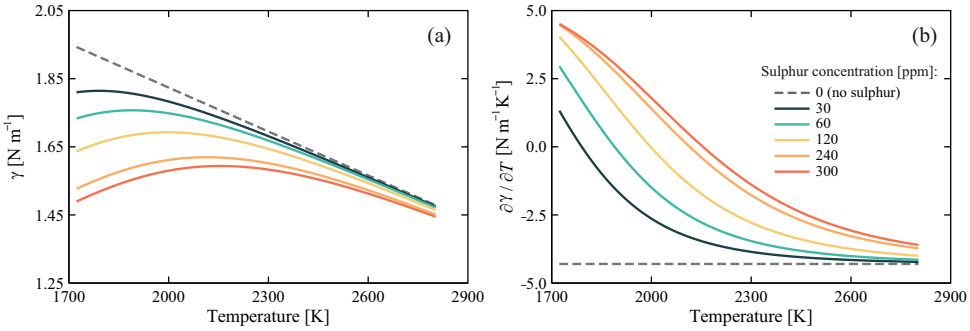

Figure 3.2: Variations of surface tension (a) and its temperature gradient (b) as a function of temperature obtained from equation (3.78) for Fe–S alloys with different sulphur concentrations.

3.5. Time-frequency analysis

Complex unsteady molten metal flow in melt pools give rise to time-variant frequency spectra in oscillations of the melt-pool during fusion-based welding and additive manufacturing. Determining the time localisation of the frequency spectra of melt-pool oscillation signals is of interest to monitor and control welding and additive manufacturing processes. However, the dynamic features of the oscillation signals cannot easily be derived employing conventional Fourier transform (FT) analysis [43] since the oscillation signals are assumed to be stationary (*i.e.* the behaviour of the system is linear and time-invariant). For instance, the spectral descriptions obtained from the conventional Fourier transform analysis for the response of a linear system to the 'impulse response function' and the 'stationary white noise' with unit amplitude would be identical, while they have conspicuously different transient features.

Time resolution of the frequency spectra can be obtained using 'short-time Fourier transform' (STFT) analysis [44], which employs a time-window of finite length to extract the corresponding frequency content using the Fourier transform, assuming that the signal is stationary within each window. A major drawback of the short-time Fourier transform is related to the window function that has a fixed finite length, limiting the application of the STFT analysis in extracting time and frequency resolutions simultaneously [45]. In other words, the wider the window is chosen, the better the frequency resolution, but the poorer the time resolution.

The continuous wavelet transform (CWT) [46] is employed in the present study to overcome the shortcomings of the conventional fast Fourier transform (FFT) analysis in characterising the non-stationary features of the signals that may contain abrupt changes in their frequency spectra. Employing the continuous wavelet transform, the time-resolved melt-pool surface oscillation signals obtained from the numerical simulations can be decomposed into time and frequency spaces simultaneously. The principle of signal processing based on the wavelet transform is reviewed comprehensively by Mallat [46], and is briefly described here.

The continuous wavelet transform of a signal $s(t)$ is defined using a convolution

integral as follows:

$$\mathcal{W}(l,t) = \frac{1}{\sqrt{l}} \int_{-\infty}^{+\infty} \mathfrak{s}(t) \Psi^* \left(\frac{t-\tau}{l} \right) \mathrm{d}t, \tag{3.79}$$

where, l is the scale (dilation) parameter ($l > 0$), τ the translation parameter, Ψ^* the complex conjugate of the translated and dilated mother wavelet Ψ that is localised on both the physical and transformed spaces, and t the time. Accordingly, the wavelet coefficients $\mathcal{W}(l,t)$ are obtained relative to the mother wavelet Ψ. The Morlet wavelet [47], which is a Gaussian-windowed complex sinusoid, was chosen as the mother wavelet that yields an adequate balance in both time and frequency domains. The Morlet wavelet is defined as follows:

$$\Psi(t) = \exp\left(\frac{-t^2}{2} \right) \exp(i\omega_0 t), \tag{3.80}$$

where, i is the square root of -1, and ω_0 is chosen to equal 6 to satisfy the admissibility condition [45]. The Python programming language was employed to perform time-frequency analysis using the oscillation signals acquired from the numerical simulations.

3.6. Verification of the computational models

The reliability and accuracy of numerical predictions obtained from the present computational model were rigorously verified using available experimental, theoretical and numerical data for various benchmark problems. Apart from the cases reported in this section, the validity of the model in predicting the melt-pool shape and internal flow dynamics is further investigated and discussed in the following chapters. The source terms in the momentum and energy equations, as well as the boundary conditions for laser heat input and the temperature-dependent surface-tension model, are implemented through user-defined functions (UDFs) programmed in the C programming language.

3.6.1. Solid–liquid phase transformation

Solidification of a semi-infinite slab (one-dimensional benchmark)

The transient solidification of a semi-infinite slab of Al–4.5%Cu alloy was considered as a one-dimensional problem. The slab is initially in the liquid phase with a uniform temperature of 969 K above the liquidus temperature $T_\mathrm{l} = 919\,\mathrm{K}$. The phase-change process starts at $t = 0\,\mathrm{s}$ by suddenly changing the temperature of one side of the slab to 573 K, below the solidus $T_\mathrm{s} = 821\,\mathrm{K}$. The results of the present model on a uniform mesh with cell size $\Delta x = 0.01\,\mathrm{m}$ are compared with semi-analytical [48] and numerical results [2] in figure 3.3. The present results are in better agreement with the semi-analytical solution from [48] than the numerical results presented in [2], with the maximum absolute difference between present results and the semi-analytical solution being less than 0.5%.

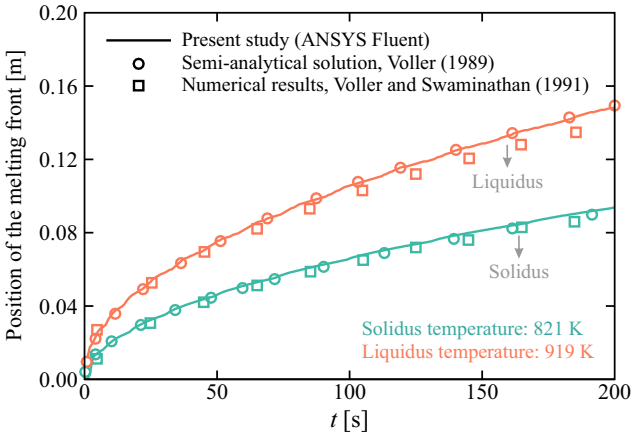

Figure 3.3: One-dimensional solidification benchmark problem; time evolution of the mushy-zone thickness (green: solidus; orange: liquidus) predicted by the present model compared with available semi-analytical [48] and numerical [2] results.

Melting with convection in rectangular enclosures (two-dimensional benchmarks)
Melting with convection of pure tin in a square enclosure was considered as a two-dimensional benchmark problem. Details of the problem can be found in [49]. The results obtained from the present model on a uniform mesh with quadrilateral grid cells, $\Delta x_i/W = 4 \times 10^{-4}$ for isothermal phase-change including convection are compared with numerical results presented by Hannoun *et al.* [49] in figure 3.4. The maximum difference between the results predicted by the present model and the reference case [49] is within 1%.

Numerical predictions of solid–liquid interface morphologies in a rectangular enclosure subject to natural convection was compared with the experimental observations of Kumar *et al.* [50] for isothermal melting of lead. Figure 3.5 indicates a reasonable agreement between the results obtained from the present numerical simulations and the reference data. The deviations between the numerical and experimental data are attributed to both the simplifying assumptions made in the numerical model and the uncertainties associated with the experiments such as the uncertainty in determining the position of solid–liquid interface, which is reported to be about 8.7% [50].

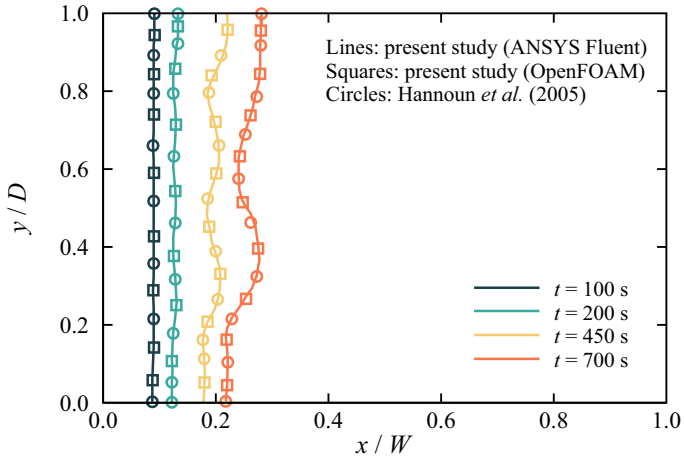

Figure 3.4: Two-dimensional melting benchmark problem; time evolution of solid–liquid interface during isothermal phase-change with convection predicted by the present model implemented in ANSYS Fluent and OpenFOAM compared with numerical results of Hannoun *et al.* [49]. D and W are the height and width of the enclosure respectively.

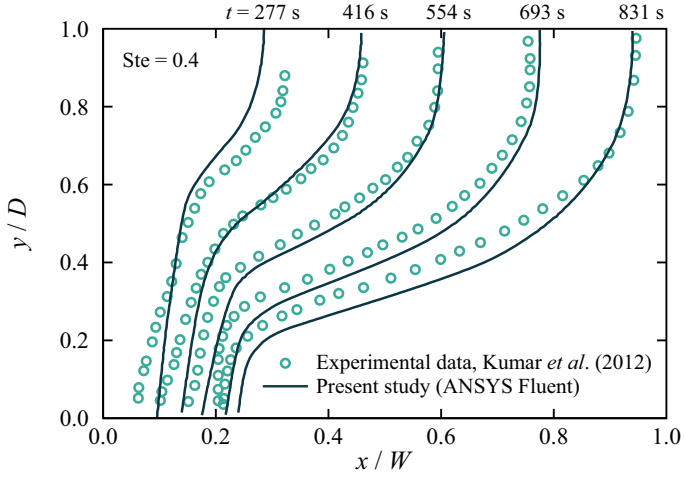

Figure 3.5: Comparisons of numerically determined melting-front positions in a rectangular enclosure subject to natural convection using the present model implemented in ANSYS Fluent with experimental observations of isothermal melting of lead using thermal neutron radiography [50]. D and W are the height and width of the enclosure respectively.

3.6.2. Laser melting

To verify the reliability and accuracy of the present numerical simulations, the melt-pool shapes obtained from the present simulations are compared to experimental observations reported by Pitscheneder *et al.* [51]. In this problem, a defocused CO_2 laser-beam with a power of 3850 W heats the material locally for 5 s, forming a melt pool in the ma-

terial. The laser beam has a radius of 1.4 mm with a top-hat intensity distribution, and the averaged laser absorptivity of the material surface remains constant at 13% [51]. Figure 3.6 shows a comparison between the melt-pool shape obtained from the numerical simulation after 5 s of heating and the post-solidification experimental observation, which indicates a reasonable agreement. The maximum absolute deviations between the present numerical predictions and experimental data for the melt-pool width and depth is less than 5% and 2%, respectively. However, it should be noted that the thermal conductivity and viscosity of the liquid material were artificially increased in the simulations by a factor of 7 with respect to their reported experimental values, as suggested by Pitscheneder *et al.* [51]. This is known as employing 'enhancement factors', mainly to achieve agreement between numerical and experimental results [52]. Independent studies conducted by Saldi *et al.* [52] and Ehlen *et al.* [53] revealed that without using such enhancement factors, the fluid flow structure and the melt-pool shape in simulations differ drastically from experimental observations.

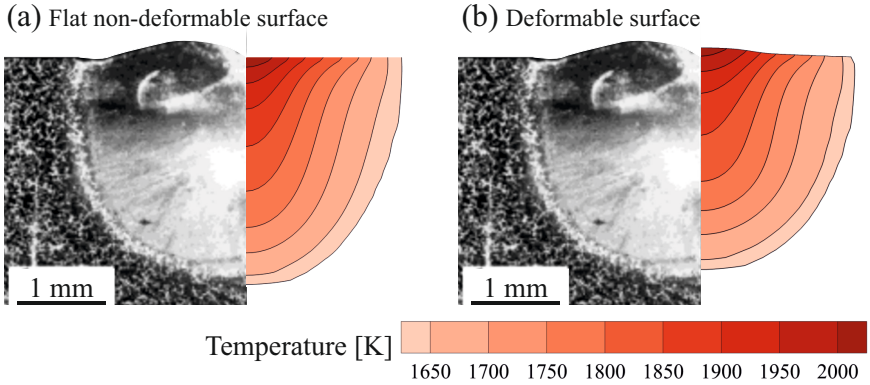

Figure 3.6: Comparison of the numerically predicted melt-pool shape after 5 s of heating with the corresponding experimentally measured post-solidification melt-pool shape reported by Pitscheneder *et al.* [51]. Laser power was set to 3850 W and the material contains 150 ppm sulphur. Numerical predictions obtained from the present model assuming (a) non-deformable and (b) deformable gas-metal interface.

The use of an enhancement factor is often justified by the possible occurrence of turbulence and its influence on heat and momentum transfer in the melt pool, which is assumed to be uniform in the melt pool. However, the high-fidelity numerical simulations conducted by Kidess *et al.* [54, 55] on a melt pool with a flat non-deformable melt-pool surface revealed that turbulent enhancement is strongly non-uniform in the melt pool, resulting in a ω-shaped melt pool that differs notably from the results of simulations assuming uniform transport enhancement. In the present work, high-fidelity simulations were performed based on the large eddy simulation (LES) turbulence model that took the effects of surface deformations into consideration [56]. The results indicate that for the conduction-mode laser melting problem considered, the influence of surface oscillations on melt pool behaviour is larger compared to the effects of turbulent flow in the melt pool; nevertheless the results do not agree with experiments without using

some enhancement. These observations along with previous studies [52, 53, 57] suggest that the published weld pool models lack the inclusion of significant physics. The neglect in simulations of relevant physics such as chemical reactions and unsteady oxygen absorption by the melt-pool surface, non-uniform unsteady surfactant distribution over the melt-pool surface, re-solidification, free surface evolution and three-dimensionality of the fluid flow field has been postulated as reasons why such an *ad hoc* and unphysical enhancement factor is needed to obtain agreement with experimental data [58–60]. However, the inclusion of such factors will increase the model complexity and computational costs. Further investigations are essential to fully explain this behaviour. In section 5.6.3, the effects of the value used for the enhancement factor on the thermal and fluid flow fields and melt-pool oscillatory behaviour are discussed in more detail.

The experimental and numerical data reported by He *et al.* [61], who investigated unsteady heat and fluid flow in the melt pool during conduction-mode laser spot welding of stainless steel (AISI 304) plates, are also considered to validate the reliability of the present model. The melt pool shape obtained from the present model assuming a non-deformable free surface is compared with experimental and numerical data reported by He *et al.* [61] and the results are shown in figure 3.7. In this study, an Nd:YAG laser with a laser power of 1967 W was used. The beam radius was 570 µm with a Gaussian intensity distribution, and laser pulse duration was 3 ms. The averaged laser absorptivity of the material was assumed to remain constant at 27% [61]. The thermal conductivity and viscosity of the molten material were artificially increased in the simulations by a factor 17 and 11, respectively, as suggested by He *et al.* [61]. The maximum absolute deviations between the present numerical predictions and experimental data for the melt-pool width and depth is less than 8% and 2.5%, respectively. The results obtained from the present model are indeed in reasonable agreement with the reference data, indicating the validity of the present model in reproducing the results reported in literature.

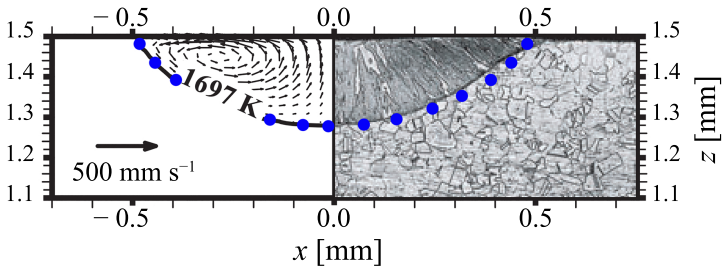

Figure 3.7: Comparison of the spot melt-pool shape obtained from the present numerical simulation with the corresponding experimentally observed (the right side of the figure) and numerically predicted (the left side of the figure) post-solidification melt-pool shape reported by He *et al.* [61]. Laser power was set to 1967 W and the beam radius was 570 µm. Blue circles show the melt-pool shape predicted using the present model. The 500 mm s^{-1} reference vector is provided for scaling the velocity field shown in the melt pool.

The reliability of the present model was also investigated by comparing the numerically predicted melt-pool size and surface deformations with experimental observations of Cunningham *et al.* [62]. The evolutions of the melt pool shape and its sur-

face depression under stationary laser melting of a Ti-6Al-4V plate under conduction mode were studied. In this study, an ytterbium fibre laser was employed and the laser power was 156 W. The laser beam had a Gaussian intensity distribution, the radius of the laser spot was 7×10^{-5} m, and the averaged laser absorptivity of the material was assumed to remain constant at 30%. The thermophysical properties of Ti-6Al-4V suggested by Sharma *et al.* [63] were employed for calculations. Since the melt pool surface temperature reaches the boiling point, the effects of recoil pressure p_{recoil} and vaporisation heat loss $q_{\text{vaporisation}}$ were included in the model through source terms in momentum and energy equations. The recoil pressure [6] and vaporisation heat loss [9] were determined respectively as follows:

$$p_{\text{recoil}} = 0.54 \cdot p_0 \exp\left(\frac{\mathscr{L}_{\text{v}} M\,(T - T_{\text{b}})}{\text{R}\,T\,T_{\text{b}}}\right), \tag{3.81}$$

$$q_{\text{vaporisation}} = -0.82 \cdot \frac{\mathscr{L}_{\text{v}} M}{\sqrt{2\pi M \text{R}\,T}}\, p_0 \exp\left(\frac{\mathscr{L}_{\text{v}} M\,(T - T_{\text{b}})}{\text{R}\,T\,T_{\text{b}}}\right), \tag{3.82}$$

where, p_0 is the ambient pressure, $\mathscr{L}_{\text{v}}$ the latent heat of vaporisation, M the molar mass, R the universal gas constant, T the temperature and $T_{\text{b}} = 3315$ K the boiling temperature. The results obtained from the present numerical simulations are compared with those reported by Cunningham *et al.* [62] in figure 3.8, which show a reasonable agreement. The maximum absolute deviations between the present numerical predictions and experimental data for the melt-pool aspect ratio is less than 12%.

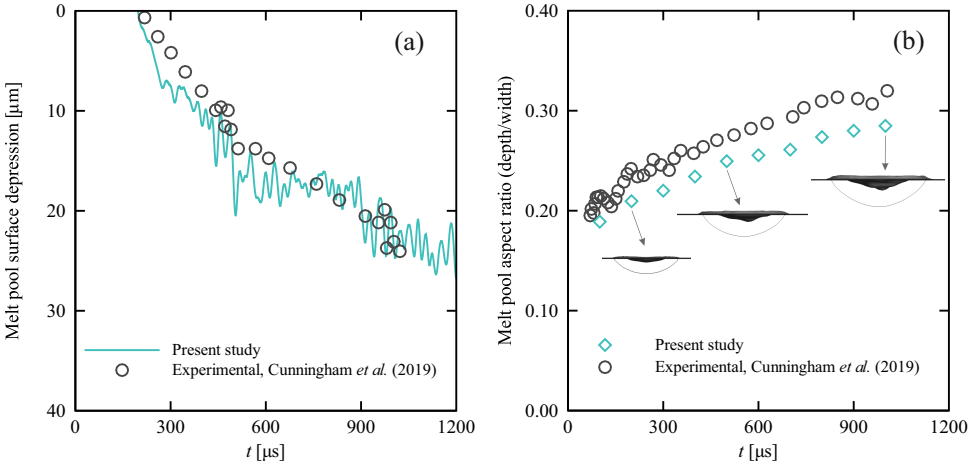

Figure 3.8: Comparison of (a) the melt-pool surface depression and (b) the melt pool aspect ratio (depth to width ratio) obtained from the present numerical simulation with the corresponding experimental observations of Cunningham *et al.* [62]. Laser power was set to 156 W and the beam radius was 70 μm. Snapshots of the melt pool and its deformed surface are shown in the right subfigure for three different time instances.

3.6.3. Arc welding

To validate the accuracy of the present model in predicting the melt pool shape during stationary gas tungsten arc welding, morphological evolution of the melt pool obtained from the present numerical simulation are compared to *in situ* experiments conducted by Aucott *et al.* [64]. In this problem, a gas tungsten arc weld with a steady-current of 125 A and an initial arc length of 1.027 mm was considered. The thermophysical properties of the alloy were obtained from Kidess *et al.* [55]. Figure 3.9 shows the evolution of the melt pool width and depth obtained from the present numerical simulation and the experimental data reported by Aucott *et al.* [64], which indicates a reasonable agreement. The deviation between the numerically predicted melt pool shape and the reference data can be attributed to uncertainties associated with material properties employed in the simulation, particularly for temperatures above the melting temperature, and the simplifying assumptions made to develop the present model.

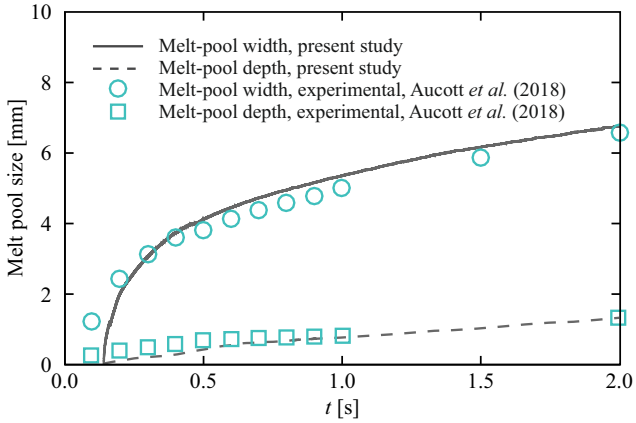

Figure 3.9: Comparison of the melt-pool shape evolution during stationary gas tungsten arc welding (GTAW) obtained from the present numerical simulation (solid and dashed lines) with the corresponding experimentally observed (symbols) melt-pool shape reported by Aucott *et al.* [64]. (Steady-current gas tungsten arc welding, $I = 125$ A)

3.6.4. Spurious currents in Eulerian-based multiphase flow simulations

Particular attention has also been paid to the effect of spurious currents on numerical predictions of molten metal flow in melt pools with free surface deformations. Spurious currents are an unavoidable numerical artefact generating unphysical parasitic velocity fields that do not vanish with grid refinement when using the continuum surface force technique for modelling surface tension effects in the VOF method. This problem has been thoroughly investigated by Mukherjee *et al.* [65] and the results of their study show that the Reynolds number based on the time-averaged maximum spurious velocity is $\mathcal{O}(10)$. The results of the present simulations show that the flow Reynolds number is $\mathcal{O}(10^3)$ that is at least two orders of magnitude larger than that induced by spurious currents. Furthermore, to suppress fluid velocities in the solid regions a momentum sink term is defined based on the enthalpy porosity technique that further weakens the spuri-

ous currents in solid regions. Therefore, the influence of spurious currents on numerical predictions is considered to be negligible in the present study.

References

[1] Cho, M. H., Lim, Y. C., and Farson, D. F. Simulation of weld pool dynamics in the stationary pulsed gas metal arc welding process and final weld shape. *Welding Journal*, 85(12):271s–283s, 2006. URL: http://files.aws.org/wj/supplement/WJ_2006_12_s271.pdf.

[2] Voller, V. R. and Swaminathan, C. R. General source-based method for solidification phase change. *Numerical Heat Transfer, Part B: Fundamentals*, 19(2):175–189, 1991. doi:10.1080/10407799108944962.

[3] Hirt, C. W. and Nichols, B. D. Volume of fluid (VOF) method for the dynamics of free boundaries. *Journal of Computational Physics*, 39(1):201–225, 1981. doi:10.1016/0021-9991(81)90145-5.

[4] Voller, V. R. and Prakash, C. A fixed grid numerical modelling methodology for convection-diffusion mushy region phase-change problems. *International Journal of Heat and Mass Transfer*, 30(8):1709–1719, 1987. doi:10.1016/0017-9310(87)90317-6.

[5] Brackbill, J. U., Kothe, D. B., and Zemach, C. A continuum method for modeling surface tension. *Journal of Computational Physics*, 100(2):335–354, 1992. doi:10.1016/0021-9991(92)90240-y.

[6] Anisimov, S. I. *Instabilities in Laser-matter interaction*. CRC Press, Boca Raton, Fla, 1995. ISBN 0849386608.

[7] Lee, J. Y., Ko, S. H., Farson, D. F., and Yoo, C. D. Mechanism of keyhole formation and stability in stationary laser welding. *Journal of Physics D: Applied Physics*, 35(13):1570–1576, 2002. doi:10.1088/0022-3727/35/13/320.

[8] Cho, J.-H. and Na, S.-J. Implementation of real-time multiple reflection and Fresnel absorption of laser beam in keyhole. *Journal of Physics D: Applied Physics*, 39(24):5372–5378, 2006. doi:10.1088/0022-3727/39/24/039.

[9] von Allmen, M. and Blatter, A. *Laser-Beam Interactions with Materials*. Springer Berlin Heidelberg, 1995. doi:10.1007/978-3-642-57813-7.

[10] Johnson, K. L., Rodgers, T. M., Underwood, O. D., Madison, J. D., Ford, K. R., Whetten, S. R., Dagel, D. J., and Bishop, J. E. Simulation and experimental comparison of the thermo-mechanical history and 3D microstructure evolution of 304L stainless steel tubes manufactured using LENS. *Computational Mechanics*, 61(5):559–574, 2017. doi:10.1007/s00466-017-1516-y.

[11] Sridharan, K., Allen, T., Anderson, M., Cao, G., and Kulcinski, G. Emissivity of candidate materials for VHTR applicationbs: Role of oxidation and surface modification treatments. Technical report, 2011. URL: https://www.osti.gov/biblio/1022709.

[12] Ebrahimi, A., Kleijn, C. R., and Richardson, I. M. Numerical study of molten metal melt pool behaviour during conduction-mode laser spot melting. *Journal of Physics D: Applied Physics*, 54:105304, 2021. doi:10.1088/1361-6463/abca62.

[13] Cho, J., Farson, D. F., Hollis, K. J., and Milewski, J. O. Numerical analysis of weld pool oscillation in laser welding. *Journal of Mechanical Science and Technology*, 29(4):1715–1722, 2015. doi:10.1007/s12206-015-0344-2.

[14] Kim, Y.-D. and Kim, W.-S. A numerical analysis of heat and fluid flow with a deformable curved free surface in a laser melting process. *International Journal of Heat and Fluid Flow*, 29(5): 1481–1493, 2008. doi:10.1016/j.ijheatfluidflow.2008.06.009.

[15] Zacharia, T., Eraslan, A. H., Aidun, D. K., and David, S. A. Three-dimensional transient model for arc welding process. *Metallurgical Transactions B*, 20(5):645–659, 1989. doi:10.1007/bf02655921.

[16] Bai, X., Colegrove, P., Ding, J., Zhou, X., Diao, C., Bridgeman, P., roman Hönnige, J., Zhang, H., and Williams, S. Numerical analysis of heat transfer and fluid flow in multilayer deposition of PAW-based wire and arc additive manufacturing. *International Journal of Heat and Mass Transfer*, 124:504–516, 2018. doi:10.1016/j.ijheatmasstransfer.2018.03.085.

[17] Lee, S. Y. and Na, S. J. A numerical analysis of a stationary gas tungsten welding arc considering various electrode angles. *Welding Journal*, 75(9):269s–279s, 1996. URL: `http://files.aws.org/wj/supplement/WJ_1996_09_s269.pdf`.

[18] Lee, S. Y. and Na, S. J. Analysis of TIG welding arc using boundary-fitted coordinates. *Proceedings of the Institution of Mechanical Engineers, Part B: Journal of Engineering Manufacture*, 209(2):153–164, 1995. doi:10.1243/pime_proc_1995_209_067_02.

[19] Unnikrishnakurup, S., Rouquette, S., Soulié, F., and Fras, G. Estimation of heat flux parameters during static gas tungsten arc welding spot under argon shielding. *International Journal of Thermal Sciences*, 114:205–212, 2017. doi:10.1016/j.ijthermalsci.2016.12.008.

[20] Lin, M. L. and Eagar, T. W. Pressures produced by gas tungsten arcs. *Metallurgical Transactions B*, 17(3):601–607, 1986. doi:10.1007/bf02670227.

[21] Tsai, N. S. and Eagar, T. W. Distribution of the heat and current fluxes in gas tungsten arcs. *Metallurgical Transactions B*, 16(4):841–846, 1985. doi:10.1007/bf02667521.

[22] Ebrahimi, A., Kleijn, C. R., and Richardson, I. M. A simulation-based approach to characterise melt-pool oscillations during gas tungsten arc welding. *International Journal of Heat and Mass Transfer*, 164:120535, 2021. doi:10.1016/j.ijheatmasstransfer.2020.120535.

[23] Meng, X., Qin, G., and Zou, Z. Investigation of humping defect in high speed gas tungsten arc welding by numerical modelling. *Materials & Design*, 94:69–78, 2016. doi:10.1016/j.matdes.2016.01.019.

[24] Liu, J. W., Rao, Z. H., Liao, S. M., and Tsai, H. L. Numerical investigation of weld pool behaviors and ripple formation for a moving GTA welding under pulsed currents. *International Journal of Heat and Mass Transfer*, 91:990–1000, 2015. doi:10.1016/j.ijheatmasstransfer.2015.08.046.

[25] Tsao, K. C. and Wu, C. S. Fluid flow and heat transfer in GMA weld pools. *Welding journal*, 67 (3):70s–75s, 1988. URL: `https://app.aws.org/wj/supplement/WJ_1988_03_s70.pdf`.

[26] Tritton, D. J. *Physical Fluid Dynamics*. Springer Netherlands, 1st edition, 1977. ISBN 978-94-009-9992-3. doi:10.1007/978-94-009-9992-3.

[27] Murphy, A. B. and Lowke, J. J. Heat transfer in arc welding. In *Handbook of Thermal Science and Engineering*, pages 2657–2727. Springer International Publishing, 2018. doi:10.1007/978-3-319-26695-4_29.

[28] Richardson, I. M. *Properties of the constricted gas tungsten (plasma) welding arc at elevated pressures*. PhD dissertation, Industrial and Manufacturing Science, Cranfield Institute of Technology, 1991.

[29] Goodarzi, M., Choo, R., and Toguri, J. M. The effect of the cathode tip angle on the GTAW arc and weld pool: I. mathematical model of the arc. *Journal of Physics D: Applied Physics*, 30(19): 2744–2756, 1997. doi:10.1088/0022-3727/30/19/013.

[30] Rao, Z. H., Zhou, J., Liao, S. M., and Tsai, H. L. Three-dimensional modeling of transport phenomena and their effect on the formation of ripples in gas metal arc welding. *Journal of Applied Physics*, 107(5):054905, 2010. doi:10.1063/1.3326163.

[31] Xu, G., Hu, J., and Tsai, H. L. Three-dimensional modeling of arc plasma and metal transfer in gas metal arc welding. *International Journal of Heat and Mass Transfer*, 52(7-8):1709–1724, 2009. doi:10.1016/j.ijheatmasstransfer.2008.09.018.

[32] Schnick, M., Fuessel, U., Hertel, M., Haessler, M., Spille-Kohoff, A., and Murphy, A. B. Modelling of gas–metal arc welding taking into account metal vapour. *Journal of Physics D: Applied Physics*, 43(43):434008, 2010. doi:10.1088/0022-3727/43/43/434008.

[33] Lin, Q., Li, X., and Simpson, S. W. Metal transfer measurements in gas metal arc welding. *Journal of Physics D: Applied Physics*, 34(3):347–353, 2001. doi:10.1088/0022-3727/34/3/317.

[34] Lancaster, J. F., editor. *The Physics of Welding*. International series on materials science of technology. Pergamon Press, Oxford, UK, 2nd edition, 1986. ISBN 0080340768.

[35] Zhang, G., Goett, G., Kozakov, R., Uhrlandt, D., Reisgen, U., Willms, K., Sharma, R., Mann, S., and Lozano, P. Study of the arc voltage in gas metal arc welding. *Journal of Physics D: Applied Physics*, 52(8):085202, 2018. doi:10.1088/1361-6463/aaf588.

[36] Zhang, G., Goett, G., Uhrlandt, D., Lozano, P., and Sharma, R. A simplified voltage model in GMAW. *Welding in the World*, 64(9):1625–1634, 2020. doi:10.1007/s40194-020-00943-x.

[37] Khairallah, S. A., Anderson, A. T., Rubenchik, A., and King, W. E. Laser powder-bed fusion additive manufacturing: Physics of complex melt flow and formation mechanisms of pores, spatter, and denudation zones. *Acta Materialia*, 108:36–45, 2016. doi:10.1016/j.actamat.2016.02.014.

[38] Yang, Z., Bauereiß, A., Markl, M., and Körner, C. Modeling laser beam absorption of metal alloys at high temperatures for selective laser melting. *Advanced Engineering Materials*, page 2100137, 2021. doi:10.1002/adem.202100137.

[39] Mahrle, A. and Beyer, E. Theoretical aspects of fibre laser cutting. *Journal of Physics D: Applied Physics*, 42(17):175507, 2009. doi:10.1088/0022-3727/42/17/175507.

[40] Belton, G. R. Langmuir adsorption, the gibbs adsorption isotherm, and interracial kinetics in liquid metal systems. *Metallurgical Transactions B*, 7(1):35–42, 1976. doi:10.1007/bf02652817.

[41] March, N. H. and Tosi, M. P. *Atomic Dynamics in Liquids*. Dover, New York, 1991.

[42] Sahoo, P., Debroy, T., and McNallan, M. J. Surface tension of binary metal—surface active solute systems under conditions relevant to welding metallurgy. *Metallurgical Transactions B*, 19(3):483–491, 1988. doi:10.1007/bf02657748.

[43] Rioul, O. and Vetterli, M. Wavelets and signal processing. *IEEE Signal Processing Magazine*, 8 (4):14–38, 1991. doi:10.1109/79.91217.

[44] Allen, J. Short term spectral analysis, synthesis, and modification by discrete Fourier transform. *IEEE Transactions on Acoustics, Speech, and Signal Processing*, 25(3):235–238, 1977. doi:10.1109/tassp.1977.1162950.

[45] Farge, M. Wavelet Transforms and their Applications to Turbulence. *Annual Review of Fluid Mechanics*, 24(1):395–458, 1992. doi:10.1146/annurev.fl.24.010192.002143.

[46] Mallat, S. *A Wavelet Tour of Signal Processing*. Elsevier Inc., 2009. doi:10.1016/B978-0-12-374370-1.X0001-8.

[47] Grossmann, A., Morlet, J., and Paul, T. Transforms associated to square integrable group representations. I. General results. *Journal of Mathematical Physics*, 26(10):2473–2479, 1985. doi:10.1063/1.526761.

[48] Voller, V. R. Development and application of a heat balance integral method for analysis of metallurgical solidification. *Applied Mathematical Modelling*, 13(1):3–11, 1989. doi:10.1016/0307-904x(89)90191-1.

[49] Hannoun, N., Alexiades, V., and Mai, T. Z. A reference solution for phase change with convection. *International Journal for Numerical Methods in Fluids*, 48(11):1283–1308, 2005. doi:10.1002/fld.979.

[50] Kumar, L., Manjunath, B., Patel, R., Markandeya, S., Agrawal, R., Agrawal, A., Kashyap, Y., Sarkar, P., Sinha, A., Iyer, K., and Prabhu, S. Experimental investigations on melting of lead in a cuboid with constant heat flux boundary condition using thermal neutron radiography. *International Journal of Thermal Sciences*, 61:15–27, 2012. doi:10.1016/j.ijthermalsci.2012.06.014.

[51] Pitscheneder, W., DebRoy, T., Mundra, K., and Ebner, R. Role of sulfur and processing variables on the temporal evolution of weld pool geometry during multikilowatt laser beam welding of steels. *Welding Journal*, 75(3):71s–80s, 1996. URL: `https://app.aws.org/wj/supplement/WJ_1996_03_s71.pdf`.

[52] Saldi, Z. S., Kidess, A., Kenjereš, S., Zhao, C., Richardson, I. M., and Kleijn, C. R. Effect of enhanced heat and mass transport and flow reversal during cool down on weld pool shapes in laser spot welding of steel. *International Journal of Heat and Mass Transfer*, 66:879–888, 2013. doi:10.1016/j.ijheatmasstransfer.2013.07.085.

[53] Ehlen, G., Ludwig, A., and Sahm, P. R. Simulation of time-dependent pool shape during laser spot welding: Transient effects. *Metallurgical and Materials Transactions A*, 34(12):2947–2961, 2003. doi:10.1007/s11661-003-0194-x.

[54] Kidess, A., Kenjereš, S., Righolt, B. W., and Kleijn, C. R. Marangoni driven turbulence in high energy surface melting processes. *International Journal of Thermal Sciences*, 104:412–422, 2016. doi:10.1016/j.ijthermalsci.2016.01.015.

[55] Kidess, A., Kenjereš, S., and Kleijn, C. R. The influence of surfactants on thermocapillary flow instabilities in low Prandtl melting pools. *Physics of Fluids*, 28(6):062106, 2016. doi:10.1063/1.4953797.

[56] Ebrahimi, A., Kleijn, C. R., and Richardson, I. M. The influence of surface deformation on thermocapillary flow instabilities in low Prandtl melting pools with surfactants. In *Proceedings of the 5th World Congress on Mechanical, Chemical, and Material Engineering*. Avestia Publishing, 2019. doi:10.11159/htff19.201.

[57] Mundra, K., DebRoy, T., Zacharia, T., and David, S. A. Role of thermophysical properties in weld pool modeling. *Welding Journal*, 71(9):313s–320s, 1992. URL: `https://app.aws.org/wj/supplement/WJ_1992_09_s313.pdf`.

[58] Do-Quang, M., Amberg, G., and Pettersson, C.-O. Modeling of the adsorption kinetics and the convection of surfactants in a weld pool. *Journal of Heat Transfer*, 130(9):092102, 2008. doi:10.1115/1.2946476.

[59] Winkle, C., Amberg, G., Inoue, H., Koseki, T., and Fuji, M. Effect of surfactant redistribution on weld pool shape during gas tungsten arc welding. *Science and Technology of Welding and Joining*, 5(1):8–20, 2000. doi:10.1179/stw.2000.5.1.8.

[60] Tsai, M. C. and Kou, S. Marangoni convection in weld pools with a free surface. *International Journal for Numerical Methods in Fluids*, 9(12):1503–1516, 1989. doi:10.1002/fld.1650091206.

[61] He, X., Fuerschbach, P. W., and DebRoy, T. Heat transfer and fluid flow during laser spot welding of 304 stainless steel. *Journal of Physics D: Applied Physics*, 36(12):1388–1398, 2003. doi:10.1088/0022-3727/36/12/306.

[62] Cunningham, R., Zhao, C., Parab, N., Kantzos, C., Pauza, J., Fezzaa, K., Sun, T., and Rollett, A. D. Keyhole threshold and morphology in laser melting revealed by ultrahigh-speed x-ray imaging. *Science*, 363(6429):849–852, 2019. doi:10.1126/science.aav4687.

[63] Sharma, S., Mandal, V., Ramakrishna, S. A., and Ramkumar, J. Numerical simulation of melt hydrodynamics induced hole blockage in quasi-CW fiber laser micro-drilling of TiAl6V4. *Journal of Materials Processing Technology*, 262:131–148, 2018. doi:10.1016/j.jmatprotec.2018.06.038.

[64] Aucott, L., Dong, H., Mirihanage, W., Atwood, R., Kidess, A., Gao, S., Wen, S., Marsden, J., Feng, S., Tong, M., Connolley, T., Drakopoulos, M., Kleijn, C. R., Richardson, I. M., Browne, D. J., Mathiesen, R. H., and Atkinson, H. V. Revealing internal flow behaviour in arc welding and additive manufacturing of metals. *Nature Communications*, 9(1), 2018. doi:10.1038/s41467-018-07900-9.

[65] Mukherjee, S., Zarghami, A., Haringa, C., van As, K., Kenjereš, S., and den Akker, H. E. A. V. Simulating liquid droplets: A quantitative assessment of lattice Boltzmann and Volume of Fluid methods. *International Journal of Heat and Fluid Flow*, 70:59–78, 2018. doi:10.1016/j.ijheatfluidflow.2017.12.001.

4

The Influence of the Mushy Zone Constant on Simulations of Solidification and Melting

The high degree of uncertainty and conflicting literature data on the value of the permeability coefficient (also known as the mushy-zone constant), which is employed to dampen fluid velocities in the mushy zone and suppress them in solid regions, is a critical drawback when using the fixed-grid enthalpy-porosity technique for modelling non-isothermal phase-change processes. In this chapter, the sensitivity of numerical predictions to the value of this coefficient is scrutinised. Using finite-volume based numerical simulations of isothermal and non-isothermal melting and solidification problems, the causes of increased sensitivity are identified. It is found that depending on the mushy-zone thickness and the velocity field, the solid-liquid interface morphology and the rate of phase-change are sensitive to the permeability coefficient. It is demonstrated that numerical predictions of an isothermal phase-change problem are independent of the permeability coefficient for sufficiently fine meshes. It is also shown that sensitivity to the choice of permeability coefficient can be assessed by means of an appropriately defined Péclet number.

The contents of this chapter have been published in *Energies*, **2019**, *12*(22), 4360, DOI: 10.3390/en12224360.

4.1. Introduction

Numerical simulations of melting and solidification processes are critical to develop our understanding of phase transformations that occur in various technologies such as additive manufacturing, thermal energy storage, anti-icing and materials processing. It is however challenging due to the involvement of the moving boundary problem [1] and the wide range of length and time scales in transport phenomena during solid-liquid phase transformations [2]. Different numerical techniques have been developed to resolve the transport phenomena and the solid-liquid phase transition at different scales, which have been reviewed in [3–6].

Techniques for numerically modelling solid-liquid phase transitions at the continuum level have generally been divided into transformed-grid and fixed-grid approaches [4]. Detailed information on the derivation and implementation of these approaches can be found in the literature [7–9]. The focus of the present chapter is on the fixed-grid approach in which latent heat effects and fluid flow near the liquid-solid interface are taken into account through the inclusion of thermal energy and momentum source terms in that region [3]. One of the advantages of the fixed-grid approach over the transformed-grid approach is its robustness in treating changes in the interface topology. However, interface smearing is an inherent disadvantage, which may be diminished by applying local grid refinement near the solid-liquid interface [10–12].

Flow velocities in the liquid phase, particularly in the so called mushy zone close to the solid interface, where phase-change takes place over a melting temperature range [13], can have a significant influence on the local heat transfer [14]; it is therefore crucial to predict fluid flow in the mushy zone with a sufficient level of accuracy. Of the various approaches that have been employed for this purpose [15–17], the porosity approach is the most common. In this approach, it is assumed that the fluid flow in the mushy zone is analogous to that in a porous medium. Consequently, Darcy's law is assumed to govern the flow and a corresponding sink term ($\mathbf{S}_\mathrm{d}$) is added to the momentum equation,

$$\mathbf{S}_\mathrm{d} = \frac{-\mu}{K}\mathbf{u}, \tag{4.1}$$

where $\mathbf{u}$ is the fluid velocity vector and μ dynamic viscosity. Assuming isotropy for the solid-liquid morphology and using the Blake-Kozeny equation [18], the permeability (K) can be defined as a function of the liquid fraction (f_L) as follows:

$$K = \frac{\mu}{C}\frac{f_\mathrm{L}^3}{\left(1-f_\mathrm{L}\right)^2}, \tag{4.2}$$

with C the so called permeability coefficient (or the mushy-zone constant). The Blake-Kozeny equation is valid for liquid fractions lower than 0.7 [19, 20] however, is typically used for the entire range of liquid fractions. The value of the permeability coefficient C and its influence on numerical simulations of melting and solidification is generally uncertain.

The values reported for the permeability coefficient C in the literature generally range between 10^3 and $10^{15}\,\mathrm{kg\,s^{-1}\,m^{-3}}$ [21, 22], however values between 10^4 and $10^8\,\mathrm{kg\,s^{-1}\,m^{-3}}$

are often applied. The proposed values for C do not seem to have a one-to-one relation to the type of material being studied. For instance, values between $\mathcal{O}(10^4)$ [23] and $\mathcal{O}(10^8)$ [24] have been proposed for stainless steel, and values between $\mathcal{O}(10^4)$ [25] and $\mathcal{O}(10^{15})$ [26] have been proposed for gallium. Thus, the values proposed for C in the literature seem to depend markedly on the process parameters and the associated boundary conditions, and thus lack generality. In other words, tuning the value of C is essential for every set of boundary conditions and material properties, which requires considerable trial and error evaluation. Previous studies on the influence of the permeability coefficient in simulations of melting and solidification have mainly concentrated on finding a value for C to diminish discrepancies between numerical and experimental data for a specific problem (see, for instance, [27–32]). Additionally, they have often focused on the phase-change materials for thermal energy storage applications, for which material properties and operating conditions differ from those for materials processing applications (*e.g.* casting, welding and additive manufacturing). It is necessary to know under which circumstance and to what extent the numerical predictions of melting and solidification are sensitive to the value of the permeability coefficient to avoid the need for excessive computation. However, there is as yet no general guideline for assessing the appropriate value of C.

The degree of sensitivity of the numerical predictions to the value of the permeability coefficient C appears to be diverse. Several studies reported that the chosen value of C affect the numerical results predicted by the enthalpy-porosity method for isothermal phase-change problems [33–36], in which phase transformation occurs at the melting temperature of the material. This effect is not physically realistic for isothermal phase transformations and should be considered as a numerical artefact [37]. Pan *et al.* [28] studied the melting of calcium chloride hexahydrate ($CaCl_2H_{12}O_6$) in a vertical cylinder and stated that the value of C depends on the temperature difference that drives melting and should be tuned to obtain a reasonable agreement with experimental data. Fadl and Eames [21] reported that the numerical predictions are less sensitive to the value of C in regions where heat transfer is dominated by conduction. Assessing the degree of sensitivity of the numerical prediction to the value of C for different materials and boundary conditions is an open question, despite its significance, as already emphasised in the literature [21, 22, 30, 38].

Realising the degree of sensitivity of the numerical predictions to the value of the permeability coefficient in phase-change simulations with a particular interest in melting and solidification during welding and additive manufacturing is the motivation for the present study in this chapter. The aim is to quantitatively assess the influence of the permeability coefficient (C) on the results of the enthalpy-porosity method in predicting heat and fluid flow and the position of the solid-liquid interface during solid-liquid phase transformations. The sensitivity of the results to the permeability coefficient is analysed for both isothermal and non-isothermal melting and solidification problems and possible roots of errors in the simulation of solidification and melting processes are highlighted. The present study quantifies the influence of the permeability coefficient on the numerical predictions as a function of numerical simulation parameters and physical process parameters and elucidates the limitations of the enthalpy-porosity method.

4.2. Problem description

Isothermal and non-isothermal phase transformations in a two-dimensional rectangular enclosure shown in figure 4.1 are studied. The length of the enclosure (W) is twice its height ($D = 0.1$m). The enclosure is initially filled with solid material at a temperature (T_i) below the melting temperature T_m (for isothermal phase-change) or solidus temperature T_s (for non-isothermal phase-change). The left and the right solid walls are isothermal walls and the upper and the lower walls are adiabatic. At the starting time of the simulation the left wall temperature is suddenly raised from the initial temperature (T_i) to the hot wall temperature (T_h), whereas the cold wall is kept at a temperature $T_c = T_i$. The thermophysical properties of the artificial materials are presented in table 4.1, which represent a wide range of metallic and non-metallic phase-change materials. The liquid phase is assumed to be incompressible and Newtonian, with constant dynamic viscosity μ. All other thermophysical material properties are assumed to be the same for both the solid and liquid phases and are temperature independent.

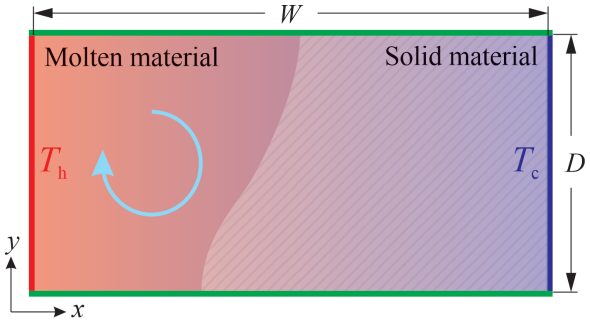

Figure 4.1: The schematic of the system under consideration. From $t = 0$, the left vertical wall is kept at an isothermal temperature T_h, and the right vertical wall is kept at an isothermal temperature T_c, whereas the horizontal walls are adiabatic.

Table 4.1: Thermophysical properties of the artificial materials used in the simulations.

Property	Value	Unit
Density ρ	10^3	$\mathrm{kg\,m^{-3}}$
Specific heat capacity c_p	10^3	$\mathrm{J\,kg^{-1}\,K^{-1}}$
Thermal conductivity k	1, 10 and 100	$\mathrm{W\,m^{-1}\,K}$
Dynamic viscosity μ	10^{-3}	$\mathrm{kg\,m^{-1}\,s^{-1}}$
Latent heat of fusion $\mathscr{L}_f$	10^5	$\mathrm{J\,kg^{-1}}$
Thermal expansion coefficient β	10^{-6}	$\mathrm{K^{-1}}$
Melting temperature $T_m = \frac{(T_l+T_s)}{2}$	1.5×10^3	K
Melting-temperature range ΔT_m	0, 5, 10, 25 and 50	K

4.3. Mathematical formulation

Since the Rayleigh number for the problems considered here is less than 10^6, the fluid flow is assumed to be laminar. Thermal buoyancy effects are taken into account using the Boussinesq assumption [39]. Utilising the dimensionless variables $\mathrm{Fo} = t\alpha/D^2$, $\mathbf{u}^* = \mathbf{u}D/\alpha$, $T^* = T/(T_\mathrm{h} - T_\mathrm{melt})$, $H^* = T^* + f_\mathrm{L}/\mathrm{Ste}$, $p^* = pD^2/(\rho\alpha^2)$ and $K^* = K/D^2$ [10], the unsteady momentum and energy equations are respectively cast in conservative dimensionless form as follows:

$$\frac{1}{\mathrm{Pr}}\left(\frac{\partial \mathbf{u}^*}{\partial \mathrm{Fo}} + \mathbf{u}^* \cdot \nabla \mathbf{u}^* + \nabla p^*\right) = \nabla^2 \mathbf{u}^* + \mathrm{Ra}T^* \hat{\mathbf{y}} - \frac{\mathbf{u}^*}{K^*}, \tag{4.3}$$

$$\frac{\partial H^*}{\partial \mathrm{Fo}} + \mathbf{u}^* \cdot \nabla H^* = \nabla^2 T^* + \frac{1}{\mathrm{Ste}}\left(\frac{\partial f_\mathrm{L}}{\partial \mathrm{Fo}} + \nabla \mathbf{u}^*\right), \tag{4.4}$$

where the Prandtl number (Pr) represents the ratio of momentum diffusivity to thermal diffusivity $(\alpha = k/(\rho c_\mathrm{p}))$ in molten materials and is defined as

$$\mathrm{Pr} = \frac{\mu}{\rho\alpha}. \tag{4.5}$$

To evaluate the relative importance of buoyancy to viscous forces acting on the molten materials, the Grashof number (Gr) and Rayleigh number (Ra) can be defined as

$$\mathrm{Gr} = \frac{\|\mathbf{g}\|\beta\rho^2 D^3 (T_\mathrm{h} - T_\mathrm{melt})}{\mu^2}, \tag{4.6}$$

$$\mathrm{Ra} = \mathrm{Gr} \cdot \mathrm{Pr} = \frac{\|\mathbf{g}\|\beta\rho D^3 (T_\mathrm{h} - T_\mathrm{melt})}{\mu\alpha}. \tag{4.7}$$

The Stefan number (Ste) is the ratio of sensible to latent heat and is defined as

$$\mathrm{Ste} = \frac{c_\mathrm{p}(T_\mathrm{h} - T_\mathrm{melt})}{\mathscr{L}_\mathrm{f}}. \tag{4.8}$$

In the above, ρ is density, μ dynamic viscosity, p the static pressure, k thermal conductivity, c_p specific heat capacity at constant pressure, f_L the local liquid fraction, $\mathscr{L}_\mathrm{f}$ the latent heat of melting or solidification, β the thermal expansion coefficient, $\mathbf{g}$ the gravitational acceleration vector, t time, $\mathbf{u}$ the fluid velocity vector, and $\hat{\mathbf{y}}$ the unit vector in the y-axis direction. T_melt is the melting-temperature (for isothermal phase-change) or solidus temperature (for non-isothermal phase-change).

For the sake of simplicity, the local liquid fraction is considered to be a function of temperature only, which is a reasonable assumption for the cases where under-cooling is not significant [40]. Different relationships have been proposed for temperature-dependence of the liquid fraction, depending on the materials and the nature of the micro-segregation [41, 42]. Based on the method suggested by Voller and Swaminathan [41], the relationship between the local liquid fraction and the temperature is defined to be linear as follows:

$$f_\mathrm{L}(T) = \frac{T - T_\mathrm{s}}{T_\mathrm{l} - T_\mathrm{s}}; T_\mathrm{s} \leq T \leq T_\mathrm{l}, \tag{4.9}$$

where, T_l and T_s are liquidus and solidus temperatures, respectively. In the case of isothermal phase-transformation, a step change in the liquid fraction occurs at the melting-temperature according to the method given by Voller and Prakash [16]. Additionally, the convective part of the enthalpy source term in the energy equation (*i.e.* $\nabla \mathbf{u}^*$) takes the value zero for the isothermal phase transformation due to the step change in the latent heat and a zero velocity at the solid-liquid interface [16].

In order to deal with the fluid velocity in the mushy zone, a sink term based on the Blake-Kozeny equation (*i.e.* equation (4.1) and equation (4.2)) is introduced into the momentum equation [16].

$$\frac{-\mathbf{u}^*}{K^*} = -\frac{D^2\mathbf{u}^*}{K} = -\frac{C}{\mu}\frac{\left(1-f_L\right)^2}{f_L^3+\epsilon}D^2\mathbf{u}^*, \tag{4.10}$$

where, C is the permeability coefficient and ϵ is a small constant, here chosen to be equal to 10^{-3}, to avoid division by zero. The sink term is zero in the liquid region $\left(f_L = 1\right)$ while its limiting value for $f_L = 0$ should be large enough to dominate the other terms in the momentum equation to suppress the fluid velocities in the solid region. The value of the permeability coefficient C can be expected to depend on the morphology of the mushy zone. No consensus was found on the value of the permeability coefficient in the literature [24, 43–47]. The effects of this parameter on numerical results are therefore reported here.

The following dimensionless parameters are utilised to construct a framework for analysing the results. The ratio θ of melting-temperature range ($\Delta T_m = T_l - T_s$) to the temperature difference between the hot and cold wall ($\Delta T_w = T_h - T_c$) is defined as

$$\theta = \frac{T_l - T_s}{T_h - T_c} = \frac{\Delta T_m}{\Delta T_w}. \tag{4.11}$$

The volumetric fraction of liquid inside the computational domain at a time instant t is evaluated as

$$\phi(t) = \frac{1}{W \cdot D}\iint_{\text{domain}} f_L(t)\,\mathrm{d}A. \tag{4.12}$$

The relative difference $\Delta\phi(t) = \left|\phi_2(t) - \phi_1(t)\right| / \phi_1(t)$ between two solutions obtained using different permeability coefficients C_2 and C_1 is used to quantify the sensitivity of a solution to the chosen value of the permeability coefficient C. In addition, a dimensionless parameter (Γ) is employed to quantify the difference between the solid-liquid interface morphology predicted using different permeability coefficients C_1 and C_2 as follows:

$$\Gamma = \frac{1}{W \cdot D}\int_{y=0}^{y=D}\sqrt{\left(x_{f,C_1} - x_{f,C_2}\right)^2}\,\mathrm{d}y, \tag{4.13}$$

where x_f is the position of the liquidus line.

4.4. Numerical procedure

Numerical predictions obtained from an open-source (OpenFOAM [48]) and a proprietary solver (ANSYS Fluent [49]) were compared for simulations of solid-liquid phase transformations, and the results were found to be virtually identical (see section 3.6.1). ANSYS Fluent [49] was selected to carry out further calculations, and simulations were performed in parallel on 8 cores (Intel Xeon E5-2630 v4) of a high-performance computing cluster. The computational domain was discretised on a uniform mesh with quadrilateral grid cells. After performing a grid independence test (results presented in sections 4.5.1 and 4.5.2), a base grid with a cell size $\Delta x_\mathrm{i}/D = \Delta y_\mathrm{i}/D = 4\times10^{-3}$ was chosen. To capture a sharp solid-liquid interface and to reduce errors associated with high-gradient regions, especially when the thickness of the mushy zone is smaller than the base grid size, (*i.e.* $W\,(\Delta T_\mathrm{m}/\Delta T_\mathrm{w}) \leq \Delta x_\mathrm{i}$), a dynamic solution-adaptive mesh refinement was applied using the 'gradient approach' [50] based on the liquid fraction gradients. Four levels of mesh refinement ($\Delta x_\mathrm{N} = \Delta x_\mathrm{i}/2^\mathrm{N}, \mathrm{N} = 1,\cdots,4$) were applied every ten time-steps. A fixed time-step size of $\mathrm{Fo} = k\Delta t/\left(\rho c_\mathrm{p}\Delta x_\mathrm{i}^2\right) = 10^{-4}$ was selected, corresponding to a Courant number ($\mathrm{Co} = \|\mathbf{u}\|\Delta t/\Delta x$) less than 0.25.

The conservation equations were discretised using the finite-volume method. The central-differencing scheme was utilised for the discretisation of the convection and diffusion terms both with second-order accuracy. The PISO (pressure-implicit with splitting of operators) scheme [51] was used for pressure-velocity coupling. Additionally, the PRESTO (pressure staggering option) scheme [52] was used for the pressure interpolation. The time derivative was discretised with a second order implicit scheme. Convergence requires that scaled residuals of the continuity, momentum and the energy equations fall below 10^{-10}, 10^{-12} and 10^{-14} respectively, and that the relative change in the volumetric fraction of liquid ϕ from one iteration to the next is less than 10^{-10}.

4.5. Results

4.5.1. Grid size and sensitivity to the permeability coefficient for isothermal phase change

Sensitivity of the solution to the grid size and the value of the permeability coefficient is studied for isothermal phase-change of gallium melting at $T_\mathrm{m} = 302.78\,\mathrm{K}$, in a side-heated rectangular enclosure with $T_\mathrm{i} = T_\mathrm{c} = 301.30\,\mathrm{K}$, and $T_\mathrm{h} = 311.0\,\mathrm{K}$, which is experimentally investigated by Gau and Viskanta [53]. This benchmark case has often been considered for validation of phase-change simulations in the literature [4]. Detailed information regarding the benchmark case is available in [53, 54].

Figure 4.2 shows the influence of the permeability coefficient on the predicted liquid fraction, using uniform fixed meshes with 42 × 32, 105 × 80, 210 × 160 and 420 × 320 computational grid cells and $C = 10^4$ and $10^8\,\mathrm{kg\,s^{-1}\,m^{-3}}$. When a coarse mesh is utilised, resulting in a non-physical mushy zone of significant thickness, the solution appears to be very sensitive to the value of the permeability coefficient. This sensitivity is attributed to the enhanced heat transfer from the hot fluid to the solid-liquid interface due to higher fluid velocities in the mushy zone, predicted with a smaller permeability coefficient. Reducing the grid cell size, and thus reducing the thickness of the non-physical mushy zone, decreases the total volume of the grid cell in which the permeability coefficient affects

the numerical predictions. Consequently, the sensitivity of the solution to the value of the permeability coefficient decreases with grid refinement. A finite amount of time is required for the mass in a computational cell to absorb heat and melt. A change in the value of C therefore affects the convective heat transfer to the cells located at the solid-liquid interface that can lead to a change in the predicted interface morphology and the rate of melting during the transient phase. This effect reduces by refining the grid size adjacent to the solid-liquid interface [10]. In figure 4.3, the sensitivity to the value of C is quantified as a function of grid cell size by looking at the parameters $\Delta\phi$ and Γ (defined below equation (4.12) and in equation (4.13), representing the relative difference in the predicted liquid fractions, and the relative difference between the solid-liquid interface morphologies) for $C_1 = 1 \times 10^8\,\mathrm{kg\,s^{-1}\,m^{-3}}$ and $C_2 = 1 \times 10^4\,\mathrm{kg\,s^{-1}\,m^{-3}}$ at $t = 150\,\mathrm{s}$. Reducing the cell size decreases the influence of the permeability coefficient on the results, with Γ scaling approximately linearly with cell size, and $\Delta\phi$ scaling approximately quadratically with cell size. Thus, although in principle the chosen value of C should be irrelevant for isothermal phase change, sufficient grid refinement is needed to obtain solutions which are indeed insensitive to the value of C. In addition, sufficient grid resolution in the liquid zone was found to be required to predict the multicellular convection [14, 55–57] early in the phase-change process, which leads to the formation of a wavy solid-liquid interface. According to equation (4.10), the magnitude of the sink-term in solid regions ($f_\mathrm{L} = 0.0$) should be large compared to the viscous term ($\nabla^2\mathbf{u}^*$) to suppress fluid velocities (*i.e.* $CD^2/(\mu\epsilon) \gg 1$). The influence of the sink-term magnitude on predicted liquid fraction ϕ and the ratio of the maximum velocity magnitude in solid regions to that in liquid regions (*i.e.* $\|\mathbf{u}_\mathrm{solid}\|_\mathrm{Max}$ / $\|\mathbf{u}_\mathrm{liquid}\|_\mathrm{Max}$) is shown in figure 4.4. Here, D is chosen to be the size of the heated wall. For magnitudes of $CD^2/(\mu\epsilon)$ roughly larger than 2.5×10^7, the predicted liquid fraction is independent of the sink-term. For smaller values of the sink-term, even-though the velocity magnitude in the solid region is orders of magnitude smaller than that in the liquid region, the energy transfer to the solid material is affected, which leads to a change in the predicted liquid-fraction.

The fine-grid results presented in figure 4.2 represent a mathematically converged solution of the governing equations for the given set of boundary conditions. However, the grid independent results of this particular case do not closely match the experimental results reported in [53]. Obtaining a better agreement between numerical predictions and experimental observations by using a coarser grid (*i.e.* grid-dependent results), or by tuning the mathematical model has been reported in the literature [34] that is coincidental, but such *ad hoc* tuning lacks generality [11, 54, 58].

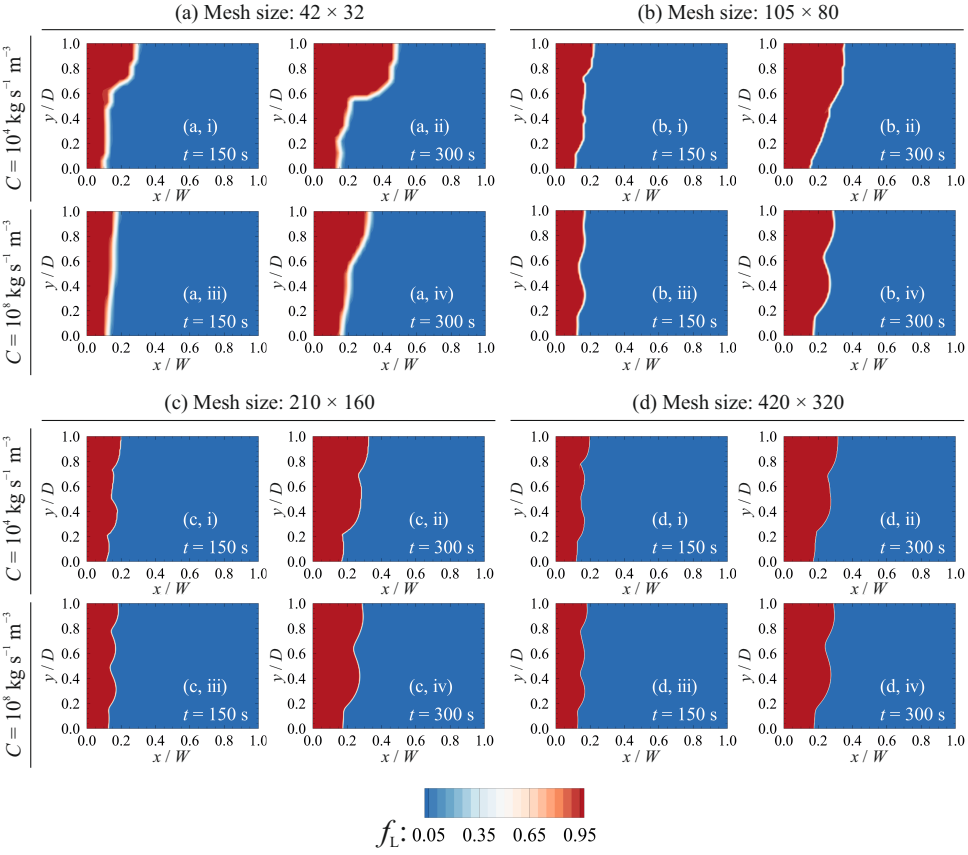

Figure 4.2: The influence of the computational cell size and the permeability coefficient on predicted melting front position for the gallium melting problem. Grid cell size: (a) $\Delta x/D \approx 3.33 \times 10^{-2}$, (b) $\Delta x/D \approx 1.33 \times 10^{-2}$, (c) $\Delta x/D \approx 6.67 \times 10^{-3}$ and (d) $\Delta x/D \approx 3.33 \times 10^{-3}$.

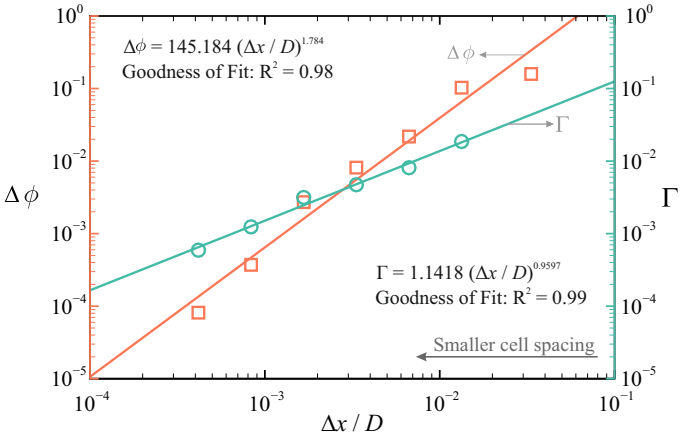

Figure 4.3: The relative difference between the solid-liquid interface morphologies (Γ (defined in equation (4.13)), circles in blue), and the relative difference between the liquid fractions ($\Delta\phi$ (defined below equation (4.12)), squares in red) at $t = 150\,\mathrm{s}$ when using permeability coefficients $C_1 = 1 \times 10^8\,\mathrm{kg\,s^{-1}\,m^{-3}}$ and $C_2 = 1 \times 10^4\,\mathrm{kg\,s^{-1}\,m^{-3}}$ as a function of grid size (Δx). Larger values of $\Delta\phi$ and Γ indicate more sensitivity to the value of the permeability coefficient C. Symbols: results obtained from numerical simulations; dashed lines: curve-fit.

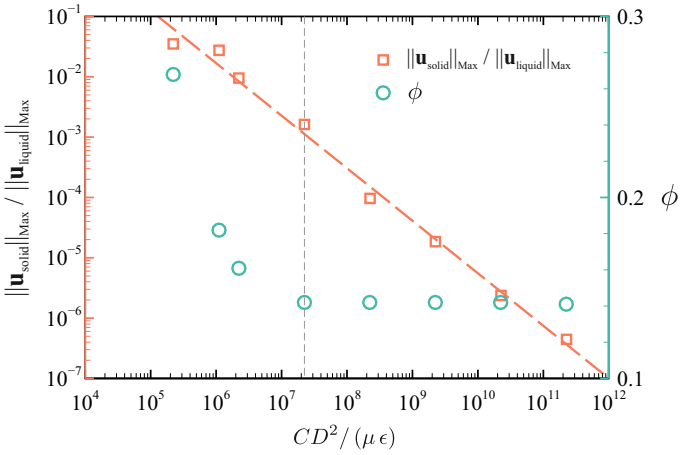

Figure 4.4: The ratio of the maximum velocity magnitude in solid regions to that in liquid regions ($\|\mathbf{u}_{\mathrm{solid}}\|_{\mathrm{Max}}$ / $\|\mathbf{u}_{\mathrm{liquid}}\|_{\mathrm{Max}}$, blue circles) and the predicted liquid fractions ϕ (red squares) for various values of the sink term ($CD^2/(\mu\epsilon)$).

4.5.2. Non-isothermal phase-change

Grid sensitivity

Having seen the importance of sufficient grid resolution for isothermal phase-change, the non-isothermal phase-change problem defined in section 4.2 was subsequently considered, examining the impact of grid refinement on the sensitivity to the permeability coefficient C. For $\Delta T_m = 50\,\mathrm{K}$, figure 4.5 shows the sensitivity parameter $\Delta\phi$, for short time (Fo = 0.12) and steady-state (Fo = 9.0) obtained with $C_1 = 1\times10^8\,\mathrm{kg\,s^{-1}\,m^{-3}}$ and $C_2 = 1\times10^4\,\mathrm{kg\,s^{-1}\,m^{-3}}$. For comparison, the same problem is also solved assuming isothermal phase change ($\Delta T_m = 0\,\mathrm{K}$). For isothermal phase change, the results are insensitive to the chosen value of C in the steady-state, and exhibit a small sensitivity to the chosen value of C during the transient phase before reaching the steady-state that becomes negligible with reducing grid size. For non-isothermal phase change, the sensitivity to the chosen value of C is much stronger and does not vanish with decreasing grid size, even in the steady-state, as is to be expected from the fact that a physically realistic mushy zone is now present, in which flow and convective heat transfer are sensitive to the value of C. However, the sensitivity to C becomes grid independent for base grid sizes below $\Delta x_i/D = 4\times10^{-3}$. Consequently, this base grid size is used in the next sections. In addition, a four-level dynamic solution-adaptive mesh refinement (*i.e.* $\Delta x_N = \Delta x_i/2^N, N = 1,\cdots,4$) is applied to further enhance the accuracy with which the solid-liquid interface is captured.

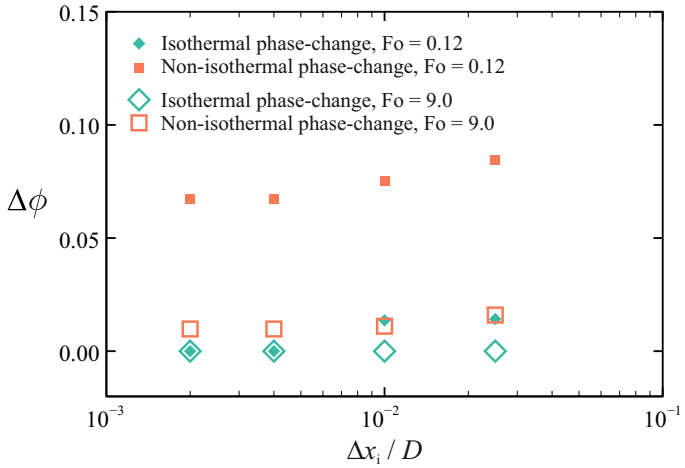

Figure 4.5: The relative difference between liquid fractions predicted with different permeability coefficients (*i.e.* $C_1 = 1\times10^8\,\mathrm{kg\,s^{-1}\,m^{-3}}$ and $C_2 = 1\times10^4\,\mathrm{kg\,s^{-1}\,m^{-3}}$) on different grid densities. Diamonds (in blue): isothermal phase-change, squares (in red): non-isothermal phase-change, Unfilled symbols: Fo = 9.0 (steady-state condition), Filled symbols: Fo = 0.12.

Influence of the permeability coefficient on predicted results

For the non-isothermal phase change problem defined in section 4.2, the influence of the permeability coefficient on the predicted steady-state liquidus-line position ($f_L = 1$) is

shown in figure 4.6 for a fixed wall temperature difference (ΔT_w), a fixed melting temperature range (ΔT_m) and varying Rayleigh number (*i.e.* varying fluid velocities). In the virtual absence of flow, for Ra = 1, the results are insensitive to the value of the permeability coefficient. In this case, heat conduction dominates the total energy transfer around and in the mushy zone. By increasing the value of Ra, *i.e.* increasing fluid flow velocities and increasing convective heat transfer, the results become more sensitive to the chosen value of C. This can be understood from the fact that the value of C, through the momentum sink term, only influences the convective terms and therefore the results become more sensitive to C when convection plays an important role in total heat transfer in the mushy zone.

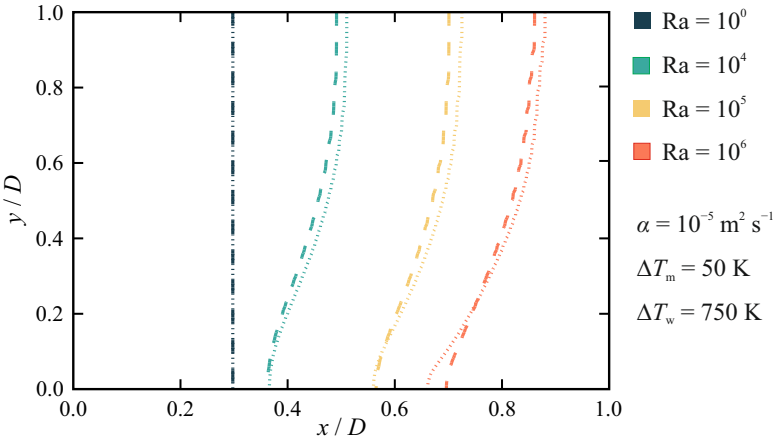

Figure 4.6: The influence of the permeability coefficient on predicted liquidus-line ($f_L = 1$) position for different Rayleigh numbers ($\Delta T_m = 50$ K, $\Delta T_w = 750$ K, Dashed lines: $C = 1 \times 10^8$ kg s^{-1} m^{-3}, Dotted lines: $C = 1 \times 10^4$ kg s^{-1} m^{-3}). The results are given for Fo = 9, in which steady-state solutions are achieved.

Figure 4.7 shows the effect of the permeability coefficient for a fixed melting temperature range (ΔT_m) with different wall-temperature differences (ΔT_w). Here, a higher value of ΔT_w (*i.e.* smaller θ) leads to a smaller mushy zone thickness, and consequently a reduced sensitivity to the permeability coefficient. Similarly, for a fixed (ΔT_w), reducing ΔT_m decreases the mushy zone thickness and as a result, lowers the sensitivity to the permeability coefficient C, as shown in figure 4.8. In summary, the results show that non-isothermal phase-change simulations are less affected by the chosen value of the permeability coefficient C when the mushy zone has a smaller thickness (*i.e.* smaller θ), as this leads to the conductive heat transfer through the mushy zone being large compared to the convective heat transfer. A change in the thermal diffusivity of the material can therefore affect the sensitivity of the numerical predictions to the value of the permeability coefficient. Figure 4.9 indicates the sensitivity of the results to the chosen value of the permeability coefficient as a function of thermal diffusivity of the material for a fixed melting temperature range (ΔT_m) and wall-temperature difference (ΔT_w). It is seen that sensitivity to the permeability coefficient decreases with increasing thermal

diffusivity of the material, which can be attributed to the enhancement of heat conduction contribution to the total heat transfer.

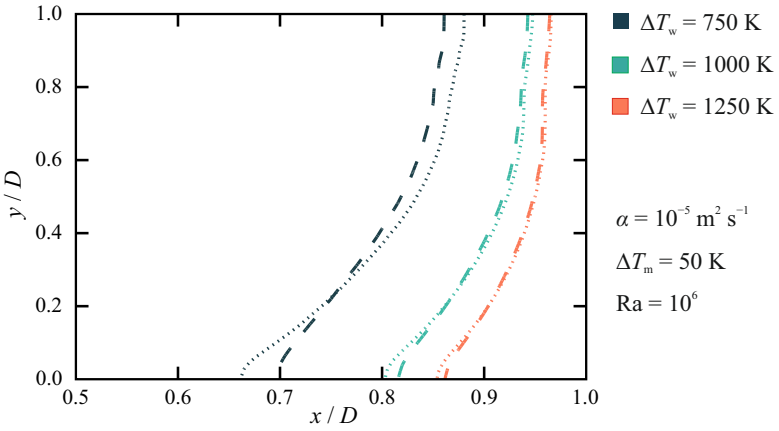

Figure 4.7: The influence of the permeability coefficient on predicted liquidus-line ($f_L = 1$) position for different wall-temperature differences ΔT_w, at $\Delta T_m = 50$ K, Ra = 10^6. Dashed lines: $C = 1 \times 10^8$ kg s^{-1} m^{-3}, Dotted lines: $C = 1 \times 10^4$ kg s^{-1} m^{-3}. The results are given for Fo = 9, in which steady-state solutions are achieved.

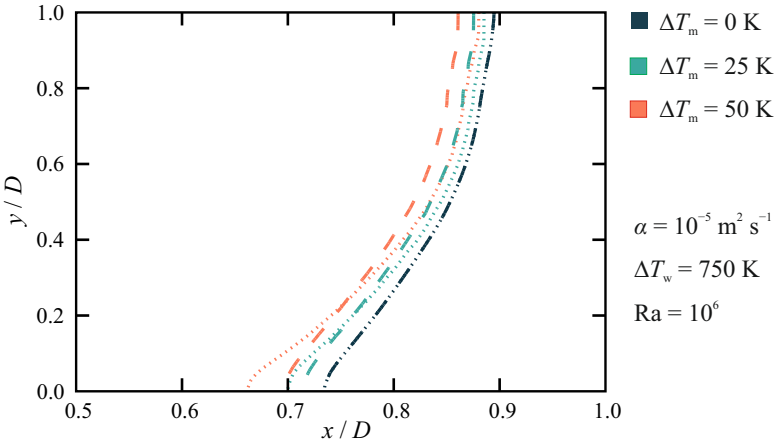

Figure 4.8: The influence of the permeability coefficient on predicted liquidus-line ($f_L = 1$) position for different melting-temperature ranges ΔT_m, at $\Delta T_w = 750$ K, Ra = 10^6. Dashed lines: $C = 1 \times 10^8$ kg s^{-1} m^{-3}, Dotted lines: $C = 1 \times 10^4$ kg s^{-1} m^{-3}. The results are given for Fo = 9, in which steady-state solutions are achieved.

The influence of the permeability coefficient on the time evolution of the melt pool shape is presented in figure 4.10. The results are indeed independent of the permeability coefficient for an isothermal phase-change. A similar conclusion has also been drawn after monitoring the time variations of the liquid-fraction obtained from numerical

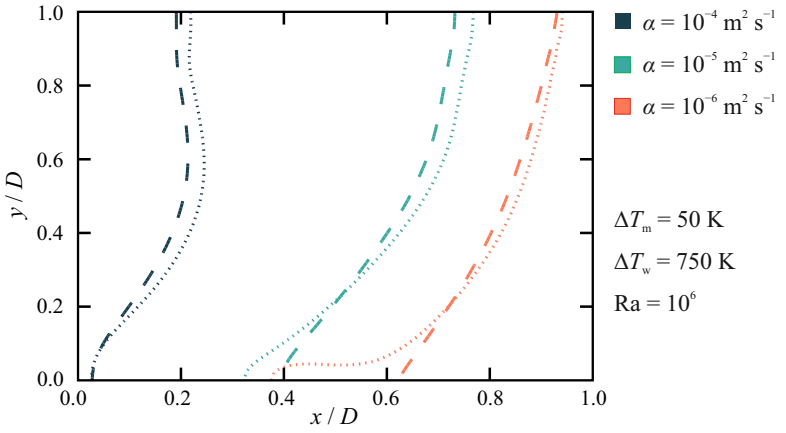

Figure 4.9: The influence of the permeability coefficient on predicted liquidus-line ($f_L = 1$) position for different values of thermal diffusivity α, at $\Delta T_m = 50\,K$, $\Delta T_w = 750\,K$ and $Ra = 10^6$. Dashed lines: $C = 1 \times 10^8\,kg s^{-1} m^{-3}$, Dotted lines: $C = 1 \times 10^4\,kg s^{-1} m^{-3}$. The results are given for Fo = 9, in which steady-state solutions are achieved.

simulations [59, 60]. However, for non-isothermal phase change with a thick mushy zone ($\theta = 1/15$) and strong flow ($Ra = 10^6$), the results are very sensitive to the chosen value of the permeability coefficient, resulting in different pool shapes and rates of phase-change. Less sensitivity to the value of C is found for a thin mushy zone ($\theta = 1/30$). The numerical predictions are also less sensitive to the permeability coefficient at early time instances, when the fluid flow is characterised by low velocities.

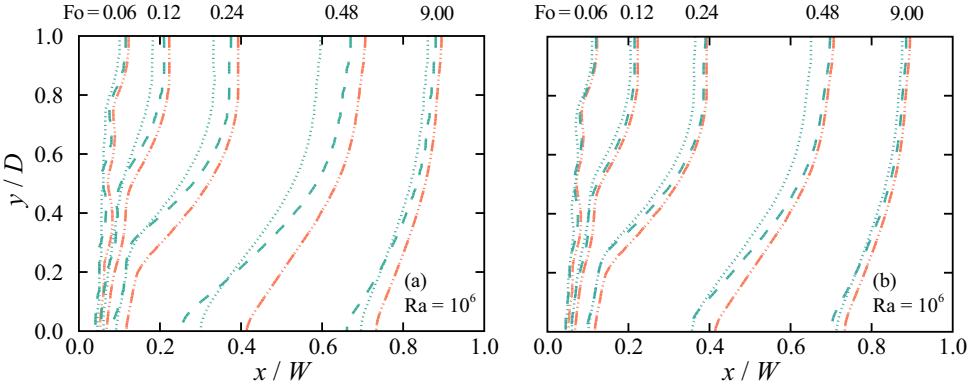

Figure 4.10: Time evolution of melting front positions ($f_L = 1$) for isothermal phase-change (blue lines, $\theta = 0$) and non-isothermal phase-change (red lines, (a) $\Delta T_m = 50\,K$, $\Delta T_w = 750\,K$, $\theta = 1/15$ and (b) $\Delta T_m = 25\,K$, $\Delta T_w = 750\,K$, $\theta = 1/30$) problems. Dashed lines: $C = 1 \times 10^4\,kg s^{-1} m^{-3}$, Dotted lines: $C = 1 \times 10^8\,kg s^{-1} m^{-3}$. ($Ra = 10^6$).

4.6. Discussion

The results reveal that depending on the temperature gradient, velocity field and thermo-physical properties of the phase-change material, which in turn determine the mushy zone thickness, numerical predictions of phase-change problems can show sensitivity to the value of the permeability coefficient. A general guideline is presented here that allows prediction and evaluation of the influence of the permeability coefficient in phase-change simulations. This concept involves both the heat transfer mechanism and the mushy zone thickness.

For phase-change problems without fluid flow, the mushy zone thickness (m_t) can be estimated as

$$m_t = \frac{\Delta T_m}{\|\nabla T\|} = \frac{\Delta T_m \cdot \mathscr{D}}{T_h - T_c}, \tag{4.14}$$

where $\mathscr{D}$ is a characteristic length scale. The fluid flow can alter the mushy zone thickness when convective heat transfer in the mushy zone is of significance. This can be expressed through a Péclet number, which expresses the ratio between the rate of heat advection and heat diffusion. To identify the regions where there is a significant heat transfer enhancement or reduction due to convection, and consequently where the results are sensitive to the permeability coefficient, Pe^* is defined as follows:

$$\mathrm{Pe}^* = \frac{\|\mathbf{u}\| \cdot m_t}{\alpha} = \frac{\|\mathbf{u}\| \cdot \Delta T_m \cdot \mathscr{D}}{\alpha\,(T_h - T_c)}. \tag{4.15}$$

Non-zero values of Pe^* adjacent to the solid-liquid interface indicate increased sensitivity to the permeability coefficient. For isothermal phase-change, Pe^* is zero and predictions are independent of the permeability coefficient.

Sensitivity of the numerical predictions to the value of permeability coefficient C has been appraised for the problem defined in section 4.2, using three different melting temperature ranges ΔT_m and a fixed $\Delta T_w = 750\,\mathrm{K}$, and the results are shown in figure 4.11. Higher values of Pe^* ($\approx \mathcal{O}(10)$) along the melting front for the case with $\Delta T_m = 55\,\mathrm{K}$ (figure 4.11(c)) compared to the case with $\Delta T_m = 10\,\mathrm{K}$ (figure 4.11(b)) indicate that the numerical predictions are more sensitive to the permeability coefficient, which is consistent with the results presented in figures 4.8 and 4.10. When the values of Pe^* along the interface are small (*i.e.* $\mathrm{Pe}^* \ll 1$) the results appear to be insensitive to the permeability coefficient, while for $\mathrm{Pe}^* \gg 1$ the results are sensitive to C.

The general applicability of the proposed Pe^* criterion is also examined for a simulation of a laser spot melting process, which was carried out experimentally by Pitscheneder *et al.* [61]. A steel plate containing 20 ppm of sulphur was heated using a stationary laser beam with a power of 5200 W and a top-hat radius of 1.4 mm. The surface absorptivity is set to 0.13 [61]. Material properties of the steel plate are assumed to be constant and temperature independent, except for the surface tension of the molten material, and can be found in [61–63]. Variations of surface tension with temperature are modelled using the expression proposed by Sahoo *et al.* [64]. Melting of the material and associated heat and fluid flow are numerically predicted using permeability coefficients of $C = 10^6$, 10^8 and $10^{10}\,\mathrm{kg\,s^{-1}\,m^{-3}}$. To study the influence of the mushy-zone thickness

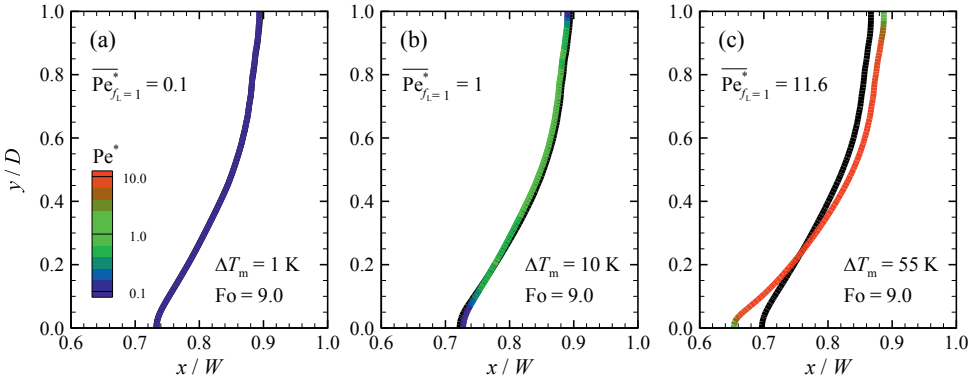

Figure 4.11: Melting front positions ($f_L = 1$) for the problem described in section 4.2, ($\Delta T_w = 750\,K$ and $Ra = 10^6$) at the steady-state condition ($Fo = 9$) and values of Pe^* along the melting fronts for (a) $\Delta T_m = 1\,K$, (b) $\Delta T_m = 10\,K$, and (c) $\Delta T_m = 55\,K$ predicted using different permeability coefficients of $C = 10^4\,kg\,s^{-1}\,m^{-3}$ (coloured lines), and $10^8\,kg\,s^{-1}\,m^{-3}$ (black lines). Values of Pe^* along the melting front are $\mathcal{O}(0.1)$, $\mathcal{O}(1)$ and $\mathcal{O}(10)$ for $\Delta T_m = 1\,K$, $10\,K$ and $55\,K$, respectively. The results are more sensitive to the permeability coefficient for large Pe^*. For the case with $\Delta T_m = 1\,K$ (a), predictions with different permeability coefficient are almost identical and therefore the coloured line covers the black line.

on the sensitivity to C through Pe^*, the melting-temperature range (ΔT_m) of the material is changed artificially to 40 K and 200 K.

Figure 4.12 shows the position of melting front ($f_L = 1$) at $t = 5\,s$, as well as the value of Pe^* along it when using different permeability coefficients and melting temperature ranges. The laser-beam diameter is chosen here as the characteristic length scale $\mathcal{D}$ to calculate Pe^*. Higher values of Pe^* are found for larger ΔT_m, predicting more sensitivity to the permeability coefficient, as is indeed observed when comparing figure 4.12(a) and figure 4.12(b). Due to a steep increase in the momentum sink term with liquid fraction for large permeability coefficients, all predictions are found to converge to an identical solution for very large C. However, a very large value of the permeability can lead to numerical instabilities.

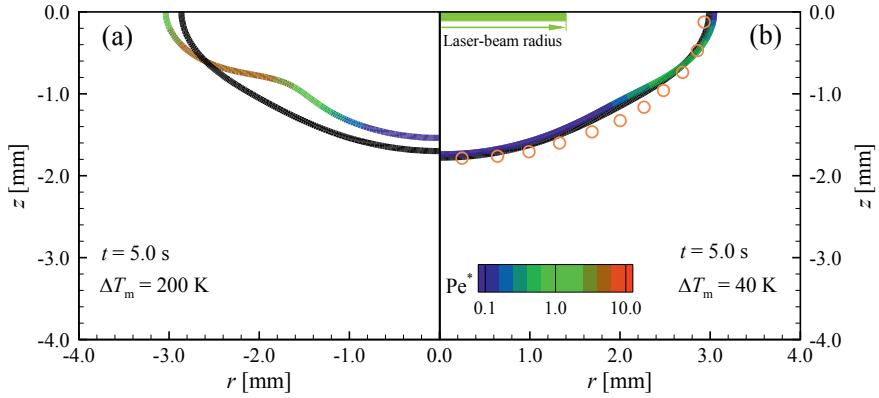

Figure 4.12: Laser spot melting of Fe–S binary alloys with 20 ppm sulphur content. Melting front positions ($f_L = 1$) at $t = 5$ s and values of Pe* along the melting fronts, predicted using different permeability coefficients of $C = 10^6$ kg s^{-1} m^{-3} (coloured lines), and 10^{10} kg s^{-1} m^{-3} (black lines). (a) $\Delta T_m = 200$ K, and (b) $\Delta T_m = 40$ K. Orange symbols show the experimental observation of the melting front position reported by Pitscheneder *et al.* [61].

4.7. Conclusion

A systematic study was performed to scrutinise the influence of the permeability coefficient on the numerical predictions of isothermal and non-isothermal phase-change simulations using the enthalpy-porosity method.

For isothermal phase-change problems, reducing the cell size diminishes the influence of the permeability coefficient on the results, which become independent of the permeability coefficient for fine enough meshes. A grid independent solution of an isothermal phase-change problem is independent of the permeability coefficient. However, not every numerical result that is independent of the permeability coefficient is grid independent.

Numerical predictions of non-isothermal phase-change problems are inherently dependent on the permeability coefficient. The sensitivity of the numerical predictions to the permeability coefficient increases with increased mushy zone thickness and increased fluid flow velocities perpendicular to the solid-liquid interface. A method is proposed to predict and evaluate the influence of the permeability coefficient on numerical predictions, and verified for two-dimensional phase-change problems including laser spot melting. Large values of Pe* $\gg 1$ adjacent to the solid-liquid interface indicate a strong sensitivity and Pe* $\ll 1$ indicates insensitivity to the permeability coefficient C.

References

[1] Crank, J. *Free and moving boundary problems.* Clarendon Press, Oxford, UK, 1984.

[2] Shyy, W. Multi-scale computational heat transfer with moving solidification boundaries. *International Journal of Heat and Fluid Flow*, 23(3):278–287, 2002. doi:10.1016/s0142-727x(02)00175-3.

[3] Rappaz, M. Modelling of microstructure formation in solidification processes. *International Materials Reviews*, 34(1):93–124, 1989. doi:10.1179/imr.1989.34.1.93.

[4] Dutil, Y., Rousse, D. R., Salah, N. B., Lassue, S., and Zalewski, L. A review on phase-change materials: Mathematical modeling and simulations. *Renewable and Sustainable Energy Reviews*, 15(1):112–130, 2011. doi:10.1016/j.rser.2010.06.011.

[5] Verma, S. and Dewan, A. Solidification modeling: Evolution, benchmarks, trends in handling turbulence, and future directions. *Metallurgical and Materials Transactions B*, 45(4):1456–1471, 2014. doi:10.1007/s11663-014-0039-6.

[6] Jaafar, M. A., Rousse, D. R., Gibout, S., and Bédécarrats, J.-P. A review of dendritic growth during solidification: Mathematical modeling and numerical simulations. *Renewable and Sustainable Energy Reviews*, 74:1064–1079, 2017. doi:10.1016/j.rser.2017.02.050.

[7] Basu, B. and Date, A. W. Numerical modelling of melting and solidification problems—a review. *Sadhana*, 13(3):169–213, 1988. doi:10.1007/bf02812200.

[8] Lacroix, M. and Voller, V. R. Finite difference solutions of solidification phase change problems: transformed versus fixed grids. *Numerical Heat Transfer, Part B: Fundamentals*, 17(1):25–41, 1990. doi:10.1080/10407799008961731.

[9] Voller, V. R. *Numerical Methods for Phase-Change Problems*, chapter 19, pages 593–622. Wiley-Blackwell, 2009. ISBN 9780470172599. doi:10.1002/9780470172599.ch19.

[10] Mencinger, J. Numerical simulation of melting in two-dimensional cavity using adaptive grid. *Journal of Computational Physics*, 198(1):243–264, 2004. doi:10.1016/j.jcp.2004.01.006.

[11] Hannoun, N., Alexiades, V., and Mai, T. Z. A reference solution for phase change with convection. *International Journal for Numerical Methods in Fluids*, 48(11):1283–1308, 2005. doi:10.1002/fld.979.

[12] Lan, C. W., Liu, C. C., and Hsu, C. M. An adaptive finite volume method for incompressible heat flow problems in solidification. *Journal of Computational Physics*, 178(2):464–497, 2002. doi:10.1006/jcph.2002.7037.

[13] Worster, M. G. Convection in mushy layers. *Annual Review of Fluid Mechanics*, 29(1):91–122, 1997. doi:10.1146/annurev.fluid.29.1.91.

[14] Quéré, P. L. and Gobin, D. A note on possible flow instabilities in melting from the side. *International Journal of Thermal Sciences*, 38(7):595–600, 1999. doi:10.1016/s0035-3159(99)80039-7.

[15] Morgan, K. A numerical analysis of freezing and melting with convection. *Computer Methods in Applied Mechanics and Engineering*, 28(3):275–284, 1981. doi:10.1016/0045-7825(81)90002-5.

[16] Voller, V. R. and Prakash, C. A fixed grid numerical modelling methodology for convection-diffusion mushy region phase-change problems. *International Journal of Heat and Mass Transfer*, 30(8):1709–1719, 1987. doi:10.1016/0017-9310(87)90317-6.

[17] Voller, V. R., Cross, M., and Markatos, N. C. An enthalpy method for convection/diffusion phase change. *International Journal for Numerical Methods in Engineering*, 24(1):271–284, 1987. doi:10.1002/nme.1620240119.

[18] Brinkman, H. C. A calculation of the viscous force exerted by a flowing fluid on a dense swarm of particles. *Flow, Turbulence and Combustion*, 1(1), 1949. doi:10.1007/bf02120313.

[19] Poirier, D. R. Permeability for flow of interdendritic liquid in columnar-dendritic alloys. *Metallurgical Transactions B*, 18(1):245–255, 1987. doi:10.1007/bf02658450.

[20] Singh, A. K., Pardeshi, R., and Basu, B. Modelling of convection during solidification of metal and alloys. *Sadhana*, 26(1-2):139–162, 2001. doi:10.1007/bf02728483.

[21] Fadl, M. and Eames, P. C. Numerical investigation of the influence of mushy zone parameter amush on heat transfer characteristics in vertically and horizontally oriented thermal energy storage systems. *Applied Thermal Engineering*, 151:90–99, 2019. doi:10.1016/j.applthermaleng.2019.01.102.

[22] Hong, Y., Ye, W.-B., Du, J., and Huang, S.-M. Solid-liquid phase-change thermal storage and release behaviors in a rectangular cavity under the impacts of mushy region and low gravity. *International Journal of Heat and Mass Transfer*, 130:1120–1132, 2019. doi:10.1016/j.ijheatmasstransfer.2018.11.024.

[23] Rai, R., Roy, G. G., and DebRoy, T. A computationally efficient model of convective heat transfer and solidification characteristics during keyhole mode laser welding. *Journal of Applied Physics*, 101(5):054909, 2007. doi:10.1063/1.2537587.

[24] Zheng, Y., Li, Q., Zheng, Z., Zhu, J., and Cao, P. Modeling the impact, flattening and solidification of a molten droplet on a solid substrate during plasma spraying. *Applied Surface Science*, 317:526–533, 2014. doi:10.1016/j.apsusc.2014.08.032.

[25] Yang, X.-H., Tan, S.-C., and Liu, J. Numerical investigation of the phase change process of low melting point metal. *International Journal of Heat and Mass Transfer*, 100:899–907, 2016. doi:10.1016/j.ijheatmasstransfer.2016.04.109.

[26] Kousksou, T., Mahdaoui, M., Ahmed, A., and Msaad, A. A. Melting over a wavy surface in a rectangular cavity heated from below. *Energy*, 64:212–219, 2014. doi:10.1016/j.energy.2013.11.033.

[27] Karami, R. and Kamkari, B. Investigation of the effect of inclination angle on the melting enhancement of phase change material in finned latent heat thermal storage units. *Applied Thermal Engineering*, 146:45–60, 2019. doi:10.1016/j.applthermaleng.2018.09.105.

[28] Pan, C., Charles, J., Vermaak, N., Romero, C., Neti, S., Zheng, Y., Chen, C.-H., and Bonner, R. Experimental, numerical and analytic study of unconstrained melting in a vertical cylinder with a focus on mushy region effects. *International Journal of Heat and Mass Transfer*, 124: 1015–1024, 2018. doi:10.1016/j.ijheatmasstransfer.2018.04.009.

[29] Prieto, M. and González, B. Fluid flow and heat transfer in PCM panels arranged vertically and horizontally for application in heating systems. *Renewable Energy*, 97:331–343, 2016. doi:10.1016/j.renene.2016.05.089.

[30] Kheirabadi, A. C. and Groulx, D. Simulating phase change heat transfer using COMSOL and Fluent: Effect of the mushy-zone constant. *Computational Thermal Sciences: An International Journal*, 7(5-6):427–440, 2015. doi:10.1615/computthermalscien.2016014279.

[31] Hosseinizadeh, S., Darzi, A. R., Tan, F., and Khodadadi, J. Unconstrained melting inside a sphere. *International Journal of Thermal Sciences*, 63:55–64, 2013. doi:10.1016/j.ijthermalsci.2012.07.012.

[32] Shmueli, H., Ziskind, G., and Letan, R. Melting in a vertical cylindrical tube: Numerical investigation and comparison with experiments. *International Journal of Heat and Mass Transfer*, 53(19-20):4082–4091, 2010. doi:10.1016/j.ijheatmasstransfer.2010.05.028.

[33] Arena, S., Casti, E., Gasia, J., Cabeza, L. F., and Cau, G. Numerical simulation of a finned-tube LHTES system: influence of the mushy zone constant on the phase change behaviour. *Energy Procedia*, 126:517–524, 2017. doi:10.1016/j.egypro.2017.08.237.

[34] Kumar, M. and Krishna, D. J. Influence of mushy zone constant on thermohydraulics of a PCM. *Energy Procedia*, 109:314–321, 2017. doi:10.1016/j.egypro.2017.03.074.

[35] Sattari, H., Mohebbi, A., Afsahi, M., and Yancheshme, A. A. CFD simulation of melting process of phase change materials (PCMs) in a spherical capsule. *International Journal of Refrigeration*, 73:209–218, 2017. doi:10.1016/j.ijrefrig.2016.09.007.

[36] Hu, Z., Li, A., Gao, R., and Yin, H. Effect of the length ratio on thermal energy storage in wedge-shaped enclosures. *Journal of Thermal Analysis and Calorimetry*, 117(2):807–816, 2014. doi:10.1007/s10973-014-3843-y.

[37] Vogel, J., Felbinger, J., and Johnson, M. Natural convection in high temperature flat plate latent heat thermal energy storage systems. *Applied Energy*, 184:184–196, 2016. doi:10.1016/j.apenergy.2016.10.001.

[38] Hameter, M. and Walter, H. Influence of the mushy zone constant on the numerical simulation of the melting and solidification process of phase change materials. In *Computer Aided Chemical Engineering*, pages 439–444. Elsevier, 2016. doi:10.1016/b978-0-444-63428-3.50078-3.

[39] Tritton, D. J. *Physical Fluid Dynamics*. Springer Netherlands, 1st edition, 1977. ISBN 978-94-009-9992-3. doi:10.1007/978-94-009-9992-3.

[40] Voller, V. R., Swaminathan, C. R., and Thomas, B. G. Fixed grid techniques for phase change problems: A review. *International Journal for Numerical Methods in Engineering*, 30(4):875–898, 1990. doi:10.1002/nme.1620300419.

[41] Voller, V. R. and Swaminathan, C. R. General source-based method for solidification phase change. *Numerical Heat Transfer, Part B: Fundamentals*, 19(2):175–189, 1991. doi:10.1080/10407799108944962.

[42] Swaminathan, C. R. and Voller, V. R. A general enthalpy method for modeling solidification processes. *Metallurgical Transactions B*, 23(5):651–664, 1992. doi:10.1007/bf02649725.

[43] Ferreira, I. L., Voller, V. R., Nestler, B., and Garcia, A. Two-dimensional numerical model for the analysis of macrosegregation during solidification. *Computational Materials Science*, 46(2): 358–366, 2009. doi:10.1016/j.commatsci.2009.03.020.

[44] Faraji, M. and Qarnia, H. E. Numerical study of melting in an enclosure with discrete protruding heat sources. *Applied Mathematical Modelling*, 34(5):1258–1275, 2010. doi:10.1016/j.apm.2009.08.012.

[45] Bouabdallah, S. and Bessaih, R. Effect of magnetic field on 3D flow and heat transfer during solidification from a melt. *International Journal of Heat and Fluid Flow*, 37:154–166, 2012. doi:10.1016/j.ijheatfluidflow.2012.07.002.

[46] Mahdaoui, M., Kousksou, T., Blancher, S., Msaad, A. A., Rhafiki, T. E., and Mouqallid, M. A numerical analysis of solid–liquid phase change heat transfer around a horizontal cylinder. *Applied Mathematical Modelling*, 38(3):1101–1110, 2014. doi:10.1016/j.apm.2013.08.002.

[47] Farsani, R. Y., Raisi, A., Nadooshan, A. A., and Vanapalli, S. Does nanoparticles dispersed in a phase change material improve melting characteristics? *International Communications in Heat and Mass Transfer*, 89:219–229, 2017. doi:10.1016/j.icheatmasstransfer.2017.10.006.

[48] OpenFOAM. URL: `https://openfoam.org/`.

[49] *Release 18.1*. ANSYS Fluent. URL: `https://www.ansys.com/`.

[50] Dannenhoffer, III, J. and Baron, J. Grid adaptation for the 2-D Euler equations. In *23rd Aerospace Sciences Meeting*. American Institute of Aeronautics and Astronautics, 1985. doi:10.2514/6.1985-484.

[51] Issa, R. I. Solution of the implicitly discretised fluid flow equations by operator-splitting. *Journal of Computational Physics*, 62(1):40–65, 1986. doi:10.1016/0021-9991(86)90099-9.

[52] Patankar, S. V. *Numerical Heat Transfer and Fluid Flow*. Taylor & Francis Inc, 1st edition, 1980. ISBN 0891165223.

[53] Gau, C. and Viskanta, R. Melting and solidification of a pure metal on a vertical wall. *Journal of Heat Transfer*, 108(1):174, 1986. doi:10.1115/1.3246884.

[54] Hannoun, N., Alexiades, V., and Mai, T. Z. Resolving the controversy over tin and gallium melting in a rectangular cavity heated from the side. *Numerical Heat Transfer, Part B: Fundamentals*, 44(3):253–276, 2003. doi:10.1080/713836378.

[55] Lee, Y. and Korpela, S. A. Multicellular natural convection in a vertical slot. *Journal of Fluid Mechanics*, 126(-1):91, 1983. doi:10.1017/s0022112083000063.

[56] Dantzig, J. A. Modelling liquid-solid phase changes with melt convection. *International Journal for Numerical Methods in Engineering*, 28(8):1769–1785, 1989. doi:10.1002/nme.1620280805.

[57] Cerimele, M., Mansutti, D., and Pistella, F. Numerical modelling of liquid/solid phase transitions: Analysis of a gallium melting test. *Computers & Fluids*, 31(4-7):437–451, 2002. doi:10.1016/s0045-7930(01)00062-7.

[58] Schroeder, P. W. and Lube, G. Stabilised dG-FEM for incompressible natural convection flows with boundary and moving interior layers on non-adapted meshes. *Journal of Computational Physics*, 335:760–779, 2017. doi:10.1016/j.jcp.2017.01.055.

[59] Vogel, J. and Thess, A. Validation of a numerical model with a benchmark experiment for melting governed by natural convection in latent thermal energy storage. *Applied Thermal Engineering*, 148:147–159, 2019. doi:10.1016/j.applthermaleng.2018.11.032.

[60] Kumar, L., Manjunath, B., Patel, R., Markandeya, S., Agrawal, R., Agrawal, A., Kashyap, Y., Sarkar, P., Sinha, A., Iyer, K., and Prabhu, S. Experimental investigations on melting of lead in a cuboid with constant heat flux boundary condition using thermal neutron radiography. *International Journal of Thermal Sciences*, 61:15–27, 2012. doi:10.1016/j.ijthermalsci.2012.06.014.

[61] Pitscheneder, W., DebRoy, T., Mundra, K., and Ebner, R. Role of sulfur and processing variables on the temporal evolution of weld pool geometry during multikilowatt laser beam welding of steels. *Welding Journal*, 75(3):71s–80s, 1996. URL: `https://app.aws.org/wj/supplement/WJ_1996_03_s71.pdf`.

[62] Yan, J., Yan, W., Lin, S., and Wagner, G. J. A fully coupled finite element formulation for liquid–solid–gas thermo-fluid flow with melting and solidification. *Computer Methods in Applied Mechanics and Engineering*, 336:444–470, 2018. doi:10.1016/j.cma.2018.03.017.

[63] Saldi, Z. S., Kidess, A., Kenjereš, S., Zhao, C., Richardson, I. M., and Kleijn, C. R. Effect of enhanced heat and mass transport and flow reversal during cool down on weld pool shapes in laser spot welding of steel. *International Journal of Heat and Mass Transfer*, 66:879–888, 2013. doi:10.1016/j.ijheatmasstransfer.2013.07.085.

[64] Sahoo, P., Debroy, T., and McNallan, M. J. Surface tension of binary metal—surface active solute systems under conditions relevant to welding metallurgy. *Metallurgical Transactions B*, 19(3):483–491, 1988. doi:10.1007/bf02657748.

5

Melt Pool Behaviour in Conduction-mode Laser Spot Melting

Molten metal melt pools are characterised by highly non-linear responses, which are very sensitive to imposed boundary conditions. Temporal and spatial variations in the energy flux distribution are often neglected in numerical simulations of melt pool behaviour. Additionally, thermo-physical properties of materials are commonly changed to achieve agreement between predicted melt-pool shape and experimental post-solidification macrograph. Focusing on laser spot melting in the conduction mode, the influence of dynamically adjusted energy flux distribution and changing thermo-physical material properties on melt pool oscillatory behaviour was investigated using both deformable and non-deformable assumptions for the gas-metal interface are examined. The results demonstrate that adjusting the absorbed energy flux affects the oscillatory fluid flow behaviour in the melt pool and consequently the predicted melt-pool shape and size. Changing the thermo-physical material properties artificially or using a non-deformable surface assumption is shown to lead to significant differences in melt pool oscillatory behaviour compared to the cases in which these assumptions are not made.

The contents of this chapter have been published in *Journal of Physics D: Applied Physics*, **2021**, *54*(10), 105304, DOI: 10.1088/1361-6463/abca62.

5.1. Introduction

Laser melting is utilised for material processing such as additive manufacturing, joining, cutting and surface modification. The results of experimentation performed by Ayoola *et al.* [1] revealed that the energy flux distribution over the melt-pool surface can affect melting, convection and energy transport in liquid melt pools and subsequent re-solidification during laser melting processes. The imposed energy flux heats and melts the material and generates temperature gradients over the melt-pool surface. The resulting surface tension gradients and therefore Marangoni force is often the dominant force driving fluid flow, as can be understood from the numerical investigation conducted by Oreper and Szekely [2] and experimental observations reported by Mills *et al.* [3]. Experimental investigations of Heiple and Roper [4] showed that the presence of surfactants in molten materials can alter Marangoni convection in the melt pool, and thus the melt-pool shape. Moreover, Paul and DebRoy [5] reported that the smoothness of the melt pool surface decreases when surfactants are present in the melt pool. However, according to the literature survey conducted by Cook and Murphy [6], the influence of surfactants on variations of surface tension and its temperature gradient is often neglected in numerical simulations of welding and additive manufacturing. DebRoy and David [7] stated that fluid flow in melt pools can lead to deformation and oscillation of the liquid free surface and can affect the stability of the process and the structure and properties of the solid materials after re-solidification. Aucott *et al.* [8] confirmed that transport phenomena during fusion welding and additive manufacturing processes are characterised by highly non-linear responses that are very sensitive to material composition and imposed heat flux boundary conditions. Numerical models capable of predicting the melt pool behaviour with a sufficient level of accuracy are thus required to gain an insight into the physics of fluid flow and the nature of flow instabilities that are not accessible experimentally.

To avoid excessive simulation complexity and execution time in numerical simulations, the melt pool is often decoupled from the heat source, the latter being incorporated as a boundary condition at the melt-pool surface. These boundary conditions should be imposed with a sufficient level of accuracy, as it is known from the work of Zacharia *et al.* [9] that modelling the interfacial phenomena is critical to predicting the melt pool behaviour. Numerical studies on melt pool behaviour reported in the literature use both deformable and non-deformable surface assumptions for the gas-metal interface. Comparing the melt-pool shapes predicted using both deformable and non-deformable surface assumptions, Ha and Kim [10] concluded that free-surface oscillations can enhance convection in the melt pool and influence the melt-pool shape. Shah *et al.* [11] reported that the difference between melt-pool shapes obtained from numerical simulations with deformable and non-deformable surface assumptions depends on the laser power. The three-dimensional nature of the molten metal flow in melt pools, as observed experimentally by Zhao *et al.* [12] and numerically by Kidess *et al.* [13], is often neglected in numerical simulations. Moreover, when accounting for surface deformations, the volume-of-fluid (VOF) method developed by Hirt and Nichols [14], based on a Eulerian formulation, is the most common method for modelling the melt pool behaviour. In this diffuse boundary method, the interfacial forces and the energy fluxes applied on the melt-pool surface are treated as volumetric source terms in the surface region, instead of imposing them as boundary conditions. In this approach, however,

the fact that surface deformations lead to temporal and spatial variations of the free surface boundary conditions, as remarked by Meng *et al.* [15] and Wu *et al.* [16], is often neglected. The results reported by Choo *et al.* [17] suggest that variations in power-density distribution and changes in free-surface profile can affect molten metal flow in melt pools and its stability. Further investigations are essential to improve the understanding of the complex transport phenomena that happen during laser spot melting.

The aim of the work presented in the present chapter is to analyse the effects of a dynamically adjusting energy flux distribution over the deforming liquid surface on the nature of fluid flow instabilities in partially-penetrated liquid melt pools. Particularly focus is placed on flow instabilities in low-Prandtl number liquid metal pools during conduction-mode laser spot melting; the results should however be relevant for a much wider range of materials processing technologies. Three-dimensional calculations are carried out to numerically predict the melt pool behaviour and thermocapillary-driven flow instabilities using various heat source implementation methods. The study provides a quantitative representation and an understanding of the influence of heat flux boundary conditions on the transport phenomena and flow instabilities in the molten metal melt pool. Additionally, the influence of artificially enhanced transport coefficients on the melt-pool oscillatory behaviour is discussed.

5.2. Problem description

Laser spot melting of a metallic S705 alloy, as shown schematically in figure 5.1 and as experimentally studied by Pitscheneder *et al.* [18], was numerically simulated as a representative example in the present work. A defocused laser-beam with a radius of $r_b = 1.4\,\text{mm}$ heats the bulk material from its top surface for 4 s. The laser-beam power Q is set to 3850 W with a top-hat intensity distribution. The averaged laser absorptivity of the material surface $\bar{a}$ is assumed to remain constant at 13% [18]. The absorbed laser power leads to an increase in temperature and subsequent melting of the base material. The base material is a rectangular cuboid shape with a base size ($L \times L$) of $24 \times 24\,\text{mm}^2$ and a height (H_m) of 10 mm, initially at an ambient temperature of $T_i = 300\,\text{K}$. A layer of air with a thickness of $H_a = 2\,\text{mm}$ is considered above the base material to monitor the gas-metal interface evolution. Except for the surface tension, the material properties are assumed to be constant and temperature independent and are presented in table 5.1. Although temperature-dependent properties can be employed in the present model to enhance the model accuracy, employing temperature-independent properties facilitates comparison of the results of the present work with previous results published in the literature [10, 13, 19]. Moreover, further studies are required to enhance the accuracy of calculation and measurement of temperature-dependent material properties, particularly for the liquid phase above the melting temperature. The effects of employing temperature-dependent material properties on the thermal and fluid flow fields and melt-pool shape are discussed in detail in section 5.6.2. A change in surface-tension due to the non-uniform temperature distribution over the gas-liquid interface induces thermocapillary stresses that drive the melt flow. This fluid motion from low to high surface-tension regions changes the temperature distribution in the melt pool [20] and can lead to surface deformations that change the melt-pool shape and properties of the material after solidification [21]. The sulphur contained in the alloy can alter the surface tension of

the molten material and its variations with temperature [22].

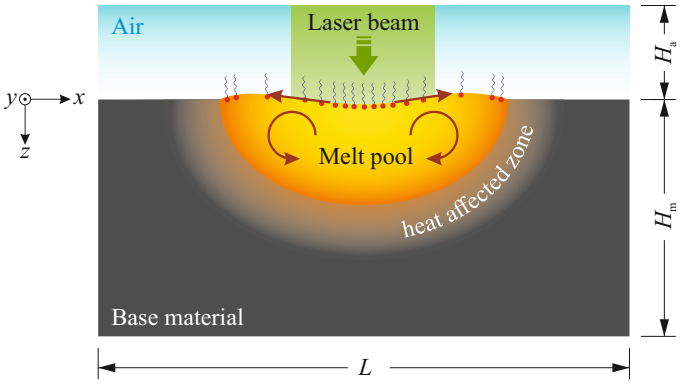

Figure 5.1: Schematic of a conduction-mode laser spot melting.

Table 5.1: Thermophysical properties of the Fe–S alloy and air used in the present study. Values are taken from [13].

Property	Fe–S alloy	Air	Unit
Density ρ	8100	1.225	$\mathrm{kg\,m^{-3}}$
Specific heat capacity c_p	670	1006	$\mathrm{J\,kg^{-1}\,K^{-1}}$
Thermal conductivity k	22.9	0.024	$\mathrm{W\,m^{-1}\,K}$
Viscosity μ	6×10^{-3}	1.8×10^{-5}	$\mathrm{kg\,m^{-1}\,s^{-1}}$
Latent heat of fusion $\mathscr{L}_f$	250 800	–	$\mathrm{J\,kg^{-1}}$
Liquidus temperature T_l	1620	–	K
Solidus temperature T_s	1610	–	K

5.3. Laser heat-source implementation

The laser supplies a certain amount of energy ($\bar{a}\,Q$) to the material. Its energy input was modelled by adding a volumetric source term S_q to the energy equation (equation (3.3)) in cells at the gas-metal interface. The surface deformations affect the total energy input to the material [23]. This effect is generally not considered in numerical simulations of melt pool behaviour. To investigate the influence of surface deformations, five different methods for the heat-source implementation were considered.

5.3.1. Case 1: ignoring the effect of surface deformations

In this case, the heat source model is defined as

$$S_q = \begin{cases} \dfrac{\bar{a}\,Q}{\pi r_b^2}\|\nabla\phi\|\dfrac{2\,\rho\,c_p}{(\rho\,c_p)_g+(\rho\,c_p)_m}, & \text{if } r \le r_b \\ 0, & \text{otherwise} \end{cases} \tag{5.1}$$

where, r is radius defined as $\sqrt{x^2+y^2}$, and subscripts 'g' and 'm' indicate gas or metal respectively. This method is the most common method in modelling melt-pool surface oscillations without having a deep penetration (keyhole formation) (see for instance, [24, 25]). However, variations in the total energy input caused by a change in melt-pool surface shape, through changes in $\|\nabla\phi\|$, causing $\iiint_{\forall} S_q \, dV$ to differ from $\bar{a}\,Q$, are an inherent consequence of using this method. Additionally, every segment of the melt-pool surface is exposed to the same amount of energy input regardless of the local surface orientation.

5.3.2. Case 2: heat source adjustment

To conserve the total energy input, an adjustment coefficient ξ is introduced to the heat source model as follows:

$$S_q = \begin{cases} \dfrac{\xi\,\bar{a}\,Q}{\pi r_b^2}\|\nabla\phi\|\dfrac{2\rho\,c_p}{(\rho\,c_p)_g+(\rho\,c_p)_m}, & \text{if } r \le r_b \\ 0, & \text{otherwise} \end{cases} \tag{5.2}$$

where, ξ is evaluated at the beginning of every time-step and is defined as

$$\xi = \frac{\bar{a}\,Q}{\iiint_{\forall} S_q \, dV}, \tag{5.3}$$

where, '$\forall$' indicates the computational domain. Utilising this technique for welding simulations has already been reported in the literature (see for instance, [15, 16, 23, 26]). Variations in energy absorption with deformations of the melt-pool surface are, however, not taken into consideration with this method.

5.3.3. Case 3: heat source redistribution

In this case, the energy flux was redistributed over the melt-pool surface assuming the energy absorption is a function of the local surface orientation. Accordingly, the local energy absorption is a maximum where the surface is perpendicular to the laser beam and is a minimum where the surface is aligned with the laser beam [27, 28]. This represents a simplified absorptivity model based on the Fresnel's equation [29] and is expressed mathematically, assuming the laser rays are parallel and in the z-direction, as follows:

$$S_q = \begin{cases} \dfrac{\bar{a}\,Q}{\pi r_b^2}\|\nabla\phi\|\dfrac{2\rho\,c_p}{(\rho\,c_p)_g+(\rho\,c_p)_m}\left|\dfrac{\nabla\phi[z]}{\|\nabla\phi\|}\right|. & \text{if } r \le r_b \\ 0. & \text{otherwise} \end{cases} \tag{5.4}$$

The total energy input is not necessarily conserved with this method.

5.3.4. Case 4: heat source adjustment and redistribution

Utilising the same technique introduced in Case 2, the heat source model in Case 3 was adjusted to guarantee that total energy input is conserved. Hence, the heat source model

is defined as

$$S_{\mathrm{q}} = \begin{cases} \dfrac{\xi\,\bar{a}\,Q}{\pi r_{\mathrm{b}}^2}\|\nabla\phi\|\dfrac{2\,\rho\,c_{\mathrm{p}}}{(\rho\,c_{\mathrm{p}})_{\mathrm{g}}+(\rho\,c_{\mathrm{p}})_{\mathrm{m}}}\left|\dfrac{\nabla\phi\,[z]}{\|\nabla\phi\|}\right|. & \text{if } r \le r_{\mathrm{b}} \\ 0. & \text{otherwise} \end{cases} \tag{5.5}$$

5.3.5. Case 5: flat non-deformable free surface

In this case, the surface is assumed to remain flat. Thermocapillary shear stresses caused by a non-uniform temperature distribution on the gas-metal interface are applied as a boundary condition, hence modelling the gas phase is not required. Consequently, the total energy absorbed by the surface is fixed in this method. The boundary conditions are described in section 5.4.

Table 5.2 presents a summary of the cases considered in the present chapter.

Table 5.2: Summary of the cases studied and the features included in the model for each case.

Name	Deformable free surface	Heat source adjustment	Heat source redistribution
Case 1	Yes	No	No
Case 2	Yes	Yes	No
Case 3	Yes	No	Yes
Case 4	Yes	Yes	Yes
Case 5	No	No	No

5.4. Boundary conditions

The bottom and lateral surfaces of the metal part were modelled to be no slip walls, but in fact they remain solid during the simulation time. At the boundaries of the gas layer above the metal part, a constant atmospheric pressure was applied (*i.e.* $p = 101.325\,\mathrm{kPa}$) allowing air to flow in and out of the domain. The outer boundaries of the computational domain were modelled as adiabatic since heat losses through these boundaries are negligible compared to the laser power [13].

For Case 5, in which no gas layer is modelled explicitly, a thermocapillary shear-stress was applied as a boundary condition in the molten regions of the top surface. In the irradiated region on the material top-surface, a constant uniform heat flux was applied, while outside of this region the surface was assumed to be adiabatic [18]. The thermal and thermocapillary shear-stress boundary conditions were defined, respectively, as

$$k\frac{\partial T}{\partial \mathbf{n}} = \begin{cases} \dfrac{\bar{a}\,Q}{\pi r_{\mathrm{b}}^2}, & \text{if } r \le r_{\mathrm{b}} \\ 0, & \text{otherwise} \end{cases} \tag{5.6}$$

and

$$-\mu\frac{\partial \mathbf{u}_{\mathrm{t}}}{\partial \mathbf{n}} = \frac{\mathrm{d}\gamma}{\mathrm{d}T}\frac{\partial T}{\partial \mathbf{t}}, \tag{5.7}$$

where, $\mathbf{u}_t$ is the tangential velocity vector, and $\mathbf{t}$ the tangential vector to the top surface.

5.5. Numerical procedure

The model was developed within the framework of the proprietary computational fluid dynamics solver ANSYS Fluent [30]. The laser heat source models and the thermocapillary boundary conditions as well as the surface-tension model were implemented through user-defined functions. After performing a grid independence study (results are presented in figure 5.2 and table 5.3), a grid containing 8.6×10^5 non-uniform hexahedral cells was utilised to discretise the computational domain. Minimum cell spacing was 2×10^{-5} m close to the gas-metal interface and 3×10^{-5} m in the melt pool central region. Cell sizes gradually increase towards the domain outer boundaries. The computational domain employed in the numerical simulations is shown in figure 5.3. The diffusion and convection terms in the governing equations were discretised using the central-differencing scheme with second order accuracy. For the pressure interpolation, the PRESTO scheme [31] was used. Pressure and velocity fields were coupled employing the PISO scheme [32]. An explicit compressive VOF formulation was utilised for the spatial discretisation of the gas-metal interface advection [33]. The transient advection terms were discretised using a first order implicit scheme. To obtain a Courant number ($\mathrm{Co} = \|\mathbf{u}\|\Delta t/\Delta x$) less than 0.25, with velocity magnitudes up to $\mathcal{O}(1)\,\mathrm{m\,s^{-1}}$, the time-step size was set to 10^{-5} s. Each simulation was executed in parallel on 40 cores (Intel Xeon E5-2630 v4) of a high-performance computing cluster. Scaled residuals of the energy, momentum and continuity equations of less than 10^{-10}, 10^{-8} and 10^{-7} respectively, were defined as convergence criteria.

Table 5.3: The influence of computational cell size on predicted melt pool size.

Minimum cell spacing	Total number of cells	Melt pool width	Melt pool depth
60 µm	5.5×10^5	4.89 mm	1.09 mm
20 µm	8.6×10^5	4.88 mm	0.96 mm
10 µm	2.1×10^6	4.88 mm	0.95 mm

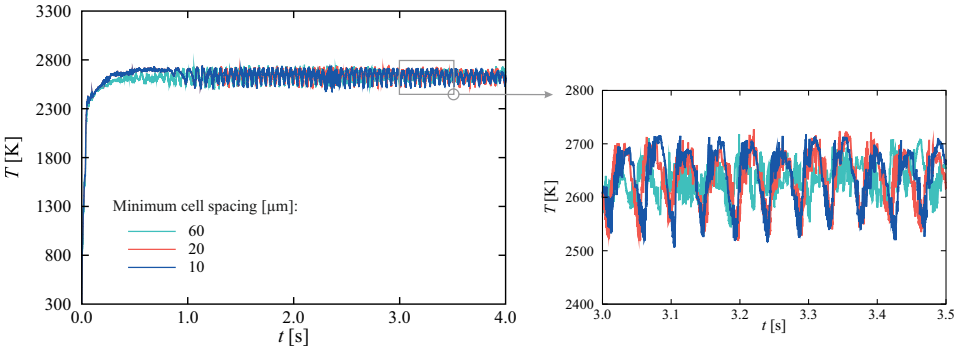

Figure 5.2: The effect of cell spacing on temperature variations predicted at the melt pool centre. The grid with minimum cell spacing of 20 μm was employed for the calculations reported in this chapter.

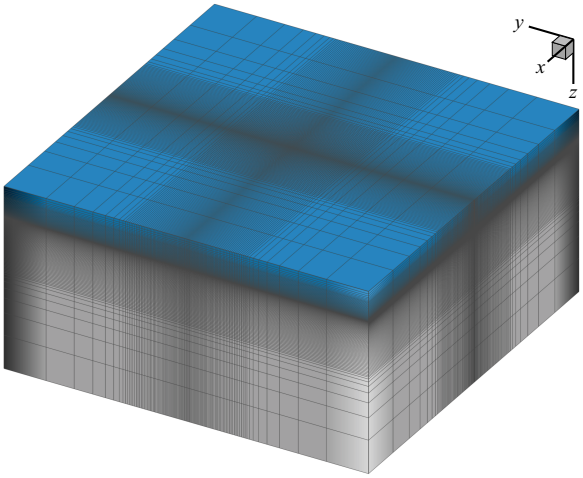

Figure 5.3: The computational grid employed for the calculations reported in this chapter. Regions highlighted in blue show the gas layer above the base material.

5.6. Results and Discussion

5.6.1. The influence of heat source adjustment

When accounting for surface deformations, the volume-of-fluid (VOF) method developed by Hirt and Nichols [14], based on a Eulerian formulation, is the most common method for modelling the melt pool behaviour. In this diffuse boundary method, the interfacial forces and the energy fluxes applied on the melt-pool surface are treated as volumetric source terms in the surface region, instead of imposing them as boundary conditions. In this approach, however, the fact that surface deformations lead to temporal and spatial variations of the free surface boundary conditions, as remarked by Meng *et al.* [15] and Wu *et al.* [16], is often neglected. The results reported by Choo *et al.* [17] suggest that

variations in power-density distribution and changes in free-surface profile can affect molten metal flow in melt pools and its stability. In this section, the influence of applying each of the five different approaches to model the laser heat source (described as Cases 1–5 in section 5.3) on the melt pool behaviour is discussed. In these simulations, no enhancement factor, as introduced in the previous section, was employed since it is *ad hoc* and has little justification in physical reality.

The energy flux distribution over the melt-pool surface determines the spatial temperature distribution and its temporal variations. Due to the temporal changes in the surface shape, the total energy absorbed by the material in Case 1 varies between 491.4 W and 538.1 W, with a median value of 515.7 W, which differs from the total energy supplied by the laser $\bar{a}\,Q = 500.5\,\mathrm{W}$. This issue is resolved by utilising a dynamic adjustment coefficient in Case 2, while the relative energy flux distribution remains unchanged. However, the results reported by Courtois *et al.* [34] and Bergström *et al.* [35] showed that the energy flux distribution varies with surface deformation during a laser melting process. When surface deformations are too small to cause multiple reflections, redistributing the energy flux over the free surface results in a better input energy conservation as obtained in Case 3. The total energy absorbed by the material in Case 3 ranges between 482.6 W and 532.3 W, with a median value of 503.8 W. By further introducing an adjustment coefficient (equation (5.3)), the absorbed energy can be made to exactly match the supplied laser power $\bar{a}\,Q$. Finally, for the most simple approach without any surface deformations (*i.e.* Case 5), the total absorbed energy exactly matches the supplied laser power and remains unchanged in time.

The variations of temperature distribution over the melt-pool surface over time determine the thermocapillary driven flow pattern and melt-pool shape, as shown in figure 5.4. An unsteady, asymmetric, outwardly directed fluid flow emanating from the pool centre is found for all 5 cases. Flow accelerates towards the pool rim, where it meets inwardly directed fluid flow from the rim, due to the change of sign of $\left(\partial\gamma/\partial T\right)$ at a certain pool temperature (see figure 3.2). Close to the region where these two flows meet, velocity magnitudes are high due to the large thermocapillary stresses generated by the steep temperature gradients, in contrast to the low flow velocities in the central region of the pool surface. Interactions between these two opposing flows, and their interactions with the fusion boundary, cause the fluid flow inside the melt pool to be asymmetric and unstable [13], leading to a distorted melt-pool shape.

Melt-pool surface temperatures are roughly 7%–16% higher when surface deformations are taken into consideration (Cases 1–4), compared to flat surface simulations (Case 5). Temperature gradients over the melt-pool surface are also on average larger in Case 1–4 (with a deformable surface) and particularly in Case 2–4 (with heat source adjustment and/or redistribution), compared to Case 5 (with a non-deformable surface). Consequently, local fluid velocities caused by thermocapillary stresses are almost 25% higher for Case 1–4, compared to those of Case 5, and are of the order of $0.6\,\mathrm{m\,s^{-1}}$, in reasonable agreement with experimental measurements performed by Aucott *et al.* [8] and estimated values from the scaling analyses reported by Oreper and Szekely [2], Rivas and Ostrach [36] and Chakraborty and Chakraborty [37].

Free surface deformations have a destabilising effect on the melt pool due to the augmentation of temperature gradients over the melt-pool surface, leading to higher ther-

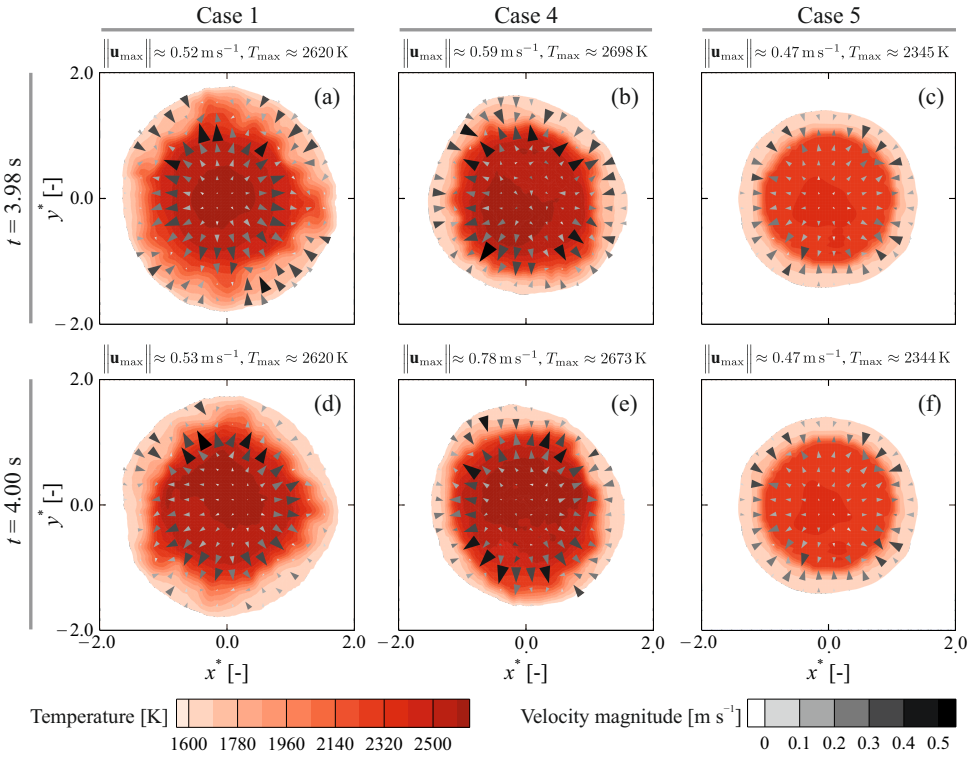

Figure 5.4: Contours of temperature and the velocity vectors on the melt pool free surface at two different time instances for Case 1, 4 and 5. Coordinates are non-dimensionalised using the laser-beam radius r_b as the characteristic length scale.

mocapillary stresses [38]. Additionally, the stagnation region, where the sign of $(\partial\gamma/\partial T)$ and thus thermocapillary flow direction change, is sensitive to small spatial disturbances and further enhances melt pool instabilities. Furthermore, variations in magnitude and direction of velocities can cause rotational and pulsating fluid motions, leading to cross-cellular flow patterns with a stochastic behaviour in the melt pool [12, 39].

All such flow instabilities reinforce unsteady energy transport from the melt pool to the surrounding solid material, resulting in continuous melting and re-solidification of the material close to the solid-liquid boundary. This complex interplay leads to the melt-pool surface width for Case 5 to be 23% smaller than that for Case 1, and 10% smaller than for Case 2–4. The higher amount of heat absorbed by the deformed free-surface in Case 1, and the enhanced convective heat transfer in Case 1–4, are the main causes for the observed pool size differences.

To investigate the rotational fluid motion, the spatially-averaged angular momentum over the melt-pool surface ($\mathscr{L}$) about the z-axis (*i.e.* the axis of rotation) with respect to

the origin $\mathcal{O}(0,0,0)$ is calculated as follows:

$$\mathscr{L}(t) = \frac{1}{A} \iint_{\text{free surface}} \hat{z} \cdot (\mathbf{r} \times \mathbf{u}) \, \mathrm{d}A, \tag{5.8}$$

where, $\hat{z}$ is a unit vector in the z-direction, $\mathbf{r}$ the position vector, $\mathbf{u}$ the velocity vector and A the area of gas-metal interface. Figure 5.5 shows the temporal variations of angular momentum over the melt-pool surface as a function of time. Positive values of the angular momentum in figure 5.5 show a clockwise flow rotation, and negative values show anti-clockwise rotation. Kidess *et al.* [13] applied a similar approach to investigate rotational fluid motion over a flat non-deformable melt-pool surface. Continuous fluctuations in the sign of angular momentum indicate an oscillatory rotational fluid motion in the pool that is indeed self-excited. In Case 1–4, flow pulsations start to take place after roughly 1 s and continue thereafter. This is not however valid for Case 5, where flow pulsations start to occur already after about 0.1 s, and a clockwise rotation is established after 1.8 s, which lasts for roughly two seconds. These instabilities in the flow field are attributed to a large extent to the interactions between the two opposing flows meeting at the melt-pool surface [13, 40], and to a lesser extent the effects of hydrothermal waves [41, 42].

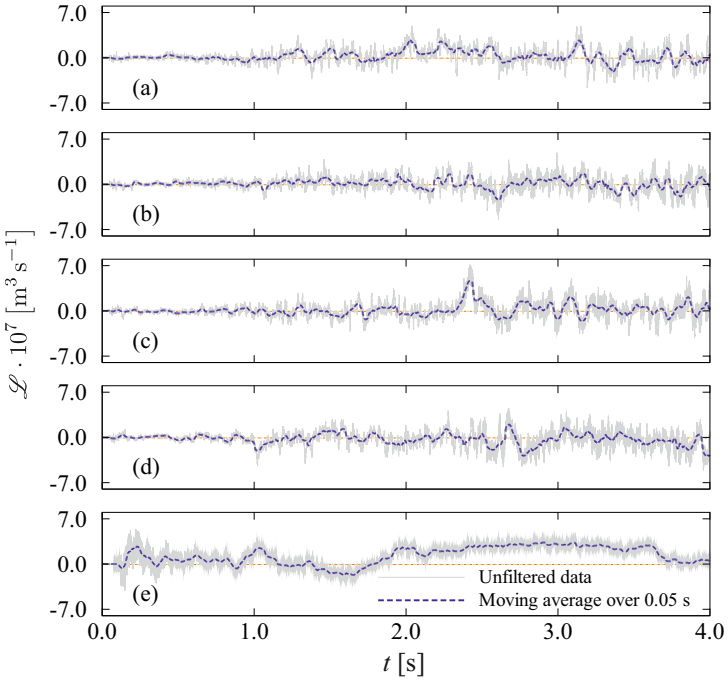

Figure 5.5: Variations of the averaged angular momentum over the melt-pool surface over a time period of 4 s for (a) Case 1, (b) Case 2, (c) Case 3, (d) Case 4 and (e) Case 5. Unfiltered data: grey lines, Moving average of the data over 0.05 s: dashed blue lines. $\mathscr{L} > 0$ indicates a clockwise rotation.

Free surface deformations evolve rapidly because of the thermocapillary stresses act-

ing on the melt-pool surface and are shown in figure 5.6 at three different time instances. Free surface deformations are smaller and less intermittent in Case 1 compared with Case 2–4. This is due to the smaller thermocapillary stresses and the wider stagnation region, which makes the surface flow field less sensitive to spatial disturbances. Additionally, the Capillary number ($\mathrm{Ca} = \mu\|\mathbf{u}\|/\gamma$), which represents the ratio between viscous and surface-tension forces and which is $\mathcal{O}(10^{-3})$ for all the cases studied in the present chapter, appears to be larger in Case 2–4 ($\mathrm{Ca} \approx 2.5 \times 10^{-3}$) compared with Case 1 ($\mathrm{Ca} \approx 1.5 \times 10^{-3}$), particularly in the central region of the melt-pool surface. Redistributing the energy flux based on the free surface profile (Case 3 and 4) disturbs the temperature field locally and thus the velocity distribution over the melt-pool surface.

Fluid flow may influence the energy transport and associated phase change significantly during laser melting [7], which can be assessed through the Péclet number; that is, the ratio between advective and diffusive heat transport, defined as follows:

$$\mathrm{Pe} = \frac{\mathscr{D}\|\mathbf{u}\|\rho c_\mathrm{p}}{k}, \tag{5.9}$$

where, $\mathscr{D}$ is a characteristic length scale, here chosen to be r_b. The value of the Péclet number is much larger than one ($\mathrm{Pe} = \mathcal{O}(10^2)$), which indicates a large contribution of advection to the total energy transport, compared with diffusion.

The predicted melt-pool depth is shown in figure 5.7 at two different time instances. When surface deformations are taken into account (Case 1–4), the predicted melt-pool shape is shallow, with its maximum depth located in the central region and its largest width at the surface. When the surface is assumed to be non-deformable (Case 5), on the other hand, the depth profile of the melt-pool resembles a doughnut-shaped, with its maximum width located below the gas-metal interface. The predicted fusion boundaries of all the cases presented in this chapter are asymmetric and unstable. Flow instabilities in the melt pool increase when surface deformations are taken into account, which enhance convection in the pool resulting in a smooth melt-pool depth profile. Variations in the melt-pool shape for Case 5 are less conspicuous compared to those for Case 1–4 because of the smaller fluctuations in the fluid flow field.

To understand the three-dimensional oscillatory flow behaviour, three monitoring points were selected over the melt-pool surface in different non-azimuthal directions $p_1\left(x^*, y^*\right) = (5/7, 0)$, $p_2\left(x^*, y^*\right) = (5/7, 5/7)$ and $p_3\left(x^*, y^*\right) = (0, 5/7)$ in addition to a point $p_4\left(x^*, y^*\right) = (0, 0)$ on the melt-pool surface, in which x^* and y^* are non-dimensionalized with the laser beam radius r_b. Temperature signals, recorded from the monitoring point p_4, and the corresponding 'fast Fourier transform' (FFT) [43] frequency spectra are shown in figure 5.8. In the presence of surface deformations (Case 1–4), self-excited temperature fluctuations, initiated by numerical noise, grow and reach a quasi-steady state after about 1 s. Without surface deformations (Case 5), on the other hand, the amplitudes of temperature fluctuations remain very small. In Case 1, where surface deformations are taken into account, the temperature fluctuations with large amplitudes have a fundamental frequency of $f_0 \approx 22\,\mathrm{Hz}$, with harmonics at $f_1 \approx 2f_0$ and $f_2 \approx 3f_0$. Irregular patterns appear in the spectrum of temperature fluctuations for Case 2–4, showing a highly unsteady behaviour that results from the enhancement of thermocapillary stresses and the variations in energy flux distribution.

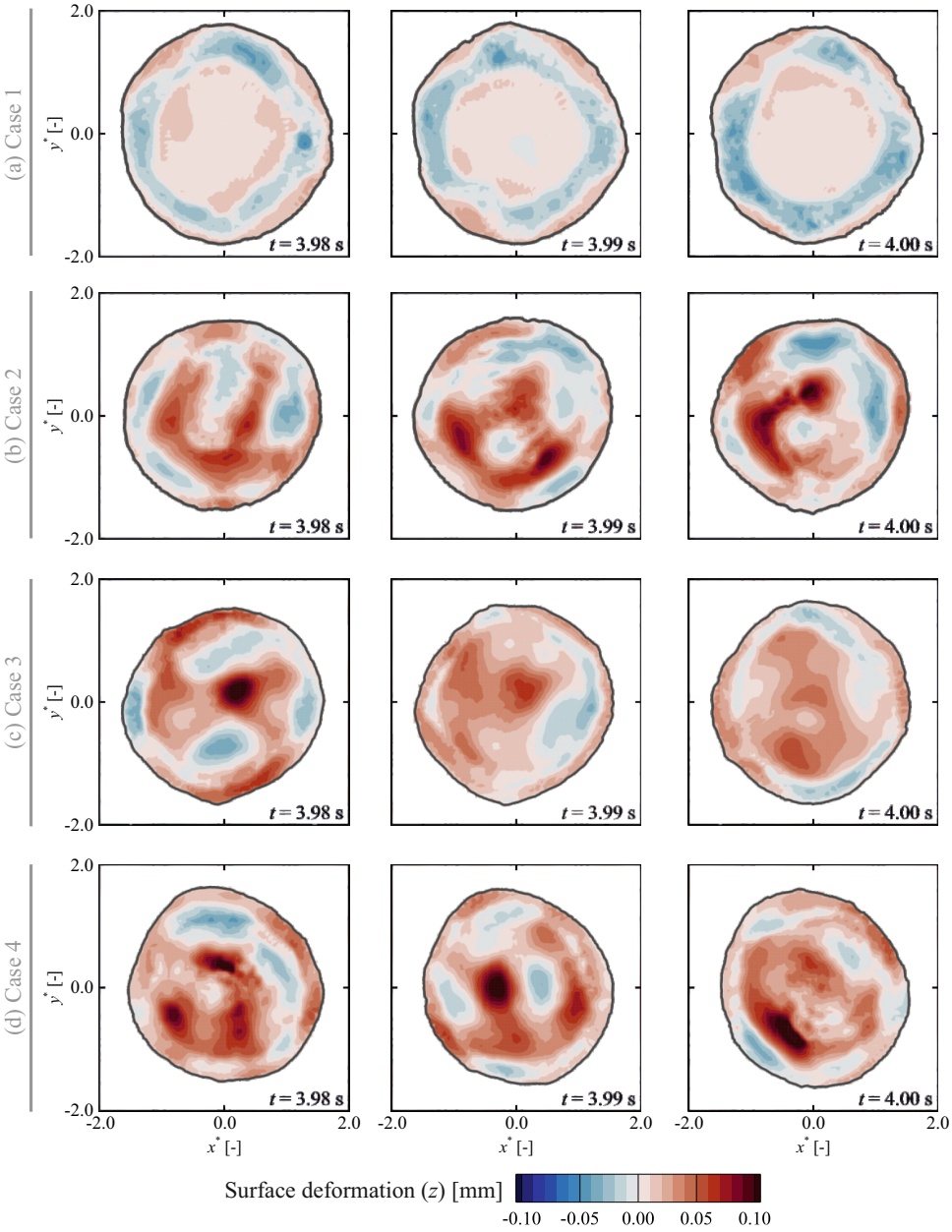

Figure 5.6: Contours of melt pool free surface deformation at three different time instances for (a) Case 1, (b) Case 2, (c) Case 3, and (d) Case 4. Coordinates are non-dimensionalised using the laser-beam radius r_b as the characteristic length scale. Positive and negative values of z indicate surface depression and elevation, respectively.

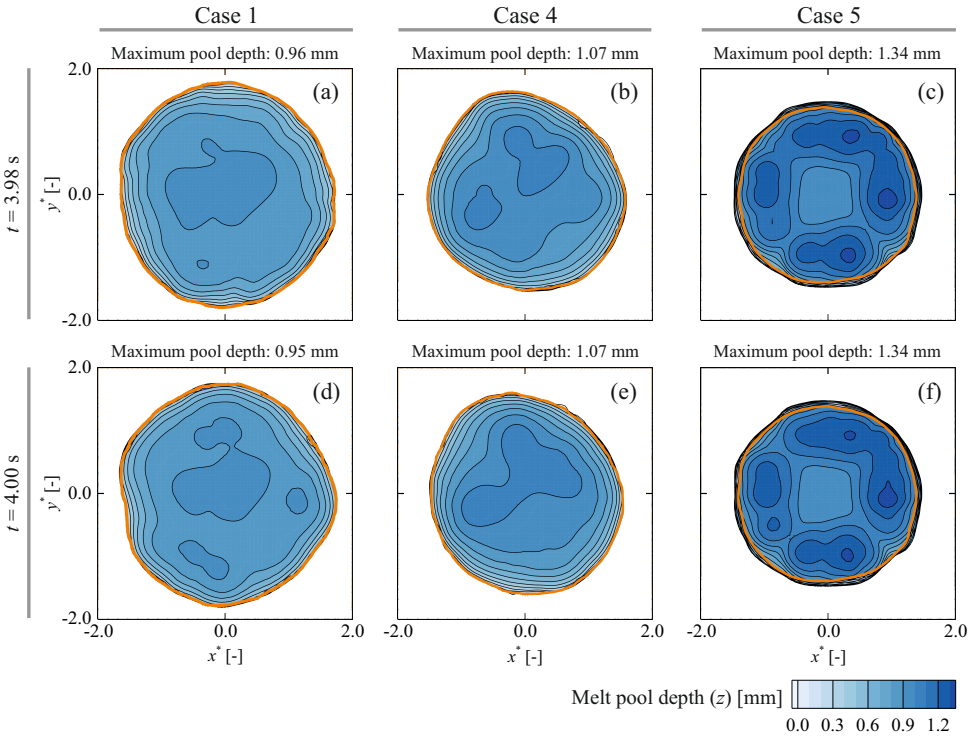

Figure 5.7: Contours of melt-pool depth at $t = 3.98$ and 4.00 s for Case 1, 4 and 5. Coordinates are non-dimensionalised using the laser-beam radius r_b as the characteristic length scale. The orange circular line shows the melt pool boundary at its top surface.

Temperature signals recorded from monitoring points p_1, p_2 and p_3 in the time interval of 2–3 s are shown in figure 5.9. The data for Case 1 indicate that the thermal and fluid flow fields are dominated by a pulsating behaviour. This is also valid for Case 4 up to roughly 2.5 s; however, after 2.5 s modulation of temperature fluctuations takes place, which is probably due to changes in temperature gradients, melt pool size and the complex interactions between vortices generated inside the melt pool. Similar behaviour was observed for Case 2 and 3 (not shown here). The amplitudes of temperature fluctuations appear to be smaller for Case 5 compared to the other cases and show an irregular behaviour, revealing complex unsteady flow in the melt pool.

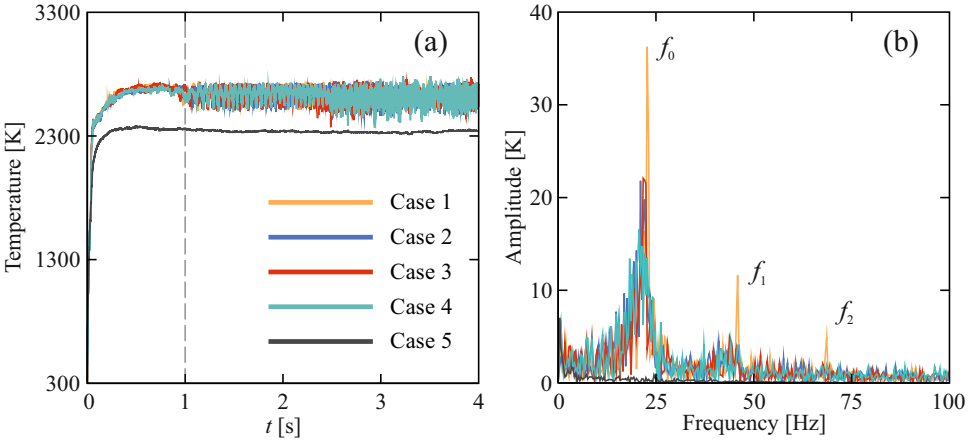

Figure 5.8: (a) Temperature signals recorded from the monitoring point p_4 located at $(x^*, y^*) = (0,0)$ on the melt-pool surface and (b) the corresponding frequency spectra. Temperature signals in the period of 1 to 4 s are employed for FFT analysis.

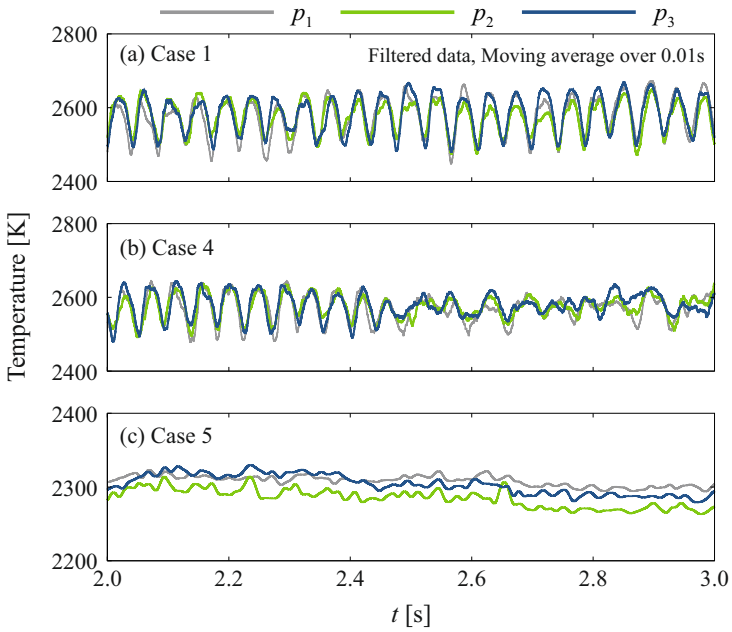

Figure 5.9: Temperature signals recorded from three monitoring points at the melt pool free surface placed at a radius of 1 mm and along different azimuthal directions ($p_1(x^*, y^*) = (5/7, 0)$, $p_2(x^*, y^*) = (5/7, 5/7)$ and $p_3(x^*, y^*) = (0, 5/7)$). (a) Case 1, (b) Case 4, and (c) Case 5. Signals are smoothed using a moving averaging window of 0.01 s.

5.6.2. The effects of employing temperature-dependent properties

In this section, the effects of employing temperature-dependent properties on numerical predictions of thermal and flow fields as well as the melt-pool shape using two different heat source models (Case 1 and 4) are reported. Temperature-dependent properties for the metallic alloy considered in the present study (S705) are given in table 5.4, where the values are estimated by analogy with the values for iron-based alloys [44]. Temperature distribution over the melt-pool surface and free-surface flow after 5 s of heating are shown in figure 5.10 for both temperature-dependent and temperature-independent thermophysical properties. Melt-pool surface temperatures predicted using temperature-independent properties are about 1–6% lower than those predicted using temperature-dependent properties. This is mainly attributed to the changes in the thermal diffusivity $\left(\alpha = k/\left(\rho c_\mathrm{p}\right)\right)$ of the molten material. The thermal conductivity of the molten material changes from $21.8\,\mathrm{W\,m^{-1}\,K^{-1}}$ at $T = 1620\,\mathrm{K}$ to $33.4\,\mathrm{W\,m^{-1}\,K^{-1}}$ at $T = 2700\,\mathrm{K}$. Hence, the average thermal diffusivity of the molten material obtained from a temperature-dependent model is about 10% lower than that estimated using temperature-independent properties. The fluid velocities are roughly 15–32% lower when temperature-independent properties are employed, compared to those predicted using temperature-dependent properties, which is due to the decrease in the viscosity of the molten material at elevated temperatures. With an increase in temperature, the thermal conductivity of the molten metal increases and the viscosity of the molten metal decreases, resulting in a reduction of momentum diffusivity and enhancement of thermal diffusivity and thus reduction of the Prandtl number $\left(\mathrm{Pr} = c_\mathrm{p}\,\mu/k\right)$. Although the heat source models affect the thermal and flow fields in the melt pool, it is found that the numerical predictions are less sensitive to the heat source models when temperature-dependent properties are employed for the cases studied here. However, it should be noted that for the cases where surface deformations are larger, the effects of heat source adjustment on numerical predictions become critical, as discussed in section 5.6.1.

Table 5.4: Temperature-dependent thermophysical properties of the Fe–S alloy used in the present study. Values are estimated by analogy with the values for iron-based alloys [44].

Property	Fe–S alloy	Unit
Density ρ	8100	$\mathrm{kg\,m^{-3}}$
Specific heat capacity c_p	627 (solid phase) 723.14 (liquid phase)	$\mathrm{J\,kg^{-1}\,K^{-1}}$
Thermal conductivity k	$8.8521 + 0.0114 \cdot T$ (solid phase) $4.5102 + 0.0107 \cdot T$ (liquid phase)	$\mathrm{W\,m^{-1}\,K^{-1}}$
Viscosity μ	$0.0659 - 7\times10^{-5}\cdot T + 3\times10^{-8}\cdot T^2 - 3\times10^{-12}\cdot T^3$	$\mathrm{kg\,m^{-1}\,s^{-1}}$
Latent heat of fusion $\mathscr{L}_\mathrm{f}$	250800	$\mathrm{J\,kg^{-1}}$
Thermal expansion coefficient β	2×10^{-6}	$\mathrm{K^{-1}}$
Liquidus temperature T_l	1620	K
Solidus temperature T_s	1610	K

Changes in the material properties with temperature affect thermal and flow fields in the melt pool, resulting in changes in the predicted melt-pool shape, as shown in figure 5.11. When temperature-dependent properties are employed, the melt-pool depth

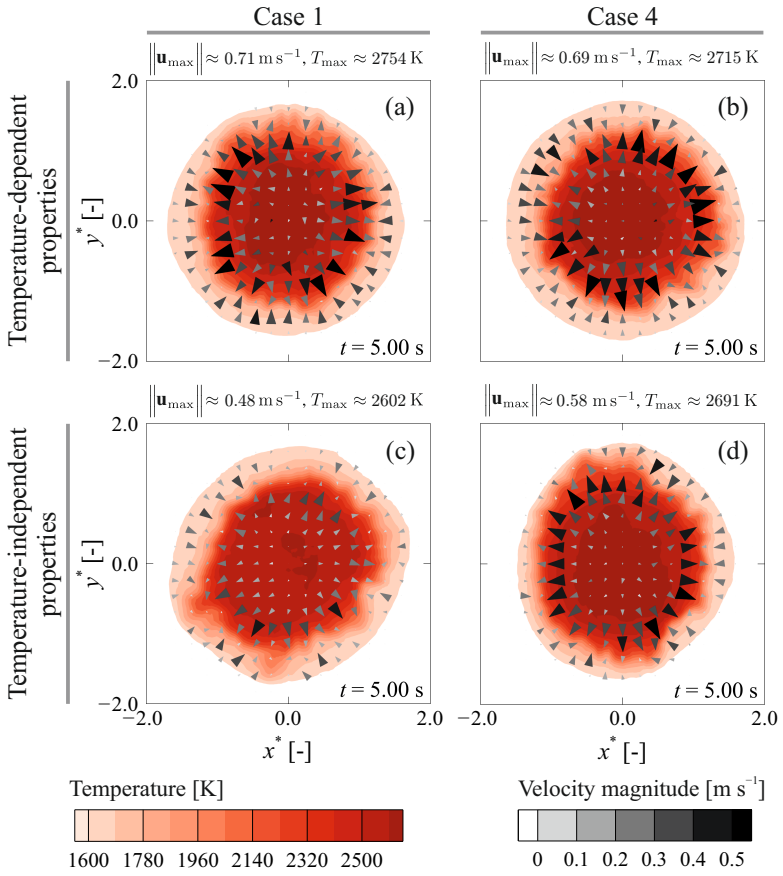

Figure 5.10: Contours of temperature and the velocity vectors on the melt pool free surface after 5 s of heating predicted using the heat source models Case 1 and 4 with temperature-dependent (table 5.4) and temperature-independent (table 5.1) material properties. Coordinates are non-dimensionalised using the laser-beam radius r_b as the characteristic length scale.

is significantly larger (about 36–74%) than that predicted using temperature-independent properties.

Temperature signals recorded from the monitoring point p_4 and the corresponding frequency spectra are shown in figure 5.12. Temperature signals received from the monitoring point p_4 are almost in the same range and vary between 2320 K and 2820 K. Employing temperature-dependent properties affects the frequency spectra of fluctuations, however the amplitude of fluctuations remains almost unaffected. The results presented in figure 5.12 indicate that adjusting the heat source dynamically during simulations can result in a decrease in the amplitude of temperature fluctuations, however its effect on the frequency spectrum is insignificant.

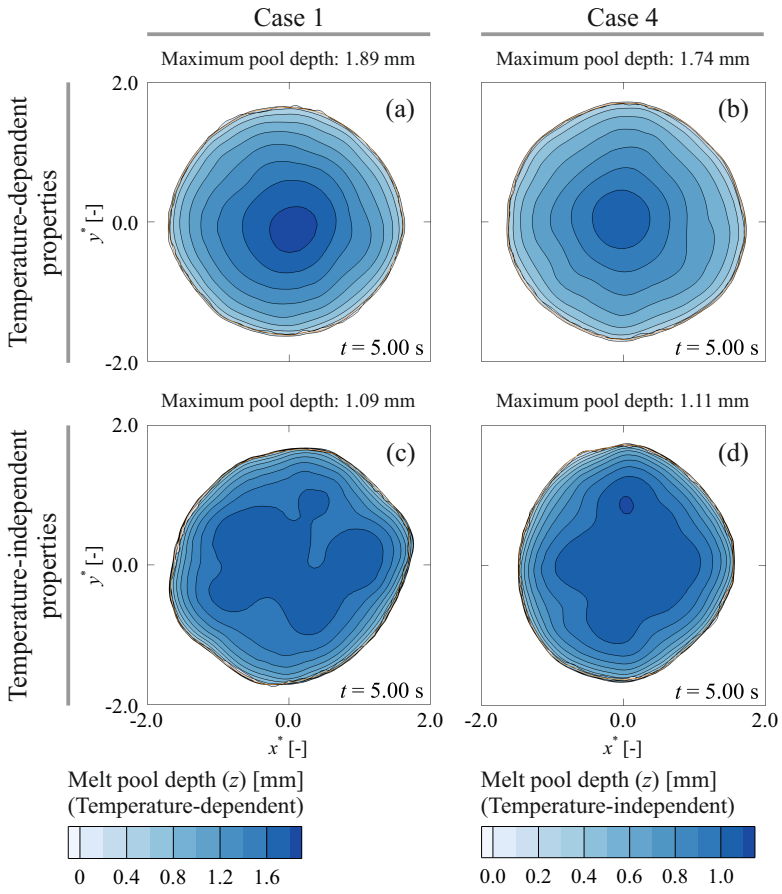

Figure 5.11: Contours of melt-pool depth at 5s for Case 1 and 4 predicted using temperature-dependent and temperature-independent material properties. Coordinates are non-dimensionalised using the laser-beam radius r_b as the characteristic length scale. The orange circular line shows the melt pool boundary at its top surface.

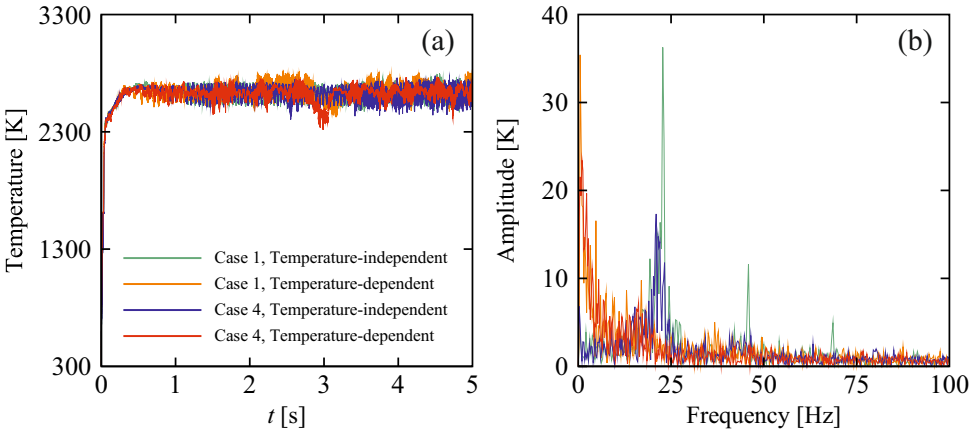

Figure 5.12: The influence of employing temperature-dependent material properties on temperature signals received from the melt pool and the corresponding frequency spectra. (a) Temperature signals recorded from the monitoring point p_4 located at $(x^*, y^*) = (0, 0)$ on the melt-pool surface and (b) the corresponding frequency spectra. Temperature signals in the period of 1 to 5s are employed for FFT analysis.

5.6.3. The effects of the enhancement factor

In section 3.6 it was mentioned that, in many simulation studies reported in the literature, the thermal conductivity and viscosity of the liquid metal were artificially increased by a so-called 'enhancement factor' e, in order to obtain better agreement between experimental and simulated post-solidification melt-pool shapes. Numerical studies carried out by De and DebRoy [45, 46, 47] showed that the values reported for the enhancement factor in the literature depend greatly on operating conditions and range from 2 to 100 (see for instance, [48–51]), however values between 2 and 10 are most often employed. The effects of the enhancement factor e on thermal and fluid flow fields in molten metal melt pools as well as the melt-pool shape can be found in [19, 52, 53], thus are not repeated here. Focusing on Case 4 in which free surface deformations are accounted for, the influence of the enhancement factor on the oscillatory flow behaviour is investigated. Temperatures recorded from the monitoring point p_4 and the temperature fluctuation spectra are shown in figure 5.13. Temperatures and the amplitudes of fluctuations reduce when increasing the enhancement factor. The contribution of diffusion in total energy transport increases with increasing enhancement factor, which results in a reduction of temperature gradients and therefore thermocapillary stresses generated over the melt-pool surface. The reduced thermocapillary stresses in addition to the enhanced viscosity of the molten metal lead to a reduction of fluid velocities that decrease convection in the melt pool further, which significantly affects the fluid flow structure. Increasing the enhancement factor e to 2.5 results in relatively deeper melt pool with a corresponding reduction of the fundamental frequency of fluctuations. Using higher values of the enhancement factor e, the melt-pool shape approaches a spherical-cap shape and the frequency spectrum becomes rather uniform with small amplitude fluctuations.

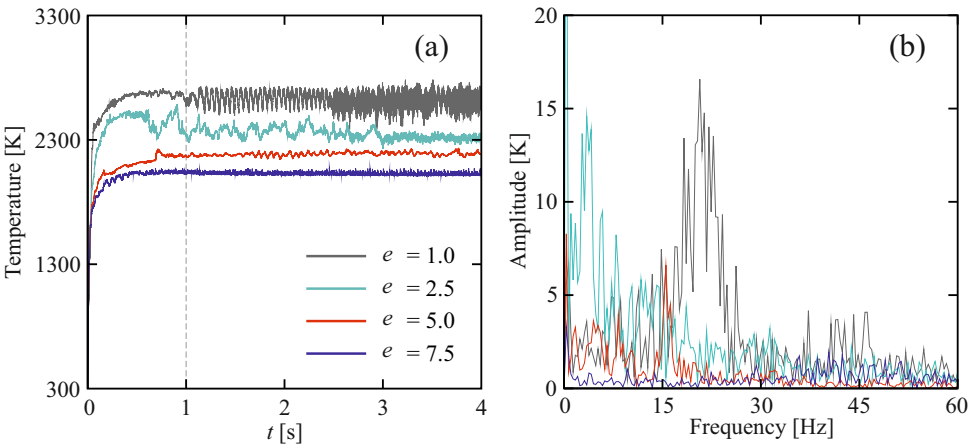

Figure 5.13: (a) Temperature signals recorded from the monitoring point $p_4\left(x^*, y^*\right) = (0,0)$ on the melt-pool surface and (b) the corresponding frequency spectra for different values of the enhancement factor e. Temperature signals in the period of 1 to 4 s are employed for FFT analysis.

5.7. Conclusions

Molten metal melt pool behaviour during a laser spot melting was studied to investigate the influence of dynamically adjusted energy flux distribution on thermal and fluid flow fields using both deformable and non-deformable gas-metal interfaces.

For the material and laser power presented here, self-excited flow instabilities arise rapidly and fluid flow inside the melt pool is inherently three-dimensional and unstable. Flow instabilities in the melt pool have a significant influence on solidification and melting by altering the thermal and fluid flow fields. Free surface deformations, even small compared to the melt pool size, can significantly influence the fluid flow pattern in the melt pool. When in the numerical simulations the gas-metal interface is assumed to remain flat and non-deformable, lower temperatures with smaller fluctuations were found in comparison to those of the cases with a deformable interface, which results in a different melt-pool shape. Taking the surface deformations into account leads to erratic flow patterns with relatively large fluctuations, which are caused by the intensified interactions between vortices generated in the melt pool resulting from the augmented thermocapillary stresses. When surface deformations are taken into account, various tested methods for adjusting the absorbed energy flux resulted in smaller melt-pool sizes compared to those without an adjustment. However, the melt pool behaves quite similarly for various adjustment methods studied in the present chapter. It should be noted that the utilisation of temperature-dependent properties can enhance the accuracy of numerical predictions in simulations of molten metal flow in melting pools; however, the results presented here show the importance of employing a physically-realistic heat-source model that is also applicable if temperature-dependent properties are employed.

Although the enhancement factors are widely used to achieve agreement between numerically predicted melt-pool sizes and solidification rates with experiments, they do not represent the physics of complex transport phenomena governing laser spot melting. The use of an enhancement factor can significantly affect the numerical predictions of melt pool oscillatory behaviour.

References

[1] Ayoola, W. A., Suder, W. J., and Williams, S. W. Parameters controlling weld bead profile in conduction laser welding. *Journal of Materials Processing Technology*, 249:522–530, 2017. doi:10.1016/j.jmatprotec.2017.06.026.

[2] Oreper, G. M. and Szekely, J. Heat- and fluid-flow phenomena in weld pools. *Journal of Fluid Mechanics*, 147(-1):53, 1984. doi:10.1017/s0022112084001981.

[3] Mills, K. C., Keene, B. J., Brooks, R. F., and Shirali, A. Marangoni effects in welding. *Philosophical Transactions of the Royal Society A: Mathematical, Physical and Engineering Sciences*, 356(1739): 911–925, 1998. doi:10.1098/rsta.1998.0196.

[4] Heiple, C. R. and Roper, J. R. Mechanism for minor element effect on GTA fusion zone geometry. *Welding Journal*, 61(4):97s–102s, 1982. URL: `https://app.aws.org/wj/supplement/WJ_1982_04_s97.pdf`.

[5] Paul, A. and DebRoy, T. Free surface flow and heat transfer in conduction mode laser welding. *Metallurgical Transactions B*, 19(6):851–858, 1988. doi:10.1007/bf02651409.

[6] Cook, P. S. and Murphy, A. B. Simulation of melt pool behaviour during additive manufacturing: Underlying physics and progress. *Additive Manufacturing*, 31:100909, 2020. doi:10.1016/j.addma.2019.100909.

[7] DebRoy, T. and David, S. A. Physical processes in fusion welding. *Reviews of Modern Physics*, 67(1):85–112, 1995. doi:10.1103/revmodphys.67.85.

[8] Aucott, L., Dong, H., Mirihanage, W., Atwood, R., Kidess, A., Gao, S., Wen, S., Marsden, J., Feng, S., Tong, M., Connolley, T., Drakopoulos, M., Kleijn, C. R., Richardson, I. M., Browne, D. J., Mathiesen, R. H., and Atkinson, H. V. Revealing internal flow behaviour in arc welding and additive manufacturing of metals. *Nature Communications*, 9(1), 2018. doi:10.1038/s41467-018-07900-9.

[9] Zacharia, T., David, S. A., Vitek, J. M., and Debroy, T. Modeling of interfacial phenomena in welding. *Metallurgical Transactions B*, 21(3):600–603, 1990. doi:10.1007/bf02667874.

[10] Ha, E.-J. and Kim, W.-S. A study of low-power density laser welding process with evolution of free surface. *International Journal of Heat and Fluid Flow*, 26(4):613–621, 2005. doi:10.1016/j.ijheatfluidflow.2005.03.009.

[11] Shah, A., Kumar, A., and Ramkumar, J. Analysis of transient thermo-fluidic behavior of melt pool during spot laser welding of 304 stainless-steel. *Journal of Materials Processing Technology*, 256:109–120, 2018. doi:10.1016/j.jmatprotec.2018.02.005.

[12] Zhao, C. X., Kwakernaak, C., Pan, Y., Richardson, I. M., Saldi, Z., Kenjeres, S., and Kleijn, C. R. The effect of oxygen on transitional Marangoni flow in laser spot welding. *Acta Materialia*, 58 (19):6345–6357, 2010. doi:10.1016/j.actamat.2010.07.056.

[13] Kidess, A., Kenjereš, S., and Kleijn, C. R. The influence of surfactants on thermocapillary flow instabilities in low Prandtl melting pools. *Physics of Fluids*, 28(6):062106, 2016. doi:10.1063/1.4953797.

[14] Hirt, C. W. and Nichols, B. D. Volume of fluid (VOF) method for the dynamics of free boundaries. *Journal of Computational Physics*, 39(1):201–225, 1981. doi:10.1016/0021-9991(81)90145-5.

[15] Meng, X., Qin, G., and Zou, Z. Investigation of humping defect in high speed gas tungsten arc welding by numerical modelling. *Materials & Design*, 94:69–78, 2016. doi:10.1016/j.matdes.2016.01.019.

[16] Wu, D., Nguyen, A. V., Tashiro, S., Hua, X., and Tanaka, M. Elucidation of the weld pool convection and keyhole formation mechanism in the keyhole plasma arc welding. *International Journal of Heat and Mass Transfer*, 131:920–931, 2019. doi:10.1016/j.ijheatmasstransfer.2018.11.108.

[17] Choo, R. T. C., Szekely, J., and Westhoff, R. C. Modeling of high-current arcs with emphasis on free surface phenomena in the weld pool. *Welding Journal*, 69(9):346s–361s, 1990. URL: `http://files.aws.org/wj/supplement/WJ_1990_09_s346.pdf`.

[18] Pitscheneder, W., DebRoy, T., Mundra, K., and Ebner, R. Role of sulfur and processing variables on the temporal evolution of weld pool geometry during multikilowatt laser beam welding of steels. *Welding Journal*, 75(3):71s–80s, 1996. URL: `https://app.aws.org/wj/supplement/WJ_1996_03_s71.pdf`.

[19] Saldi, Z. S., Kidess, A., Kenjereš, S., Zhao, C., Richardson, I. M., and Kleijn, C. R. Effect of enhanced heat and mass transport and flow reversal during cool down on weld pool shapes in laser spot welding of steel. *International Journal of Heat and Mass Transfer*, 66:879–888, 2013. doi:10.1016/j.ijheatmasstransfer.2013.07.085.

[20] Heiple, C. R., Roper, J. R., Stagner, R. T., and Aden, R. J. Surface active element effects on the shape of GTA, laser, and electron beam welds. *Welding Journal*, 62(3):72s–77s, 1983. URL: `http://files.aws.org/wj/supplement/WJ_1983_03_s72.pdf`.

[21] Mills, K. C. and Keene, B. J. Factors affecting variable weld penetration. *International Materials Reviews*, 35(1):185–216, 1990. doi:10.1179/095066090790323966.

[22] Sahoo, P., Debroy, T., and McNallan, M. J. Surface tension of binary metal—surface active solute systems under conditions relevant to welding metallurgy. *Metallurgical Transactions B*, 19(3):483–491, 1988. doi:10.1007/bf02657748.

[23] Gao, M., Kawahito, Y., and Kajii, S. Observation and understanding in laser welding of pure titanium at subatmospheric pressure. *Optics Express*, 25(12):13539, 2017. doi:10.1364/oe.25.013539.

[24] Cho, J., Farson, D. F., Hollis, K. J., and Milewski, J. O. Numerical analysis of weld pool oscillation in laser welding. *Journal of Mechanical Science and Technology*, 29(4):1715–1722, 2015. doi:10.1007/s12206-015-0344-2.

[25] Kim, Y.-D. and Kim, W.-S. A numerical analysis of heat and fluid flow with a deformable curved free surface in a laser melting process. *International Journal of Heat and Fluid Flow*, 29(5): 1481–1493, 2008. doi:10.1016/j.ijheatfluidflow.2008.06.009.

[26] Ebrahimi, A., Kleijn, C. R., and Richardson, I. M. A simulation-based approach to characterise melt-pool oscillations during gas tungsten arc welding. *International Journal of Heat and Mass Transfer*, 164:120535, 2021. doi:10.1016/j.ijheatmasstransfer.2020.120535.

[27] Arrizubieta, J. I., Lamikiz, A., Klocke, F., Martínez, S., Arntz, K., and Ukar, E. Evaluation of the relevance of melt pool dynamics in laser material deposition process modeling. *International Journal of Heat and Mass Transfer*, 115:80–91, 2017. doi:10.1016/j.ijheatmasstransfer.2017.07.011.

[28] Amara, E. H. and Fabbro, R. Modeling of humps formation during deep-penetration laser welding. *Applied Physics A*, 101(1):111–116, 2010. doi:10.1007/s00339-010-5768-z.

[29] Indhu, R., Vivek, V., Sarathkumar, L., Bharatish, A., and Soundarapandian, S. Overview of laser absorptivity measurement techniques for material processing. *Lasers in Manufacturing and Materials Processing*, 5(4):458–481, 2018. doi:10.1007/s40516-018-0075-1.

[30] *Release 19.2*. ANSYS Fluent. URL: `https://www.ansys.com/`.

[31] Patankar, S. V. *Numerical Heat Transfer and Fluid Flow*. Taylor & Francis Inc, 1st edition, 1980. ISBN 0891165223.

[32] Issa, R. I. Solution of the implicitly discretised fluid flow equations by operator-splitting. *Journal of Computational Physics*, 62(1):40–65, 1986. doi:10.1016/0021-9991(86)90099-9.

[33] Ubbink, O. *Numerical Prediction of Two Fluid Systems with Sharp Interfaces*. PhD dissertation, Imperial College London (University of London), London, United Kingdom, 1997. URL: http://hdl.handle.net/10044/1/8604.

[34] Courtois, M., Carin, M., Masson, P. L., Gaied, S., and Balabane, M. Guidelines in the experimental validation of a 3D heat and fluid flow model of keyhole laser welding. *Journal of Physics D: Applied Physics*, 49(15):155503, 2016. doi:10.1088/0022-3727/49/15/155503.

[35] Bergström, D., Powell, J., and Kaplan, A. F. H. A ray-tracing analysis of the absorption of light by smooth and rough metal surfaces. *Journal of Applied Physics*, 101(11):113504, 2007. doi:10.1063/1.2738417.

[36] Rivas, D. and Ostrach, S. Scaling of low-prandtl-number thermocapillary flows. *International Journal of Heat and Mass Transfer*, 35(6):1469–1479, 1992. doi:10.1016/0017-9310(92)90037-s.

[37] Chakraborty, N. and Chakraborty, S. Thermal transport regimes and generalized regime diagram for high energy surface melting processes. *Metallurgical and Materials Transactions B*, 38(1):143–147, 2007. doi:10.1007/s11663-006-9000-7.

[38] Davis, S. H. and Homsy, G. M. Energy stability theory for free-surface problems: buoyancy-thermocapillary layers. *Journal of Fluid Mechanics*, 98(03):527, 1980. doi:10.1017/s0022112080000274.

[39] Czerner, S. *Schmelzbaddynamik beim Laserstrahl-Wärmeleitungsschweißen von Eisenwerkstoffen*. PhD dissertation, Leibniz Universität Hannover, 2005. URL: http://nbn-resolving.de/urn:nbn:de:gbv:089-4942690490.

[40] Kidess, A., Kenjereš, S., Righolt, B. W., and Kleijn, C. R. Marangoni driven turbulence in high energy surface melting processes. *International Journal of Thermal Sciences*, 104:412–422, 2016. doi:10.1016/j.ijthermalsci.2016.01.015.

[41] Kuhlmann, H. C. and Schoisswohl, U. Flow instabilities in thermocapillary-buoyant liquid pools. *Journal of Fluid Mechanics*, 644:509, 2010. doi:10.1017/s0022112009992953.

[42] Davis, S. H. Thermocapillary instabilities. *Annual Review of Fluid Mechanics*, 19(1):403–435, 1987. doi:10.1146/annurev.fl.19.010187.002155.

[43] Temperton, C. Implementation of a self-sorting in-place prime factor FFT algorithm. *Journal of Computational Physics*, 58(3):283–299, 1985. doi:10.1016/0021-9991(85)90164-0.

[44] Mills, K. C. *Recommended Values of Thermophysical Properties for Selected Commercial Alloys*. Woodhead Publishing, woodhead publishing series in metals and surface engineering edition, 2002. ISBN 978-1-85573-569-9.

[45] De, A. and DebRoy, T. Improving reliability of heat and fluid flow calculation during conduction mode laser spot welding by multivariable optimisation. *Science and Technology of Welding and Joining*, 11(2):143–153, 2006. doi:10.1179/174329306x84346.

[46] De, A. and DebRoy, T. Reliable calculations of heat and fluid flow during conduction mode laser welding through optimization of uncertain parameters. *Welding Journal*, 84(7):101s–112s, 2005. URL: https://app.aws.org/wj/supplement/WJ_2005_07_s101.pdf.

[47] De, A. and DebRoy, T. A smart model to estimate effective thermal conductivity and viscosity in the weld pool. *Journal of Applied Physics*, 95(9):5230–5240, 2004. doi:10.1063/1.1695593.

[48] Zhang, W., Roy, G. G., Elmer, J. W., and DebRoy, T. Modeling of heat transfer and fluid flow during gas tungsten arc spot welding of low carbon steel. *Journal of Applied Physics*, 93(5): 3022–3033, 2003. doi:10.1063/1.1540744.

[49] Choo, R. T. C. and Szekely, J. The possible role of turbulence in GTA weld pool behavior. *Welding Journal*, 73(2):25s–31s, 1994. URL: `http://files.aws.org/wj/supplement/WJ_1994_02_s25.pdf`.

[50] Mundra, K. and DebRoy, T. Toward understanding alloying element vaporization during laser beam welding of stainless steel. *Welding Journal*, 72(1):1s–9s, 1993. URL: `http://files.aws.org/wj/supplement/WJ_1993_01_s1.pdf`.

[51] Choo, R. T. C., Szekely, J., and Westhoff, R. C. On the calculation of the free surface temperature of gas-tungsten-arc weld pools from first principles: Part I. modeling the welding arc. *Metallurgical and Materials Transactions B*, 23(3):357–369, 1992. doi:10.1007/bf02656291.

[52] Ehlen, G., Ludwig, A., and Sahm, P. R. Simulation of time-dependent pool shape during laser spot welding: Transient effects. *Metallurgical and Materials Transactions A*, 34(12):2947–2961, 2003. doi:10.1007/s11661-003-0194-x.

[53] Mundra, K., DebRoy, T., Zacharia, T., and David, S. A. Role of thermophysical properties in weld pool modeling. *Welding Journal*, 71(9):313s–320s, 1992. URL: `https://app.aws.org/wj/supplement/WJ_1992_09_s313.pdf`.

6

Melt Pool Behaviour in Moving Laser Melting: The Effects of Laser Characteristics

The absorptivity of a material is a major uncertainty in numerical simulations of laser welding and additive manufacturing, and its value is often calibrated through trial-and-error exercises. This adversely affects the capability of numerical simulations when predicting the process behaviour and can eventually hinder the exploitation of fully digitised manufacturing processes, which is a goal of "industry 4.0". In the present work, an enhanced absorption model that takes into account the effects of laser characteristics, incident angle, surface temperature, and material composition is utilised to predict internal heat and fluid flow in laser melting. Employing such an absorption model is physically more realistic than assuming a constant absorptivity and can reduce the costs associated with calibrating an appropriate value. High-fidelity three-dimensional numerical simulations were performed using both variable and constant absorptivity models and the predictions compared with experimental data. The results of the present work unravel the crucial effect of absorptivity on the physics of internal flow in laser material processing. The difference between melt-pool shapes obtained using fibre and CO_2 laser sources is explained, and factors affecting the local energy absorption are discussed.

The contents of this chapter have been published in *Materials & Design*, **2022**, *214*, 110385, DOI: 10.1016/j.matdes.2022.110385.

6.1. Introduction

Laser-beam melting of metallic substrates forms the basis of many advanced fusion-based manufacturing processes (such as laser welding, laser cladding, laser metal deposition (LMD), and selective laser melting (SLM)) and has brought new perspectives on advancement of materials processing and manufacturing of high-integrity products. Successful adoption of laser-beam melting in real-world engineering applications requires finding processing windows within which the product quality should meet the intended standards [1]. However, determining the processing window through trial-and-error experiments is challenging and involves significant costs due to the large number of process parameters and the coupling between various physical phenomena. Simulation-based approaches have been recognised as a promising alternative to costly and time-inefficient experiments and can be utilised to reduce the costs of design-space exploration [2, 3]. Moreover, numerical simulations can enhance our understanding of the complex transport phenomena in laser material processing that are not easily accessible through experiments [4, 5].

Successful adoption of simulation-based approaches for process development and optimisation relies predominantly on adequate modelling of various physical phenomena that occur during laser melting (*e.g.* laser-matter interaction, heat and fluid flow, and solid-liquid phase transformation) [6]. Assumptions made to develop computational models often affect their reliability, accuracy and performance in predicting and describing the process behaviour. For instance, studies suggest that melt-pool surface deformations affect power-density distribution, leading to changes in the thermal field, Marangoni flow pattern and the melt-pool shape [7–9]. Conversely, previous investigations [10–13] have shown a considerable influence of laser characteristics and power-density distribution on molten metal flow behaviour in laser welding and additive manufacturing. Thus, there seems to be an important bi-directional coupling between laser power-density distribution and melt-pool behaviour. Neglecting such effects in numerical simulations of laser-beam melting can negatively affect the quality of numerical predictions of thermal fields, microstructures and properties of the product [8, 14]. Moreover, assumptions made to develop a computational model may necessitate the incorporation of unphysical tuning parameters to obtain agreement between numerical and experimental data [8, 15]. This can reduce the model reliability for design-space explorations since a change in process parameters or material properties may require recalibrating the tuning parameters [16, 17]. Understanding the influence of such assumptions on numerical predictions is therefore essential and can guide the modelling efforts to enhance the current numerical simulations.

Absorption of laser-energy, energy-density distribution and its variation over time are critical components influencing the modelling of laser-beam melting [18] and depend on a variety of process parameters including the characteristics of the laser system (*e.g.* laser intensity and wavelength), thermophysical properties of the material, surface roughness and chemistry, and interactions of the melt-pool surface with the laser beam [19–21]. In the majority of previous studies on laser-beam melting, the absorption of laser energy is assumed to be constant [13], neglecting the unsteady interactions between laser-beam and material surface [22]. Studies have shown that changes in melt-pool surface morphology and temperature can affect the local absorptivity of the material [10, 23–25].

The Fresnel absorption model [26], which is commonly employed in numerical simulations of laser melting (particularly when the ray-tracing method is used), accounts for the effects of laser-beam incident angle and material refractive index, but neglects the temperature dependence of material absorptivity [20]. In laser melting of metallic substrates, the material often experiences large changes in temperature that can significantly affect the thermophysical properties of the material, including the material absorptivity [27, 28]. Moreover, the complex molten metal flow in melt-pools continuously disturbs temperature distribution over the surface [8], affecting the local absorptivity of the material. The Fresnel model cannot reflect the variation of local energy absorption that occurs due to changes in melt-pool surface temperature [12, 29, 30]. Hence, the Fresnel model cannot describe variations in material absorptivity with sufficient accuracy, particularly in cases where the melt-pool surface deformations are small compared to the melt-pool depth (for instance, laser cladding, conduction-mode laser welding and laser metal deposition).

Realising that in practical applications the laser type is not a control parameter, as commercial machines come with a fixed laser type, the present work focuses on understanding the influence of laser characteristics on complex heat and molten metal flow in laser-beam melting. Such an understanding allows us to explain, for example, the difference between melt-pool shapes obtained using fibre transmissible and CO_2 lasers (*i.e.* the most widely employed lasers for industrial applications). High-fidelity three-dimensional numerical simulations are performed using an enhanced laser-beam absorption model that takes into account the effects of laser characteristics, surface temperature, incident angle and base-material composition. The results obtained using the enhanced absorption model for different laser systems and laser powers are compared with those obtained using a constant absorptivity and factors affecting the local energy absorption are discussed. Additionally, experiments are reported for different laser powers to validate the melt-pool shapes predicted using the present computational model. The results and discussions provided in the present work guide the modelling efforts to improve simulations of fusion-based welding and additive manufacturing.

6.2. Problem description

As shown in figure 6.1, a moving laser beam is employed to locally heat and melt the substrate that is made of a stainless steel alloy (AISI 316L) and is initially at an ambient temperature of 300 K. The gas layer above the plate is included in simulations to track the motion of the gas-metal interface. The influence of laser characteristics on melting of a metallic substrate is studied numerically for fibre and CO_2 lasers, whose wavelengths differ by a factor of 10. The laser beam is perpendicular to the substrate surface and has a Gaussian intensity profile.

Three batches of three-dimensional numerical simulations are executed for different laser types and powers using both constant and variable absorptivity models to describe the complex thermal and fluid flow fields in the melt pool. For cases where the absorptivity is assumed to be constant, different values of the absorptivity are examined, as reported in table 6.1. The dimensions of the computational domain defined in a Cartesian coordinate system, and the boundary conditions applied to the outer boundaries, are shown in figure 6.1. Heat input from the laser, heat losses due to convection, radiation and vaporisation, as well as forces acting on the melt pool (*i.e.* Marangoni shear force, capillary

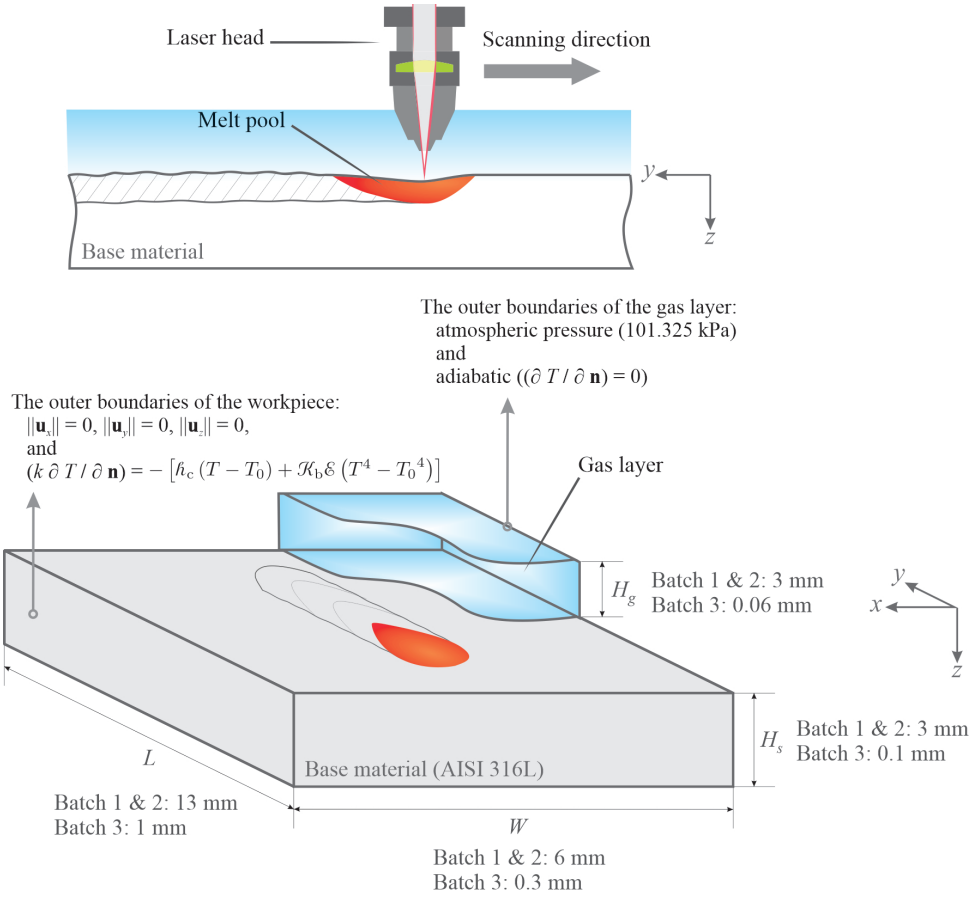

Figure 6.1: Schematic of laser melting, dimensions of the computational domain and the mathematical expressions used for the boundary conditions. Parts of the gas layer are clipped for visualisation.

force, and recoil pressure) are implemented in the simulations by adding source and sink terms to the governing equations, as described in section 3.2.1. Although the thermal buoyancy force is often negligible compared with Marangoni force in driving the molten metal flow in laser melting [8], a variable density model is employed in the present work to account for thermal buoyancy force as well as the solidification shrinkage. Temperature-dependent material properties are employed for both the solid and the molten metal in the present numerical simulations and the values are reported in table 6.2 and figure 6.2. The values for the surface tension are estimated using an empirical correlation proposed by Sahoo *et al.* [31], which takes the influence of surfactants (*i.e.* sulphur) into account (see section 3.4 and figure 3.2). Although the properties of argon are also temperature-dependent, they have been assumed to be constant in the present work for the sake of simplicity, see table 6.2. This assumption is made based on the fact that the density, viscosity and thermal conductivity of argon are very small compared to those of the metal,

therefore variations of those gas properties with temperature have negligible influence on the numerical predictions [32].

Table 6.1: Summary of the process parameters studied in the present work.

Parameter	Batch 1	Batch 2	Batch 3
Laser type	CO_2 laser	Nd:YAG laser	Fibre laser [a]
Laser power $\mathcal{P}$ [W]	900–2100 (interval: 300)	500–900 (100)	200
Wavelength λ [m]	1.060×10^{-5}	1.064×10^{-6}	1.070×10^{-6}
Constant absorptivity a [–]	0.10–0.14 (2) and 0.18	0.3–0.4 (5)	0.3–0.4 (5)
Travel speed $\mathcal{V}$ [m s^{-1}]	10^{-2}	10^{-2}	1.5
Spot size (D4σ) d_b [m]	2×10^{-3}	2×10^{-3}	1.1×10^{-4}
Interaction time $t_i = d_b/\mathcal{V}$ [s]	0.2	0.2	7.3×10^{-5}

[a] continuous wave fibre laser (YLR-500-AC, IPG Photonics) [1]

Table 6.2: Material properties employed in the present work.

Property	Stainless steel (AISI 316L)	Gas (argon)
Density ρ [kg m^{-3}]	see figure 6.2	1.623
Specific heat capacity c_p [J kg^{-1} K^{-1}]	see figure 6.2	520.64
Thermal conductivity k [W m^{-1} K^{-1}]	see figure 6.2	1.58×10^{-2}
Dynamic viscosity μ [kg m^{-1} s^{-1}]	see figure 6.2	2.12×10^{-5}
Molar mass M [kg mol^{-1}]	5.58×10^{-2}	3.9948×10^{-2}
Latent heat of fusion $\mathscr{L}_f$ [J kg^{-1}]	2.7×10^5	–
Latent heat of vaporisation $\mathscr{L}_v$ [J kg^{-1}]	7.45×10^6	–
Solidus temperature T_s [K]	1658	–
Liquidus temperature T_l [K]	1723	–
Boiling temperature T_b [K]	3086	–

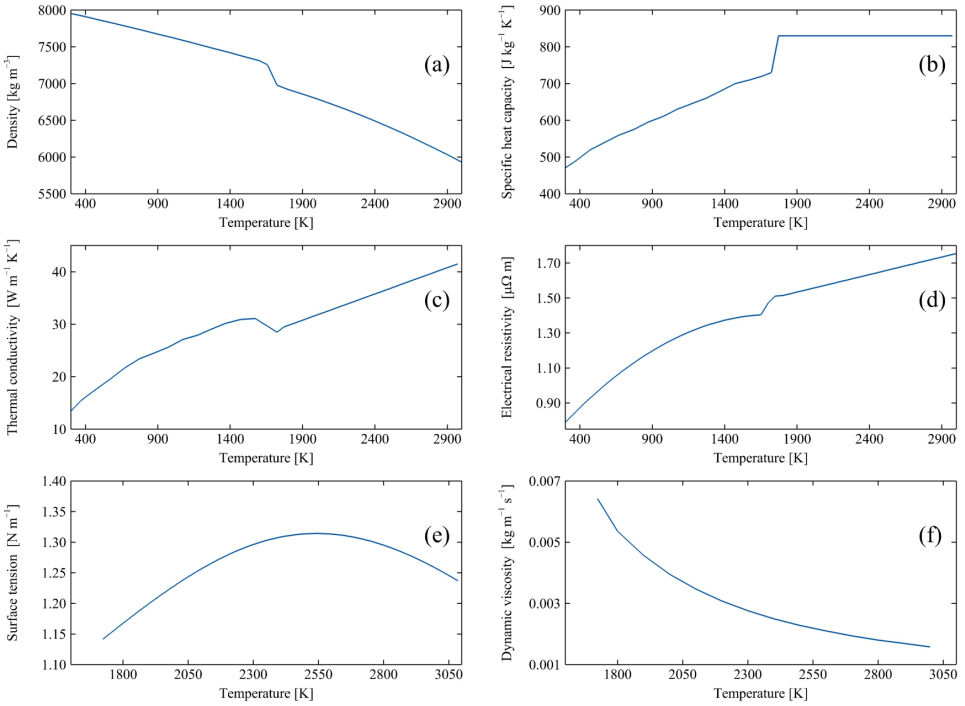

Figure 6.2: Temperature-dependent properties of stainless steel 316L. (a) density [33], (b) specific heat capacity [34], (c) thermal conductivity [34], (d) electrical resistivity [35], and (e) dynamic viscosity [33].

6.3. Numerical procedure

The present numerical simulations were constructed on the foundation of a proprietary flow solver, ANSYS Fluent [36]. User-defined functions (UDFs) programmed in the C programming language were developed to implement the absorptivity model, source and sink terms in the momentum and energy equations as well as the surface tension model in the simulations. Hexahedral cells were used to discretise the computational domain with minimum cell spacing of 50 μm for cases in batch 1 and 2 (CO_2 and Nd:YAG welds), and 3 μm for cases in batch 3 (continuous wave fibre laser welds), as shown in figure 6.3. These cell spacings result in at least 35 cells in the melt pool region along its width, which is sufficient to achieve grid independent results [3, 8, 9, 37]. Accordingly, the total number of computational cells is about 1.2×10^6 for cases in batch 1 and 2, and about 1.0×10^6 for cases in batch 3.

The central differencing scheme with second-order accuracy and a first-order implicit scheme were employed for spatial discretisation and time marching respectively. A fixed time-step size Δt was used in the simulations and its value was chosen sufficiently small ($10^{-8}\,\text{s} < \Delta t < 10^{-5}\,\text{s}$) to achieve a Courant number ($\text{Co} = \|\mathbf{u}\|\Delta t/\Delta x$) less than 0.2. The PRESTO (pressure staggering option) scheme [38] was used for the pressure inter-

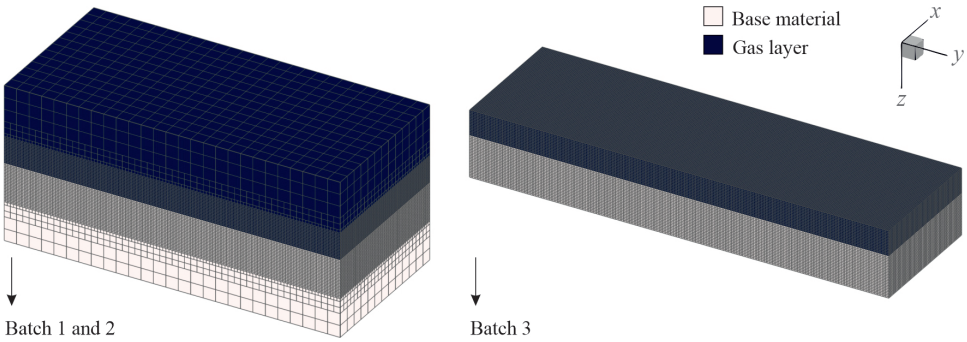

Figure 6.3: The computational meshes employed in the present work.

polation, and the PISO (pressure-implicit with splitting of operators) scheme [39] was used to couple velocity and pressure fields. An explicit compressive VOF method [40] was employed to formulate the advection of the scalar field ϕ. Each simulation was run in parallel on 16 cores (AMD EPYC 7452) of a high-performance computing cluster with 256 GB memory.

6.4. Experimental setup and procedure

The experimental setup employed in the present work is shown in figure 6.4. An Yb:YAG disk laser (Trumpf TruDisk 10001) that was connected to a fibre with a core diameter of 6×10^{-4} m was employed. The fibre transports the laser light towards the focusing optics (Trumpf BEO D70), consisting of a 200 mm collimator and 400 mm focusing lens. The focusing optics are mounted to a 6-DOF robot (ABB IRB-2600M2004). Using this setup, a laser spot with a diameter of 1.2 mm and a top-hat power-density distribution was produced (see figure 6.4(b)). Melting tracks with a length of 80 mm were made on an AISI 316L plate with dimensions of 250 mm × 100 mm × 10 mm. The travel speed was set to 20 mm s^{-1}. The melt pool was protected from oxidation during the process using argon gas at a flow rate of about 20 l/ min. Each experiment was repeated at least three times to ensure that the results are reproducible. The samples were cut transversely, polished and etched to capture macrographs using a digital microscope (Keyence VHX 7000). A solution of 100 ml HCl, 100 ml H_2O and 10 ml NHO_3 with a temperature of about 310 K was used for etching the samples.

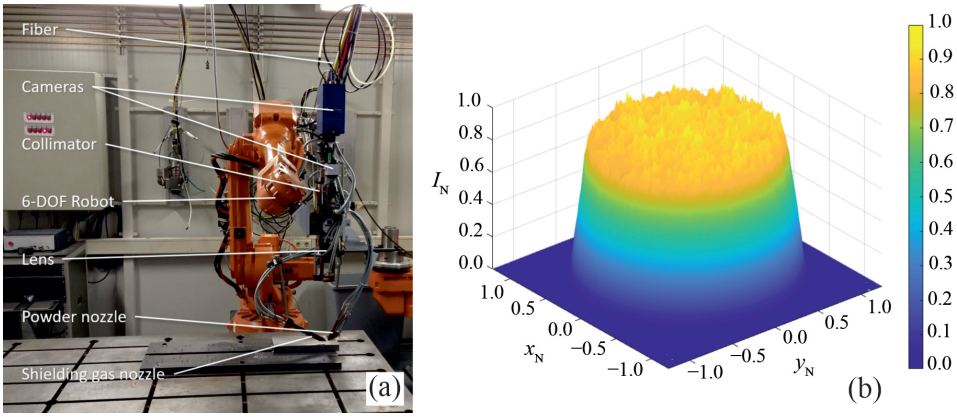

Figure 6.4: (a) The experimental setup employed in the present work. (b) Power-density distribution produced using the present experimental setup. In subfigure (b), the power-density profile is normalised with the respective maximum peak, and coordinates are non-dimensionalised using the laser-beam radius r_b.

6.5. Results and discussion

6.5.1. Model validation

The reliability and accuracy of the present computational model are examined by comparing the numerically predicted melt-pool shapes with those obtained from experiments with different laser systems, laser powers and power-density distributions. To visualise the melt-pool shapes, cross-sectional macrographs were prepared *ex situ* after experiments and iso-surfaces of solidus temperature were projected on the x-z plane after numerical simulations. It should be noted that the numerical results were obtained using the variable absorptivity model described in section 3.3 without calibration. Figure 6.5 shows a comparison between the melt-pool shapes obtained from the present computational model with those obtained from experiments using an Yb:YAG laser ($\lambda = 1.030 \times 10^{-6}$ m) and different laser powers, which indicates a reasonable agreement (generally less than 5% difference in melt-pool dimensions).

The characteristics of the laser system used in laser melting can affect the absorptivity and hence can change the resulting melt-pool shape. The results of the present computational model are also benchmarked against the experimental data reported by Kell *et al.* [41] for laser melting of a 1 mm-thick steel plate using a CO_2 laser ($\lambda = 1.060 \times 10^{-5}$ m) with the energy-density ($\mathcal{E} = \mathcal{P}/(\mathcal{V} d_b)$) being set to 120 MJ m^{-2}, and the results are shown in figure 6.6. In this case, the deviation between the numerically predicted and the experimentally measured melt-pool dimensions is less than 2%, demonstrating the reliability of the present computational model in predicting the melt-pool shape. The deviation between the numerical and experimental results can be attributed to uncertainties in modelling temperature-dependent material properties, particularly in the liquid phase, the assumptions made to develop the present computational model as well as uncertainties associated with the experimental measurements.

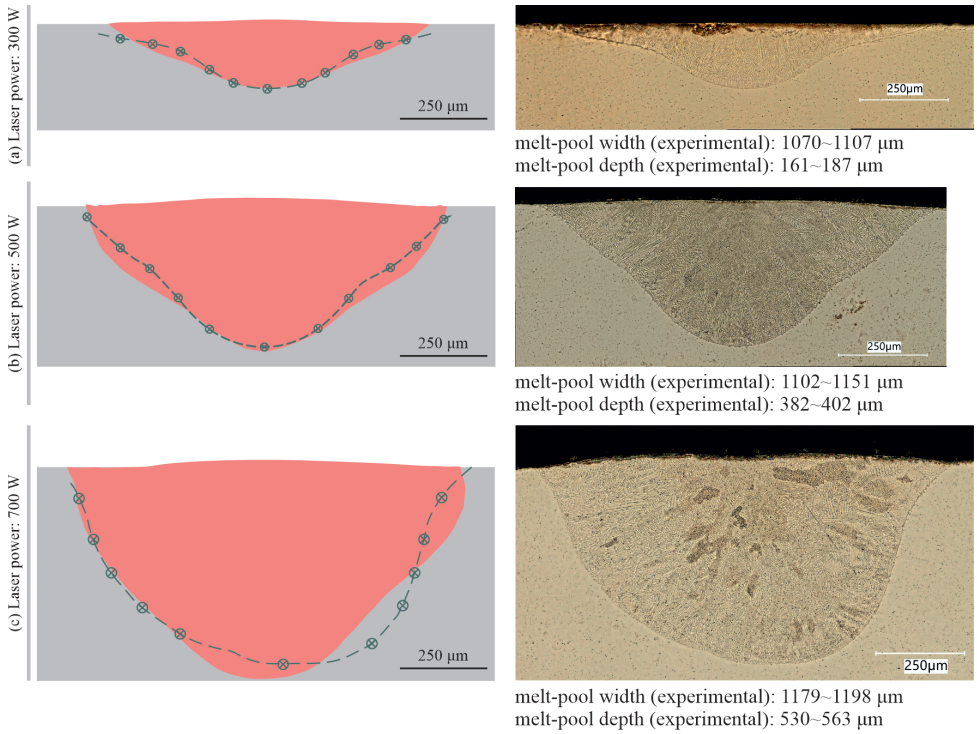

Figure 6.5: Numerically predicted melt-pool shapes obtained from the present computational model (left column, regions shaded in pink) compared with the experimental macrographs (right column, circles and dashed lines). The base material is stainless steel 316L. An Yb:YAG laser ($\lambda = 1.030 \times 10^{-6}$ m) was used, the laser beam had a top-hat power-density distribution, the spot size d_b was 1.2 mm and travel speed $\mathcal{V}$ was set to 20 mm s^{-1}. The energy-density ($\mathcal{E} = \mathcal{P}/(\mathcal{V} d_b)$) ranges between 12.5 MJ m^{-2} and 29.2 MJ m^{-2}.

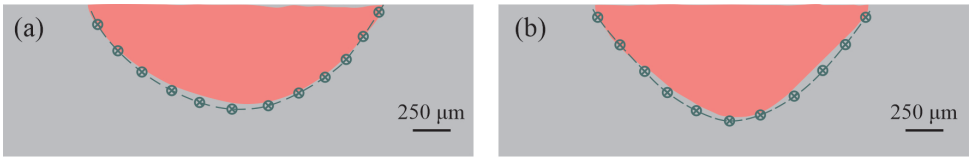

Figure 6.6: Comparison of the melt-pool shapes obtained from the present computational model (regions shaded in pink) with the experimental measurements of Kell *et al.* [41] (circles and dashed line). (a) Circular laser beam with a Gaussian power-density distribution and a spot size (D4σ) of d_b = 1.25 mm, and (b) Square-shaped laser beam with a top-hat power-density distribution and a spot size of d_b = 1.25 mm. The base material is stainless steel 316L. A CO_2 laser ($\lambda = 1.060 \times 10^{-5}$ m) was used and the energy-density ($\mathcal{E} = \mathcal{P}/(\mathcal{V} d_b)$) was set to 120 MJ m^{-2} for both cases.

6.5.2. Melt-pool shape and dimensions

To be able to systematically study the effects of laser characteristics and melt-pool surface deformations on variation of local absorptivity, three batches of simulations are considered for different laser types. For cases in batch 1 and 2, the power density is too low to cause significant vaporisation and surface deformations are small compared to the melt-pool depth. Thus, changes in the absorptivity for a specific laser and material can be attributed primarily to changes in surface temperature. The laser spot size for the cases in batch 3 is intentionally chosen smaller than that for the cases in batch 1 and 2 to achieve high values of power-density, resulting in significant vaporisation of the material and melt-pool surface deformations compared to its depth. For all three batches, the results obtained using the enhanced absorption model are compared with those obtained using a constant absorptivity. Figure 6.7 shows the numerically predicted melt-pool dimensions obtained for different laser powers using CO_2 and Nd:YAG lasers (*i.e.* cases in batch 1 and 2). The melt-pool dimensions obtained using the variable absorptivity model are compared with those obtained using different constant values of the absorptivity. For cases in batch 1 and 2, the power density is too low to cause significant vaporisation and surface deformations are small compared to the melt-pool depth. Thus, changes in the absorptivity for a specific laser and material can be attributed primarily to changes in surface temperature (see figure 3.1).

For the cases where the CO_2 laser was employed (figure 6.7(a–c)), melt-pool dimensions predicted using a constant absorptivity between 0.12 and 0.14 seem to agree with those obtained using the variable absorptivity model. However, the results suggest that employing a constant absorptivity does not necessarily render all the melt-pool dimensions with the same level of accuracy, which means the results are less reliable with respect to those obtained using the variable absorptivity model. This can be attributed to the fact that changes in local energy absorption due to changes in surface temperature, and changes in total energy absorption over time are both neglected when a constant absorptivity is employed. Surface temperature in the spot region after reaching a quasi-steady-state condition for CO_2 laser melting with a laser power of $\mathcal{P} = 2100\,\mathrm{W}$ ranges between 1900 K and 2650 K, resulting in absorptivities that range between 0.130 and 0.136 according to the variable absorptivity model and in agreement with the results shown in figure 6.7(a–c). Although a good agreement between numerical and experimental melt-pool dimensions might be achievable using a constant absorptivity model, the use of a constant absorptivity requires a *posteriori* fitting of the absorptivity value to the experiments, whereas such a fitting is not required employing the variable absorptivity model described in section 3.3.

The results shown in figure 6.7 suggest that for a certain set of process parameters, a lower laser power is required to obtain a melt-pool with similar dimensions using an Nd:YAG laser with an emission wavelength of $\lambda = 1.064 \times 10^{-6}\,\mathrm{m}$ than a CO_2 laser with an emission wavelength of $\lambda = 1.060 \times 10^{-5}\,\mathrm{m}$. This arises because the absorptivity for a CO_2 laser is generally lower than that for an Nd:YAG laser when the incident angle is too small to affect the absorptivity significantly ($\theta < 40°$, as is suggested by the data shown in figure 3.1), which is the case in conduction-mode laser melting. For the cases where the Nd:YAG laser was employed (figure 6.7(d–f)), using a constant absorptivity of 0.35 can render the melt-pool dimensions with a reasonable resolution. When an Nd:YAG laser

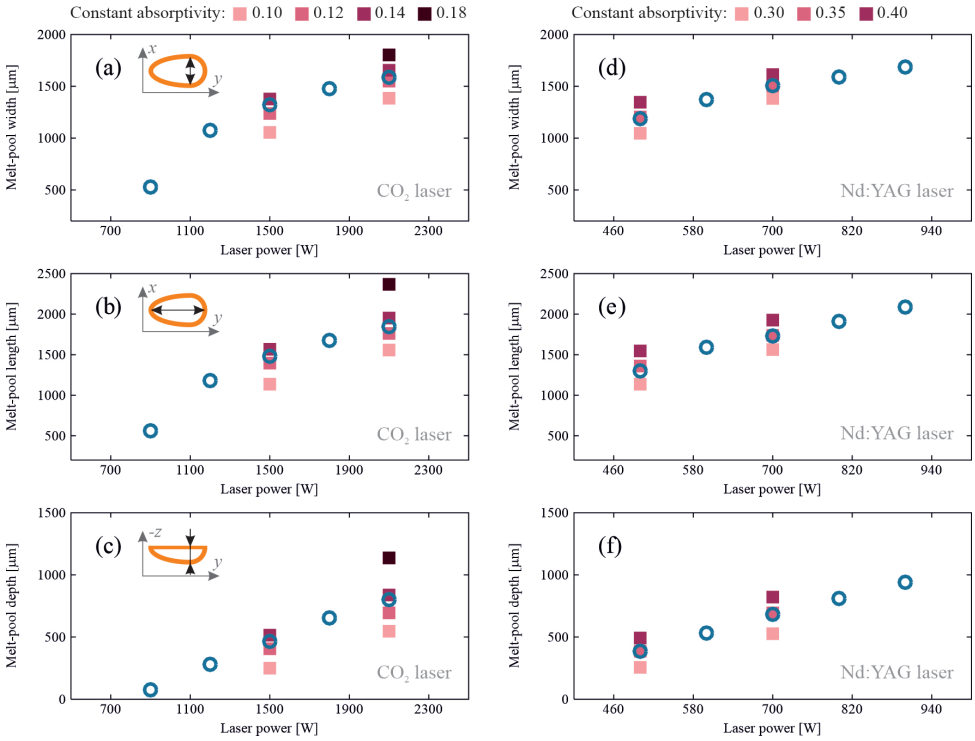

Figure 6.7: Melt-pool dimensions obtained from the present computational model using variable absorptivity (circles) and constant absorptivity (squares) for different laser powers and laser systems ((a–c) CO_2 laser ($\lambda = 1.060 \times 10^{-5}$ m) and (d–f) Nd:YAG laser ($\lambda = 1.064 \times 10^{-6}$ m)). Travel speed $\mathcal{V}$ was set to $10^{-2}\,\mathrm{m\,s^{-1}}$ for all the cases.

with a laser power of $\mathcal{P} = 700$ W is employed, numerically predicted surface temperature in the spot region after reaching a quasi-steady-state condition ranges between 1900 K and 2600 K. For this temperature range, the absorptivity varies between 0.347 and 0.36 according to the variable absorptivity model, and its arithmetic average 0.354 is close to 0.35. Since the melt-pool surface temperature and its distribution are not known *a priory* and are significantly influenced by the process parameters as well as the complex internal molten metal flow, running trial-and-error tests is indispensable to calibrate the value of constant absorptivity. Running such trial-and-error tests increases the total costs of computational analyses and such *ad hoc* calibration often lacks generality.

Figure 6.8 shows the numerically predicted melt-pool shapes obtained using both variable and constant absorptivity models for a fibre laser with an emission wavelength of $\lambda = 1.070 \times 10^{-6}$ m (*i.e.* cases in batch 3). The power density for the cases in batch 3 is relatively high, resulting in significant vaporisation of the material and melt-pool surface deformations compared to its depth. In contrast to the cases in batch 1 and 2, the absorptivity for the cases in batch 3 are affected by both temperature and incident angle of the laser beam (see figure 3.1).

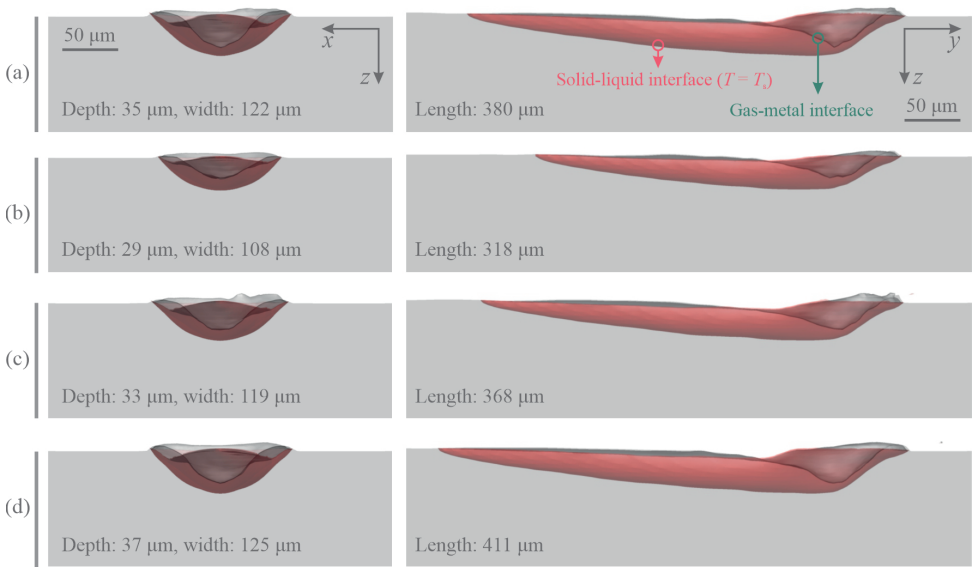

Figure 6.8: Melt-pool shapes obtained from the present computational model for different cases in batch 3 (fibre laser ($\lambda = 1.070 \times 10^{-6}$ m), $\mathcal{P} = 200$ W, spot size $d_b = 1.1 \times 10^{-4}$ m and travel speed $\mathcal{V} = 1.5\,\mathrm{m\,s^{-1}}$). (a) variable absorptivity, (b) constant absorptivity $a = 0.30$, (c) $a = 0.35$ and (d) $a = 0.40$.

The results presented in figure 6.8 show an agreement between the melt-pool dimensions predicted using a constant absorptivity of 0.35 and those obtained using the variable absorptivity model. For the cases in batch 3, surface temperature in the laser spot region ranges roughly from 800 K (because of the relatively high travel speed, the material is in the solid state in front part of the laser spot region) to the boiling temperature of 3086 K corresponding to absorptivities between 0.30 and 0.37 (with an arithmetic average of 0.335) based on the variable absorptivity model for $\theta = 0°$. Demonstrably, reducing the absorptivity from 0.35 to 0.335 decreases the total amount of energy absorbed by the material, resulting in smaller melt-pool dimensions than those predicted using the variable absorptivity model. The increase in local energy absorption due to the increase in temperature and laser incident angle is neglected when a constant absorptivity model is employed. For the cases in batch 3, the incident angle of the laser beam θ increases from 0° to 50° with melt-pool surface depression, resulting in an increase in the local energy absorption according to the variable absorptivity model and in turn increases the melt-pool surface temperature, which leads to further increase in absorptivity. Eventually, the material reaches the boiling temperature and vaporisation limits further increase of melt-pool surface temperature. Variations of total energy input and energy-density distribution due to dynamic changes of surface temperature and morphology affect material vaporisation and thus the recoil pressure that is responsible for melt-pool surface depression. Consequently, these effects cannot be described adequately when a constant absorptivity model is employed in numerical simulations of laser welding and additive manufacturing.

Modelling such phenomena with sufficient accuracy is crucial in numerical simulations of transition from conduction to keyhole mode laser melting as well as those developed to predict solidification microstructure and texture.

6.5.3. Thermal and fluid flow fields

Soon after exposing the material to laser radiation, a melt pool forms and grows over time and if the boundary conditions allow, reaches a quasi-steady-state condition. Figure 6.9 shows the thermal and fluid flow fields over the melt-pool surface at different time instances after reaching the quasi-steady-state condition during laser melting using an Nd:YAG laser ($\lambda = 1.064 \times 10^{-6}\,\mathrm{m}$) with different laser powers. The temperature gradient induced over the surface generates Marangoni shear forces that drive molten metal flow. The molten metal moves from the cold regions adjacent to the melt-pool rim towards the central part of the pool while absorbing energy from the laser beam. This agrees well with experimental observations and discussions reported by Mills *et al.* [42] for stainless steel alloys. The absorbed energy advects with the flow and diffuses through the material into the surrounding solid regions. As the material absorbs energy, surface temperature increases and if the power-density is high enough, the surface temperature reaches a critical value at which the sign of the temperature gradient of surface tension ($\mathrm{d}\gamma/\mathrm{d}T$) changes (see figure 6.2(e)), resulting in a change in flow direction. Interactions between the inward and the outward streams result in a complex flow pattern in the pool that is inherently unsteady and three-dimensional [8, 43]. Two vortices are observed over the melt-pool surface close to the hot spot, generating an asymmetric flow pattern that fluctuates around the centre-line of the pool. This fluid motion forms a rotational flow pattern in the pool that transfers the absorbed heat from the surface to the bottom of the pool [44]. Because of this rotational fluid motion, an element of molten metal volume may move from one side of the pool to the other side, resulting in a cross-cellular flow [45] that enhances mixing in the pool. Maximum fluid velocity in the pool reach values of about $0.6\,\mathrm{m\,s^{-1}}$, corresponding to a Péclet number ($\mathrm{Pe} = \rho c_\mathrm{p} \mathscr{D} \|\mathbf{u}\| / k$) in the order of $\mathcal{O}(100)$ that indicates the significant contribution of advection to the total energy transfer. Molten metal flow in the pool disturbs the thermal field and in turn affects the absorptivity and Marangoni forces. A similar flow pattern is observed over the surface when a CO_2 laser is employed, and representative results are provided in the supplementary materials.

Figure 6.10 shows a time series of numerically predicted thermal and fluid flow fields over the melt-pool surface after reaching the quasi-steady-state condition during laser melting using a fibre laser ($\lambda = 1.070 \times 10^{-6}\,\mathrm{m}$) with a laser power of $\mathscr{P} = 200\,\mathrm{W}$ and a travel speed of $\mathscr{V} = 1.5\,\mathrm{m\,s^{-1}}$. In this case, three distinctive regions are identified: a region with significant surface depression under the effect of recoil pressure, a trailing region characterised by low fluid velocities (less than $0.2\,\mathrm{m\,s^{-1}}$) and temperature (less than 1750 K), and a transition zone in between. A similar choice of subdivision is reported by Khairallah *et al.* [46] to describe the anatomy of a melt track in selective laser melting of a powder bed, where the surface tension temperature gradient ($\mathrm{d}\gamma/\mathrm{d}T$) was assumed to be a negative constant value. Because of the relatively high laser power-density, surface temperature in the spot region increases rapidly and reaches the boiling temperature T_b, leading to significant material vaporisation and increase in recoil pressure that locally deforms the melt-pool surface. Beneath the front part of the depressed region, a relatively

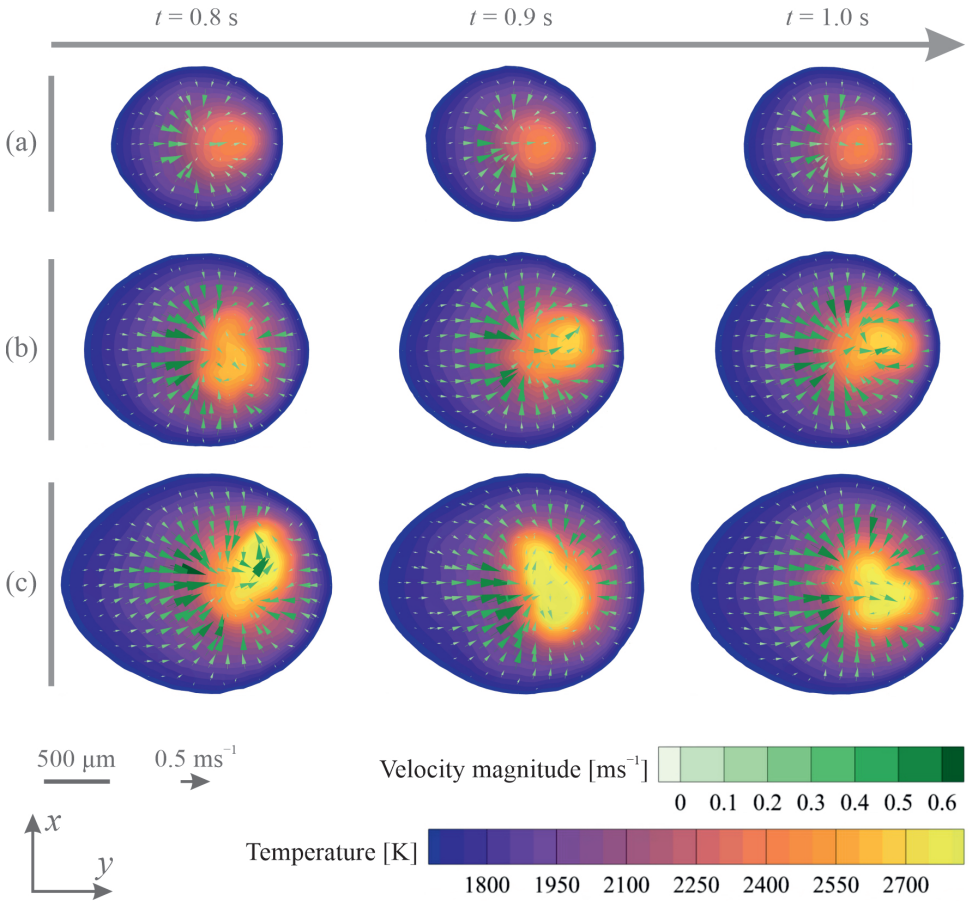

Figure 6.9: Evolution of thermal and fluid flow fields over the melt-pool surface during laser melting of stainless steel 316L with different laser powers. (a) $\mathcal{P} = 500\,\mathrm{W}$, (b) $\mathcal{P} = 700\,\mathrm{W}$, and (c) $\mathcal{P} = 900\,\mathrm{W}$. The variable absorptivity model is utilised. Cases belong to batch 2, where an Nd:YAG laser ($\lambda = 1.064 \times 10^{-6}\,\mathrm{m}$) is employed with a travel speed of $10^{-2}\,\mathrm{m\,s^{-1}}$.

thin layer of molten metal exists as shown in figure 6.8. The maximum molten metal velocity over the surface in the depressed region is about $6\,\mathrm{m\,s^{-1}}$ due to the large temperature gradients, forming a multi-cellular flow pattern in the thin molten metal layer due to Marangoni flow instabilities [45]. The maximum molten metal velocity predicted for cases in batch 3 is higher than that for cases in batch 1 and 2. This is primarily attributed to larger temperature gradients induced over the surface, increasing the magnitude of Marangoni shear force. Moreover, for temperatures above a critical value at which the sign of the temperature gradient of surface tension ($\mathrm{d}\gamma/\mathrm{d}T$) changes from positive to negative (see figure 6.2(e)), the absolute value of the temperature gradient of surface tension increases with temperature, increasing the magnitude of Marangoni force applied to the molten material. Due to the recoil pressure and the outward fluid motion on the surface,

molten metal accumulates ahead of the depressed region, which is also observed experimentally by Nakamura *et al.* [47] and simulated numerically by Khairallah *et al.* [1, 46]. Elements of the accumulated liquid volume can be ejected from the pool and form spatters as shown in figure 6.10(a and c). Spatters are small compared to the melt-pool volume and generally cool down during their flight and thus do not have sufficient thermal energy to melt the substrate and stick to the surface. Molten metal moves from the central region of the depressed region towards the melt-pool rim and transfers the heat absorbed from the laser. This fluid velocity corresponds to a Péclet number (Pe) in the order of $\mathcal{O}(100)$, which is similar to the conduction-mode laser melting. Molten metal moving from the depressed region towards the rear part of the pool meets an inward flow in the transition region, resulting in the formation of two vortices over the surface. In the transition region, surface temperature is less than the critical temperature at which the sign of the temperature gradient changes (see figure 6.2(e)), thus the surface tension increases with increasing the temperature (*i.e.* $\mathrm{d}\gamma/\mathrm{d}T > 0$) in the transition region, resulting in a fluid motion from the cold to the hot regions. In the trailing region, temperature gradients are too small to generate significant Marangoni forces to drive the molten metal flow, and thus thermal diffusion dominates the energy transfer.

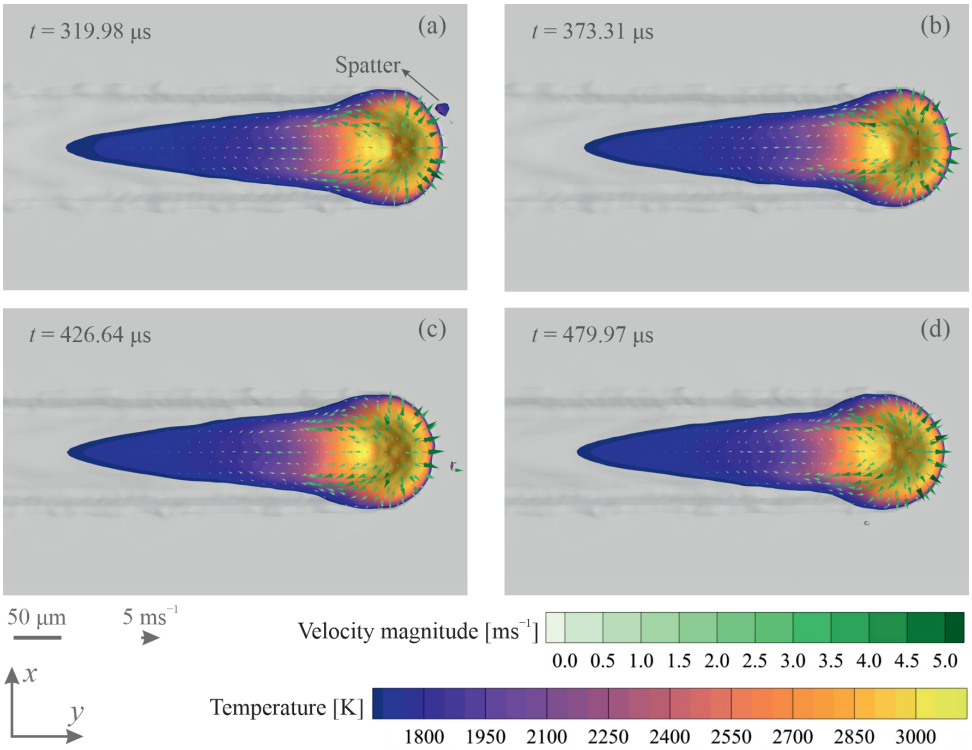

Figure 6.10: Evolution of thermal and fluid flow fields over the melt-pool surface during laser melting of stainless steel 316L using a fibre laser ($\lambda = 1.070 \times 10^{-6}$ m) with a laser power of $\mathcal{P} = 200$ W and a travel speed of $1.5\,\mathrm{m\,s^{-1}}$. The case belong to batch 3 and the variable absorptivity model is utilised.

6.6. Conclusions

The influence of laser characteristics on internal molten metal flow in laser-beam melting of a metallic substrate was investigated numerically using a high-fidelity three-dimensional model. An enhanced absorption model that accounts for laser emission wavelength, surface temperature, laser-beam incident angle and material composition was utilised in the model, and the results compared with experimental measurements as well as numerical data predicted using a constant absorption model. The physics of complex heat and molten metal flow in laser melting is described for various test cases with different laser powers, laser emission wavelengths, and power-density distributions.

For conduction-mode laser melting, where surface deformations are small compared to the melt-pool depth, the absorptivity changes primarily because of changes in surface temperature. However, for cases that surface deformations are significant with respect to the melt-pool depth, changes in the absorptivity are affected by both the surface temperature and the laser-beam incident angle. Changes in the absorptivity affect energy-density distribution over the surface and hence the thermal field over the melt-pool surface, which in turn can influence the Marangoni-driven molten metal flow as well as the distribution of recoil pressure over the surface. These physical processes are tightly coupled to one another, resulting in highly non-linear responses to changes in process parameters.

For laser melting processes with a relatively low power density using a CO_2 or fibre transmissible laser (with an emission wavelength close to 1 µm), the molten metal velocities and surface deformations are relatively small. Because of the small incident angle, the absorptivity for a CO_2 laser is lower than that for an Nd:YAG laser; thus, a lower laser power is required to obtain a melt-pool with similar dimensions using an Nd:YAG laser as compared to a CO_2 laser. Switching to a relatively high power density laser melting process, molten metal velocities increase compared to the low power density processes. For sufficiently high power densities, melt-pool surface deformations become significant, resulting in strongly enhanced laser absorption which in turn further enhances metal vaporisation.

The results of the present work demonstrate that the coupling between these physical processes cannot be rendered with sufficient resolution employing a constant absorptivity model, reducing the range of predictability of the computational models developed to describe the dynamics of melt-pool behaviour in laser welding and additive manufacturing. Moreover, considering absorptivity as a calibration parameter in computational models necessitates trial-and-error simulations, which increases the total costs of computational analyses.

Although the focus of the present work is primarily on laser melting of bare metallic substrates without powder layers, the fundamental laser-matter interaction mechanisms described here are similar to those in laser melting of powder beds. The enhanced laser-absorptivity model employed in the present work can also be utilised in numerical simulations of melt-pool behaviour in laser melting of powder beds, provided that multiple reflections are included in the model.

References

[1] Khairallah, S. A., Martin, A. A., Lee, J. R. I., Guss, G., Calta, N. P., Hammons, J. A., Nielsen, M. H., Chaput, K., Schwalbach, E., Shah, M. N., Chapman, M. G., Willey, T. M., Rubenchik, A. M., Anderson, A. T., Wang, Y. M., Matthews, M. J., and King, W. E. Controlling interdependent meso-nanosecond dynamics and defect generation in metal 3D printing. *Science*, 368(6491): 660–665, 2020. doi:10.1126/science.aay7830.

[2] Markl, M. and Körner, C. Multiscale modeling of powder bed–based additive manufacturing. *Annual Review of Materials Research*, 46(1):93–123, 2016. doi:10.1146/annurev-matsci-070115-032158.

[3] Ebrahimi, A., Kleijn, C. R., and Richardson, I. M. A simulation-based approach to characterise melt-pool oscillations during gas tungsten arc welding. *International Journal of Heat and Mass Transfer*, 164:120535, 2021. doi:10.1016/j.ijheatmasstransfer.2020.120535.

[4] Francois, M. M., Sun, A., King, W. E., Henson, N. J., Tourret, D., Bronkhorst, C. A., Carlson, N. N., Newman, C. K., Haut, T., Bakosi, J., Gibbs, J. W., Livescu, V., Wiel, S. A. V., Clarke, A. J., Schraad, M. W., Blacker, T., Lim, H., Rodgers, T., Owen, S., Abdeljawad, F., Madison, J., Anderson, A. T., Fattebert, J.-L., Ferencz, R. M., Hodge, N. E., Khairallah, S. A., and Walton, O. Modeling of additive manufacturing processes for metals: Challenges and opportunities. *Current Opinion in Solid State and Materials Science*, 21(4):198–206, 2017. doi:10.1016/j.cossms.2016.12.001.

[5] DebRoy, T., Mukherjee, T., Wei, H. L., Elmer, J. W., and Milewski, J. O. Metallurgy, mechanistic models and machine learning in metal printing. *Nature Reviews Materials*, 6(1):48–68, 2020. doi:10.1038/s41578-020-00236-1.

[6] Cook, P. S. and Murphy, A. B. Simulation of melt pool behaviour during additive manufacturing: Underlying physics and progress. *Additive Manufacturing*, 31:100909, 2020. doi:10.1016/j.addma.2019.100909.

[7] Simonds, B. J., Tanner, J., Artusio-Glimpse, A., Williams, P. A., Parab, N., Zhao, C., and Sun, T. The causal relationship between melt pool geometry and energy absorption measured in real time during laser-based manufacturing. *Applied Materials Today*, 23:101049, 2021. doi:10.1016/j.apmt.2021.101049.

[8] Ebrahimi, A., Kleijn, C. R., and Richardson, I. M. Numerical study of molten metal melt pool behaviour during conduction-mode laser spot melting. *Journal of Physics D: Applied Physics*, 54:105304, 2021. doi:10.1088/1361-6463/abca62.

[9] Ebrahimi, A., Kleijn, C. R., Hermans, M. J. M., and Richardson, I. M. The effects of process parameters on melt-pool oscillatory behaviour in gas tungsten arc welding. *Journal of Physics D: Applied Physics*, 54(27):275303, 2021. doi:10.1088/1361-6463/abf808.

[10] Xie, J., Kar, A., Rothenflue, J. A., and Latham, W. P. Temperature-dependent absorptivity and cutting capability of CO_2, Nd:YAG and chemical oxygen–iodine lasers. *Journal of Laser Applications*, 9(2):77–85, 1997. doi:10.2351/1.4745447.

[11] Mahrle, A. and Beyer, E. Theoretical aspects of fibre laser cutting. *Journal of Physics D: Applied Physics*, 42(17):175507, 2009. doi:10.1088/0022-3727/42/17/175507.

[12] Ren, Z., Zhang, D. Z., Fu, G., Jiang, J., and Zhao, M. High-fidelity modelling of selective laser melting copper alloy: Laser reflection behavior and thermal-fluid dynamics. *Materials & Design*, 207:109857, 2021. doi:10.1016/j.matdes.2021.109857.

[13] Yang, Z., Bauereiß, A., Markl, M., and Körner, C. Modeling laser beam absorption of metal alloys at high temperatures for selective laser melting. *Advanced Engineering Materials*, page 2100137, 2021. doi:10.1002/adem.202100137.

[14] Shu, Y., Galles, D., Tertuliano, O. A., McWilliams, B. A., Yang, N., Cai, W., and Lew, A. J. A critical look at the prediction of the temperature field around a laser-induced melt pool on metallic substrates. *Scientific Reports*, 11(1), 2021. doi:10.1038/s41598-021-91039-z.

[15] Kidess, A., Kenjereš, S., Righolt, B. W., and Kleijn, C. R. Marangoni driven turbulence in high energy surface melting processes. *International Journal of Thermal Sciences*, 104:412–422, 2016. doi:10.1016/j.ijthermalsci.2016.01.015.

[16] Grange, D., Queva, A., Guillemot, G., Bellet, M., Bartout, J.-D., and Colin, C. Effect of processing parameters during the laser beam melting of Inconel 738: Comparison between simulated and experimental melt pool shape. *Journal of Materials Processing Technology*, 289:116897, 2021. doi:10.1016/j.jmatprotec.2020.116897.

[17] De, A. and DebRoy, T. A smart model to estimate effective thermal conductivity and viscosity in the weld pool. *Journal of Applied Physics*, 95(9):5230–5240, 2004. doi:10.1063/1.1695593.

[18] King, W. E., Anderson, A. T., Ferencz, R. M., Hodge, N. E., Kamath, C., Khairallah, S. A., and Rubenchik, A. M. Laser powder bed fusion additive manufacturing of metals; physics, computational, and materials challenges. *Applied Physics Reviews*, 2(4):041304, 2015. doi:10.1063/1.4937809.

[19] Khairallah, S. A. and Anderson, A. Mesoscopic simulation model of selective laser melting of stainless steel powder. *Journal of Materials Processing Technology*, 214(11):2627–2636, 2014. doi:10.1016/j.jmatprotec.2014.06.001.

[20] Indhu, R., Vivek, V., Sarathkumar, L., Bharatish, A., and Soundarapandian, S. Overview of laser absorptivity measurement techniques for material processing. *Lasers in Manufacturing and Materials Processing*, 5(4):458–481, 2018. doi:10.1007/s40516-018-0075-1.

[21] Svetlizky, D., Das, M., Zheng, B., Vyatskikh, A. L., Bose, S., Bandyopadhyay, A., Schoenung, J. M., Lavernia, E. J., and Eliaz, N. Directed energy deposition (DED) additive manufacturing: Physical characteristics, defects, challenges and applications. *Materials Today*, 2021. doi:10.1016/j.mattod.2021.03.020.

[22] Trapp, J., Rubenchik, A. M., Guss, G., and Matthews, M. J. In situ absorptivity measurements of metallic powders during laser powder-bed fusion additive manufacturing. *Applied Materials Today*, 9:341–349, 2017. doi:10.1016/j.apmt.2017.08.006.

[23] Ready, J. *Industrial applications of lasers*. Academic Press, San Diego, 2nd edition, 1997. ISBN 9780125839617.

[24] Katayama, S. *Handbook of laser welding technologies*. Woodhead Publishing Limited, Philadelphia, PA, 2013. ISBN 9780857092649.

[25] Kouraytem, N., Li, X., Cunningham, R., Zhao, C., Parab, N., Sun, T., Rollett, A. D., Spear, A. D., and Tan, W. Effect of laser-matter interaction on molten pool flow and keyhole dynamics. *Physical Review Applied*, 11(6):064054, 2019. doi:10.1103/physrevapplied.11.064054.

[26] Lvovsky, A. I. Fresnel equations. In *Encyclopedia of Optical and Photonic Engineering*. CRC Press, Boca Raton, Florida, 2nd edition, 2015. ISBN 9781351247184.

[27] Bass, M. *Laser materials processing*. Elsevier Science, Amsterdam, North-Holland, 1983. ISBN 9780444863966.

[28] Simonds, B. J., Sowards, J., Hadler, J., Pfeif, E., Wilthan, B., Tanner, J., Harris, C., Williams, P., and Lehman, J. Time-resolved absorptance and melt pool dynamics during intense laser irradiation of a metal. *Physical Review Applied*, 10(4):044061, 2018. doi:10.1103/physrevapplied.10.044061.

[29] Ujihara, K. Reflectivity of metals at high temperatures. *Journal of Applied Physics*, 43(5): 2376–2383, 1972. doi:10.1063/1.1661506.

[30] Wang, D. and Lu, H. Numerical analysis of internal flow of molten pool in pulsed gas tungsten arc welding using a fully coupled model with free surface. *International Journal of Heat and Mass Transfer*, 165:120572, 2021. doi:10.1016/j.ijheatmasstransfer.2020.120572.

[31] Sahoo, P., Debroy, T., and McNallan, M. J. Surface tension of binary metal—surface active solute systems under conditions relevant to welding metallurgy. *Metallurgical Transactions B*, 19(3):483–491, 1988. doi:10.1007/bf02657748.

[32] Saldi, Z. S. *Marangoni driven free surface flows in liquid weld pools*. PhD dissertation, Delft University of Technology, Delft University of Technology, 2012.

[33] Kim, C. S. Thermophysical properties of stainless steels. Technical Report ANL-75-55, Illinois, United States, 1975.

[34] Mills, K. C. Fe-316 stainless steel. In *Recommended Values of Thermophysical Properties for Selected Commercial Alloys*, pages 135–142. Elsevier, 2002. doi:10.1533/9781845690144.135.

[35] Pichler, P., Simonds, B. J., Sowards, J. W., and Pottlacher, G. Measurements of thermophysical properties of solid and liquid NIST SRM 316L stainless steel. *Journal of Materials Science*, 55 (9):4081–4093, 2019. doi:10.1007/s10853-019-04261-6.

[36] *Release 19.2*. ANSYS Fluent. URL: `https://www.ansys.com/`.

[37] Ebrahimi, A., Kleijn, C. R., and Richardson, I. M. The influence of surface deformation on thermocapillary flow instabilities in low Prandtl melting pools with surfactants. In *Proceedings of the 5th World Congress on Mechanical, Chemical, and Material Engineering*. Avestia Publishing, 2019. doi:10.11159/htff19.201.

[38] Patankar, S. V. *Numerical Heat Transfer and Fluid Flow*. Taylor & Francis Inc, 1st edition, 1980. ISBN 0891165223.

[39] Issa, R. I. Solution of the implicitly discretised fluid flow equations by operator-splitting. *Journal of Computational Physics*, 62(1):40–65, 1986. doi:10.1016/0021-9991(86)90099-9.

[40] Ubbink, O. *Numerical Prediction of Two Fluid Systems with Sharp Interfaces*. PhD dissertation, Imperial College London (University of London), London, United Kingdom, 1997. URL: `http://hdl.handle.net/10044/1/8604`.

[41] Kell, J., Tyrer, J., Higginson, R., Thomson, R., Jones, J., and Noden, S. Holographic diffractive optical elements allow improvements in conduction laser welding of steels. In *International Congress on Applications of Lasers & Electro-Optics*. Laser Institute of America, 2006. doi:10.2351/1.5060749.

[42] Mills, K. C., Keene, B. J., Brooks, R. F., and Shirali, A. Marangoni effects in welding. *Philosophical Transactions of the Royal Society A: Mathematical, Physical and Engineering Sciences*, 356(1739): 911–925, 1998. doi:10.1098/rsta.1998.0196.

[43] Kidess, A., Kenjereš, S., and Kleijn, C. R. The influence of surfactants on thermocapillary flow instabilities in low Prandtl melting pools. *Physics of Fluids*, 28(6):062106, 2016. doi:10.1063/1.4953797.

[44] Zhao, C. X., Kwakernaak, C., Pan, Y., Richardson, I. M., Saldi, Z., Kenjeres, S., and Kleijn, C. R. The effect of oxygen on transitional Marangoni flow in laser spot welding. *Acta Materialia*, 58 (19):6345–6357, 2010. doi:10.1016/j.actamat.2010.07.056.

[45] Schatz, M. F. and Neitzel, G. P. Experiments on thermocapillary instabilities. *Annual Review of Fluid Mechanics*, 33(1):93–127, 2001. doi:10.1146/annurev.fluid.33.1.93.

[46] Khairallah, S. A., Anderson, A. T., Rubenchik, A., and King, W. E. Laser powder-bed fusion additive manufacturing: Physics of complex melt flow and formation mechanisms of pores, spatter, and denudation zones. *Acta Materialia*, 108:36–45, 2016. doi:10.1016/j.actamat.2016.02.014.

[47] Nakamura, H., Kawahito, Y., Nishimoto, K., and Katayama, S. Elucidation of melt flows and spatter formation mechanisms during high power laser welding of pure titanium. *Journal of Laser Applications*, 27(3):032012, 2015. doi:10.2351/1.4922383.

7

Melt Pool Behaviour in Stationary Gas Tungsten Arc Welding

Development, optimisation and qualification of welding and additive manufacturing procedures to date have largely been undertaken on an experimental trial and error basis, which imposes significant costs. Numerical simulations are acknowledged as a promising alternative to experiments, and can improve the understanding of the complex process behaviour. A simulation-based approach is adopted to study and characterise molten metal melt pool oscillatory behaviour during arc welding. A high-fidelity three-dimensional model based on the finite-volume method is implemented that takes into account the effects of surface deformation on arc power-density and force distributions. These factors are often neglected in numerical simulations of welding and additive manufacturing. Utilising this model, the complex molten metal flow in melt pools and associated melt-pool surface oscillations during both steady-current and pulsed-current gas tungsten arc welding (GTAW) are predicted. An analysis based on a wavelet transform was performed to extract the time-frequency content of the displacement signals obtained from numerical simulations. The results confirm that the frequency of oscillations for a fully penetrated melt pool is lower than that of a partially penetrated melt pool with an abrupt change from partial to full penetration. During transition from a partial to a full penetration state, it is found that two dominant frequencies coexist in the time-frequency spectrum. The results demonstrate that melt-pool oscillations profoundly depend on melt-pool shape and convection in the melt pool, which in turn is influenced by process parameters and material properties. The present numerical simulations reveal the unsteady evolution of melt pool oscillatory behaviour that is not predictable from published analytical analyses. Additionally, using the proposed simulation-based approach, the need of triggering the melt-pool oscillations is obviated since even small surface displacements are detectable, which are not sensible to the current measurement devices employed in experiments.

The contents of this chapter have been published in *International Journal of Heat and Mass Transfer*, **2021**, *164*, 120535, DOI: 10.1016/j.ijheatmasstransfer.2020.120535.

7.1. Introduction

Molten metal behaviour during fusion-based welding and additive manufacturing affects energy transport in melt pools, which in turn influences their geometrical evolution [1, 2]. Melt pool behaviour appears to substantially determine the properties, structure and quality of weldments or additively-manufactured products [3]. Correct control of melt pools (*e.g.* penetration, shape and size) is therefore crucial to achieve desirable properties and to reduce the number of failures in production. However, melt pool control is usually a challenging task since its behaviour is characterised by highly non-linear responses to variations in process parameters and material properties [3, 4]. Moreover, limitations of experimental methods in detecting molten metal flow in melt pools coupled with excessive costs of trial-and-error experiments, which are commonly applied in industry to date, pose additional challenges to understanding the melt pool behaviour, and thus to developing effective melt pool control. A promising alternative to trial-and-error experiments is to utilise a simulation-based approach to predict and describe the melt pool behaviour [5], which results in a decrease in the number of experiments required for process development and optimisation.

Molten metal flow in melt pools during welding and additive manufacturing is driven by various forces such as Marangoni, buoyancy, electromagnetic (in case of applying an electric arc or an electron beam) and plasma shear force [2, 6]. These driving forces and the interplay between them coupled with non-linearly varying material properties determine the fluid flow in a melt pool and can generate complex unsteady flow patterns as observed experimentally [7] and visualised numerically [8]. This fluid motion can result in self-excited oscillations of the melt-pool surface that may occur in various modes depending on melt-pool shape and size as well as the surface tension of the molten material [9–11]. Oscillations of the melt-pool surface can also be triggered by exposing the melt pool to external loadings such as welding current pulsation and filler droplet impingement. The melt-pool surface oscillations correlate with process conditions [12] and liquid metal properties [13, 14] and can be utilised to measure, predict and control welding and additive manufacturing processes [15].

The available literature on melt-pool surface oscillations, to a large extent, is experimental and focuses on employing the melt-pool oscillation signals for real-time penetration sensing [16]. The most common experimental techniques for detecting melt-pool surface oscillations are based on the processing of arc voltage [15], arc light-intensity [17] and laser vision [18] recorded during the process. These techniques only render information about the movement of the melt-pool surface and disregard the molten metal flow. Measurement schemes based on sensing the arc voltage or arc light-intensity cannot be employed to reflect local surface movements [19] since the recorded voltages and light intensities are averaged values across the melt pool at any given time during the process. Additionally, the signal-to-noise ratio in measurements decreases with a decrease in the amplitude of melt-pool surface deformations and may result in the obscuration of certain peaks in the frequency spectrum [20]. Numerical simulations, with an adequate level of accuracy, offer considerable potential to improve the current understanding of the pool surface oscillations by describing convection in the melt pool and its influence on geometrical evolution of the melt-pool boundary.

On the basis of a numerical study, Ko *et al.* [21, 22] argued that the direction of

the Marangoni flow affects the oscillations of the melt-pool surface during gas tungsten arc welding (GTAW). In their axisymmetric model, the surface tension of the molten metal was assumed to change linearly with temperature and the surface-tension temperature coefficient was assumed to remain constant (*i.e.* $\partial\gamma/\partial T = \mathscr{C}$, where, $\mathscr{C}$ is a constant value). However, the surface tension of molten materials generally changes non-linearly with temperature if surfactants are present [23], which can locally affect the direction of the Marangoni flow at the melt-pool surface and thus convection and subsequent solid-liquid phase transformations, resulting in complex three-dimensional flow patterns [3, 8, 24]. Cho *et al.* [25] implemented a three-dimensional model to investigate melt-pool oscillations during laser spot melting of titanium, assuming that the surface tension of molten titanium increases linearly with temperature, and stated that the period of oscillations changes during solidification. Huang *et al.* [26] employed a three-dimensional model to study the melt-pool surface oscillations during pulsed-current GTAW and confirmed that the melt-pool oscillation frequency depends on the melt-pool size. Further investigations are required to foster our understanding of the influence of process parameters and material properties on melt pool oscillatory behaviour.

Deformations of the melt-pool surface can alter the surface power density and arc pressure distributions [21] and thus affect the melt-pool oscillatory behaviour. This effect is often neglected in numerical simulations implemented to study the melt-pool dynamic behaviour, where the process is decoupled from the melt pool and is represented as a boundary condition at the gas-metal interface. Additionally, conventional Fourier transform analysis, which requires a sufficiently large sample size to return adequate stationary frequency spectra, is commonly employed to extract the frequency characteristics of melt-pool oscillations during fusion-based manufacturing processes [27]. This approach is not meticulously representative due to abrupt changes in the signals.

In the present study, a numerical approach is utilised to predict melt-pool formation, molten metal flow and oscillations of the melt-pool surface during stationary gas tungsten arc welding. Three-dimensional calculations have been performed to study the effects of the process parameters as well as surfactants on melt-pool surface oscillations. The model developed in the present work takes the influence of temporal surface deformations on arc power-density and arc pressure distributions into account, which is physically realistic and can affect the numerically predicted convection in the melt pool and hence the associated melt-pool surface oscillations. Using the time-resolved data obtained from the numerical simulations, time-frequency analysis is conducted to enhance the understanding of melt-pool oscillatory behaviour. The present study elucidates molten metal oscillations during arc welding and arc-based additive manufacturing and offers an enhanced simulation-based approach to process development and optimisation. The proposed approach provides detailed information on molten metal flow in weld pools and the evolution of melt pool oscillatory behaviour.

7.2. Problem description

Gas tungsten arc welding of a stainless steel (AISI 304) plate with a thickness of $H_{\mathrm{m}} = 3\,\mathrm{mm}$, as shown schematically in figure 7.1, is investigated numerically and results are reported in the present chapter. Both steady current and pulsed current conditions (with different current pulsation frequencies) are studied. An electric arc plasma generates the power

required to heat and melt the base material that is initially at an ambient temperature of $T_0 = 300\,\mathrm{K}$. The distance between the electrode tip and the nominal plate top-surface (*i.e.* the arc length, ℓ) is set to 2.5 mm before igniting the arc; however, arc length obviously changes as the melt-pool surface deforms. Changes in the arc length $\Delta\ell$ result in variations of the electric arc voltage ΔU and thus the arc power and power-density distribution as well as the forces induced by the arc plasma [28, 29]. These variations are accounted for in the present model by adjusting the source terms dynamically as described in section 3.2.2. The arc plasma is decoupled from the melt pool to reduce simulation complexity and run-time.

The computational domain in the present study is a rectangular cube that encompasses the base material and two layers of gas with a thickness of $H_a = 2\,\mathrm{mm}$ above and below the sample. The gas layers are included to monitor the melt-pool surface oscillations. The width of the computational domain in the x and y directions is $W = 40\,\mathrm{mm}$, which is considerably larger than the melt pool size. Variation of the surface tension with temperature is modelled using an empirical correlation that takes the influence of surfactants into consideration [23]. The thermophysical properties of the base-material and the gas employed in the numerical simulations are presented in table 7.1.

Table 7.1: Thermophysical properties of the stainless steel (AISI 304) and the gas (argon) employed in the numerical simulations. Values for AISI 304 are taken from [30, 31], and T is in Kelvin.

Property	Stainless steel (AISI 304)	Gas (argon)	Unit
Density ρ	7200	1.623	$\mathrm{kg\,m^{-3}}$
Specific heat capacity c_p	702.24 (solid phase) 806.74 (liquid phase)	520.64	$\mathrm{J\,kg^{-1}\,K^{-1}}$
Thermal conductivity k	$10.865 + 0.014 \cdot T$ (solid phase) $5.5357 + 0.0131 \cdot T$ (liquid phase)	1.58×10^{-2}	$\mathrm{W\,m^{-1}\,K^{-1}}$
Viscosity μ	6.7×10^{-3}	2.12×10^{-5}	$\mathrm{kg\,m^{-1}\,s^{-1}}$
Thermal expansion coefficient β	2.1×10^{-6}	–	$\mathrm{K^{-1}}$
Latent heat of fusion $\mathscr{L}_f$	2.47×10^{5}	–	$\mathrm{J\,kg^{-1}}$
Liquidus temperature T_l	1723	–	K
Solidus temperature T_s	1673	–	K

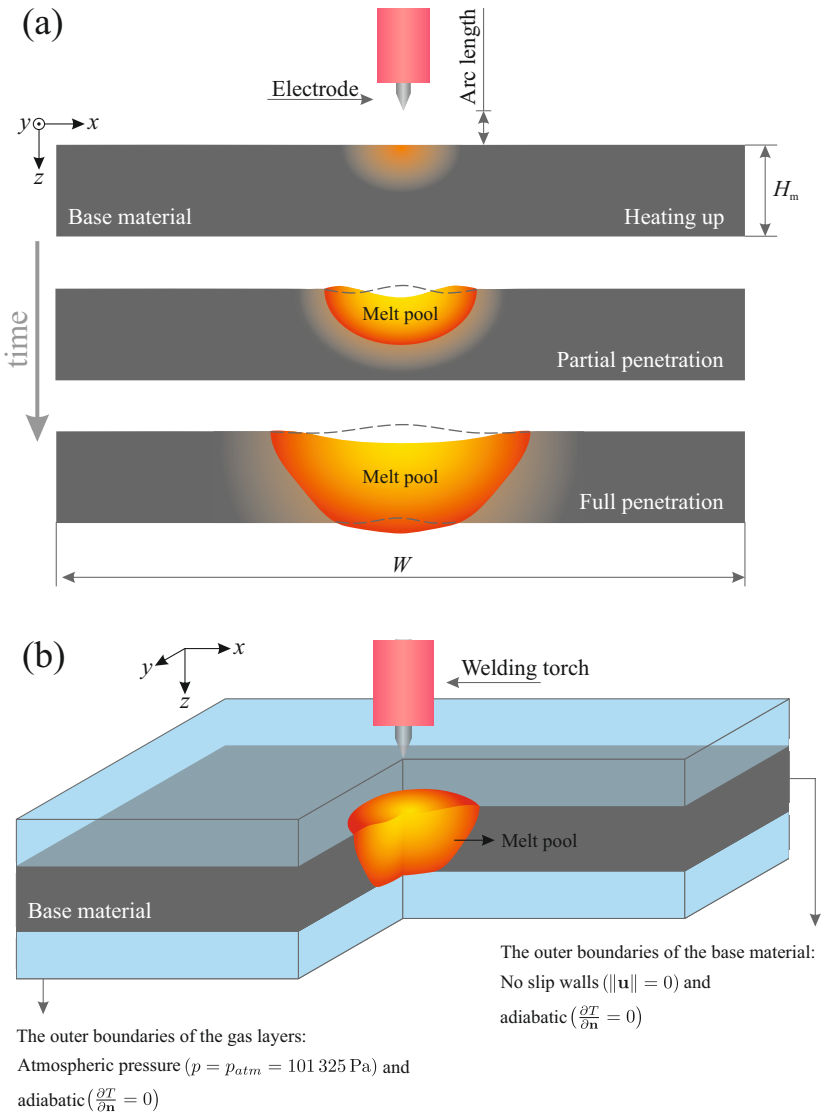

Figure 7.1: Schematic of gas tungsten arc welding (GTAW). (a) After the arc ignition, the heat generated by the electric arc plasma heats the base material and leads to the melt pool formation. The partially-penetrated melt pool can grow over time and forms a fully-penetrated melt pool. The melt-pool surface oscillates during the process, as indicated by the dashed black lines. (b) Schematic of the computational domain and the boundary conditions prescribed in the numerical simulations. One quarter of the domain is clipped for visualisation. Regions shaded in blue show the gas layers.

7.3. Numerical procedure

The model was developed within the framework of the proprietary solver ANSYS Fluent [32] based on the finite-volume approach. The source terms in the momentum and energy equations as well as the temperature-dependent surface-tension model are implemented through user-defined functions. After analysing the sensitivity of numerical predictions to the computational grid size, the computational domain was discretised using non-uniform hexahedral cells with a minimum cell spacing of 35 µm in the melt pool central region close to the gas-metal interface. Cell spacing increases gradually towards the outer boundaries of the computational domain with a maximum cell spacing of 500 µm resulting in a grid with about 3×10^6 cells. The central-differencing scheme with second order accuracy was employed to discretise the diffusion and convection terms in the governing equations, and the transient advection terms were discretised using a first order implicit scheme. The PISO (pressure-implicit with splitting of operators) scheme [33] was utilised to couple velocity and pressure fields, and the PRESTO (pressure staggering option) scheme [34] was employed for the pressure interpolation. The spatial discretisation of the gas-metal interface advection was performed using an explicit compressive VOF formulation [35]. A time-step size of 10^{-5} s was chosen to achieve a Courant number ($\mathrm{Co} = \|\mathbf{u}\|\Delta t/\Delta x$) less than 0.3. Scaled residuals of less than 10^{-7} were defined as the convergence criterion for each time-step. Each case was run in parallel on 40 cores (Intel Xeon E5-2630 v4) of a high-performance computing cluster and took roughly about 500 h to complete.

7.4. Results

In this section, the influence of welding current, current pulsation and surfactants on the melt-pool shape and its oscillatory behaviour during both partial and full penetration conditions are described. To monitor melt-pool surface oscillations, several monitoring points were defined in different locations over the melt-pool surface and displacement signals were recorded at these monitoring points. Signals received from a melt pool during fusion welding and additive manufacturing are generally time-variant and encompass abrupt changes. Therefore, time-frequency analysis based on a wavelet transform is preferred over the conventional Fourier transform analysis [36]. Signals recorded from the monitoring point located at the melt pool surface $p_c\left(x, y, z\right) = (0, 0, z_{\mathrm{surface}})$ in the period of 0.1 s to 3.7 s were utilised for time-frequency analysis and the results are shown in figure 7.2. In case of steady-current GTAW with $I = 110$ A and sulphur content of 240 ppm (figure 7.2(a)), the melt-pool surface starts to oscillate with a fundamental frequency f_0 of about 195 Hz. Other frequencies are also observed in the time-frequency spectrum at $f_1 \approx 1.6 f_0$ and $f_2 \approx 2.3 f_0$, which resemble the oscillation frequencies of a thin circular membrane predicted from analytical analysis [20, 37]. The frequency of oscillations decreases as the melt pool grows under partial penetration and reaches values of $\mathcal{O}(100)$ Hz. It is also found that the amplitude of oscillations increases as the melt pool grows. Oscillations with a frequency of about 40 Hz then appear in the frequency spectrum at $t \approx 2.8$ s, as indicated by arrow in figure 7.2(a), when the melt-pool depth approaches the metal plate thickness (*i.e.* full penetration). Interestingly, there is a period in the time-frequency spectrum ($2.7\,\mathrm{s} < t < 3.5\,\mathrm{s}$) that both high and low frequencies coexist while

the transition from partial to full penetration is occurring. The oscillation frequencies obtained from the numerical simulations agree fairly well with the experimental measurements reported by Li *et al.* [19] and Yu *et al.* [27] and analytical approximations reported by Xiao and den Ouden [12, 15] for stationary GTAW.

Figure 7.2(b) shows the displacement signals obtained from numerical simulations of GTAW with $I = 150$ A and sulphur content of 240 ppm and its corresponding time-frequency spectrum. The melting rate increases with increasing welding current from 110 A to 150 A, which is obvious because of the enhancement of total heat input to the bulk material and fluid velocities induced in the melt pool. Under partial penetration, the melt-pool width grows rapidly due to the outward Marangoni flow and the melt pool oscillates at a frequency of about 200 Hz up to $t \approx 1.75$ s. The first arrow in the frequency spectrum of figure 7.2(b) indicates that from $t \approx 1.8$ s the frequency of oscillations decreases to values of about 125–140 Hz that persists for approximately 0.5 s, during which the increase in the melt-pool depth is more pronounced compared to its width. The second arrow in the frequency spectrum of figure 7.2(b) at $t = 2.2$ s indicates that once the melt pool becomes fully-penetrated ($t \approx 2.4$ s), the melt pool oscillates at frequencies between about 70 Hz and 40 Hz. These observations demonstrate the significant effect of the melt-pool shape and size on oscillatory behaviour.

Figure 7.2(c) shows the frequency spectrum for a pulsed-current GTA weld with a 240 ppm sulphur content. In this case, the melt pool size and shape, as well as flow pattern, changes continuously. During current peaks, the melt pool enlarges, and the melt pool surface depression increases due to augmented arc pressure. In the partial penetration state, after each current peak, the melt pool shrinks and the dominant frequency of oscillations increases with time and reaches values up to $\mathcal{O}(200)$ Hz. However, the dominant frequency of oscillations remains almost constant at about 60 Hz under a full penetration condition ($t > 2.8$ s).

The behaviour of a 150 A steady current weld with a high sulphur (240 ppm) material (figure 7.2b) is compared with the same welding condition on a low sulphur (30 ppm) material (figure 7.2d). The melt pool evolves differently when the sulphur content of the material is lower. In contrast to the cases with 240 ppm sulphur content, after melt pool formation, the fluid flow on the melt-pool surface is directed outward forming a wide and shallow melt pool. Thermocapillary flow instabilities arose in this wide and shallow melt pool, generating an unsteady multi-cellular flow pattern in the melt pool [38] resulting in melt-pool surface deformations that are reflected in the displacement signals and the frequency spectrum, with frequencies of 200–310 Hz up to $t \approx 0.8$ s. Changes in the melt-pool shape lead to the decay of these thermocapillary flow instabilities and the amplitude of melt-pool oscillations diminishes until $t \approx 2$ s. Similar to the other cases described previously and as indicated by dashed lines in the frequency spectrum of figure 7.2(d), the frequency of oscillations decreases as the melt pool grows under partial penetration. Flow instabilities grow again at $t \approx 2.3$ s as the melt-pool depth increases, particularly in the central region, leading to an increase in the amplitude of surface oscillations. With further increase in the melt-pool depth, the frequency of oscillations drops to values of about 30–45 Hz at $t \approx 2.3$ s, which is indicated by an arrow in the frequency spectrum of figure 7.2(d).

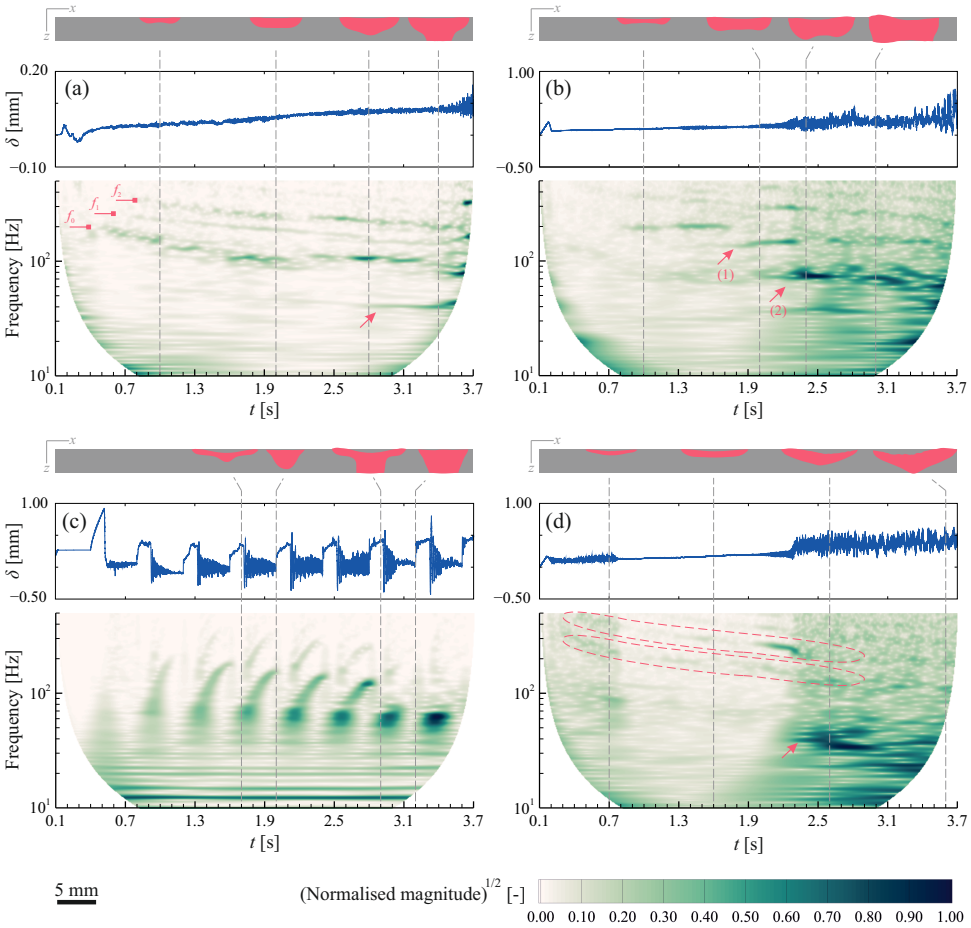

Figure 7.2: Displacement of the melt-pool surface δ recorded from the monitoring point $p_c(x,y) = (0,0)$ and its corresponding time-frequency spectrum. Magnitudes in time-frequency spectra are normalised with the respective maximum magnitude. Cross-sections of the melt pool in the x-y plane are also shown at different time instances. (a) steady current, $I = 110$ A, sulphur content: 240 ppm, (b) steady current, $I = 150$ A, sulphur content: 240 ppm, (c) pulsed current, $I_b = 50$ A, $I_p = 250$ A, current pulsation frequency: 2.5 Hz, duty cycle: 30%, sulphur content: 240 ppm, and (d) steady current, $I = 150$ A, sulphur content: 30 ppm.

7.5. Discussion

The results indicate that melt-pool oscillations strongly depend on melt-pool shape that oscillations are indeed affected by convection in the melt pool. Figure 7.3 shows the melt-pool shape and temperature profiles over the melt-pool surfaces at different time instances during steady-current GTAW ($I = 110$ A and sulphur content of 240 ppm). After arc ignition at $t = 0$ s, the bulk material heats up locally and a melt pool forms that grows over time. The forces applied to the molten metal in the melt pool (*i.e.* Marangoni,

electromagnetic, arc pressure, arc plasma shear and thermal buoyancy forces), drives the molten metal flow and generates a complex three-dimensional flow pattern. This fluid motion transfers the heat absorbed from the heat source to the surrounding solid material. The Péclet number ($\mathrm{Pe} = \mathscr{D}\|\mathbf{u}\|\rho c_\mathrm{p}/k$), which quantifies the ratio of advective to diffusive heat transport, is greater than unity ($\mathscr{O}(100)$) in the melt pool and indicates the remarkable influence of advection on total energy transfer and thus, on the melt-pool shape. Under partial penetration, the maximum temperature in the melt pool increases in time and reaches a quasi steady-state condition; however, it decreases slightly when the melt pool becomes fully penetrated, which in turn affects the average surface tension of the molten material. This decrease in maximum surface temperature is attributed to the flow of colder material from the bottom surface of the melt pool towards its top surface and the increase in the amount of heat loss from the surfaces due to radiation and convection.

Numerical predictions reveal an outward fluid flow from the central region of the melt pool that meets an inward flow from its outer edge. This occurs because of the change in the sign of surface-tension temperature coefficient ($\partial\gamma/\partial T$) at a specific temperature ($T \approx 2115\,\mathrm{K}$ for an Fe–S alloy with a sulphur concentration of 240 ppm, according to the model proposed by Sahoo *et al.* [23]) due to the presence of sulphur in the melt pool that is an active surface agent. The flow direction on the bottom surface of the melt pool is mostly inward, since the temperature over the bottom surface is below the critical temperature of 2115 K. In this case, the maximum local fluid velocities predicted over the melt pool surface for partially penetrated melt pools are about $0.4\,\mathrm{m\,s^{-1}}$, which agrees reasonably with the experimental measurements reported by Aucott *et al.* [3]. Nevertheless, the average bulk fluid velocity in fully penetrated melt pools are larger than those predicted in partially penetrated melt pools.

While the melt pool is partially penetrated, the melt-pool surface is depressed in the central region and is elevated in regions where the inward and outward streams meet each other. The unsteady interactions between these two streams coupled with continuous changes in the melt-pool shape disturb the fluid flow and consequently, the melt-pool surface oscillates with relatively small amplitudes and high frequencies. The amplitude of oscillations increases and the frequency of oscillations decreases as the melt pool grows. Once the melt pool becomes fully penetrated, the flow pattern changes due to Marangoni stresses induced over the lower melt-pool surface and changes in melt pool surface temperature. This change in flow pattern along with changes in the melt-pool shape and the average surface tension of the molten material result in an increase in the amplitude of melt-pool surface oscillations and a decrease in dominant oscillation frequency. The amplitudes of oscillations in a fully-penetrated melt pool appear to be larger in comparison with those of a partially penetrated pool. Changes in the melt-pool surface profile subsequently result in changes in the power available from the arc and its spatial distribution over the melt-pool surface, which enhances flow disturbances.

Figure 7.4 shows the evolution of the melt-pool shape and temperature distribution over its surfaces during steady-current GTAW with $I = 150\,\mathrm{A}$ and sulphur content of 240 ppm. The average heat input to the bulk material increases with increasing welding current from 110 A to 150 A, resulting in a higher melting rate and a larger melt pool.

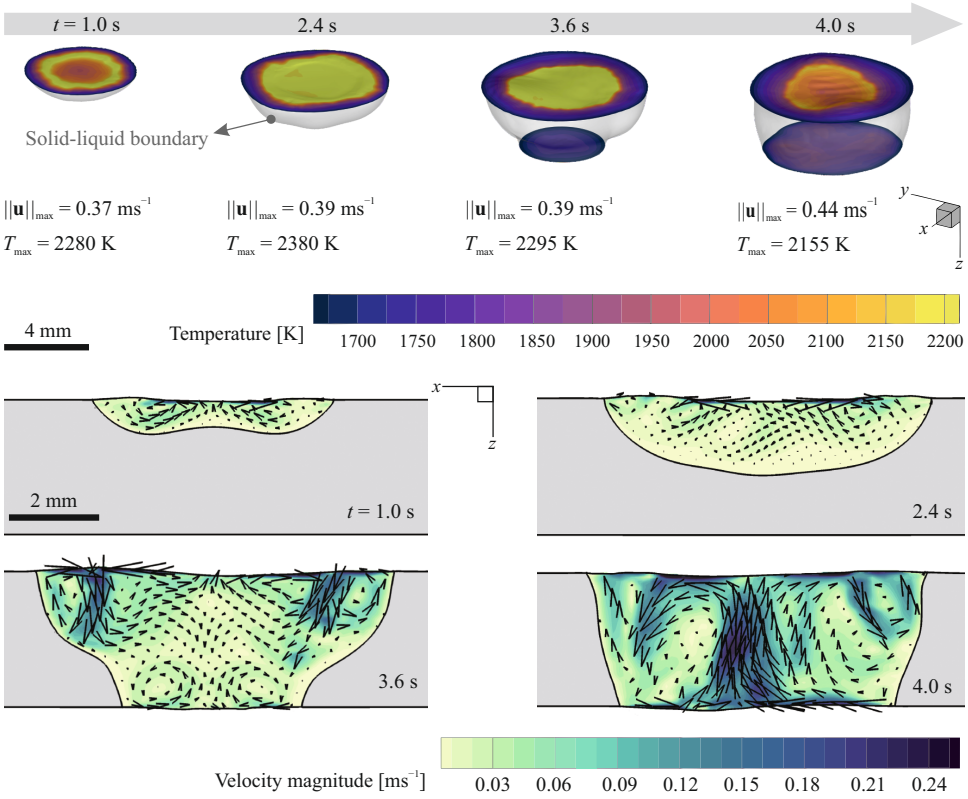

Figure 7.3: Evolution of melt-pool shape and temperature profile over the melt-pool surfaces (3D diagrams), and contours of velocity magnitudes overlaid with velocity vectors (2D diagrams) during steady-current GTAW obtained from numerical simulations. ($I = 110$ A, sulphur content: 240 ppm)

The arc plasma force also increases with increasing the welding current, augmenting the melt-pool surface depression. Although the overall melt pool behaviour of the case with $I = 150$ A looks similar to that of the case with $I = 110$ A, with the same sulphur content of 240 ppm, the amplitudes of oscillations are larger. Additionally, higher fluid velocities up to $\mathcal{O}(0.6)\,\mathrm{m\,s^{-1}}$ under partial penetration and up to $\mathcal{O}(1.2)\,\mathrm{m\,s^{-1}}$ under full penetration are predicted in the melt pool during welding with $I = 150$ A. Since the outer boundaries of the computational domain were assumed to be adiabatic, the melt pool keeps growing and collapses (*i.e.* burns-through) eventually at $t \approx 3.8$ s.

Figure 7.5 shows the evolution of melt-pool shape and temperature profile over its surfaces at different time instances during pulsed-current GTAW of AISI 304 with 240 ppm sulphur content. In this case, the current was pulsed from $I_\mathrm{b} = 50$ A to $I_\mathrm{p} = 250$ A at a frequency of 2.5 Hz and a duty cycle of 30% resulting in an average current of $\bar{I} = 110$ A. During the peak current, the heat input and arc forces applied to the bulk material increase, resulting in an increase in the surface temperature. An outward fluid flow is

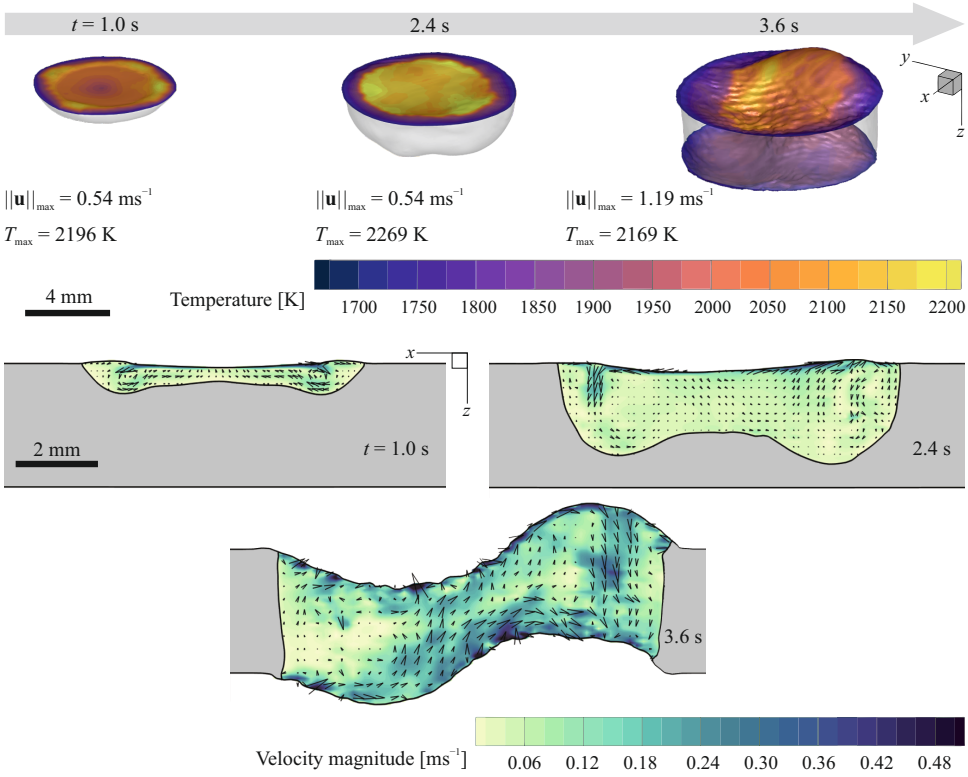

Figure 7.4: Numerical predictions of melt-pool shape and temperature profile over the melt-pool surfaces at different time instances during steady-current GTAW. (I = 150 A, sulphur content: 240 ppm)

observed at the melt pool top surface during peak current that makes the melt pool wider and enhances surface depression in the central region of the melt pool surface. The flow direction at the melt-pool surface reverses during the base current period due to the change in the sign of surface-tension temperature coefficient ($\partial\gamma/\partial T$) from negative to positive, which occurs because of melt-pool surface temperature reduction, resulting in a reduction in the melt-pool width and an increase in its depth. The melt-pool surface oscillates during the base current, and the amplitude of oscillations decays in time until the next current increase. In this chapter, results have been reported for pulsed current welding at one specific pulsation frequency of 2.5 Hz. However, different current pulsation frequencies (1–10 Hz) have also been examined. All general qualitative behaviour discussed here were similarly observed for all studied pulsation frequencies.

The influence of Marangoni flow on melt-pool oscillations was examined by reducing sulphur concentration in the material from 240 ppm to 30 ppm, while the welding current I was set to 150 A (DC mode); the results are presented in figure 7.6. In contrast to the cases with 240 ppm sulphur content, the fluid flow at the melt-pool surface is predominantly directed outward and transfers the heat absorbed from the heat source to the surrounding solid boundary. This leads to the formation of a wide and shallow melt pool, which

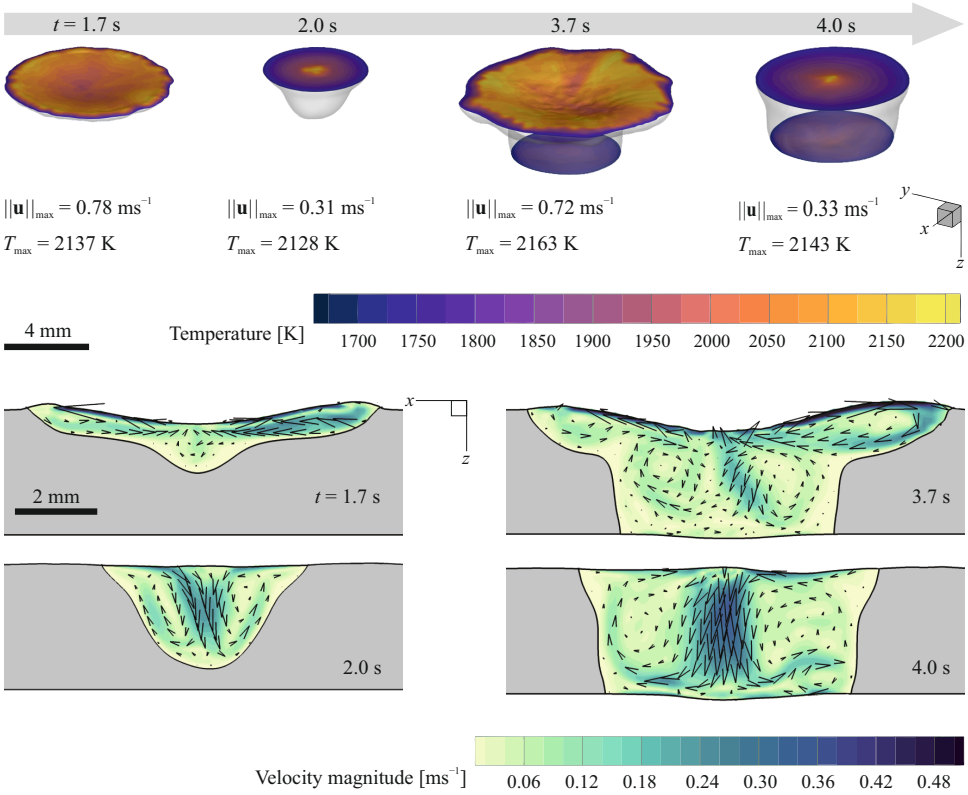

Figure 7.5: Variations of melt-pool shape and temperature profile over the melt-pool surfaces at different time instances (3D diagrams), and contours of velocity magnitudes overlaid with velocity vectors (2D diagrams) during pulsed-current GTAW obtained from numerical simulations. (I_b = 50 A, I_p = 250 A, current pulsation frequency: 2.5 Hz, duty cycle: 30%, sulphur content: 240 ppm)

differs notably from that predicted for the case with a sulphur concentration of 240 ppm (see figure 7.4). Additionally, this outward fluid flow enhances the melt pool depression in the central region. In steady-current GTAW, changes in power-density distribution over the melt pool surface due to surface deformations are more pronounced for the case with 30 ppm sulphur compared with those for the case with 240 ppm sulphur. This results in augmentation of flow disturbances because of changes in temperature distribution and thus Marangoni stresses induced over the melt-pool surface. These effects lead to oscillations with amplitudes that are larger than those predicted for the case with 240 ppm sulphur content.

The melt-pool oscillation frequencies obtained from the simulations are compared with the experimental data reported by Xiao and den Ouden [15] and analytical predictions calculated using the model proposed by the same authors [12, 15] for both partial and full penetration conditions, and the results are shown in figure 7.7. Xiao and den Ouden [15] employed a plate made of AISI 304 with 170 ppm sulphur content and they

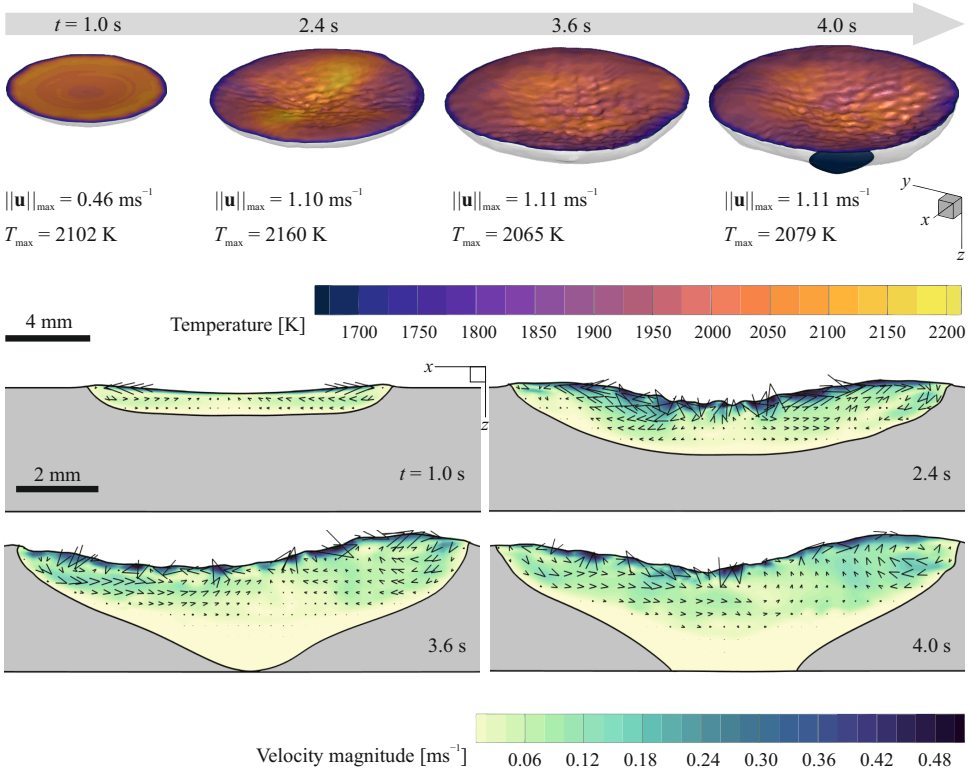

Figure 7.6: Evolution of melt-pool shape and temperature profile over the melt-pool surfaces during steady-current GTAW obtained from numerical simulations. ($I = 150$ A, sulphur content: 30 ppm)

applied a pulsed current with a base current I_b ranging between 70 A and 150 A and a peak current I_p ranging between 100 A and 180 A at a frequency of 25 Hz under partial penetration and 10 Hz under full penetration. The first two modal frequencies of oscillations under partial penetration are calculated from the following equations [15]:

$$\text{Mode 1: } f = 5.84\left(\frac{\bar{\gamma}}{\rho}\right)^{0.5} D_e^{-1.5}, \tag{7.1}$$

$$\text{Mode 2: } f = 3.37\left(\frac{\bar{\gamma}}{\rho}\right)^{0.5} D_e^{-1.5}, \tag{7.2}$$

where, D_e is the equivalent melt-pool diameter and is equal to the melt-pool diameter on the top surface D_t. The frequency of oscillation under full penetration is calculated from the following equation [15]:

$$\text{Mode 3: } f = 1.08\left(\frac{\bar{\gamma}}{\rho H_m}\right)^{0.5} D_e^{-1}, \tag{7.3}$$

where, D_e is the equivalent melt-pool diameter under full penetration condition defined as follows [15]:

$$D_e = \sqrt{\frac{1}{3}\left(D_t^2 + D_t D_b + D_b^2\right)}. \tag{7.4}$$

Here, D_t and D_b are the melt-pool diameters measured on the top and bottom surfaces, respectively. To calculate oscillation frequencies from the analytical models, the average surface tension of the molten metal $\bar{\gamma}$ is assumed to be $1.6\,\mathrm{N\,m^{-1}}$, which is the mean value of surface tension in the temperature range of 1673–2300 K for an Fe–S alloy with a sulphur concentration of 240 ppm, according to the model proposed by Sahoo *et al.* [23]. The results indicate that depending on the processing condition, the melt pool can oscillate in different modes. It seems that the melt pool is more likely to oscillate in the sloshy mode (mode 2) with a reduced mean welding current. The predictions obtained from the analytical models agree reasonably with the present numerical results and the experimental measurements, which confirms their adequacy in predicting the melt pool oscillation frequencies. The deviation between analytical predictions and the numerical and experimental data is attributed to the simplifying assumptions made to develop the models and uncertainties in prescribing the average surface tension of the molten metal. It should be noted that although analytical models can provide information about oscillation frequencies, they fail to predict the variation of oscillation amplitude as well as changes in the oscillation mode, which are influenced by the complex melt flow. Additionally, employing the proposed simulation-based approach, the need of triggering the melt-pool oscillations by a current pulsation, mainly to amplify the oscillation amplitudes to make them sensible for measurement devices, is obviated.

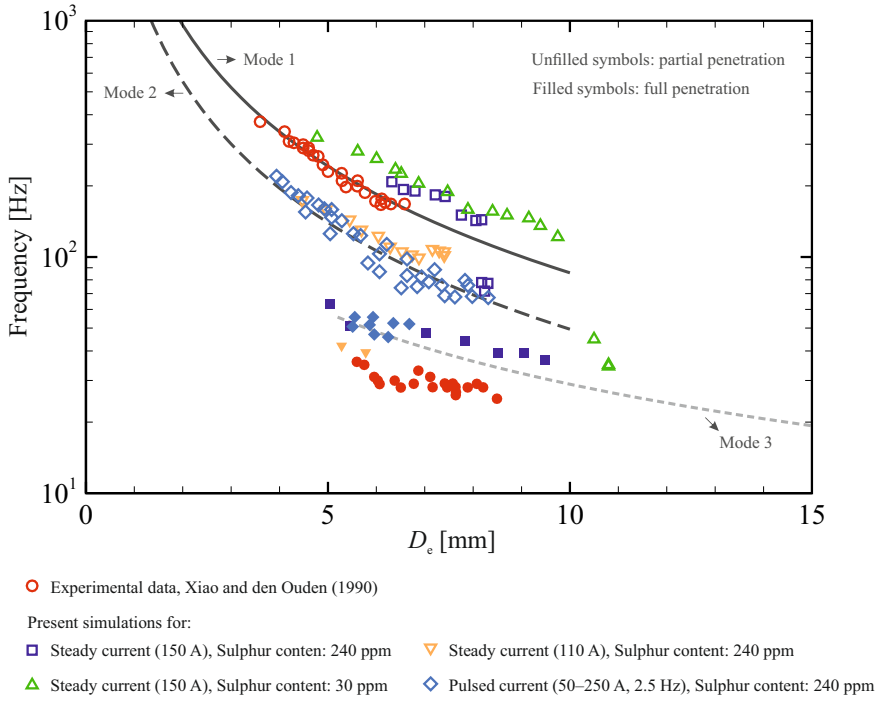

Figure 7.7: The frequency of melt pool surface oscillations during stationary GTAW. Unfilled symbols and dark grey continuous and dashed lines: partially penetrated melt pool, filled symbols and Dashed light grey line: fully penetrated melt pool. Under partial penetration conditions, the solid line and the dashed-line show the frequencies of oscillations in mode 1 (axisymmetric oscillations) and mode 2 (sloshy oscillation), respectively.

7.6. Conclusions

A simulation-based approach was implemented to study heat and fluid flow in molten metal melt pools and associated surface oscillations during gas tungsten arc welding (GTAW). Utilising the proposed approach, the effects of surfactants and various welding process parameters on melt-pool oscillations were investigated. Time-frequency analysis based on a wavelet transform was carried out to improve our understanding of melt pool oscillatory behaviour with time dependent responses that may encompass abrupt changes. The results obtained from the present numerical simulations are compared with experimental and analytical results. Using this approach, the frequency and amplitude of melt pool oscillation and changes in the oscillation modes were predicted, which are not predictable using published analytical models and are generally difficult to measure experimentally.

The melt-pool oscillations strongly relate to melt-pool shape that is determined by convection in the melt pool to a large extent. Convection in the melt pool and thus the melt-pool shape are both affected by flow instabilities that arise rapidly in the melt pool. The spatial distribution of arc power-density and forces imposed on the melt

pool change with surface deformations that can affect the temperature distribution over the melt-pool surface, and thus flow instabilities that are often dominated by Marangoni flow. Oscillations with relatively low amplitudes and high frequencies were observed during partial penetration. The frequency of melt-pool oscillations decreases as the melt pool grows. The numerical predictions confirm the existence of a sharp drop in oscillation frequency when the melt pool becomes fully penetrated. It is found that there is a period during which both high and low frequencies coexist while the transition from partial to full penetration is occurring. Additionally, the results show that the melt pool oscillation mode can change during processing, depending on material properties and prescribed process parameters. The melt pool oscillation and thus the process stability can be optimised through adjusting welding process parameters and adjusting the concentration of surfactants.

References

[1] DebRoy, T., Wei, H. L., Zuback, J. S., Mukherjee, T., Elmer, J. W., Milewski, J. O., Beese, A. M., Wilson-Heid, A., De, A., and Zhang, W. Additive manufacturing of metallic components – Process, structure and properties. *Progress in Materials Science*, 92:112–224, 2018. doi:10.1016/j.pmatsci.2017.10.001.

[2] DebRoy, T. and David, S. A. Physical processes in fusion welding. *Reviews of Modern Physics*, 67(1):85–112, 1995. doi:10.1103/revmodphys.67.85.

[3] Aucott, L., Dong, H., Mirihanage, W., Atwood, R., Kidess, A., Gao, S., Wen, S., Marsden, J., Feng, S., Tong, M., Connolley, T., Drakopoulos, M., Kleijn, C. R., Richardson, I. M., Browne, D. J., Mathiesen, R. H., and Atkinson, H. V. Revealing internal flow behaviour in arc welding and additive manufacturing of metals. *Nature Communications*, 9(1), 2018. doi:10.1038/s41467-018-07900-9.

[4] Mills, K. C. and Keene, B. J. Factors affecting variable weld penetration. *International Materials Reviews*, 35(1):185–216, 1990. doi:10.1179/095066090790323966.

[5] Cook, P. S. and Murphy, A. B. Simulation of melt pool behaviour during additive manufacturing: Underlying physics and progress. *Additive Manufacturing*, 31:100909, 2020. doi:10.1016/j.addma.2019.100909.

[6] Wu, F., Falch, K. V., Guo, D., English, P., Drakopoulos, M., and Mirihanage, W. Time evolved force domination in arc weld pools. *Materials & Design*, 190:108534, 2020. doi:10.1016/j.matdes.2020.108534.

[7] Zhao, C. X., Kwakernaak, C., Pan, Y., Richardson, I. M., Saldi, Z., Kenjeres, S., and Kleijn, C. R. The effect of oxygen on transitional Marangoni flow in laser spot welding. *Acta Materialia*, 58 (19):6345–6357, 2010. doi:10.1016/j.actamat.2010.07.056.

[8] Kidess, A., Kenjereš, S., and Kleijn, C. R. The influence of surfactants on thermocapillary flow instabilities in low Prandtl melting pools. *Physics of Fluids*, 28(6):062106, 2016. doi:10.1063/1.4953797.

[9] Renwick, R. J. and Richardson, R. W. Experimental investigation of GTA weld pool oscillations. *Welding Journal*, 62(2):29s–35s, 1983. URL: `https://app.aws.org/wj/supplement/WJ_1983_02_s29.pdf`.

[10] Sorensen, C. D. and Eagar, T. W. Modeling of oscillations in partially penetrated weld pools. *Journal of Dynamic Systems, Measurement, and Control*, 112(3):469–474, 1990. doi:10.1115/1.2896166.

[11] Ebrahimi, A., Kleijn, C. R., and Richardson, I. M. The influence of surface deformation on thermocapillary flow instabilities in low Prandtl melting pools with surfactants. In *Proceedings of the 5th World Congress on Mechanical, Chemical, and Material Engineering*. Avestia Publishing, 2019. doi:10.11159/htff19.201.

[12] Xiao, Y. H. and den Ouden, G. Weld pool oscillation during GTA welding of mild steel. *Welding Journal*, 72(8):428s–434s, 1993. URL: `http://files.aws.org/wj/supplement/WJ_1993_08_s428.pdf`.

[13] Xiao, Y. H. and den Ouden, G. Measurement of surface tension of liquid metalsand alloys under arc welding conditions. *Materials Science and Technology*, 13(9):791–794, 1997. doi:10.1179/mst.1997.13.9.791.

[14] Li, H., Peng, Z., Ma, B., Wang, P., and Li, J. Numerical analysis of thermal energy charging performance of spherical cu@cr@ni phase-change capsules for recovering high-temperature waste heat. *Journal of Materials Research*, 32(06):1138–1148, 2017. doi:10.1557/jmr.2016.493.

[15] Xiao, Y. H. and den Ouden, G. A study of GTA weld pool oscillation. *Welding Journal*, 69(8):289s–293s, 1990. URL: `http://files.aws.org/wj/supplement/WJ_1990_08_s289.pdf`.

[16] Li, C., Shi, Y., Du, L., Yufen, G., and Zhu, M. Real-time measurement of weld pool oscillation frequency in GTAW-P process. *Journal of Manufacturing Processes*, 29:419–426, 2017. doi:10.1016/j.jmapro.2017.08.011.

[17] Yoo, C. D. and Richardson, R. W. An experimental study on sensitvity and signal characteristics of welds pool oscillation. *Transactions of the Japan Welding Society*, 24(2):54–62, 1993. URL: `https://ci.nii.ac.jp/naid/110003379951/en/`.

[18] Shi, Y., Zhang, G., Ma, X. J., Gu, Y. F., Huang, J. K., and Fan, D. Laser-vision-based measurement and analysis of weld pool oscillation frequency in GTAW-P. *Welding Journal*, 94(5):176s–187s, 2015. URL: `https://app.aws.org/wj/supplement/WJ_2015_05_s176.pdf`.

[19] Li, C., Shi, Y., Gu, Y., and Yuan, P. Monitoring weld pool oscillation using reflected laser pattern in gas tungsten arc welding. *Journal of Materials Processing Technology*, 255:876–885, 2018. doi:10.1016/j.jmatprotec.2018.01.037.

[20] Tam, A. S. and Hardt, D. E. Weld pool impedance for pool geometry measurement: Stationary and nonstationary pools. *Journal of Dynamic Systems, Measurement, and Control*, 111(4):545–553, 1989. doi:10.1115/1.3153090.

[21] Ko, S. H., Yoo, C. D., Farson, D. F., and Choi, S. K. Mathematical modeling of the dynamic behavior of gas tungsten arc weld pools. *Metallurgical and Materials Transactions B*, 31(6):1465–1473, 2000. doi:10.1007/s11663-000-0031-1.

[22] Ko, S. H., Choi, S. K., and Yoo, C. D. Effects of surface depression on pool convection and geometry in stationary GTAW. *Welding Journal*, 80(2):39s–45s, 2001. URL: `https://app.aws.org/wj/supplement/Ko02-01.pdf`.

[23] Sahoo, P., Debroy, T., and McNallan, M. J. Surface tension of binary metal—surface active solute systems under conditions relevant to welding metallurgy. *Metallurgical Transactions B*, 19(3):483–491, 1988. doi:10.1007/bf02657748.

[24] Joshi, Y., Dutta, P., Schupp, P. E., and Espinosa, D. Nonaxisymmetric convection in stationary gas tungsten arc weld pools. *Journal of Heat Transfer*, 119(1):164–172, 1997. doi:10.1115/1.2824082.

[25] Cho, J., Farson, D. F., Hollis, K. J., and Milewski, J. O. Numerical analysis of weld pool oscillation in laser welding. *Journal of Mechanical Science and Technology*, 29(4):1715–1722, 2015. doi:10.1007/s12206-015-0344-2.

[26] Huang, J. K., Yang, M. H., Chen, J. S., Yang, F. Q., Zhang, Y. M., and Fan, D. The oscillation of stationary weld pool surface in the GTA welding. *Journal of Materials Processing Technology*, 256:57–68, 2018. doi:10.1016/j.jmatprotec.2018.01.018.

[27] Yu, S., Chunkai, L., Leiming, D., YuFen, G., and Ming, Z. Frequency characteristics of weld pool oscillation in pulsed gas tungsten arc welding. *Journal of Manufacturing Processes*, 24: 145–151, 2016. doi:10.1016/j.jmapro.2016.08.010.

[28] Tsai, N. S. and Eagar, T. W. Distribution of the heat and current fluxes in gas tungsten arcs. *Metallurgical Transactions B*, 16(4):841–846, 1985. doi:10.1007/bf02667521.

[29] Lin, M. L. and Eagar, T. W. Pressures produced by gas tungsten arcs. *Metallurgical Transactions B*, 17(3):601–607, 1986. doi:10.1007/bf02670227.

[30] Mishra, S., Lienert, T. J., Johnson, M. Q., and DebRoy, T. An experimental and theoretical study of gas tungsten arc welding of stainless steel plates with different sulfur concentrations. *Acta Materialia*, 56(9):2133–2146, 2008. doi:10.1016/j.actamat.2008.01.028.

[31] Mills, K. C. *Recommended Values of Thermophysical Properties for Selected Commercial Alloys*. Woodhead Publishing, woodhead publishing series in metals and surface engineering edition, 2002. ISBN 978-1-85573-569-9.

[32] *Release 19.2*. ANSYS Fluent. URL: `https://www.ansys.com/`.

[33] Issa, R. I. Solution of the implicitly discretised fluid flow equations by operator-splitting. *Journal of Computational Physics*, 62(1):40–65, 1986. doi:10.1016/0021-9991(86)90099-9.

[34] Patankar, S. V. *Numerical Heat Transfer and Fluid Flow*. Taylor & Francis Inc, 1st edition, 1980. ISBN 0891165223.

[35] Ubbink, O. *Numerical Prediction of Two Fluid Systems with Sharp Interfaces*. PhD dissertation, Imperial College London (University of London), London, United Kingdom, 1997. URL: `http://hdl.handle.net/10044/1/8604`.

[36] Mallat, S. *A Wavelet Tour of Signal Processing*. Elsevier Inc., 2009. doi:10.1016/B978-0-12-374370-1.X0001-8.

[37] Haberman, R. *Applied Partial Differential Equations: With Fourier Series and Boundary Value Problems*. Featured Titles for Partial Differential Equations. PEARSON, 2013. ISBN 9780321797056.

[38] Schatz, M. F. and Neitzel, G. P. Experiments on thermocapillary instabilities. *Annual Review of Fluid Mechanics*, 33(1):93–127, 2001. doi:10.1146/annurev.fluid.33.1.93.

8

Melt Pool Behaviour in Positional Gas Tungsten Arc Welding

Internal flow behaviour and melt-pool surface oscillations during arc welding are complex and not yet fully understood. In the present work, high-fidelity numerical simulations are employed to describe the effects of welding position, sulphur concentration (60–300 ppm) and travel speed ($1.25–5\,mm\,s^{-1}$) on molten metal flow dynamics in fully-penetrated melt-pools. A wavelet transform is implemented to obtain time-resolved frequency spectra of the oscillation signals, which overcomes the shortcomings of the Fourier transform in rendering time resolution of the frequency spectra. Comparing the results of the present numerical calculations with available analytical and experimental datasets, the robustness of the proposed approach in predicting melt-pool oscillations is demonstrated. The results reveal that changes in the surface morphology of the pool resulting from a change in welding position alter the spatial distribution of arc forces and power-density applied to the molten material, and in turn affect flow patterns in the pool. Under similar welding conditions, changing the sulphur concentration affects the Marangoni flow pattern, and increasing the travel speed decreases the size of the pool and increases the offset between top and bottom melt-pool surfaces, affecting the flow structures (vortex formation) on the surface. Variations in the internal flow pattern affect the evolution of melt-pool shape and its surface oscillations.

The contents of this chapter have been published in *Journal of Physics D: Applied Physics*, **2021**, *54*(27), 275303, DOI: 10.1088/1361-6463/abf808.

8.1. Introduction

Fusion joining of metallic materials is an essential requirement in many industries. The integrity of products depends critically on the joining technique employed and the quality of the joints produced [1, 2], which in turn is influenced by the dynamic stability of the melt-pool [3]. A better understanding of the complex transport phenomena inside melt-pools offers considerable opportunities for improved monitoring and control of joining processes. To date, control and optimisation of welding processes relies largely on trial-and-error experiments that often pose challenges due to the non-linearity of melt-pool responses to changes in operating conditions, material properties and process parameters [4–6]. Moreover, welding process development requires tolerance to parameter variations, within which the resultant weld integrity must be fit for the intended purpose, irrespective of the particular parameter combinations within the defined procedural range.

The present chapter focuses on positional gas tungsten arc (GTA) welding, which involves several significant operating parameters, the number increasing when complex time-dependent phenomena are considered [7]. The simulation-based approach utilised in the present work offers the potential to reduce procedure development costs and will enhance our understanding of melt-pool behaviour during positional GTA welding.

The majority of published studies on GTA melt-pool oscillatory behaviour are experimentally based, consider only the flat (1G or PA) welding orientation (*i.e.* position C1 shown in figure 8.1) and focus on processing the signals received from the melt pool to sense penetration [8]. Experimental techniques employed are often based on laser vision [9], arc voltage [10] or arc-light intensity [11] measurements. A critical limitation is related to the inadequate signal-to-noise ratio for low-amplitude surface oscillations [12], which makes the application of a triggering action essential [13]. Moreover, these techniques ignore convection in the melt pool, which is difficult to measure due to opacity, the fast dynamic response of the molten metal flow and high temperatures [1]. In addition to the experimental measurements, analytical models have been developed to predict dominant oscillation frequencies. These models are based on similarities between oscillations of the melt-pool surface and the vibrations of a thin stretched membrane [10, 11, 14–16]. Unfortunately, the absolute accuracy of these analytical models is critically dependent on the melt-pool shape, temperature-dependent material properties and processing conditions [12], which in turn are affected by unsteady transport phenomena in the pool [17]; factors that are not known *a priori*. Moreover, changes in oscillation mode and amplitude are not predictable using these models. Conversely, high-fidelity numerical simulations have demonstrated a remarkable potential to describe the complex internal flow behaviour in melt pools and associated surface deformations [18, 19].

Although many numerical models are available (*e.g.*, [20–27]), numerical studies on melt-pool surface oscillations are scarce and the melt-pool oscillatory behaviour is not yet fully understood, particularly for positional welding conditions. Previous studies often focused on the influence of surface deformations on the melt-pool shape [28–32] or the morphology of the melt-pool surface, to study ripple formation [33], welding defects such as undercut [34] or humping [35–37]. Chen *et al.* [38] revealed that the flow patterns in pools with one free surface, representative of partially penetrated welds, differ from those in pools with two free surfaces, representative of fully penetrated welds. In their

model, they neglected solidification and melting, assumed that the flow inside the pool is axisymmetric and that the surface tension of the molten material is a linear function of temperature. Using a similar model, including electromagnetic forces and solid-liquid phase transformations, Ko *et al.* [39, 40] showed that pool oscillations during stationary GTA welding depend on the direction of the Marangoni flow. For many real-world welding applications, non-pure materials are involved for which the surface tension changes non-linearly with temperature [41]. This coupled with movements of the melt-pool boundaries due to solid-liquid phase transformations form complex unsteady flow patterns that are inherently three-dimensional [42–44], affecting the melt-pool surface oscillations.

In Chapter 7, it has been demonstrated that changes in welding current and material properties can alter the time-frequency response of melt-pool oscillations under both partial and full penetration conditions. The welding position can also influence the shape of the deformations of the melt-pool surface and its shape during GTA welding [45, 46]. Moreover, morphology of the melt-pool surface can affect the spatial and temporal distribution of arc-pressure and power-density and thus the melt-pool dynamic behaviour [18, 39]. Further investigations are essential to broaden our understanding of complex internal flow behaviour in melt pools and melt-pool surface oscillations in positional GTA welding. In the present chapter, the results of numerical simulations employed to reveal complex unsteady transport phenomena in the melt-pool and associated surface oscillations during positional GTA welding are reported. The focus here is particularly on fully-penetrated pools, where the melt-pool oscillations are critical for process stability; however, the present model is equally applicable to partial penetration conditions. The coupling between melt-pool surface deformations, arc force and power-density distributions, which represent physical realism and can affect the predicted thermal and flow fields, are taken into account. The continuous wavelet transform is applied to the time-resolved displacement signals acquired from the simulations to enhance our understanding of the evolution of surface oscillations and its correlation with process parameters and material properties. A novel insight into the evolution of melt-pool surface oscillations and the complex flow inside molten metal melt pools is provided, which offers a computational approach to fusion welding process development and optimisation.

8.2. Problem description

Molten metal flow behaviour and associated surface oscillations during positional gas tungsten arc welding of a stainless steel (AISI 316) plate are studied numerically. As shown schematically in figure 8.1, the plate has a thickness of $H_m = 2\,\text{mm}$ and is heated locally by an electric arc plasma (with the electrode being perpendicular to the workpiece surface) to create a melt pool in the plate that is initially at $T_0 = 300\,\text{K}$. The current is set to 85 A and the initial arc length (electrode tip to workpiece distance) before igniting the arc is 2.5 mm. Obviously, the melt-pool surface deforms during the process, leading to changes in the length, voltage and power of the arc as well as power-density distribution and the magnitude and distribution of forces induced by the arc plasma [18, 47, 48]. In the present model, the melt-pool is decoupled from the arc plasma to reduce the computation time and complexity of simulations. Accordingly, the related source terms for momentum and thermal energy are adjusted dynamically in the present model to take these changes into

account, as explained in section 3.2.2. Argon gas is employed to shield the melt-pool. The temperature-dependent thermophysical properties of AISI 316L and argon are presented in table 8.1. The temperature-dependent surface tension of the molten material is modelled using an empirical correlation [41] introduced in section 3.4, which accounts for the influence of surface-active elements (*i.e.* sulphur).

A moving reference frame is employed in the present numerical simulations to simulate unsteady convection in the melt pool. Hence, instead of moving the heat source, the material enters the computational domain, translates at a fixed speed (*i.e.* the welding travel speed) opposite to the welding direction shown in figure 8.1, and leaves the computational domain. Applying the moving reference frame technique facilitates a decrease in the size of the computational domain and thus the runtime. The computational domain is designed in the form of a rectangular cube encompassing the workpiece and two layers of gas below and above the sample to monitor the oscillations of the melt-pool surfaces. The width and the length of the computational domain is $W = 40\,\text{mm}$ and $L = 70\,\text{mm}$ respectively, which is substantially larger than the dimensions of the melt-pool. The boundary conditions applied to the computational domain in the simulations are shown in figure 8.1(b). The outer boundaries of the workpiece are adiabatic and are treated as no-slip moving walls. The gas layers have a thickness of $H_\text{a} = 2\,\text{mm}$ and a fixed atmospheric pressure ($p = p_\text{atm} = 101.325\,\text{kPa}$) is applied to their outer boundaries. The electrode axis is located in the middle of the plate (*i.e.* $x = W/2$) and 15 mm away from the leading-edge of the plate (*i.e.* $y = 15\,\text{mm}$). Eight different welding positions (workpiece orientations with respect to gravity) are studied, as shown in figure 8.1(c).

Table 8.1: Thermophysical properties of the stainless steel (AISI 316L) and the gas (argon) employed in the numerical simulations. Values for AISI 316L are taken from [49], and T is in Kelvin.

Property	Stainless steel (AISI 316L)	Gas (argon)	Unit
Density ρ	7100	1.623	kg m^{-3}
Specific heat capacity c_p	$430.18 + 0.1792 \cdot T$ (solid phase) 830 (liquid phase)	520.64	$\text{J kg}^{-1}\,\text{K}^{-1}$
Thermal conductivity k	$11.791 + 0.0131 \cdot T$ (solid phase) $6.49 + 0.0129 \cdot T$ (liquid phase)	1.58×10^{-2}	$\text{W m}^{-1}\,\text{K}^{-1}$
Viscosity μ	6.42×10^{-3}	2.12×10^{-5}	$\text{kg m}^{-1}\,\text{s}^{-1}$
Thermal expansion coefficient β	2×10^{-6}	–	K^{-1}
Latent heat of fusion $\mathscr{L}_\text{f}$	2.7×10^{5}	–	J kg^{-1}
Liquidus temperature T_l	1723	–	K
Solidus temperature T_s	1658	–	K

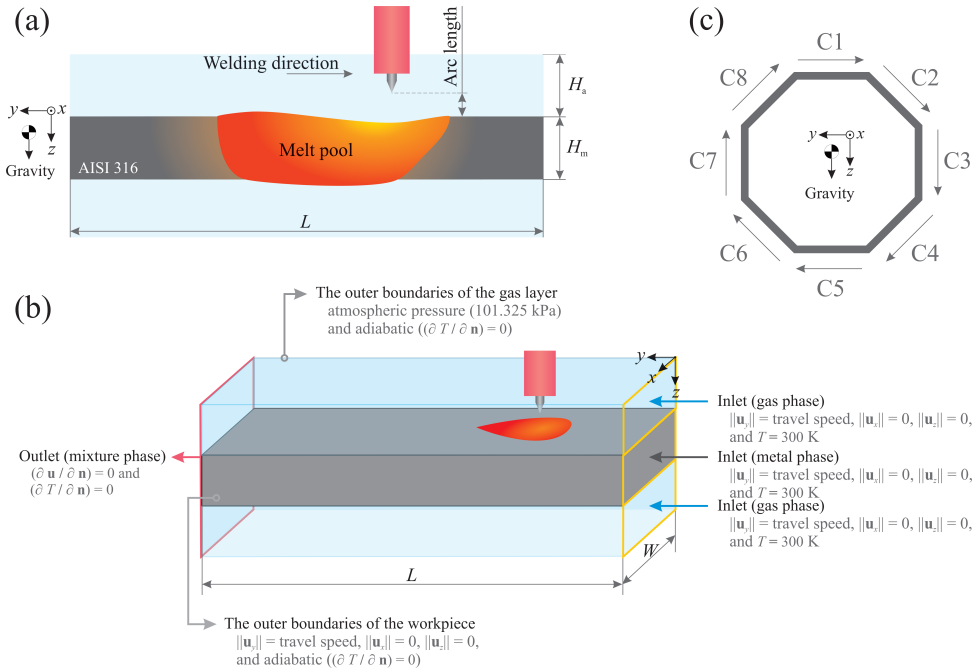

Figure 8.1: Schematic of moving gas tungsten arc welding (GTAW). (a) a cross section of the plate showing a fully-penetrated melt pool, (b) three-dimensional view of the problem under consideration and (c) different welding positions studied in the present chapter.

8.3. Numerical procedure

The numerical simulations make use of a finite-volume solver, ANSYS Fluent [50]. The surface-tension model as well as the source terms in the governing equations were implemented in the solver using user-defined functions programmed in the C programming language. The computational grid contains about 5.2×10^6 hexahedral cells, where cell spacing varies gradually from 40 µm in the melt-pool region and close to the gas-metal interface to 400 µm close to the boundaries of the computational domain. Spatial discretisation was implemented by the central-differencing scheme for momentum advection and diffusive fluxes, and time marching was performed employing a first order implicit scheme. The time-step size was set to 10^{-5} s, resulting in a Courant number ($\mathrm{Co} = \|\mathbf{u}\|\Delta t/\Delta x$) less than 0.25. Velocity and pressure fields were coupled using the PISO (pressure-implicit with splitting of operators) scheme [51] and the pressure interpolation was performed employing the PRESTO (pressure staggering option) scheme [52]. The advection of the volume-fraction field was formulated using an explicit compressive VOF method [53]. Convergence for each time-step is achieved when scaled residuals fall below 10^{-7}. Each simulation was executed in parallel on 80 cores (AMD EPYC 7452) of a computing cluster for a total run-time of about 800 h.

8.4. Results

In this section, the effects of different welding positions (shown in figure 8.1(c)) as well as travel speed (ranging between 1.25 mm s^{-1} and 5 mm s^{-1}) and sulphur concentration (ranging between 60 ppm and 300 ppm) on internal flow behaviour, evolution of the melt-pool shape and surface oscillations during GTA welding are described. Displacement signals required for characterising the molten metal oscillations were recorded from several monitoring points distributed over the melt-pool surface, and are shown in figure 8.2 for welding position C1. Although the amplitudes of oscillations are different at different locations, the frequency spectra obtained from FFT analysis look similar. Hence, the signals recorded from the monitoring point $m(x, y, z) = m(0, 0, z_{\text{interface}})$ in the period of $t = 0$ s to 10 s were analysed utilising the continuous wavelet transform. It should be noted that no triggering action (such as welding current pulsation) was taken to excite melt-pool surface oscillations in the present numerical simulations because even small surface fluctuations are detectable using the proposed computational approach [18].

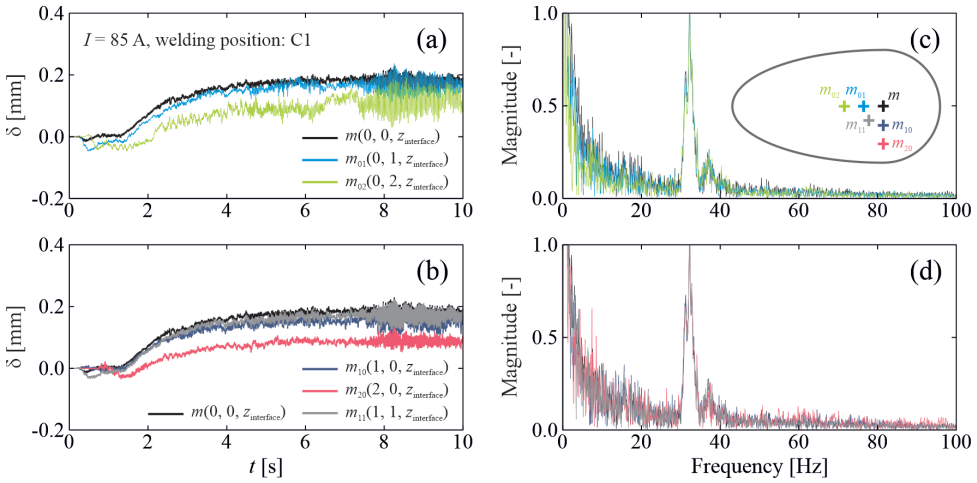

Figure 8.2: The displacement signals recorded from the monitoring points on the melt-pool top surface and the corresponding frequency spectra for welding position C1. (a and b) displacement signals obtained from the simulations, (c and d) frequency spectra obtained from FFT analysis. Magnitudes in the frequency spectrum are normalised with respect to the maximum magnitude. Positive values of δ indicate surface depression and negative values surface elevation. ($I = 85$ A, travel speed: 2.5 mm s^{-1} and sulphur concentration: 240 ppm)

The oscillation signals of the melt-pool surface and the corresponding frequency spectra for different welding positions with $I = 85$ A and sulphur concentration of 240 ppm are shown in figure 8.3 for downward welding direction (C1–C4) and in figure 8.4 for upward welding direction (C5–C8). For the cases with a travel speed of 2.5 mm s^{-1}, the melt-pool depth increases over time and reaches the plate thickness H_{m} in about 1.25 s. Then, the melt-pool surface area on the bottom surface increases and becomes almost the same as that on the top surface (*i.e.* full penetration) at $t \approx 4$ s, after which the melt-pool grows to reach a quasi-steady state. In the case of GTA welding in position C1 (figure 8.3(a)),

the frequency of oscillations decreases from $f \approx 73\,\text{Hz}$ at $t = 1.25\,\text{s}$ to values of about 32 Hz at $t = 4\,\text{s}$, while the melt-pool surface area on the bottom surface is increasing to establish full penetration. After full penetration is established, the frequency of the most energetic event increases to $f \approx 45\,\text{Hz}$, as indicated by the arrow, and subsequently decreases gradually to values of about 32 Hz as time approaches 10 s. Both low and high frequencies remain in the spectrum after full penetration. The amplitudes of oscillations also augment as the melt-pool size increases. The frequency of oscillations obtained from the present numerical simulations for welding position C1 agrees reasonably (within 10% deviation bands) with the experimental data reported by Li *et al.* [54]. The range of oscillation frequencies predicted for different welding positions (C1–C8) seems to be the same, however the results suggest that the welding position affects the amplitudes of oscillations and the evolution of melt-pool oscillatory behaviour. The frequency of oscillations varies from $f \approx 25\,\text{Hz}$ to values of about 37 Hz after full penetration for welding positions C2 and C4. Such increase in the frequency of oscillations after full penetration also occurs for the welding position C3, however the frequency decreases after about 1 s and the melt pool oscillates at low frequencies up to $t \approx 7\,\text{s}$, after which the melt pool collapses (*i.e.* burns-through).

The amplitude of oscillations predicted for cases C5–C8 are generally larger than those predicted for cases C1–C4, as shown in figure 8.4. For the welding position C5, the frequency of oscillations decreases from 66 Hz to 52 Hz within 1 s (from $t = 1.25\,\text{s}$ to $t = 2.25\,\text{s}$) and then the frequency of oscillations increases to 64 Hz, as indicated by arrow. For the cases that welding direction is upward (C6–C8), multiple changes occur in the frequency of oscillations. The abrupt changes observed in the frequency domain indicate the importance of utilising the wavelet transform instead of the Fourier transform for analysing the behaviour of oscillating melt-pools. Changes in the frequency of oscillations relate to changes in flow pattern in the melt pool, the shape and size of the melt-pool, and surface tension of the molten metal [14, 18], which is discussed in section 8.5.

Changes in the sulphur concentration of the material, as a surface-active element, can result in notable changes in surface tension of the molten material and its variation with temperature ($\partial\gamma/\partial T$), as shown in figure 3.2. Reducing the amount of sulphur in the material results in intensifying the outward fluid flow over the melt-pool surface (as shown in figure 8.10), forming a wide melt pool. The effect of sulphur concentration of the material on the evolution of the frequency of oscillations is shown in figure 8.5 for welds in position C1 and travel speed of $2.5\,\text{mm}\,\text{s}^{-1}$. The evolution of oscillation frequency is almost the same for the cases with sulphur concentrations of 120 ppm and 60 ppm, and differs both qualitatively and quantitatively from that of the case containing 240 ppm sulphur. The melt pool oscillates at higher frequencies with larger amplitudes in the case with sulphur concentration of 240 ppm compared to the cases with sulphur concentrations of 120 ppm and 60 ppm. Moreover, the fundamental frequency of oscillations does not increase markedly after full penetration in the cases with sulphur concentrations of 120 ppm and 60 ppm, as it does in the case with sulphur concentration of 240 ppm. This difference in the evolution of oscillations frequency relates to changes in the structure of the molten metal flow in the melt pool and thus melt-pool shape evolution.

The influence of travel speed on the frequency of melt-pool surface oscillations is shown in figure 8.6 for the welds in position C1 and sulphur concentration of 240 ppm.

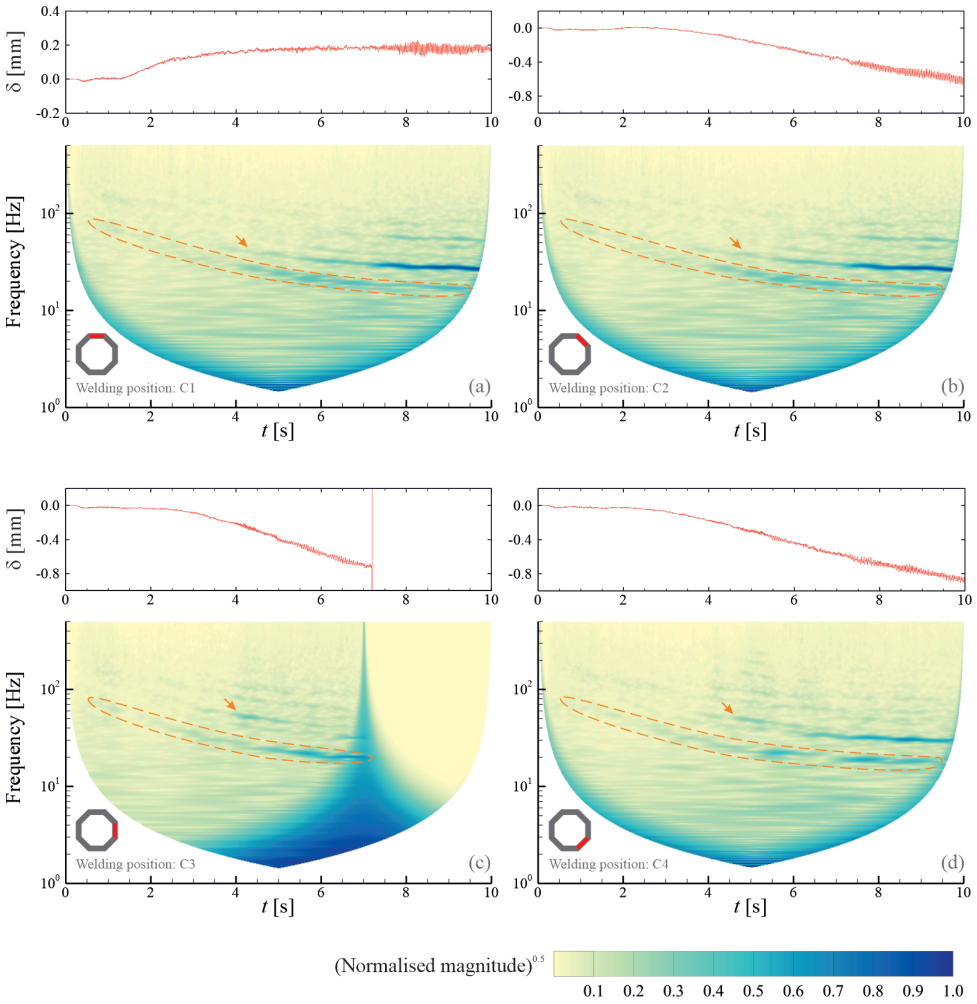

Figure 8.3: The displacement signals recorded from the monitoring point $m(x, y, z) = m(0, 0, z_{\text{interface}})$ and the corresponding time-frequency spectra for different welding positions with downward welding direction. (a) welding positions C1, (b) welding positions C2, (c) welding positions C3 and (d) welding positions C4. Magnitudes are normalised with respect to the maximum magnitude in the time-frequency spectrum. Positive values of δ indicate surface depression and its negative values indicate surface elevation. ($I = 85$ A, travel speed: 2.5 mm s^{-1} and sulphur concentration: 240 ppm)

When the travel speed was set to 1.25 mm s^{-1}, the melt pool reaches full penetration at $t \approx 3$ s and the amplitude of surface oscillations start to increase, as shown in figure 8.6(a). For the case with a travel speed of 1.25 mm s^{-1}, the frequency of oscillations gradually decreases from 69 Hz at $t = 1.25$ s to 29 Hz at $t = 10$ s while the melt-pool is growing over time. Increasing the travel speed from 1.25 mm s^{-1} to 5 mm s^{-1}, the amplitude of oscillations

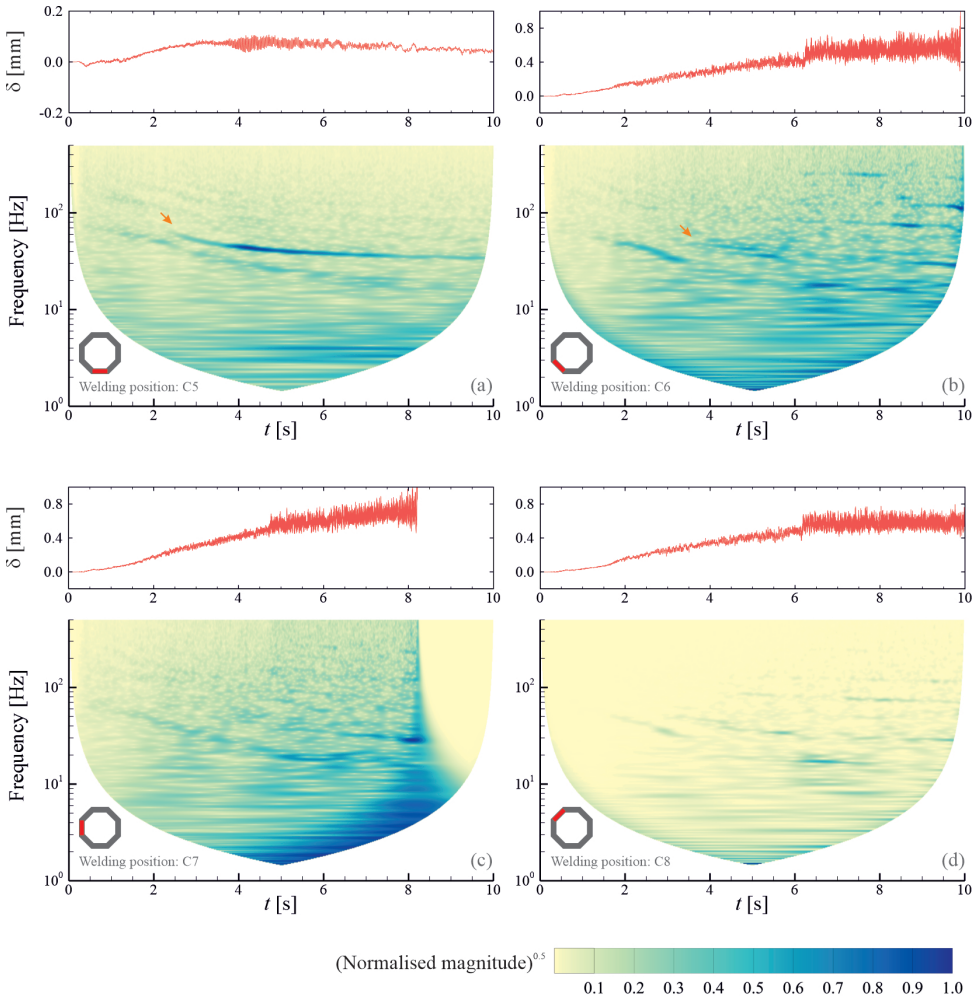

Figure 8.4: The displacement signals recorded from the monitoring point $m(x,y,z) = m(0,0,z_{\text{interface}})$ and the corresponding time-frequency spectrum for different welding positions with upward welding direction. (a) welding positions C5, (b) welding positions C6, (c) welding positions C7 and (d) welding positions C8. Magnitudes are normalised with respect to the maximum magnitude in the time-frequency spectrum. Positive values of δ indicate surface depression and its negative values indicate surface elevation. ($I = 85$ A, travel speed: 2.5 mm s^{-1} and sulphur concentration: 240 ppm)

decreases significantly. Moreover, the frequency of oscillations decreases up to $t = 4$ s while the melt-pool size is increasing. Afterwards, the melt-pool reaches a quasi-steady-state condition and the variation of the melt-pool size over time becomes insignificant, resulting in surface oscillations at an almost constant frequency of about 41 Hz. It should be noted that when the pool size has reached steady state, the surface area of the melt

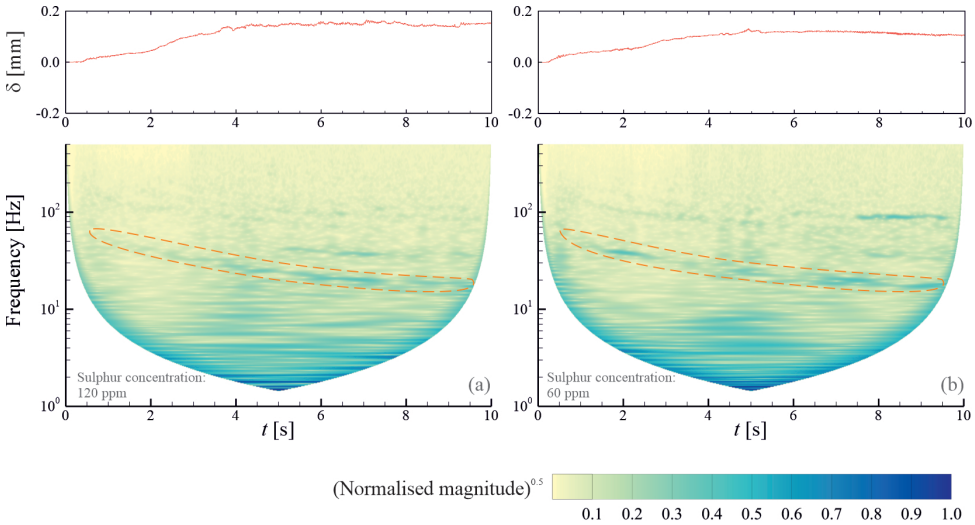

Figure 8.5: The influence of sulphur concentration on the time-frequency spectra of melt-pool oscillations during GTA welding. (a) sulphur concentration: 120 ppm, and (b) sulphur concentration: 60 ppm Magnitudes are normalised with respect to the maximum magnitude in the time-frequency spectrum. Positive values of δ indicate surface depression and its negative values indicate surface elevation. ($I = 85$ A, welding position: C1 and travel speed: 2.5 mm s^{-1})

pool on the bottom surface is consistently smaller than that on the top-surface in the case with a travel speed of 5 mm s^{-1}.

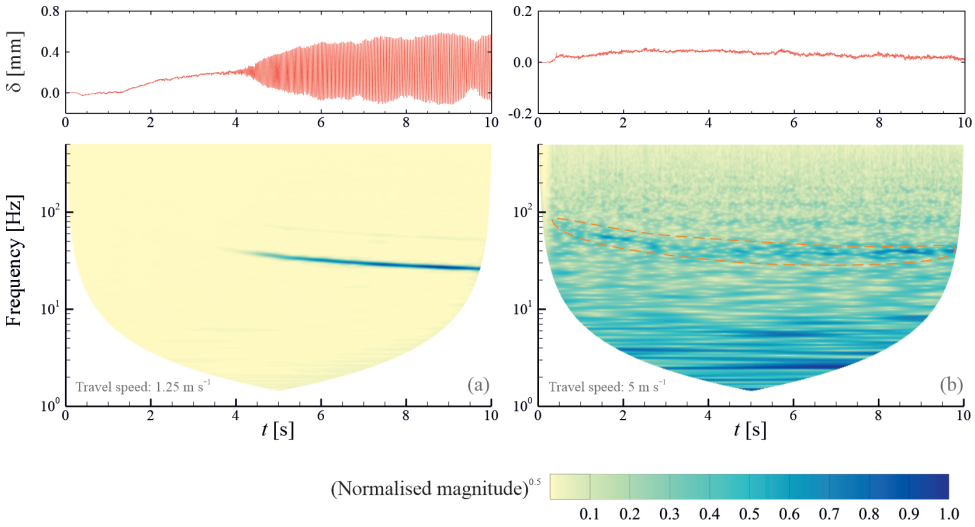

Figure 8.6: The influence of welding travel speed on the time-frequency spectra of melt-pool oscillations during GTA welding. (a) travel speed: 1.25 mm s^{-1}, and (b) travel speed: 5 mm s^{-1}. Magnitudes are normalised with respect to the maximum magnitude in the time-frequency spectrum. Positive values of δ indicate surface depression and its negative values indicate surface elevation. (I = 85 A, welding position: C1 and sulphur concentration: 240 ppm)

8.5. Discussion

The frequency of oscillations predicted using the present numerical simulations are compared to the analytical approximations calculated from the model developed by Maruo and Hirata [16] for fully-penetrated melt pools in welding position C1, and the results are presented in figure 8.7. This analytical model is expressed mathematically as follows [16]:

$$f = \frac{1}{2\pi}\sqrt{\frac{2\bar{\gamma}\hbar^2}{\rho H_\mathrm{m}} - \frac{2\|\mathbf{g}\|}{H_\mathrm{m}}}, \tag{8.1}$$

where, H_m is the plate thickness, ρ the density of the molten metal and $\bar{\gamma}$ the average surface tension of the molten material. The mean value of surface tension for the alloy considered in the present study is approximately 1.6 N m^{-1} in the temperature range of 1723–2500 K [41]. The value of $\hbar$ in equation (8.1) depends on both melt-pool size and oscillation mode and is obtained from the following equations [55]:

$$\text{Mode 3: } \hbar = 2.405\left(\frac{D_\mathrm{e}}{2}\right)^{-1}, \tag{8.2}$$

$$\text{Mode 2f: } \hbar = 3.832\left(\frac{D_\mathrm{e}}{2}\right)^{-1}, \tag{8.3}$$

where, D_e is the equivalent diameter of the melt-pool under a condition of full penetration,

defined as follows:

$$D_e = \sqrt{l\,w}, \tag{8.4}$$

where, l and w are the melt-pool length and width on the top surface respectively, as shown in figure 8.7. The analytical model of Maruo and Hirata [16] is developed for fully-penetrated melt pools, assuming that the melt-pool shape and size on the top and bottom surfaces of the workpiece are the same with no offset. It appears that for the case with a travel speed of 2.5 mm s^{-1} and sulphur concentration of 240 ppm the melt-pool surface oscillations follow the analytically predicted frequencies in mode 3 for $t > 4$ s when the surface area of the melt-pool on the bottom surface approaches the surface area on the top surface. Reducing travel speed to 1.25 mm s^{-1} while keeping the sulphur concentration unchanged (240 ppm), the melt-pool surface area on the bottom surface becomes almost the same as on the top surface and the predicted frequencies follow the analytical predictions in mode 3. For the case with a travel speed of 5 mm s^{-1} and sulphur concentration of 240 ppm, the melt pool shape and size reach a quasi-steady-state with an equivalent diameter $D_e \approx 7.5$ mm that does not change notably over time. In many practical applications, the melt-pool surface area is not necessarily the same on the top and bottom surfaces of the workpiece, particularly when the melt pool is growing before reaching a quasi-steady-state. Moreover, there is often an offset between the positions of the melt-pool surfaces on the top and bottom of the workpiece, which increases with increasing the travel speed. These differences in the melt-pool size and shape, as well as the offset between the melt-pool surfaces on the top and bottom surfaces of the workpiece, lead to deviation of the frequencies approximated using the analytical models from those predicted from numerical simulations and measured experimentally. The frequencies predicted using the present numerical simulations are in reasonably good agreement (within 10% deviation bands) with the experimental measurements of fully penetrated pools reported by Yudodibroto [55].

Despite the suitability of analytical models for predicting the frequency of oscillations under a full penetration condition, they fail to predict changes in oscillation mode during welding processes, particularly when the melt pool is evolving over time. Moreover, variation in the value of surface tension of the molten material with temperature is ignored in the analytical models, which limits their accuracy in predicting the frequency of oscillations during GTA welding. The results presented in figure 8.7 also demonstrate that changes in the sulphur concentration can affect the frequency of oscillations and their evolution due to variations in the internal flow pattern and thus the melt-pool shape, which results from changes in the Marangoni stresses acting on the melt-pool surfaces.

Figure 8.8 shows the evolution of the thermal and flow fields over the melt-pool surfaces as well as the pool shape during GTA welding in position C1 with a travel speed of 2.5 mm s^{-1} and sulphur concentration of 240 ppm. A melt pool forms soon after the arc ignition, grows and its depth reaches the plate thickness after about 1.25 s, forming a fully-penetrated melt pool. Fluid flow in the melt pool is driven by various time-variant forces acting on the molten material such as Marangoni, Lorentz, arc plasma shear and pressure and buoyancy forces, resulting in a complex flow pattern that is inherently three-dimensional. This fluid motion transfers the heat absorbed by the material and affects the melt-pool shape and its evolution over time. The relative contribution of advective

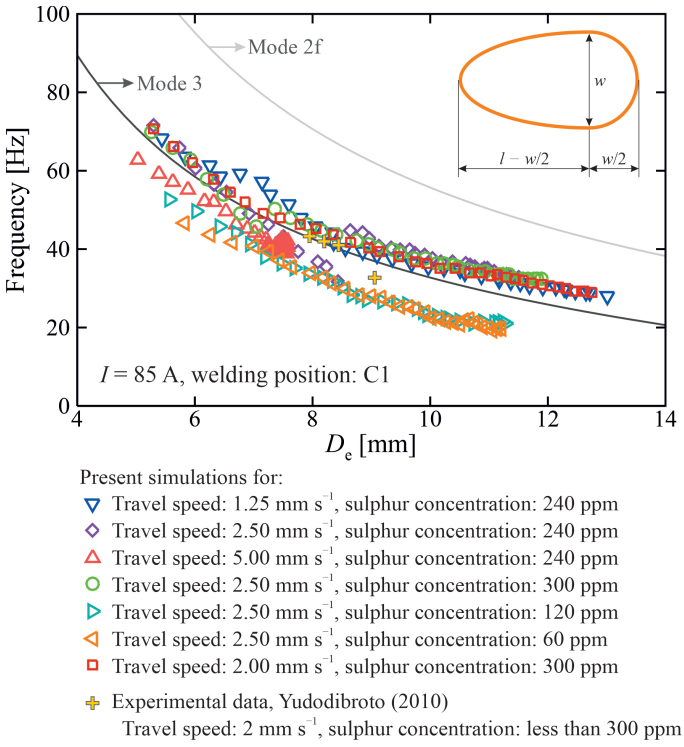

Figure 8.7: Variation of the frequency of oscillations for fully-penetrated melt-pools during GTA welding as a function of equivalent melt-pool diameter. The frequency of oscillations obtained form the present numerical simulations (unfilled symbols), experimental data reported by Yudodibroto [55] (squares), and analytical approximations using the model proposed by Maruo and Hirata [16] for oscillation frequencies in Mode 3 (up and down bulk motion, dark grey line) and Mode 2f (sloshy oscillation, light grey line). (I = 85 A and welding position: C1)

to diffusive energy transfer can be evaluated using the Péclet number (Pe = $\rho c_p \mathcal{D} \|\mathbf{u}\| / k$), which is larger than unity ($\mathcal{O}(100)$) for the cases studied in the present work, signifying the notable influence of advection on the melt-pool shape.

The results shown in figure 8.8 indicate that the maximum temperature of the melt pool after reaching a quasi-steady-state condition varies between 2260 K and 2340 K and the maximum local fluid velocity varies between 0.21 m s^{-1} and 0.34 m s^{-1}. Inward fluid flow from the boundary to the centre of the pool is observed over the top surface that meets an outward flow in the central region. This change in the flow direction is due to the sign change of the temperature gradient of surface tension ($\partial\gamma/\partial T$) at a specific temperature, as shown in figure 3.2. Interactions between these two streams disturb the thermal field over the pool surface and generate an unsteady complex flow pattern inside the pool, affecting the energy transport in the melt pool and thus the evolution of the melt-pool shape. Temperatures are below the critical temperature over the bottom surface of the pool and the temperature gradient of the surface tension is positive all over

the surface, resulting in inward fluid flow from the melt-pool boundaries. Moreover, two vortices form over the top surface as time passes that generate a periodic asymmetry in the flow field, leading to flow oscillations around the melt-pool centreline. The formation of such vortices occurs because of the fluid motion from the front part of the pool toward the rear and collision with the inward flow in the rear part of the pool. A similar flow pattern was observed during GTA welding by Zhao *et al.* [43] using particle image velocimetry (PIV).

The outward fluid flow in the central region of the melt pool coupled with the arc pressure applied to the molten material leads to melt-pool surface depressions in the front and central region of the melt pool. Variation in the flow pattern over time, as well as changes in the melt-pool shape result in changes in oscillatory behaviour. For the case shown in figure 8.8, the melt-pool surface area on the bottom surface of the workpiece increases over time and becomes almost the same as that on the top surface after 4 s. This change in pool shape coupled with the fluid flow that evolves over the bottom surface, causes a change in the melt-pool oscillatory behaviour, as reflected in figure 8.3. Variations in the pool surface morphology also result in variation of the power-density and arc force distribution over the surface and the total power input from the electric arc, enhancing flow disturbances.

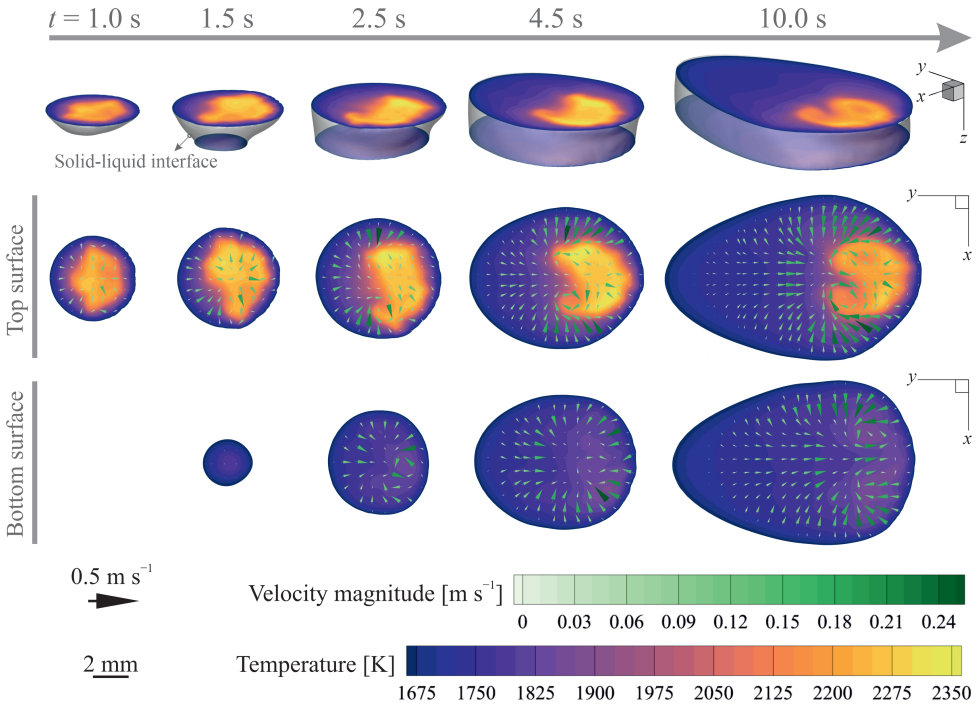

Figure 8.8: Evolution of the melt-pool shape during gas tungsten arc welding. Contours show the temperature distribution over the melt-pool surface and are overlaid with velocity vectors. The 0.5 m s^{-1} reference vector is provided for scaling the velocity field. (I = 85 A, welding position: C1, travel speed: 2.5 mm s^{-1} and sulphur concentration: 240 ppm)

Variation in the welding position can affect melt-pool surface deformations, resulting in changes in the power-density and arc force distribution over the melt-pool surface and thus the evolution of the melt-pool shape and its oscillatory behaviour. The influence of welding position on melt-pool shape is shown in figure 8.9 for cases with a travel speed of 2.5 mm s^{-1} and sulphur concentration of 240 ppm. When welding downward (C2–C4), the molten material is pulled by the gravitational force towards the front part of the melt pool and forms a bulge beneath the welding torch. This change in the melt-pool surface morphology decreases the average arc length and alters the power-density distribution, through changing the distribution parameter σ_q (equation (3.36)), and thus temperature profile over the surface. The change in the power-density distribution in turn increases the temperature gradients over the melt-pool surface and thus the magnitude of Marangoni forces. The results reveal that the molten material moves from the rear of the melt pool towards the front around the centreline, resulting in further reduction of the melt-pool thickness in the rear part of the melt pool, which can eventually lead to the rupture of the liquid layer and melt-pool collapse if the dynamic force balance cannot be maintained. In contrast, when welding upward (C6–C8), the molten material moves towards the rear part of the melt pool because of the gravitational force, forming a concavity in the front part of the pool. The formation of this concavity increases the average arc length beneath the welding torch and the distribution parameter σ_q (equation (3.36)). This increase in the distribution parameter reduces the temperature gradients over the melt pool surface and thus the magnitude of Marangoni forces. These results suggest that although the melt-pool shape and its surface morphology are influenced by the welding position, the overall flow structure in the melt pool, which is dominated by Marangoni and electromagnetic forces, is not affected significantly by the gravitational force [46]. The results in figure 8.9 also show that the material thickness H reduces locally beneath the welding torch with the increase in the average arc length in the cases that welding direction is upward (C6–C8). This reduction in the material thickness results in the establishment of full penetration somewhat earlier at $t \approx 3$ s compared to that of the case C1 and C5, changing the oscillation frequency as reflected in figure 8.4. The results suggest that when the relative material thickness (H/H_m) beneath the welding torch reduces to values less than about 0.65, an unsteady multicellular flow pattern evolves in the pool [18, 56], leading to irregular surface deformations that are reflected in the time-frequency spectra shown in figure 8.4(b and d) for $t > 6$ s.

Figure 8.10 shows the melt-pool shape and thermal and flow fields over the melt-pool surfaces at $t = 10$ s for GTA welding in welding position C1 with a travel speed of 2.5 mm s^{-1} and different sulphur concentrations in the material. The results of the present numerical simulations suggest that both the amplitude and frequency of oscillations decrease with reducing the sulphur concentration in the material. Reducing sulphur concentration results in an increase in the average surface tension, affects the variation of surface tension with temperature ($\partial\gamma/\partial T$) and reduces the critical temperature at which the sign of the temperature gradient of surface tension ($\partial\gamma/\partial T$) changes, according to equation (3.78) (see figure 3.2). The flow pattern over the melt-pool top surface becomes mostly outward when the sulphur concentration in the material is reduced. The increasingly outward fluid flow weakens disturbances caused by the interaction of inward and outward fluid flows over the melt-pool surface. Additionally, the outward

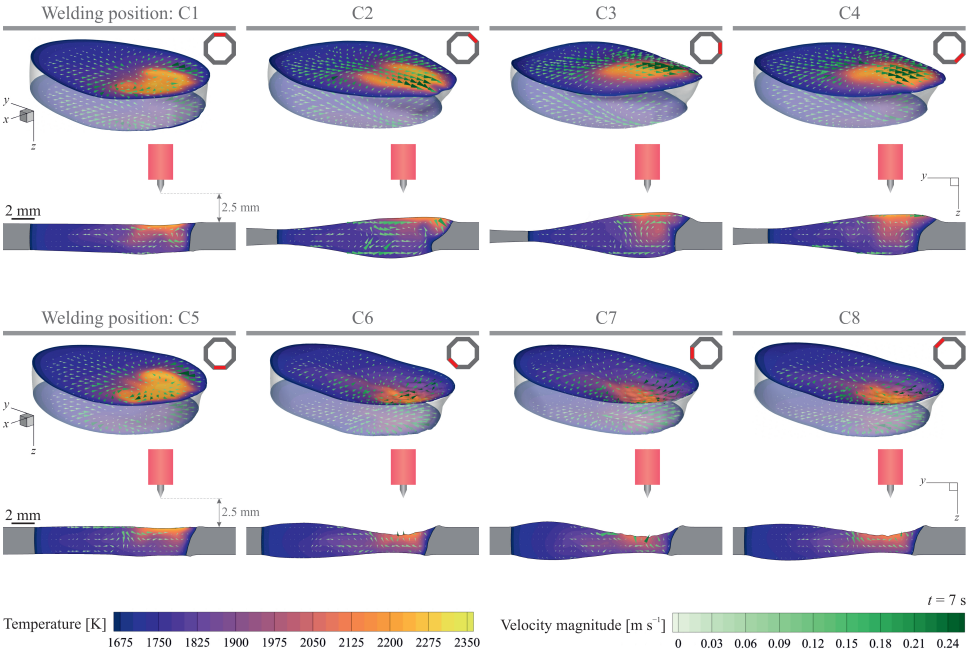

Figure 8.9: The influence of the welding position on evolution of the melt-pool shape during gas tungsten arc welding. Contours show the temperature profile at $t = 7$ s and are overlaid with velocity vectors. Cross sections on the y-z plane are located at $x = 0$. ($I = 85$ A, travel speed: 2.5 mm s^{-1} and sulphur concentration: 240 ppm)

fluid flow transfers the heat absorbed by the material towards the melt-pool boundary, reducing the maximum temperature and the magnitude of temperature gradients over the melt-pool surface. Moreover, the outward flow results in a relatively larger melt-pool surface area on the top surface compared to that on the bottom surface and fluid velocities decrease on the bottom surface. These changes in the flow field alter the melt-pool shape, as shown in figure 8.10, and in turn affect the melt-pool oscillatory behaviour. A notable change in the time-frequency spectra of the cases with sulphur concentrations of 120 ppm and 60 ppm (figure 8.5) compared to that with a sulphur concentration of 240 ppm (figure 8.3(a)) is that the frequency of oscillations decreases gradually over time and does not change suddenly as observed in figure 8.3(a) at $t \approx 4$ s.

The influence of travel speed on melt-pool shape and heat and fluid flow in the melt pool during GTA welding in position C1 is shown in figure 8.11 for the cases with a sulphur concentration of 240 ppm. Increasing the travel speed, while keeping other process parameters the same, results in a decrease in the melt-pool size, which is due to the reduction of nominal heat input to the material. Additionally, the melt-pool shape changes from a virtually circular shape to a teardrop shape with increasing travel speed. The flow pattern obtained from the numerical simulations also reveals that vortex structures do not form over the melt-pool surface for the case with a travel speed of 1.25 mm s^{-1}, in contrast to other cases with higher travel speeds. Moreover, the offset between the top

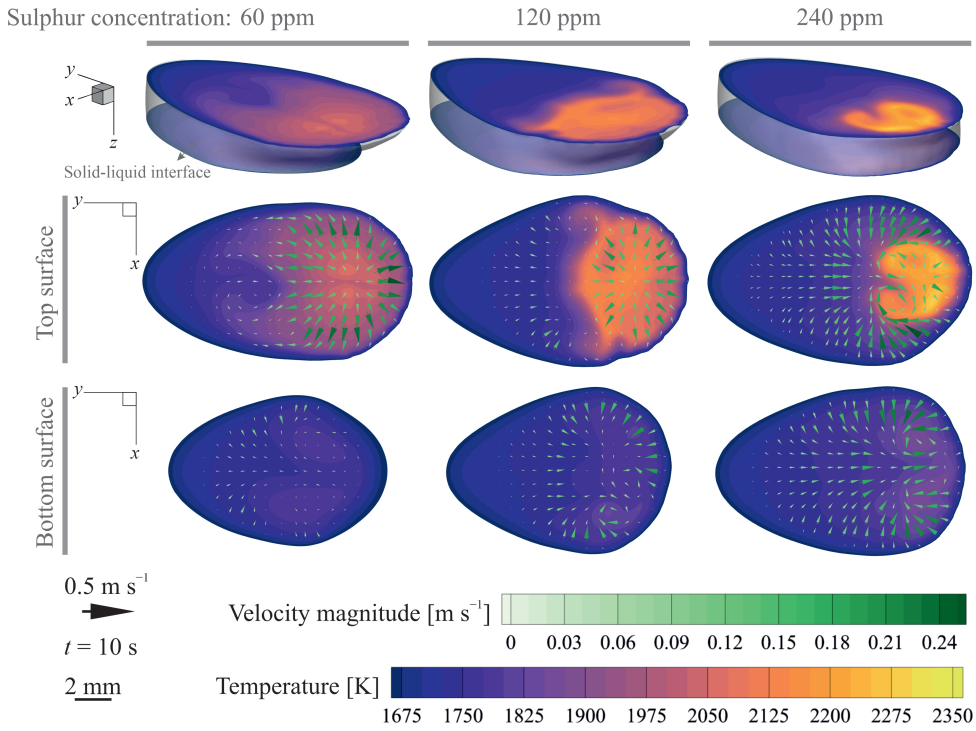

Figure 8.10: The influence of sulphur concentration in the material on the melt-pool shape during gas tungsten arc welding. Contours show the temperature profile at $t = 10\,\mathrm{s}$ and are overlaid with velocity vectors. The $0.5\,\mathrm{m\,s^{-1}}$ reference vector is provided for scaling the velocity field. ($I = 85\,\mathrm{A}$, travel speed: $2.5\,\mathrm{mm\,s^{-1}}$ and welding position: C1)

and bottom melt-pool surfaces increases with increasing the travel speed. The offset measured at the leading edge of the pool with respect to the z-axis increases from about 5° at a travel speed of $1.25\,\mathrm{mm\,s^{-1}}$ to values of about 50° at a travel speed of $5\,\mathrm{mm\,s^{-1}}$.

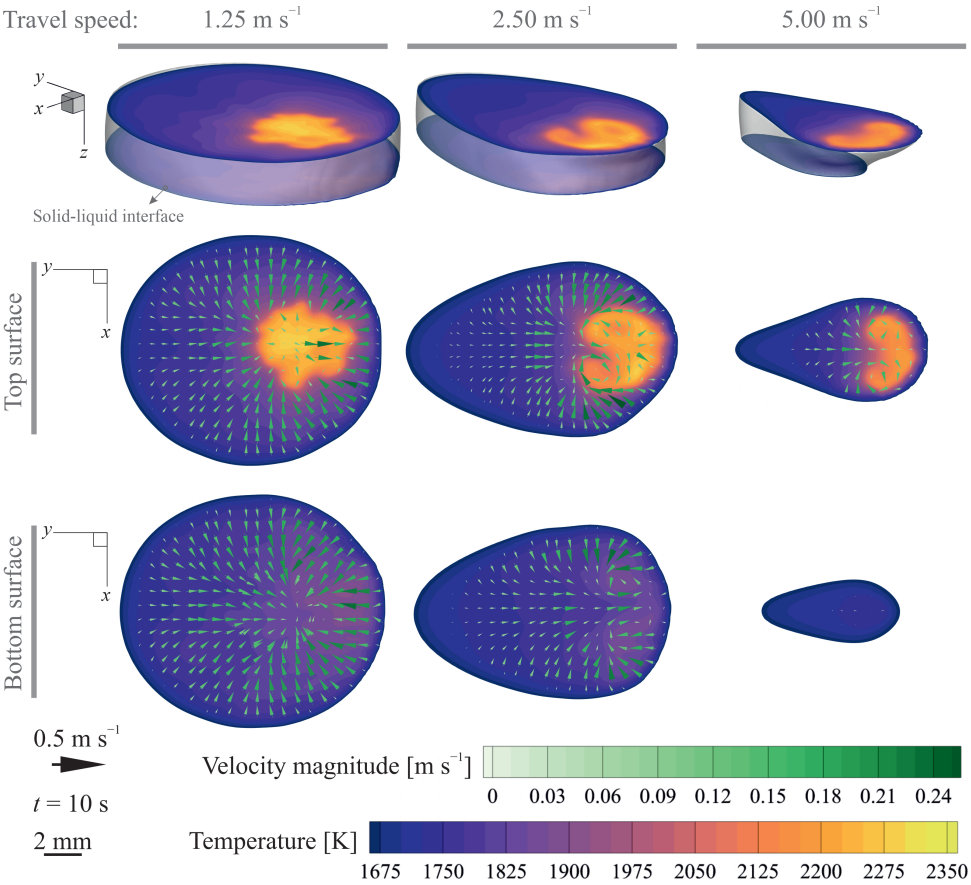

Figure 8.11: The influence of travel speed on the melt-pool shape during gas tungsten arc welding. Contours show the temperature profile at $t = 10$ s and are overlaid with velocity vectors. The 0.5 m s^{-1} reference vector is provided for scaling the velocity field. ($I = 85$ A, sulphur concentration: 240 ppm and welding position: C1)

8.6. Conclusions

High-fidelity three-dimensional numerical simulations were performed to study the oscillatory behaviour of fully-penetrated melt pools during positional gas tungsten arc welding. The influence of welding positions, the sulphur concentration in the material and travel speed on complex unsteady convection in the melt pool and oscillations of the melt-pool surface were investigated. The frequencies predicted using the present computational model were compared with analytical and experimental data, and reasonably good agreement (within 5% deviation bands) is achieved. Using the present numerical approach, evolutions of the melt-pool surface oscillations during GTA welding are described by revealing the unsteady complex flow pattern in the melt pools and subsequent changes in the melt-pool shape, which are generally difficult to visualise experimentally. Moreover,

evolution of the frequency of melt-pool oscillations during arc welding are not predictable using the analytical models that are available in the open literature.

Melt-pool oscillatory behaviour depends on surface tension of the molten material and shape and size of the melt-pool. Changes in material properties and welding process parameters affect convection in the melt pool, hydrodynamic instabilities that arise and resultant variations in the melt-pool shape. Depending on the processing condition, these instabilities can also grow in time, affecting melt-pool stability and may even lead to melt-pool collapse and process failure. Welding position affects the melt-pool surface morphology, altering the spatial distribution of arc forces and power-density applied to the molten material and thus changes flow pattern in the melt-pool. The change in the flow pattern affects the evolution of the melt-pool shape and its oscillatory behaviour. The frequency of oscillations seems to vary within the same range ($22\,\text{Hz} < f < 73\,\text{Hz}$) for different welding positions studied in the present work, however the evolution of oscillation frequencies, which depends on the melt-pool shape, is affected by welding position. Under similar welding conditions, sulphur concentration in the material significantly affects the thermal and flow fields in the melt pool and consequently the shape of the pool, changing the oscillatory behaviour of the melt-pool. Increasing the travel speed decreases the melt-pool size, increases the offset between top and bottom melt-pool surfaces and also affects the flow structures (vortex formation) on the melt-pool surface. These observations offer an insight into the complex melt-pool oscillatory behaviour during positional gas tungsten arc welding and suggest that the processing window for advanced fusion-based manufacturing processes can be determined by utilising numerical simulations that can potentially reduce the costs associated with process development and optimisation.

References

[1] Aucott, L., Dong, H., Mirihanage, W., Atwood, R., Kidess, A., Gao, S., Wen, S., Marsden, J., Feng, S., Tong, M., Connolley, T., Drakopoulos, M., Kleijn, C. R., Richardson, I. M., Browne, D. J., Mathiesen, R. H., and Atkinson, H. V. Revealing internal flow behaviour in arc welding and additive manufacturing of metals. *Nature Communications*, 9(1), 2018. doi:10.1038/s41467-018-07900-9.

[2] DebRoy, T. and David, S. A. Physical processes in fusion welding. *Reviews of Modern Physics*, 67(1):85–112, 1995. doi:10.1103/revmodphys.67.85.

[3] DebRoy, T., Wei, H. L., Zuback, J. S., Mukherjee, T., Elmer, J. W., Milewski, J. O., Beese, A. M., Wilson-Heid, A., De, A., and Zhang, W. Additive manufacturing of metallic components – Process, structure and properties. *Progress in Materials Science*, 92:112–224, 2018. doi:10.1016/j.pmatsci.2017.10.001.

[4] Mills, K. C. and Keene, B. J. Factors affecting variable weld penetration. *International Materials Reviews*, 35(1):185–216, 1990. doi:10.1179/095066090790323966.

[5] Juang, S. C. and Tarng, Y. S. Process parameter selection for optimizing the weld pool geometry in the tungsten inert gas welding of stainless steel. *Journal of Materials Processing Technology*, 122(1):33–37, 2002. doi:10.1016/s0924-0136(02)00021-3.

[6] Cunningham, R., Zhao, C., Parab, N., Kantzos, C., Pauza, J., Fezzaa, K., Sun, T., and Rollett, A. D. Keyhole threshold and morphology in laser melting revealed by ultrahigh-speed x-ray imaging. *Science*, 363(6429):849–852, 2019. doi:10.1126/science.aav4687.

[7] Lancaster, J. F., editor. *The Physics of Welding*. International series on materials science of technology. Pergamon Press, Oxford, UK, 2nd edition, 1986. ISBN 0080340768.

[8] Li, C., Shi, Y., Du, L., Yufen, G., and Zhu, M. Real-time measurement of weld pool oscillation frequency in GTAW-P process. *Journal of Manufacturing Processes*, 29:419–426, 2017. doi:10.1016/j.jmapro.2017.08.011.

[9] Shi, Y., Zhang, G., Ma, X. J., Gu, Y. F., Huang, J. K., and Fan, D. Laser-vision-based measurement and analysis of weld pool oscillation frequency in GTAW-P. *Welding Journal*, 94(5):176s–187s, 2015. URL: https://app.aws.org/wj/supplement/WJ_2015_05_s176.pdf.

[10] Xiao, Y. H. and den Ouden, G. A study of GTA weld pool oscillation. *Welding Journal*, 69(8): 289s–293s, 1990. URL: http://files.aws.org/wj/supplement/WJ_1990_08_s289.pdf.

[11] Yoo, C. D. and Richardson, R. W. An experimental study on sensitvity and signal characteristics of welds pool oscillation. *Transactions of the Japan Welding Society*, 24(2):54–62, 1993. URL: https://ci.nii.ac.jp/naid/110003379951/en/.

[12] Tam, A. S. and Hardt, D. E. Weld pool impedance for pool geometry measurement: Stationary and nonstationary pools. *Journal of Dynamic Systems, Measurement, and Control*, 111(4): 545–553, 1989. doi:10.1115/1.3153090.

[13] Xiao, Y. H. *Weld Pool Oscillation during Gas Tungsten Arc Welding*. PhD dissertation, Delft University of Technology, 1992. URL: http://resolver.tudelft.nl/uuid:f91da1e6-1a17-4223-9d73-419f1ac9c312.

[14] Xiao, Y. H. and den Ouden, G. Weld pool oscillation during GTA welding of mild steel. *Welding Journal*, 72(8):428s–434s, 1993. URL: http://files.aws.org/wj/supplement/WJ_1993_08_s428.pdf.

[15] Andersen, K., Cook, G. E., Barnett, R. J., and Strauss, A. M. Synchronous weld pool oscillation for monitoring and control. *IEEE Transactions on Industry Applications*, 33(2):464–471, 1997. doi:10.1109/28.568011.

[16] Maruo, H. and Hirata, Y. Natural frequency and oscillation modes of weld pools. 1st report: Weld pool oscillation in full penetration welding of thin plate. *Welding International*, 7(8): 614–619, 1993. doi:10.1080/09507119309548457.

[17] Wu, F., Falch, K. V., Guo, D., English, P., Drakopoulos, M., and Mirihanage, W. Time evolved force domination in arc weld pools. *Materials & Design*, 190:108534, 2020. doi:10.1016/j.matdes.2020.108534.

[18] Ebrahimi, A., Kleijn, C. R., and Richardson, I. M. A simulation-based approach to characterise melt-pool oscillations during gas tungsten arc welding. *International Journal of Heat and Mass Transfer*, 164:120535, 2021. doi:10.1016/j.ijheatmasstransfer.2020.120535.

[19] Cook, P. S. and Murphy, A. B. Simulation of melt pool behaviour during additive manufacturing: Underlying physics and progress. *Additive Manufacturing*, 31:100909, 2020. doi:10.1016/j.addma.2019.100909.

[20] Kou, S. and Sun, D. K. Fluid flow and weld penetration in stationary arc welds. *Metallurgical Transactions A*, 16(1):203–213, 1985. doi:10.1007/bf02815302.

[21] Zacharia, T., Eraslan, A. H., Aidun, D. K., and David, S. A. Three-dimensional transient model for arc welding process. *Metallurgical Transactions B*, 20(5):645–659, 1989. doi:10.1007/bf02655921.

[22] Wu, C. S. and Dorn, L. Computer simulation of fluid dynamics and heat transfer in full-penetrated TIG weld pools with surface depression. *Computational Materials Science*, 2(2): 341–349, 1994. doi:10.1016/0927-0256(94)90116-3.

[23] Wu, C. S., Chen, J., and Zhang, Y. M. Numerical analysis of both front- and back-side deformation of fully-penetrated GTAW weld pool surfaces. *Computational Materials Science*, 39(3): 635–642, 2007. doi:10.1016/j.commatsci.2006.08.018.

[24] Mishra, S., Lienert, T. J., Johnson, M. Q., and DebRoy, T. An experimental and theoretical study of gas tungsten arc welding of stainless steel plates with different sulfur concentrations. *Acta Materialia*, 56(9):2133–2146, 2008. doi:10.1016/j.actamat.2008.01.028.

[25] Traidia, A. and Roger, F. Numerical and experimental study of arc and weld pool behaviour for pulsed current GTA welding. *International Journal of Heat and Mass Transfer*, 54(9-10): 2163–2179, 2011. doi:10.1016/j.ijheatmasstransfer.2010.12.005.

[26] Mougenot, J., Gonzalez, J.-J., Freton, P., and Masquère, M. Plasma–weld pool interaction in tungsten inert-gas configuration. *Journal of Physics D: Applied Physics*, 46(13):135206, 2013. doi:10.1088/0022-3727/46/13/135206.

[27] Hao, H., Gao, J., and Huang, H. Numerical simulation for dynamic behavior of molten pool in tungsten inert gas welding with reserved gap. *Journal of Manufacturing Processes*, 58:11–18, 2020. doi:10.1016/j.jmapro.2020.07.063.

[28] Thompson, M. E. and Szekely, J. The transient behavior of weldpools with a deformed free surface. *International Journal of Heat and Mass Transfer*, 32(6):1007–1019, 1989. doi:10.1016/0017-9310(89)90003-3.

[29] Tsai, M. C. and Kou, S. Marangoni convection in weld pools with a free surface. *International Journal for Numerical Methods in Fluids*, 9(12):1503–1516, 1989. doi:10.1002/fld.1650091206.

[30] Kim, S. D. and Na, S. J. Effect of weld pool deformation on weld penetration in stationary gas tungsten arc-welding. *Welding Journal*, 71(5):179s–193s, 1992. URL: `https://app.aws.org/wj/supplement/WJ_1992_05_s179.pdf`.

[31] Zhang, Y. M., Cao, Z. N., and Kovacevic, R. Numerical analysis of fully penetrated weld pools in gas tungsten arc welding. *Proceedings of the Institution of Mechanical Engineers, Part C: Journal of Mechanical Engineering Science*, 210(2):187–195, 1996. doi:10.1243/pime_proc_1996_210_185_02.

[32] Cao, Z. N., Zhang, Y. M., and Kovacevic, R. Numerical dynamic analysis of moving GTA weld pool. *Journal of Manufacturing Science and Engineering*, 120(1):173–178, 1998. doi:10.1115/1.2830096.

[33] Liu, J. W., Rao, Z. H., Liao, S. M., and Tsai, H. L. Numerical investigation of weld pool behaviors and ripple formation for a moving GTA welding under pulsed currents. *International Journal of Heat and Mass Transfer*, 91:990–1000, 2015. doi:10.1016/j.ijheatmasstransfer.2015.08.046.

[34] Meng, X., Qin, G., Bai, X., and Zou, Z. Numerical analysis of undercut defect mechanism in high speed gas tungsten arc welding. *Journal of Materials Processing Technology*, 236:225–234, 2016. doi:10.1016/j.jmatprotec.2016.05.020.

[35] Feng, C., Qin, G., Meng, X., and Geng, P. Defect evolution of 409L stainless steel in high-speed TIG welding. *Materials and Manufacturing Processes*, 35(2):179–186, 2020. doi:10.1080/10426914.2020.1711925.

[36] Du, J., Zhao, G., and Wei, Z. Effects of welding speed and pulse frequency on surface depression in variable polarity gas tungsten arc welding of aluminum alloy. *Metals*, 9(2):114, 2019. doi:10.3390/met9020114.

[37] Pan, J., Hu, S., Yang, L., and Wang, D. Investigation of molten pool behavior and weld bead formation in VP-GTAW by numerical modelling. *Materials & Design*, 111:600–607, 2016. doi:10.1016/j.matdes.2016.09.022.

[38] Chen, Y., David, S. A., Zacharia, T., and Cremers, C. J. Marangoni convection with two free surfaces. *Numerical Heat Transfer, Part A: Applications*, 33(6):599–620, 1998. doi:10.1080/10407789808913957.

[39] Ko, S. H., Yoo, C. D., Farson, D. F., and Choi, S. K. Mathematical modeling of the dynamic behavior of gas tungsten arc weld pools. *Metallurgical and Materials Transactions B*, 31(6): 1465–1473, 2000. doi:10.1007/s11663-000-0031-1.

[40] Ko, S. H., Choi, S. K., and Yoo, C. D. Effects of surface depression on pool convection and geometry in stationary GTAW. *Welding Journal*, 80(2):39s–45s, 2001. URL: `https://app.aws.org/wj/supplement/Ko02-01.pdf`.

[41] Sahoo, P., Debroy, T., and McNallan, M. J. Surface tension of binary metal—surface active solute systems under conditions relevant to welding metallurgy. *Metallurgical Transactions B*, 19(3):483–491, 1988. doi:10.1007/bf02657748.

[42] Joshi, Y., Dutta, P., Schupp, P. E., and Espinosa, D. Nonaxisymmetric convection in stationary gas tungsten arc weld pools. *Journal of Heat Transfer*, 119(1):164–172, 1997. doi:10.1115/1.2824082.

[43] Zhao, C. X., van Steijn, V., Richardson, I. M., Kleijn, C. R., Kenjeres, S., and Saldi, Z. Unsteady interfacial phenomena during inward weld pool flow with an active surface oxide. *Science and Technology of Welding and Joining*, 14(2):132–140, 2009. doi:10.1179/136217108x370281.

[44] Kidess, A., Kenjereš, S., and Kleijn, C. R. The influence of surfactants on thermocapillary flow instabilities in low Prandtl melting pools. *Physics of Fluids*, 28(6):062106, 2016. doi:10.1063/1.4953797.

[45] Kang, N., Mahank, T. A., Kulkarni, A. K., and Singh, J. Effects of gravitational orientation on surface deformation and weld pool geometry during gas tungsten arc welding. *Materials and Manufacturing Processes*, 18(2):169–180, 2003. doi:10.1081/amp-120018903.

[46] Nguyen, M. C., Medale, M., Asserin, O., Gounand, S., and Gilles, P. Sensitivity to welding positions and parameters in GTA welding with a 3D multiphysics numerical model. *Numerical Heat Transfer, Part A: Applications*, 71(3):233–249, 2017. doi:10.1080/10407782.2016.1264747.

[47] Tsai, N. S. and Eagar, T. W. Distribution of the heat and current fluxes in gas tungsten arcs. *Metallurgical Transactions B*, 16(4):841–846, 1985. doi:10.1007/bf02667521.

[48] Lin, M. L. and Eagar, T. W. Pressures produced by gas tungsten arcs. *Metallurgical Transactions B*, 17(3):601–607, 1986. doi:10.1007/bf02670227.

[49] Mills, K. C. *Recommended Values of Thermophysical Properties for Selected Commercial Alloys*. Woodhead Publishing, woodhead publishing series in metals and surface engineering edition, 2002. ISBN 978-1-85573-569-9.

[50] *Release 19.2*. ANSYS Fluent. URL: `https://www.ansys.com/`.

[51] Issa, R. I. Solution of the implicitly discretised fluid flow equations by operator-splitting. *Journal of Computational Physics*, 62(1):40–65, 1986. doi:10.1016/0021-9991(86)90099-9.

[52] Patankar, S. V. *Numerical Heat Transfer and Fluid Flow*. Taylor & Francis Inc, 1st edition, 1980. ISBN 0891165223.

[53] Ubbink, O. *Numerical Prediction of Two Fluid Systems with Sharp Interfaces*. PhD dissertation, Imperial College London (University of London), London, United Kingdom, 1997. URL: `http://hdl.handle.net/10044/1/8604`.

[54] Li, C., Shi, Y., Gu, Y., and Yuan, P. Monitoring weld pool oscillation using reflected laser pattern in gas tungsten arc welding. *Journal of Materials Processing Technology*, 255:876–885, 2018. doi:10.1016/j.jmatprotec.2018.01.037.

[55] Yudodibroto, Y. B. *Liquid metal oscillations and arc behaviour during welding*. PhD dissertation, Delft University of Technology, 2010. URL: `http://resolver.tudelft.nl/uuid:dcae1f78-9186-4161-ad88-711f27781335`.

[56] Schatz, M. F. and Neitzel, G. P. Experiments on thermocapillary instabilities. *Annual Review of Fluid Mechanics*, 33(1):93–127, 2001. doi:10.1146/annurev.fluid.33.1.93.

9

Melt Pool Behaviour in Gas Metal Arc Welding: The Effect of Joint Shape

One of the challenges for development, qualification and optimisation of arc welding processes lies in characterising the complex melt-pool behaviour which exhibits highly non-linear responses to variations of process parameters. The present work presents a simulation-based approach to describe the melt-pool behaviour in root-pass gas metal arc welding (GMAW). Three-dimensional numerical simulations have been performed using an enhanced physics-based computational model to unravel the effect of groove shape on complex unsteady heat and fluid flow in GMAW. The influence of surface deformations on power-density distribution and the forces applied to the molten material were taken into account. Utilising this model, the complex heat and fluid flow in melt pools was visualised and described for different groove shapes. Additionally, experiments were performed to validate the numerical predictions and the robustness of the present computational model is demonstrated. The model can be used to explore physical effects of governing fluid flow and melt-pool stability during gas metal arc root welding.

The contents of this chapter have been published in *Materials*, **2021**, *14*(23), 7444, DOI: 10.3390/ma14237444.

9.1. Introduction

Gas metal arc welding (GMAW) is a fusion-based joining technique that is widely employed in industry to join metallic parts and to produce high-integrity structures. The quality of the joints made using arc welding or the structures made using wire-arc additive manufacturing depend on chosen process parameters, material properties and boundary conditions [1–3]. Changes in operating variables can alter the magnitude and distribution of the heat input and forces applied to the molten metal in melt pools (such as Marangoni, Lorentz, thermal buoyancy forces and arc plasma shear stresses and pressures), affecting fluid flow in the pool and in turn the properties, structure and quality of products [2]. Correct control of melt-pool behaviour during arc welding is crucial to produce joints with desired properties [4].

One of the challenges for development, qualification and optimisation of arc welding processes lies in characterising the complex melt-pool behaviour which exhibits highly non-linear responses to variations of process parameters [5]. Trial-and-error experiments are often employed to realise appropriate processing parameters to achieve the desired properties. Such an experimental approach is costly and time inefficient and a successful processing for a specific configuration (*e.g.* material system, welding machine and joint shape) might not apply to a different configuration. Moreover, experimental identification of the effects of various parameters on the melt-pool behaviour is generally complicated due to the high-temperature, rapid solid-liquid phase transformation, opacity and fast dynamics of the molten metal flow [4]. Simulation-based approaches offer understanding of the melt-pool behaviour during welding and additive manufacturing and can serve as an alternative to experiments to explore the design space for process optimisation [1, 6].

To date, focus has predominantly been placed on developing numerical simulations to describe melt-pool behaviour in arc welding of flat plates without a groove (*i.e.* bead-on-plate welding, see for instance, [7–15]); however little attention has been paid to understanding the effect of joint shape on complex heat and molten metal flow. Zhang *et al.* [16, 17] developed a three-dimensional model in a body-fitted coordinate system to describe the effects of various driving forces on heat and fluid flow in the melt pool during GMAW fillet welding. Hu and Tsai [18] developed a comprehensive model to simulate unsteady molten metal flow and heat transfer in melt-pools during GMA welding of a thick plate with V-groove. These studies only focus on partially penetrated pools and do not report the effect of different joint shapes on molten metal flow behaviour. Chen *et al.* [19] studied the effect of the opening angle of a V-groove on melt-pool behaviour during relatively high-current GMAW (welding current $I = 340\,\text{A}$) using a computational model developed on the basis of a body-fitted coordinate system. They reported that changes in the opening angle have an insignificant effect on the flow pattern in the pool but can affect the velocity and temperature distribution and thus the pool shape. Using the Abel inversion method, Cho and Na [20] reconstructed the emissivity distribution of an arc plasma and argued that the application of V-grooves in arc welding can affect the arc plasma characteristics, changing the distribution of the power-density, arc pressure and electromagnetic forces [21]. On the basis of their previous studies [20, 21], Cho *et al.* [22] employed an elliptically symmetric distribution functions for power-density and arc pressure (instead of an axisymmetric distribution) to simulate heat and fluid flow in GMAW of a plate with V-groove at different welding positions.

Changes in the groove shape due to filler metal deposition and its effect on the distribution of power-density and arc-induced forces were not accounted for in previous models that are available in the literature. Further investigations are required to realise the influence of the joint shape on molten metal flow behaviour in GMAW, particularly for fully-penetrated melt pools.

Focusing on understanding the melt-pool behaviour during root-pass gas metal arc welding, with particular interest in the effects of groove shape, a systematic numerical study was carried out in the present work. Three-dimensional calculations have been performed using a physics-based computational model to simulate the dynamics of heat and molten metal flow in GMAW. Additionally, experiments were performed to validate the numerical predictions. The present work explains the dynamics of internal molten metal flow in gas metal arc welding and provides an enhanced computational model for design space explorations.

9.2. Problem description

In gas metal arc welding, an electric arc between a consumable electrode (filler metal) and a workpiece provides the thermal energy required for melting the material. Melting of the filler metal results in the periodic formation of molten metal droplets that successively impinge on the workpiece surface. Thermal energy input from the arc plasma as well as the thermal energy transported by the droplets leads to the formation of a melt pool that creates a joint after solidification (see figure 9.1). In the present work, the effect of the groove shape on molten metal flow behaviour is studied for three different groove shapes, as shown schematically in figure 9.1. A torch, which is perpendicular to the workpiece top-surface is adopted here and the contact-tip to workpiece distance (CTWD) is set to 18 mm. Different values of welding current ranging between 220 A and 280 A have been studied. Details of the welding parameters in the present work are listed in table 9.1. The process parameters employed in the present work have been chosen based on preliminary trial experiments and are also comparable to those reported in previous independent studies on gas metal arc welding of steel plates with grooves (see for instance, [17, 18, 21, 22]). The plates are made of a stainless steel alloy (AISI 316L) and are initially at an ambient temperature of 300 K. The welding torch is initially located in the middle of the workpiece along the x-axis and 10 mm away from the leading-edge of the workpiece (*i.e.* $y = 10$ mm).

The computational domain is defined in a stationary Cartesian coordinate system and is in the form of a rectangular cube that encompasses the metallic workpiece and two layers of gas below and above the workpiece. The incorporation of the gas layers allows tracking of surface deformations of the pool. To reduce the complexity of simulations and computation time, the melt-pool is decoupled from the arc plasma in the simulations. Accordingly, the heat input from the arc and the arc induced forces are defined as source terms for thermal energy and momentum. These source terms are adjusted dynamically during the calculations, as explained in section 3.2.3, to account for the changes in the arc power and power-density distribution as well as the magnitude and distribution of the forces exerted by the arc plasma that occur due to melt-pool surface deformations and filler metal deposition. The conditions applied to the outer boundaries of the computational domain are shown in figure 9.1. The outer boundaries of the plates

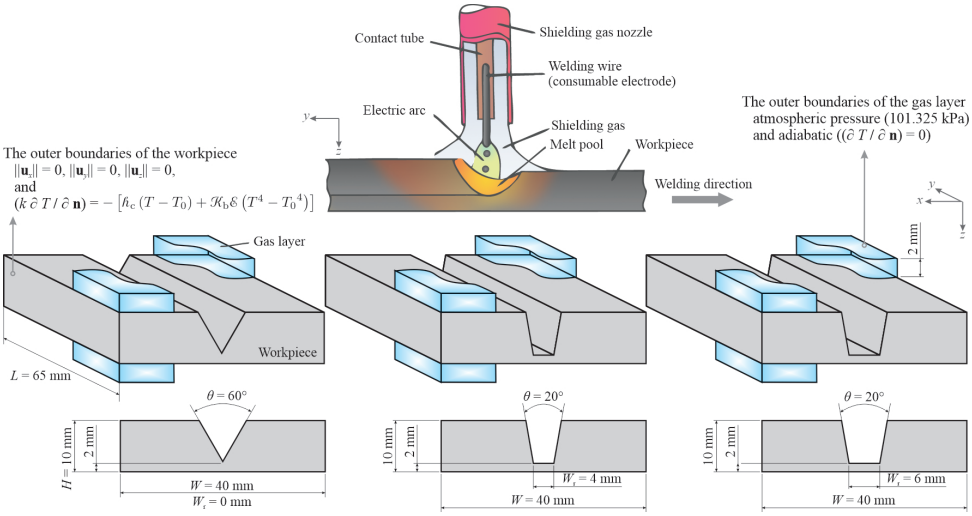

Figure 9.1: Schematic of gas metal arc welding and three different joint shapes studied in the present work. For the sake of clarity, only parts of the gas layer are shown. Here W_r refers to the width of flat region at the base of the groove, referred to as the root-leg.

Table 9.1: Welding parameters studied in the present work.

Parameter	Value	Unit
Welding current I	220 −280	A
Arc voltage U	21.4 −23.0	V
Wire feed rate u_w	7.0 −8.7	$m\,min^{-1}$
Wire diameter d_w	1.2 (0.045)	mm (inch)
Wire material	AISI 316L	–
Travel speed V	7.5	$mm\,s^{-1}$
Shielding gas	97.5% Ar + 2.5% CO_2	–
Shielding gas flow rate	20	$l\,min^{-1}$
Inner diameter of the shielding cup	20	mm
CTWD	18	mm
Distance between the contact tip and the shielding cup edge	2	mm
Torch angle	90	°

are treated as no-slip walls, as the melt-pool does not reach them, and heat losses due to radiation and convection are accounted for. A fixed atmospheric pressure (101 325 Pa) is applied to the outer boundaries of the gas layers. The thermophysical properties of AISI 316L and the gas employed in the simulations are presented in table 9.2 and figure 9.2. The values for the surface tension are estimated using an empirical correlation proposed by Sahoo *et al.* [23], which takes the influence of surfactants (*i.e.* sulphur) into account. Employing a temperature-dependent density model, thermal buoyancy force

are accounted for in the simulations. In the present work, the properties of the shielding gas are assumed to be temperature-independent, which is a common assumption in numerical simulations of arc welding and additive manufacturing where the melt-pool is decoupled from the arc plasma [7–9, 11–13, 22]. This assumption is justifiable as the transport properties of the shielding gas (*i.e.* viscosity, density and thermal conductivity) are small compared to those of the molten metal, and thus changes in the shielding gas properties with temperature negligibly affect the numerical predictions of fluid flow in the melt pool [24]. The droplet temperature T_d was approximated to 2500 K, based on the experimental data reported by Soderstrom *et al.* [25].

Table 9.2: Thermophysical properties of the stainless steel (AISI 316L) and the gas employed in the numerical simulations. Values for AISI 316 are taken from [26].

Property	Stainless steel (AISI 316)	Gas	Unit
Density ρ	see figure 9.2	1.623	$\mathrm{kg\,m^{-3}}$
Specific heat capacity c_p	see figure 9.2	520.64	$\mathrm{J\,kg^{-1}\,K^{-1}}$
Thermal conductivity k	see figure 9.2	1.58×10^{-2}	$\mathrm{W\,m^{-1}\,K^{-1}}$
Viscosity μ	see figure 9.2	2.12×10^{-5}	$\mathrm{kg\,m^{-1}\,s^{-1}}$
Latent heat of fusion $\mathscr{L}_\mathrm{f}$	2.7×10^{5}	–	$\mathrm{J\,kg^{-1}}$
Liquidus temperature T_l	1723	–	K
Solidus temperature T_s	1658	–	K

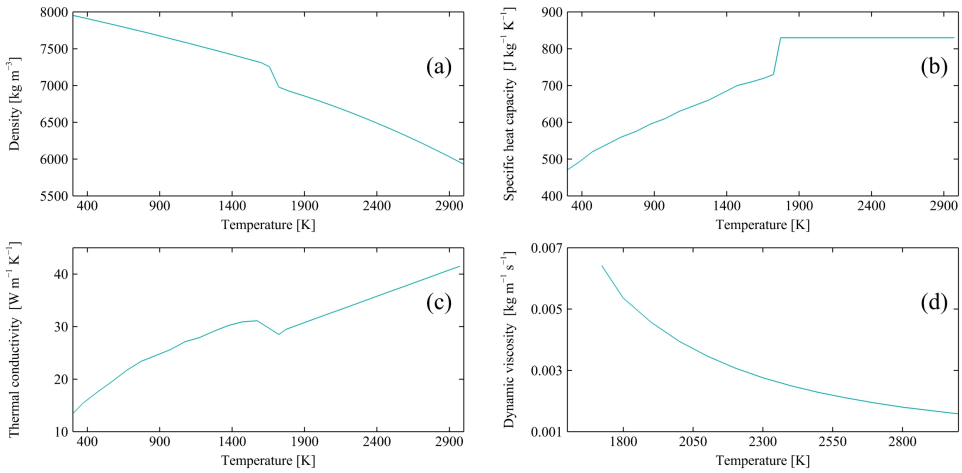

Figure 9.2: Temperature-dependent thermophysical properties of AISI 316L employed in the simulations. (a) density [27], (b) specific heat capacity at constant pressure [26], (c) thermal conductivity [26] and (d) dynamic viscosity [27].

9.3. Numerical procedure

The computational model employed in the present work was developed within the framework of a proprietary finite-volume solver, ANSYS Fluent [28]. To implement the source terms in the governing equations and the surface tension model, user-defined subroutines programmed in the C programming language were used. The computational domain contains about 2.7×10^6 non-uniform hexahedral cells, with the smallest cell spacing being set to 80 µm in the melt-pool region, which is sufficiently fine to obtain grid-independent solutions [29–32]. The cell spacing increases gradually from the melt-pool region towards the boundaries of the computational domain and the maximum cell size was limited to 400 µm. The central-differencing scheme with second-order accuracy was employed for spatial discretisation of momentum advection and diffusive fluxes. A first-order implicit scheme was employed for the time marching, and a fixed time-step size of 2×10^{-5} s was used to keep the value of the Courant number ($\mathrm{Co} = \|\mathbf{u}\|\Delta t/\Delta x$) below 0.25. To formulate the advection of the volume-fraction scalar field, an explicit compressive VOF method [33] was employed. Moreover, the PRESTO (pressure staggering option) scheme [34] and the PISO (pressure-implicit with splitting of operators) scheme [35] was employed for the pressure interpolation and coupling velocity and pressure fields, respectively. Simulations were executed in parallel on a high-performance computing cluster, each on 70 cores (AMD EPYC 7452) and the total run-time was about 290 h.

9.4. Experimental setup and procedure

The general process parameters studied in the present work are introduced in section 9.2. Figure 9.3 shows a schematic drawing of the experimental setup utilised in the present work. A Fronius CMT 5000i power source that was attached to a six-axis Fanuc robot was employed. Weld beads with a length of 80 mm were deposited on the workpiece with pre-machined grooves. Each experiment was repeated at least three times to ensure repeatability of the tests. The filler metal and the workpiece employed in the experiments were AISI 316L. Welding current and voltage were measured and recorded during the experiments at a frequency of 5 kHz using a Triton 4000 data acquisition system. Samples were cut after the experiments to extract transverse cross-sections. The cut samples were mounted and surface ground using silicon carbide (SiC) papers with grit sizes varying from 80 to 2000 grit. Finally, the samples were polished using colloidal alumina with particle sizes of 3 µm and 1 µm respectively. Fusion zones were revealed by chemical etching with Kallings Reagent I (2 g $CuCl_2$ + 40 ml HCl + 40 ml C_2H_5OH + 40 ml H_2O) for 3 s. Macrographs of the fusion zones in the etched specimens were obtained using a Keyence digital microscope.

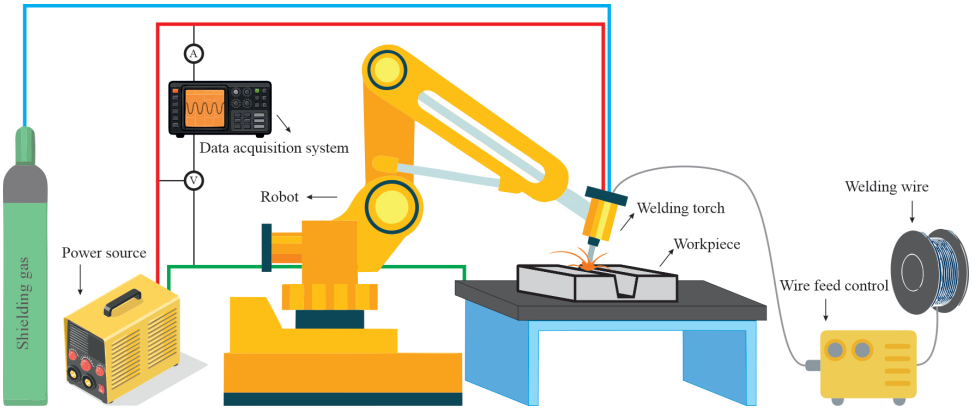

Figure 9.3: Schematic of the experimental setup utilised in the present work.

9.5. Results and discussion

9.5.1. Model validation

The reliability and accuracy of the present numerical predictions are benchmarked against experimentally measured melt-pool shapes. In this study, gas metal arc welding of workpieces with different groove shapes are considered, with a welding current of 280 A and a travel speed of 7.5 mm s^{-1}. Figure 9.4 shows a comparison between the numerically predicted melt-pool shapes with those obtained from experiments for different groove shapes. The computational cells containing molten metal were marked during the calculation to visualise the melt-pool shapes. It is worth noting that the experiments were conducted after the numerical simulations, which means no calibration is performed to tune the numerical results. The results indicate a reasonable agreement between numerically predicted and experimentally measured melt-pool shapes. The maximum deviation between the predicted melt-pool dimensions and experimental measurements is found to be less than 10%, demonstrating the validity of the present numerical simulations. This deviation might be caused by uncertainties associated with the models employed to approximate the temperature-dependent material properties at elevated temperatures, the simplifying assumptions made to develop the computational model such as those employed to determine droplet size, velocity and temperature, and uncertainties in determining the boundary conditions in the model.

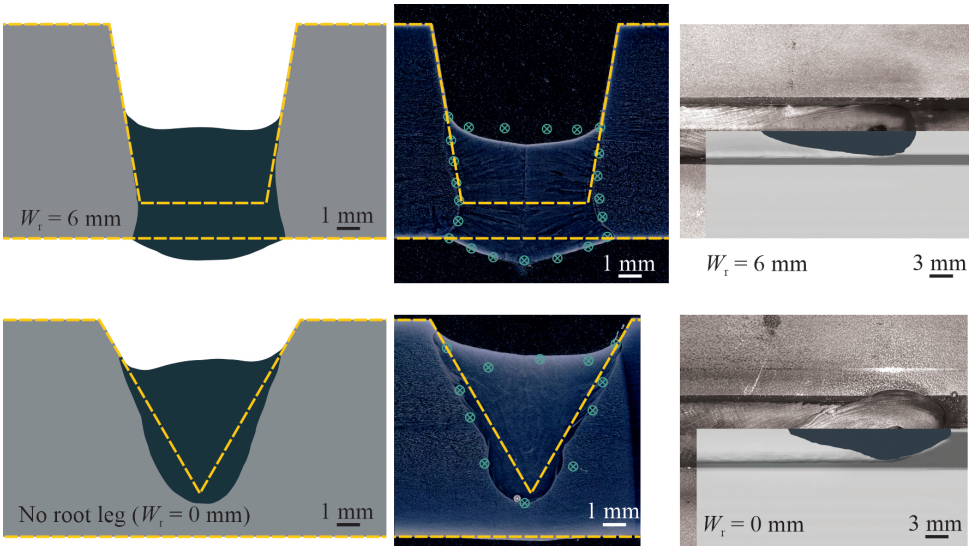

Figure 9.4: Comparison of the melt-pool shapes obtained from the present numerical simulations with experimental measurements for different groove shapes with a welding current of 280 A and a travel speed of 7.5 mm s^{-1}. Regions shaded in dark grey show the melt-pool shape obtained from numerical simulations. The computational cells that, at any stage during the transient calculations of the melting and re-solidification process, contained molten metal were marked to visualise the melt-pool shape on the transversal cross-section. Green symbols on experimental data show the melt-pool boundary obtained from numerical simulations. Yellow dashed-lines indicate the joint shape before welding.

9.5.2. Thermal and fluid flow fields

Once the arc ignites and the process begins, the welding wire heats up to the melting temperature and molten metal droplets form at the wire tip that detach periodically from the wire and deposit on the workpiece surface as shown schematically in figure 9.1. The frequency of droplet detachment is directly proportional to the wire feed rate and ranges between 147 Hz and 187 Hz for the welding process parameters studied in the present work (see table 9.1). To simplify the numerical simulations as described in section 3.2.3, the filler metal droplets are assumed to be spherical and are incorporated into the simulations with predefined velocity and temperature, which is a common practice in modelling melt-pool behaviour in gas metal arc welding (see for instance, [7, 8, 18, 21]). The qualitative melt-pool behaviour was found to be similar for different welding currents studied in the present work. Therefore, representative results for the cases with welding current of 220 A are shown and discussed in this chapter.

The thermal energy input from the plasma arc in addition to the thermal energy transported by the molten metal droplets result in the formation of a melt pool. For the process parameters studied in the present work (see table 9.1), the melt pool grows over time and reaches a quasi-steady-state condition after about 3 s. Figure 9.5 shows a partial view of the workpiece encompassing the melt pool and the corresponding thermal and fluid flow

fields over the melt-pool surface for different groove shapes at $t = 5\,\mathrm{s}$ with wire feed rate $u_\mathrm{w} = 7\,\mathrm{m\,min^{-1}}$ and welding current $I = 220\,\mathrm{A}$. For the cases shown in figure 9.5, the maximum surface temperature is less than 2310 K and the value of the temperature gradient of surface tension ($\partial\gamma/\partial T$) is mostly positive (see figure 9.2(e)). Hence, the molten metal moves from the cold area close to the melt-pool rim towards the hot central region, primarily due to the Marangoni shear force induced over the surface. Molten metal streams from the melt-pool rim collide in the central region and form a complex unsteady asymmetric flow pattern in the pool. A similar flow pattern is observed experimentally in previous independent studies conducted by Wu *et al.* [36], Zhao *et al.* [37]. The maximum local molten metal velocity is about $0.7 - 0.8\,\mathrm{m\,s^{-1}}$ and corresponds to a Péclet number ($\mathrm{Pe} = \rho c_\mathrm{p} \mathscr{D} \|\mathbf{u}\| / k$) larger than unity ($\mathcal{O}(400)$), which signifies that advection dominates the energy transfer in the melt pool and that the process cannot be described adequately using a thermal model without considering fluid flow.

The results suggest that the energy transported to the surrounding solid material markedly affects the melt-pool shape. Although the total heat input to the material is the same for the cases shown in figure 9.5, the melt-pool shapes differ notably for different groove shapes. It appears that increasing the width of the root-leg results in a decrease in the amount of heat diffused to the side walls of the groove as the height of the deposit layer reduces, leading to an increase in the length of the melt-pool as well as the mushy-zone (*i.e.* regions between the solidus and liquid iso-surfaces in figure 9.5). Moreover, the average fluid velocity in the pool decreases with increasing width of the root-leg, which can be attributed to the decrease in the magnitude of temperature gradients generated over the surface. Among all the cases studied in the present work, full-penetration is observed only for those with root-leg, even for the case with welding current $I = 280\,\mathrm{A}$. Evidently, a higher welding current or a lower travel speed is required to achieve full penetration using grooves without root-leg (*i.e.* V-groove). However, increasing the welding current or reducing the travel speed results in an increase in total heat input to the material, which is often undesirable as it decreases the cooling rate and can adversely affect the properties of the joint, particularly when austenitic stainless steels are used [38–40]. Moreover, increasing the welding current can lead to a significant increase in arc force as the arc force is proportional to the welding current squared ($\|\mathbf{F}_\mathrm{arc}\| \propto I^2$) [41], and thus limiting the welding current is necessary to avoid defects such as burn-through. Although employing a root-leg can reduce the welding current required to achieve full penetration, employing a relatively wide root-leg will increase the number of welding passes required to fill the groove.

Figure 9.6 shows thermal and fluid flow fields in the $x = 0$ plane for different joint shapes and time instances. The impingement of molten metal droplets on the surface disturbs the thermal and fluid flow field in the pool and results in the formation of a crater and a travelling wave over the melt-pool surface, as indicated by arrows in figure 9.6. Moreover, the periodic molten metal droplet impingement on the melt pool enhances mixing in the melt pool. The molten metal droplet temperature ($T_\mathrm{d} = 2500\,\mathrm{K}$) is above the critical temperature at which the sign of surface-tension temperature coefficient ($\partial\gamma/\partial T$) changes from positive to negative ($T_\mathrm{cr} \approx 2250\,\mathrm{K}$); therefore, an outward fluid flow is induced on the surface in the region where the droplet impinges due to Marangoni shear force. Soon after the droplet is merged with the melt pool, the crater closes due to

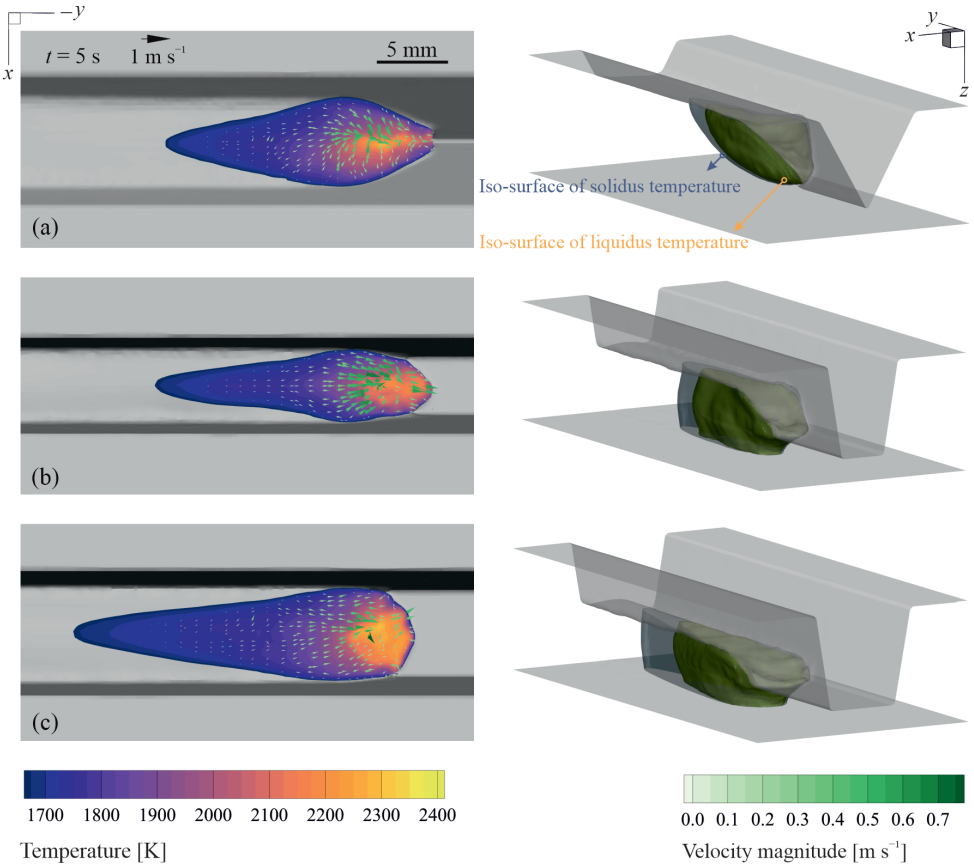

Figure 9.5: The numerically predicted thermal and fluid flow fields over the melt-pool surface (left column) and the corresponding pool shape (right column) for different joint shapes at $t = 5\,\mathrm{s}$. (a) groove angle $\theta = 60^\circ$ and no root-leg ($W_\mathrm{r} = 0\,\mathrm{mm}$), (b) $\theta = 20^\circ$ and root-leg width $W_\mathrm{r} = 4\,\mathrm{mm}$ and (c) $\theta = 20^\circ$ and root-leg width $W_\mathrm{r} = 6\,\mathrm{mm}$. Wire feed rate $u_\mathrm{w} = 7\,\mathrm{m\,min^{-1}}$, welding current $I = 220\,\mathrm{A}$, and travel speed $V = 7.5\,\mathrm{m\,s^{-1}}$. The area between iso-surfaces of solidus and liquidus temperature shows the mushy region.

surface tension and hydrostatic forces, and the surface temperature decreases to values less than 2310 K for which the value of $\partial\gamma/\partial T$ is mostly positive. The wave crests move radially outward towards the melt-pool rim and are reflected by the solid edges of the pool. Interactions between the primary and reflected waves as well as the forces acting on the molten material result in complex melt-pool surface deformations and oscillations, as shown in figure 9.5. For the cases studied in the present work, the frequency of the droplet transfer in relatively high ($\mathcal{O}(170\,\mathrm{Hz})$) and the droplet sizes are relatively small compared to the melt-pool dimension, resulting in a smooth weld bead with negligible ripple formation.

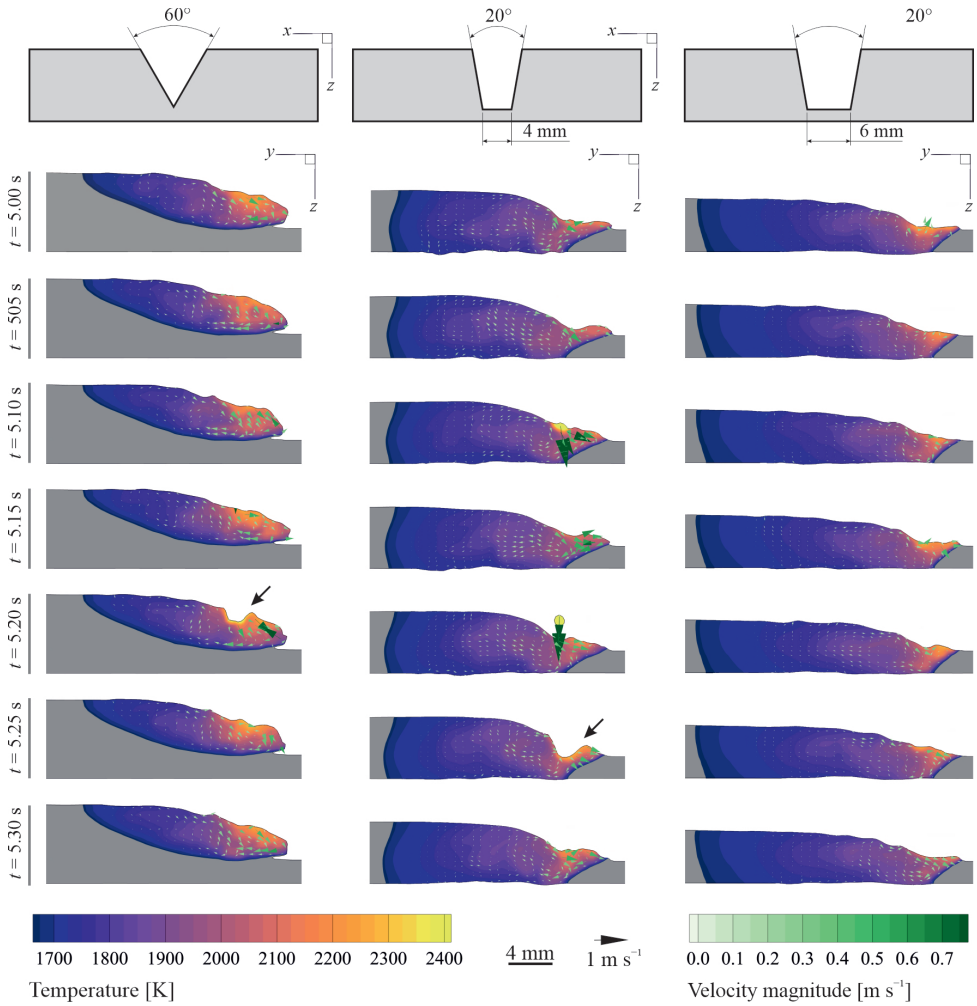

Figure 9.6: Melt-pool shape, temperature profile and velocity vectors in the $x = 0$ plane for different joint shapes and time instances. (left column) groove angle $\theta = 60°$ and no root-leg ($W_r = 0$ mm), (middle column) $\theta = 20°$ and root-leg width $W_r = 4$ mm and (right column) $\theta = 20°$ and root-leg width $W_r = 6$ mm. Wire feed rate $u_w = 7\,\mathrm{m\,min^{-1}}$, welding current $I = 220$ A, and travel speed $V = 7.5\,\mathrm{m\,s^{-1}}$.

9.6. Conclusions

Three-dimensional numerical simulations were performed to systematically investigate the effect of groove shape on melt-pool behaviour in root pass gas metal arc welding. The effects of melt-pool surface deformations on power-density distribution and the forces applied to the molten material were accounted for in the present computational model. These effects are often neglected in numerical simulations of melt-pool behaviour in arc welding. Thermal and fluid flow fields in the melt pool were visualised

and described for different groove shapes. Moreover, experiments were conducted to validate the numerical predictions.

Energy transfer in melt pools during gas metal arc welding is dominated by convection and thus thermal models without considering fluid flow cannot predict and describe the melt-pool shape with sufficient accuracy. The periodic impingement of molten metal droplets disturbs the thermal and fluid flow fields in the pool, resulting in an even more complex flow pattern. For the process parameters studied in the present work, full-penetration was observed only for the grooves with root-leg. Changes in the groove shape have an insignificant influence on the flow pattern over the surface, however the groove shape affects the energy transfer to the surrounding solid material and thus alters the melt-pool shape and can affect the properties of the joint. The groove shape also affects the melt-pool oscillatory behaviour as it influences the reflection of the waves generated due to the molten metal droplet impingement. Moreover, the groove shape can affect the process window, which can be explored using the simulation-based approach described in the present work.

References

[1] Wei, H. L., Mukherjee, T., Zhang, W., Zuback, J. S., Knapp, G. L., De, A., and DebRoy, T. Mechanistic models for additive manufacturing of metallic components. *Progress in Materials Science*, 116:100703, 2021. doi:10.1016/j.pmatsci.2020.100703.

[2] Norrish, J., Polden, J., and Richardson, I. A review of wire arc additive manufacturing: development, principles, process physics, implementation and current status. *Journal of Physics D: Applied Physics*, 54(47):473001, 2021. doi:10.1088/1361-6463/ac1e4a.

[3] DebRoy, T. and David, S. A. Physical processes in fusion welding. *Reviews of Modern Physics*, 67(1):85–112, 1995. doi:10.1103/revmodphys.67.85.

[4] Aucott, L., Dong, H., Mirihanage, W., Atwood, R., Kidess, A., Gao, S., Wen, S., Marsden, J., Feng, S., Tong, M., Connolley, T., Drakopoulos, M., Kleijn, C. R., Richardson, I. M., Browne, D. J., Mathiesen, R. H., and Atkinson, H. V. Revealing internal flow behaviour in arc welding and additive manufacturing of metals. *Nature Communications*, 9(1), 2018. doi:10.1038/s41467-018-07900-9.

[5] David, S. A. and DebRoy, T. Current issues and problems in welding science. *Science*, 257 (5069):497–502, 1992. doi:10.1126/science.257.5069.497.

[6] Cook, P. S. and Murphy, A. B. Simulation of melt pool behaviour during additive manufacturing: Underlying physics and progress. *Additive Manufacturing*, 31:100909, 2020. doi:10.1016/j.addma.2019.100909.

[7] Zong, R., Chen, J., Wu, C., and Lou, D. Numerical analysis of molten metal behavior and undercut formation in high-speed GMAW. *Journal of Materials Processing Technology*, 297: 117266, 2021. doi:10.1016/j.jmatprotec.2021.117266.

[8] Hu, Z., Hua, L., Qin, X., Ni, M., Ji, F., and Wu, M. Molten pool behaviors and forming appearance of robotic GMAW on complex surface with various welding positions. *Journal of Manufacturing Processes*, 64:1359–1376, 2021. doi:10.1016/j.jmapro.2021.02.061.

[9] Zargari, H. H., Ito, K., Kumar, M., and Sharma, A. Visualizing the vibration effect on the tandem-pulsed gas metal arc welding in the presence of surface tension active elements. *International Journal of Heat and Mass Transfer*, 161:120310, 2020. doi:10.1016/j.ijheatmasstransfer.2020.120310.

[10] Wu, D., Tashiro, S., Wu, Z., Nomura, K., Hua, X., and Tanaka, M. Analysis of heat transfer and material flow in hybrid KPAW-GMAW process based on the novel three dimensional CFD simulation. *International Journal of Heat and Mass Transfer*, 147:118921, 2020. doi:10.1016/j.ijheatmasstransfer.2019.118921.

[11] Wu, D., Hua, X., Ye, D., and Li, F. Understanding of humping formation and suppression mechanisms using the numerical simulation. *International Journal of Heat and Mass Transfer*, 104:634–643, 2017. doi:10.1016/j.ijheatmasstransfer.2016.08.110.

[12] Hu, J., Guo, H., and Tsai, H. L. Weld pool dynamics and the formation of ripples in 3D gas metal arc welding. *International Journal of Heat and Mass Transfer*, 51(9-10):2537–2552, 2008. doi:10.1016/j.ijheatmasstransfer.2007.07.042.

[13] Cho, M. H. and Farson, D. F. Understanding bead hump formation in gas metal arc welding using a numerical simulation. *Metallurgical and Materials Transactions B*, 38(2):305–319, 2007. doi:10.1007/s11663-007-9034-5.

[14] Ushio, M. and Wu, C. S. Mathematical modeling of three-dimensional heat and fluid flow in a moving gas metal arc weld pool. *Metallurgical and Materials Transactions B*, 28(3):509–516, 1997. doi:10.1007/s11663-997-0118-z.

[15] Kim, J.-W. and Na, S.-J. A study on the three-dimensional analysis of heat and fluid flow in gas metal arc welding using boundary-fitted coordinates. *Journal of Engineering for Industry*, 116 (1):78–85, 1994. doi:10.1115/1.2901812.

[16] Zhang, W., Kim, C.-H., and DebRoy, T. Heat and fluid flow in complex joints during gas metal arc welding—Part I: Numerical model of fillet welding. *Journal of Applied Physics*, 95(9): 5210–5219, 2004. doi:10.1063/1.1699485.

[17] Zhang, W., Kim, C.-H., and DebRoy, T. Heat and fluid flow in complex joints during gas metal arc welding—part II: Application to fillet welding of mild steel. *Journal of Applied Physics*, 95 (9):5220–5229, 2004. doi:10.1063/1.1699486.

[18] Hu, J. and Tsai, H. L. Modelling of transport phenomena in 3D GMAW of thick metals with V groove. *Journal of Physics D: Applied Physics*, 41(6):065202, 2008. doi:10.1088/0022-3727/41/6/065202.

[19] Chen, J., Schwenk, C., Wu, C. S., and Rethmeier, M. Predicting the influence of groove angle on heat transfer and fluid flow for new gas metal arc welding processes. *International Journal of Heat and Mass Transfer*, 2011. doi:10.1016/j.ijheatmasstransfer.2011.08.046.

[20] Cho, Y. T. and Na, S.-J. Application of Abel inversion in real-time calculations for circularly and elliptically symmetric radiation sources. *Measurement Science and Technology*, 16(3):878–884, 2005. doi:10.1088/0957-0233/16/3/032.

[21] Cho, D.-W., Na, S.-J., Cho, M.-H., and Lee, J.-S. Simulations of weld pool dynamics in V-groove GTA and GMA welding. *Welding in the World*, 57(2):223–233, 2013. doi:10.1007/s40194-012-0017-z.

[22] Cho, D. W., Na, S.-J., Cho, M. H., and Lee, J. S. A study on V-groove GMAW for various welding positions. *Journal of Materials Processing Technology*, 213(9):1640–1652, 2013. doi:10.1016/j.jmatprotec.2013.02.015.

[23] Sahoo, P., Debroy, T., and McNallan, M. J. Surface tension of binary metal—surface active solute systems under conditions relevant to welding metallurgy. *Metallurgical Transactions B*, 19(3):483–491, 1988. doi:10.1007/bf02657748.

[24] Saldi, Z. S. *Marangoni driven free surface flows in liquid weld pools*. PhD dissertation, Delft University of Technology, Delft University of Technology, 2012.

[25] Soderstrom, E. J., Scott, K. M., and Mendez, P. F. Calorimetric measurement of droplet temperature in GMAW. *Welding Journal*, 90(4):77s–84s, 2011. URL: `http://files.aws.org/wj/supplement/wj201104_s77.pdf`.

[26] Mills, K. C. Fe-316 stainless steel. In *Recommended Values of Thermophysical Properties for Selected Commercial Alloys*, pages 135–142. Elsevier, 2002. doi:10.1533/9781845690144.135.

[27] Kim, C. S. Thermophysical properties of stainless steels. Technical Report ANL-75-55, Illinois, United States, 1975.

[28] *Release 19.2*. ANSYS Fluent. URL: `https://www.ansys.com/`.

[29] Ebrahimi, A., Kleijn, C. R., and Richardson, I. M. The influence of surface deformation on thermocapillary flow instabilities in low Prandtl melting pools with surfactants. In *Proceedings of the 5th World Congress on Mechanical, Chemical, and Material Engineering*. Avestia Publishing, 2019. doi:10.11159/htff19.201.

[30] Ebrahimi, A., Kleijn, C. R., and Richardson, I. M. Numerical study of molten metal melt pool behaviour during conduction-mode laser spot melting. *Journal of Physics D: Applied Physics*, 54:105304, 2021. doi:10.1088/1361-6463/abca62.

[31] Ebrahimi, A., Kleijn, C. R., and Richardson, I. M. A simulation-based approach to characterise melt-pool oscillations during gas tungsten arc welding. *International Journal of Heat and Mass Transfer*, 164:120535, 2021. doi:10.1016/j.ijheatmasstransfer.2020.120535.

[32] Ebrahimi, A., Kleijn, C. R., Hermans, M. J. M., and Richardson, I. M. The effects of process parameters on melt-pool oscillatory behaviour in gas tungsten arc welding. *Journal of Physics D: Applied Physics*, 54(27):275303, 2021. doi:10.1088/1361-6463/abf808.

[33] Ubbink, O. *Numerical Prediction of Two Fluid Systems with Sharp Interfaces*. PhD dissertation, Imperial College London (University of London), London, United Kingdom, 1997. URL: `http://hdl.handle.net/10044/1/8604`.

[34] Patankar, S. V. *Numerical Heat Transfer and Fluid Flow*. Taylor & Francis Inc, 1st edition, 1980. ISBN 0891165223.

[35] Issa, R. I. Solution of the implicitly discretised fluid flow equations by operator-splitting. *Journal of Computational Physics*, 62(1):40–65, 1986. doi:10.1016/0021-9991(86)90099-9.

[36] Wu, F., Flint, T. F., Falch, K. V., Smith, M. C., Drakopoulos, M., and Mirihanage, W. Mapping flow evolution in gas tungsten arc weld pools. *International Journal of Heat and Mass Transfer*, 179:121679, 2021. doi:10.1016/j.ijheatmasstransfer.2021.121679.

[37] Zhao, C. X., van Steijn, V., Richardson, I. M., Kleijn, C. R., Kenjeres, S., and Saldi, Z. Unsteady interfacial phenomena during inward weld pool flow with an active surface oxide. *Science and Technology of Welding and Joining*, 14(2):132–140, 2009. doi:10.1179/136217108x370281.

[38] Kumar, S. and Shahi, A. S. Effect of heat input on the microstructure and mechanical properties of gas tungsten arc welded AISI 304 stainless steel joints. *Materials & Design*, 32(6):3617–3623, 2011. doi:10.1016/j.matdes.2011.02.017.

[39] Unnikrishnan, R., Idury, K. S. N. S., Ismail, T. P., Bhadauria, A., Shekhawat, S. K., Khatirkar, R. K., and Sapate, S. G. Effect of heat input on the microstructure, residual stresses and corrosion resistance of 304L austenitic stainless steel weldments. *Materials Characterization*, 93:10–23, 2014. doi:10.1016/j.matchar.2014.03.013.

[40] Mohammed, G., Ishak, M., Aqida, S., and Abdulhadi, H. Effects of heat input on microstructure, corrosion and mechanical characteristics of welded austenitic and duplex stainless steels: A review. *Metals*, 7(2):39, 2017. doi:10.3390/met7020039.

[41] Lancaster, J. F., editor. *The Physics of Welding*. International series on materials science of technology. Pergamon Press, Oxford, UK, 2nd edition, 1986. ISBN 0080340768.

10

General Conclusions and Outlook

10.1. Conclusions

The goal throughout the present work has been to develop a generic physics-based computational approach to predict and assess the stability of the melt-pool in fusion welding and additive manufacturing and to minimise the number of trial-and-error experiments required for process development and optimisation. It is of particular interest to provide a deeper insight into the physics of heat and fluid flow in fusion-based manufacturing processes. To this end, an advanced high-fidelity computational model based on the finite-volume method has been developed within the framework of ANSYS Fluent to unravel the complex dynamics of melt-pool behaviour whilst maintaining a physically realistic representation of the system. The details of the computational model and the underlying assumptions are described in chapter 3. The computational model has been utilised to simulate the melt-pool oscillatory behaviour in various fusion-based manufacturing processes to investigate the effects of variations in orientation and geometric boundary conditions typically employed in industry. Moreover, experiments have been conducted to validate the robustness of the present computational model in predicting and characterising melt-pool oscillatory behaviour for the challenging physical conditions involved. The conclusions drawn from the present work are summarised here.

- For isothermal phase-change problems, reducing the cell size diminishes the influence of the mushy-zone constant and results become independent of the mushy-zone constant for the fine enough meshes. A grid independent solution of an isothermal phase-change problem is therefore independent of the mushy-zone constant. However, not every numerical result that is independent of the mushy-zone constant is grid independent.

- Numerical predictions of non-isothermal phase-change problems are inherently dependent on the mushy-zone constant. To predict and evaluate the influence of the mushy-zone constant on numerical predictions, the ratio of the heat advection to the heat diffusion is quantified in regions close to the solid-liquid interface using a dimensionless Péclet number Pe^*, which is defined in equation (4.15). Large values of $\mathrm{Pe}^* \gg 1$ adjacent to the solid-liquid interface indicate a strong sensitivity and $\mathrm{Pe}^* \ll 1$ indicates insensitivity to the mushy-zone constant C.

- Artificially increasing the transport coefficients of the material (commonly known as using an 'enhancement factor') to achieve agreement between numerically predicted melt-pool sizes and solidification rates with experiments does not represent the physics of complex transport phenomena governing fusion-based manufacturing processes. The use of an enhancement factor significantly affects the numerical predictions of melt-pool oscillatory behaviour.

- Deformations of the melt-pool surface can result in temporal and spatial variations in the power-density and force distributions acting on the molten material. Thermal and fluid flow fields in the melt-pool as well as the pool shape predicted assuming a flat and non-deformable gas-metal interface differ considerably from those of the cases with a deformable interface.

- The absorptivity is a system parameter and should not be used as a calibration factor. The coupling between the absorptivity of material and thermal and fluid flow fields in the melt-pool cannot be rendered with sufficient resolution employing a constant absorptivity model, which will inevitably limit the range of predictability of the computational models developed to describe the dynamics of melt-pool behaviour in laser welding and additive manufacturing. Treating absorptivity as a physical quantity remarkably enhanced the model accuracy and can lead to results that match experimental observations.

- The melt-pool oscillations strongly relate to shape and size of the melt-pool and surface tension of the molten material. Oscillations with relatively low amplitudes and high frequencies were observed during partial penetration. The frequency of melt-pool oscillations decreases as the melt pool grows. The numerical predictions confirm the existence of a sharp drop in oscillation frequency when the melt pool becomes fully penetrated during gas tungsten arc welding (GTAW). There is a period during which both high and low frequencies coexist while the transition from partial to full penetration is developing. The melt pool oscillation mode can change during processing, depending on material properties and prescribed process parameters.

- Welding position affects the melt-pool surface morphology, altering the spatial distribution of arc forces and power-density applied to the molten material and hence the flow pattern in the melt-pool. The change in the flow pattern affects the evolution of the melt-pool shape and its oscillatory behaviour.

- Changes in the groove shape generally have an insignificant influence on the flow pattern over the surface in gas metal arc welding (GMAW), however the groove shape affects the energy transfer to the surrounding solid material and thus alters the melt-pool shape and can affect the properties of the joint. The groove shape also affects the melt-pool oscillatory behaviour as it influences the reflection of the waves generated due to the molten metal droplet impingement. Moreover, the groove shape can affect the process window, which can be explored using the simulation-based approach described in the present work.

- Complex unsteady molten metal flow in melt pools give rise to time-variant frequency spectra in oscillations of the melt-pool during fusion-based welding and additive manufacturing. Employing the continuous wavelet transform, the time-resolved melt-pool surface oscillation signals obtained from the numerical simulations can be decomposed into time and frequency spaces simultaneously, overcoming the shortcomings of the conventional fast Fourier transform (FFT) analysis in characterising the non-stationary features of the signals with abrupt changes in their frequency spectra.

10.2. Outlook

The computational model developed in the present work has a generic construction with specific process influences addressed through appropriate boundary conditions, avoiding the necessity to integrate melt pool and detailed process descriptions in a single

simulation. The model is therefore capable of representing a wide range of welding and additive manufacturing technologies through selection of appropriate material properties and boundary conditions. The current physically based model generally requires considerable calculation time ($\mathcal{O}(10^2\,\mathrm{h})$) to assess stability for a period of a few seconds in real time, which in turn limits the effectiveness of such a computational approach for industrial applications. Future developments can target reducing the calculation time by optimising and simplifying (where feasible) the current computational model. This can be done for instance by employing local adaptive mesh refinement, and utilising advanced computational resources (*e.g.* GPU-based computing systems) or by employing reduced-order models instead of full models at the cost of model accuracy.

Recent developments of Machine-learning algorithms and techniques provide a dynamic ability to statistically improve prediction capabilities based on a continuously growing database provided from a set of appropriately classified results obtained from numerical simulations. This offers the opportunity to explore the solution parameter space through data-driven computational analyses, which can significantly reduce development costs, in terms of time and therefore money. The advantage of such an approach is that the complete relationship between the key descriptors of each outcome and the quantities of interest is approximated, enabling its use for predictive purposes. Future research can focus on developing a data-driven framework to determine the transition boundaries between stability and instability in multi-parameter space to derive a fast analysis of dynamic pool stability without the need to run the full physical model multiple times for each assessment.

It has been shown in the present work that the accuracy of the numerical predictions is directly related to the accuracy of the thermo-physical material properties employed in the simulations. The existing databases of material properties at elevated temperatures (above the melting temperature) are very limited. The models that are available to approximate the material properties at elevated temperatures are often based on extrapolating data from values measured in the solid state. Further experimental measurements are required to provide reliable and accurate thermo-physical data for different material compositions. It is recommended that such experimental measurements focus on measuring thermal conductivity, viscosity, and surface tension of the material as their values are critical in thermal and fluid flow models.

The capability of the present model in predicting the melt-pool shape and behaviour in a wide range of welding and additive manufacturing technologies offers a prospect for implementation into process monitoring and control systems. Moreover, the present model can be coupled with microstructure and mechanical models to study the process more comprehensively. The results of such numerical simulations can also be used for educational purposes, as they provide a unique visual aid to understand the physics of the complex heat and fluid flow pattern in advanced fusion-based manufacturing processes.

Acknowledgements

To be a highly effective person, I believe that talent and working hard are not enough, one should also go for his own dreams to contribute to the advancement of the society. Moving to Delft was the start of a new season of my life to continue my track of success and achieve my future goals. This journey, with its all ups-and-downs, has been triumphant mainly because I had the opportunity to receive sincere support from many people to whom I would like to extend my deep heartfelt gratitude.

I would first like to thank my promoters and mentors, **Prof.dr. Ian M. Richardson** and **Prof.dr.ir Chris R. Kleijn** for giving me the opportunity to work on this exciting, novel and interdisciplinary project in the Joining and Additive Manufacturing (JAM) group. Your masterful supervision, outstanding leading skills and ability in creating a friendly and dynamic work environment allowed me to develop my personal and professional skills. You both have taught me how to tackle challenging and complex problems and solve them effectively and independently for the benefit of industry and society. I have been, and still am, fascinated by your outstanding integrity, intuition and passion for scientific research. **Ian**, I am eternally grateful for offering me your endless support and giving me the freedom to pursue my interests. You supported me to develop my research line confidently and independently, just like a dad teaching his child how to ride a bike. **Chris**, your timely feedback, critical assessments and honesty have taught me scientific rigour and excellence.

I am grateful to **Dr.ir Marcel J.M. Hermans** for his tremendous support and the fruitful discussions we had about my research findings. **Marcel**, I feel truly fortunate to be your colleague in the JAM group because of your positive energy, kindness, patience, and wisdom. You generously helped me to arrange my experiments, which demonstrably enhanced the quality of my research. Our spontaneous conversations near the coffee machine and when I popped into your office were incredible because of your humour. Many thanks for being such an amazing advisor and supporting me to finalise my research grant proposals and initiating collaboration with other research groups. I am thrilled to stay in your group as a postdoc and share the next stage of my research career with you.

This research was carried out in the framework of the partnership program of the Materials Innovation Institute (M2i) and the Foundation for Fundamental Research on Matter (FOM), which is part of the Netherlands Organisation for Scientific Research (NWO). I would like to thank the industrial partner in this project "Allseas Engineering B.V." for the financial support. It was a pleasure for me working with many bright people from industry during the course of my PhD project. My special thanks goes to **Dr. Natalia Ermolaeva** and **Dr. Bin Hu** for their insightful comments and suggestions. I also thank **Eline Heerema**, **Nick Verberkmoes**, **Bas Klok**, **Mark Potjer** and **Paul de Reuver** from Allseas Engineering. I would like to extend my special thanks to **Dr. Viktoria Savran** and all M2i staff for supporting the management of this project. I also thank all the members of

cluster 7 (Additive manufacturing) for the nice discussions we had during M2i meetings.

Our recent collaboration with the Department of Mechanics of Solids, Surfaces & Systems (MS3) at the University of Twente was indeed magnificent and proved to be invaluable. I am very grateful to **Prof.dr.ir Gert-Willem R.B.E. Römer** for supporting this collaborative research work, his scientific advice and insightful discussions during our collaboration. The success of our collaboration is indebted to the commitment of **Dr. Martin Luckabauer**, **Mohammad Sattari** and **Leon Bremer**. Many thanks to you all for your efforts in performing laser melting experiments. I am really proud of what we learned and discovered about the effects of laser absorptivity on internal flow behaviour in laser material processing. I eagerly look forward to extending our collaborations in the future.

Aravind, I would like to thank you for the kind help and professional assistance during my gas metal arc welding experiments. You are a wonderful colleague with a kind heart, with who I enjoy firing up laboratory experiments and discussing the outcomes.

I sincerely acknowledge **Jurriaan van Slingerland** and **Remko Seijffers** for their technical support during my experiments. I extend my thanks to **Frans Bosman** for training me how to make good welds. Your enthusiasm for welding and additive manufacturing experiments is fascinating, and working with you is lively and pleasant.

I would like to express my sincere gratitude to **Dr. Miguel A. Bessa**, **Dr. Peyman Mohajerin Esfahani** and **Prof.dr.ir Gert-Willem R.B.E. Römer** for supporting me in finalising my research grant proposal. You provided me with numerous inspirations and encouragement in our meetings. It was my pleasure working with you, and I hope to maintain our fruitful collaboration in the future.

I would like to acknowledge **Prof. Carolin Körner** and **Dr. Matthias Markl** for our fruitful discussions about my PhD work and for providing me the opportunity to present my work to your outstanding research group.

Dr. Walther Pitscheneder, I highly appreciate our wonderful discussions on melt-pool behaviour in laser melting. Your enthusiasm for research on laser welding and additive manufacturing is exceptional.

Over the past years, I had the privilege to mentor many brilliant students, who deserve acknowledgement. I enjoyed our friendship alongside the research work, and I wish you great success in your career. **Tim Donders**, **Joel A. Barreto de Matos**, **Jeroen Reus**, **Benyamin Naranjani**, **Shayan Milani**, **Farzad D. Javan** and **Amin Sabaghan**, I admire your enthusiasm, curiosity and persistence, and I feel exhilarated to see your developments at both professional and personal levels. I also would like to thank **Prof.dr. Saša Kenjereš** from the Department of Chemical Engineering of the Delft University of Technology, and **Prof.dr.ir Cornelis H. Venner** and **Dr.ir. Claas W. Visser** from the Department of Thermal and Fluid Engineering of the University of Twente for supporting these student research projects.

Being involved in teaching activities during my doctoral studies was a monumental experience full of joy and inspiration. I would like to thank **Prof.dr. Ian M. Richardson**, **Dr.ir. Marcel J.M. Hermans**, **Dr. Peyman Taheri** and **Dr. Shoshan T. Abrahami** for inviting me to share my knowledge with the students during their courses. I also thank **Dr. Elsa A. Olivetti** from the Department of Materials Science and Engineering of Mas-

sachusetts Institute of Technology for our discussions around the syllabus and contents of the Materials Processing course.

My time at CERN IDEAsquare, where I had the chance to meet many bright students, was amazingly full of inspiration about innovation and unleashing the potential of new technologies. I would like to thank **Romy Welschen** for inviting me as a lecturer to the Honours Programme Delft (HPD) Summer School. It was my pleasure discussing various aspects of innovation with **Dr. Dap Hartmann**, **Sem Carree** and **Tuuli Utrianen** during the course in Geneva.

Vincent Wegener, **Dr.ir. Wei Ya** (Niya) and **Benedetto Di Castri**, it was my pleasure meeting you and discussing your advancement in 3D-printing of complex metallic structures at RAMLAB. I am thrilled to collaborate with you during and after my doctoral studies.

Thanks to **Pieter Kappelhof** and **Cor Heijwegen** for providing the opportunity to visit Hittech RSP Technology and Hittech Gieterij Nunspeet. I liked our conversation about high-tech materials and their applications during our trips to Delfzijl and Nunspeet. **Roger Senden** and **Pieter Rigter**, I enjoyed our discussions on how my knowledge and computational models can be applied to improve the quality of your products. I hope we can collaborate in the future.

I would like to express my gratitude to the faculty and staff of the Department of Materials Science and Engineering of the Delft University of Technology, from who I learned a lot. I specially thank **Prof.dr.ir Jilt Sietsma**, **Prof.dr.ir Joris Dik**, **Dr. Marcel H.F. Sluiter**, **Dr. Yongxiang Yang** and **Prof.dr.ir Lucia Nicola** for nice discussions about science and art during departmental outgoings and meetings. I also thank the management and support staff of the department, **Olaf Voorwinde**, **Ellen Vendrig**, **Saskia Brandt Corstius**, **Prisca Koelman**, **Saskia van der Meer** and **Marian Smit-kooima** for their administrative assistance.

Working in a supportive and friendly environment facilitates the production of high-quality results, and I had the chance to benefit from it because of having wonderful people around me. **Aravind Babu**, **Emiliano Trodini**, **Jia Fu**, **Gautam Agarwal**, **He Gao** and **Hessel Vredeveldt**, thanks to your good humour, lively character, kindness and cheerful presence, my working days in office were delightful. You are the best office mates even with your all-day-long loud discussions. I also thank my colleagues **Xiaohui Liang**, **Konstantinos Goulas**, **Arjun Sood**, **Jia-Ning Zhu**, **José Galán Argumedo** and **Can Özkan** for making it a whole. **Jan-Henk Welink**, 'Dorood'! Your positive energy and our conversations about culture, society and sustainability are memorable.

I had the privilege to meet many amazing people around the 3mE Faculty and share my time with them during coffee breaks. **Arman** and **Amin**, you are a true confidante, especially through all the challenging situations. The level of criticism that you have developed over the years about almost everything and your brutal honesty are exceptional. I would also like to thank **Casper**, **Mohsen**, **Nilgoon**, **Saleh**, **Soroosh**, **Farnaz**, **Ali**$^{(3)}$, **Mirsajjad**, **Monireh**, **Parisa**, **Chrysa**, **Vitoria**, **Alfonso**, **Davood**, **Can** and **Behrooz**.

I had the privilege to be part of the Transport Phenomena (TP) research group during my doctoral studies and was surrounded by many wonderful people. **Anton**, **Iman**, **Manu**, **Elin**, **Siddhartha**, **Manas**, **Kevin**, **Saeid**, **Maulik**, **Romana** and **Luis**, thank you for

the lovely time at TP group meetings and NWO Physics@Veldhoven conferences.

Living in Delft is indeed wonderful thanks to many great friends. **Sanaz** and **Siamak**, **Sahar** and **Masoud**, **Sayedeh** and **Nima**, **Mahsa** and **Masoud**, **Nasim** and **Mohsen**, **Negar** and **Arash**, **Behtab** and **Farid**, **Hoda** and **Bijan**, **Sara** and **Khashayar**, **Bahar** and **Mohammad**, **Afsaneh** and **Iman**, **Farzaneh** and **Javad**, **Hengameh** and **Hamid**, **Ameneh** and **Hassan**, **Zahra** and **Parviz**, **Ali**, **Aydin**, and **Nakisa**, you always make life more fun and I would like to thank you for being a part of my life. I also thank my old good friends, comrade **Saeid**, **Majid** and **Mohaddeseh**.

Farhad, you are my wonderful, selfless and kind brother and friend that I can always trust confidently. Words cannot express how much I do appreciate your support, insights, and guidance. Thank you for being a big part of my life, and for being the one that I can relate to through thick and thin.

I would like to extend my heartfelt gratitude to my wonderful family for their endless love, support and encouragement. I cannot thank you enough for your terrific faith in me and my decisions. Whatever I achieve in my life stems from the love you shared with me limitlessly. **Fariba** and **Amir**, **Haki** and **Ahmad**, **Hanieh** and **Farhad**, **Nazila** and **Sayad**, **Neda** and **Hamed**, **Iman**, **Ali**, **Danial**, **Elvin** and **Ayhan**, you are simply the best.

I now come to the part that I do not know how to describe my gratefulness in words, and it is all about my lovely beautiful soulmate, **Maryam**. You are undoubtedly one of the strongest and smartest persons that I have ever known, and I am extremely delighted to have you on my side. We have gone through many difficulties shoulder to shoulder, and you have proved that there is nothing to worry about when we are together and that we can accomplish anything. Many thanks for agreeing to move abroad with me and start a new life in the Netherlands. You made it so easy to love you by adding unimaginable happiness and stability to every moment of our life. Dearest love, you are my one and only, my best friend and my everything. The passion I have for you is unmatched and bursts out of my chest at the mere thought of you.

Amin Ebrahimi
Delft, November 2021

Knowledge Dissemination

Peer-reviewed journal papers

PhD work

1. **Ebrahimi, A.**, Sattari, M., Bremer, S.J.L., Luckabauer, M., Römer, G.R.B.E., Richardson, I.M., Kleijn, C.R. and Hermans, M.J.M., *The influence of laser characteristics on internal flow behaviour in laser melting of metallic substrates*, Materials & Design **214**: 110385, 2022. doi: 10.1016/j.matdes.2022.110385

2. **Ebrahimi, A.**, Babu, A., Kleijn, C.R., Hermans, M.J.M. and Richardson, I.M., *The effect of groove shape on molten metal flow behaviour in gas metal arc welding*, Materials **14**(23): 7444, 2021. doi: 10.3390/ma14237444

3. **Ebrahimi, A.**, Kleijn, C.R., Hermans, M.J.M. and Richardson, I.M., *The effects of process parameters on melt-pool oscillatory behaviour in gas tungsten arc welding*, Journal of Physics D: Applied Physics **54**(27): 275303, 2021. doi: 10.1088/1361-6463/abf808

4. **Ebrahimi, A.**, Kleijn, C.R. and Richardson, I.M., *Numerical study of molten metal melt pool behaviour during conduction-mode laser spot melting*, Journal of Physics D: Applied Physics **54**(10): 105304, 2021. doi: 10.1088/1361-6463/abca62

5. **Ebrahimi, A.**, Kleijn, C.R. and Richardson, I.M., *A simulation-based approach to characterise melt-pool oscillations during gas tungsten arc welding*, International Journal of Heat and Mass Transfer **164**: 120535, 2021. doi: 10.1016/j.ijheatmasstransfer.2020.120535

6. **Ebrahimi, A.**, Kleijn, C.R. and Richardson, I.M., *Sensitivity of numerical predictions to the permeability coefficient in simulations of melting and solidification using the enthalpy-porosity method*, Energies **12**(22): 4360, 2019. doi: 10.3390/en12224360

Other works

1. **Ebrahimi, A.**, Shahabi, V. and Roohi, E., *Pressure-driven nitrogen flow in divergent microchannels with isothermal walls*, Applied Sciences **11**(8): 3602, 2021. doi: 10.3390/app11083602

2. Naranjani, B., Roohi, E. and **Ebrahimi, A.**, *Thermal and hydraulic performance analysis of a heat sink with corrugated channels and nanofluids*, Journal of Thermal Analysis and Calorimetry, **146**(6): 2549–2560, 2021. doi: 10.1007/s10973-020-10225-9

3. Bordbar, A., Kheirandish, S., Taasob, A., Kamali R. and **Ebrahimi, A.**, *High-viscosity liquid mixing in a slug-flow micromixer: a numerical study*, Journal of Flow Chemistry **10**(2): 449–459, 2020. doi: 10.1007/s41981-020-00085-7

4. **Ebrahimi, A.**, Naranjani, B., Milani, S. and Javan, F.D., *Laminar convective heat transfer of shear-thinning liquids in rectangular channels with longitudinal vortex generators*, Chemical Engineering Science **173**: 263–274, 2017. doi: 10.1016/j.ces.2017.07.044

5. **Ebrahimi, A.** and Roohi, E., *DSMC investigation of rarefied gas flow through diverging micro- and nanochannels*, Microfluidics and Nanofluidics **21**(2): 18, 2017. doi: 10.1007/s10404-017-1855-1

6. **Ebrahimi, A.** and Naranjani, B., *An investigation on thermo-hydraulic performance of a flat-plate channel with pyramidal protrusions*, Applied Thermal Engineering **106**: 316–324, 2016. doi: 10.1016/j.applthermaleng.2016.06.015

7. **Ebrahimi, A.**, Rikhtegar, F., Sabaghan, A. and Roohi, E., *Heat transfer and entropy generation in a microchannel with longitudinal vortex generators using Nanofluids*, Energy **101**: 190–201, 2016. doi: 10.1016/j.energy.2016.01.102

8. **Ebrahimi, A.** and Roohi, E., *Flow and thermal fields investigation in divergent micro/Nano channels*, Journal of Thermal Engineering **2**(2): 709–714, 2016. doi: 10.18186/jte.53652

9. **Ebrahimi, A.** and Roohi, E., *Numerical study of flow patterns and heat transfer in mini twisted oval tubes*, International Journal of Modern Physics C **26**(12): 1550140, 2015. doi: 10.1142/S0129183115501405

10. **Ebrahimi, A.**, Roohi, E. and Kheradmand, S., *Numerical study of liquid flow and heat transfer in rectangular microchannel with longitudinal vortex generators*, Applied Thermal Engineering **78**: 576–583, 2015. doi: 10.1016/j.applthermaleng.2014.12.006

11. Varade, V., Duryodhan, V., Agrawal, A., Pradeep, A.M., **Ebrahimi, A.** and Roohi, E., *Low Mach number slip flow through diverging microchannel*, Computers & Fluids **111**: 46–61, 2015. doi: 10.1016/j.compfluid.2014.12.024

Peer-reviewed conference papers

1. **Ebrahimi, A.**, Kleijn, C.R. and Richardson, I.M., *Sensitivity of numerical predictions to the permeability coefficient in simulations of melting and solidification using the enthalpy-porosity method*, XII International Conference on Computational Heat, Mass and Momentum Transfer (ICCHMT 2019), Rome, Italy, 3–6 September 2019.

2. **Ebrahimi, A.**, Kleijn, C.R. and Richardson, I.M., *The influence of surface deformation on thermocapillary flow instabilities in low Prandtl melting pools with surfactants*, The 5th World Congress on Mechanical, Chemical, and Material Engineering (MCM'19), Lisbon, Portugal, 15–17 August 2019. doi: 10.11159/htff19.201

3. **Ebrahimi, A.**, Kleijn, C.R. and Richardson, I.M., *The influence of heat source adjustment on numerical predictions of melt pool behaviour in a surface melting process*, The 12th International Seminar "Numerical Analysis of Weldability", Graz, Seggau, Austria, 23–26 September 2018.

Invited talks and poster presentation

1. *High-fidelity multiphysics numerical simulations for advanced fusion-based manufacturing*, Poster presented at the annual Applied Computational Sciences (ACOS) conference (ACOS2021), DIFFER, Eindhoven, The Netherlands, November 2021.

2. *Computers and advanced fusion-based manufacturing processes*, Poster presented at the MSE poster session, Online event, The Netherlands, February 2021.

3. *A new simulation-based approach to welding process optimisation*, Poster presented at the annual Applied Computational Sciences (ACOS) conference (ACOS2020), Online event, The Netherlands, October 2020.

4. *Heat and fluid flow in welding and additive manufacturing*, Invited talk, 20th M2i annual conference and Materials meeting, Noordwijkerhout, The Netherlands, December 2019.

5. *Advanced computer simulations for materials processing technology*, Poster presented at the joint poster day MSE and PME, Faculty of Mechanical, Maritime and Materials Engineering (3mE), Delft University of Technology, Delft, The Netherlands, July 2019. (Winner of the highest master-student-appeal)

6. *Innovation and Scientific Writing*, Invited lecturer, CERN-HPD (Honours Programme Delft) summer school, Geneva, Switzerland, July 2019.

7. *An adaptive heat source model for laser spot welding*, Poster presented at 19th M2i annual conference and Materials meeting, Noordwijkerhout, The Netherlands, December 2018.

8. *A new simulation-based approach to welding process optimisation*, Poster presented at the 4TU.HTM annual symposium (Dutch Materials 2018), Utrecht, The Netherlands, October 2018.

9. *A new simulation-based approach to welding process optimisation*, Poster presented at the Materials Technology Day annual symposium, Delft, The Netherlands, June 2018.

10. *On the influence of the permeability coefficient in phase-change simulations*, Poster presented at 18th M2i annual conference and Materials meeting, Noordwijkerhout, The Netherlands, December 2017.

11. *Challenges in numerical study of fusion welding processes*, Poster presented at the kick-off event of TU Delft Institute for Computational Science and Engineering (DCSE), Delft, The Netherlands, May 2017.

12. *A new simulation-based approach to welding process optimisation*, Poster presented at 17th M2i annual conference and Materials meeting, Nieuwegein, The Netherlands, December 2016.

Student supervision

1. T. Donders, *The effect of power-density distribution on weld pool behaviour during laser welding*, BSc thesis, 2020. (Joint project with the Chemical Engineering Department of the Delft University of Technology)
   Link to the full-text: http://resolver.tudelft.nl/uuid:67ad7fe4-2d86-4a4c-aec7-f45cee9592e2

2. Joel A. Barreto de Matos, *Molten metal droplet impingement and solidification on a solid substrate*, MSc thesis, 2019. (Joint project with the department of Thermal and Fluid Engineering (TFE) of the University of Twente)
   Link to the full-text: http://purl.utwente.nl/essays/85115

3. Jeroen Reus, *Numerical study of solidifying molten metal droplet impingement on a cold solid surface*, BSc thesis, 2018. (Joint project with the Chemical Engineering Department of the Delft University of Technology)
   Link to the full-text: http://resolver.tudelft.nl/uuid:6d35a4bd-ca5f-4416-b397-f102a4d51c40

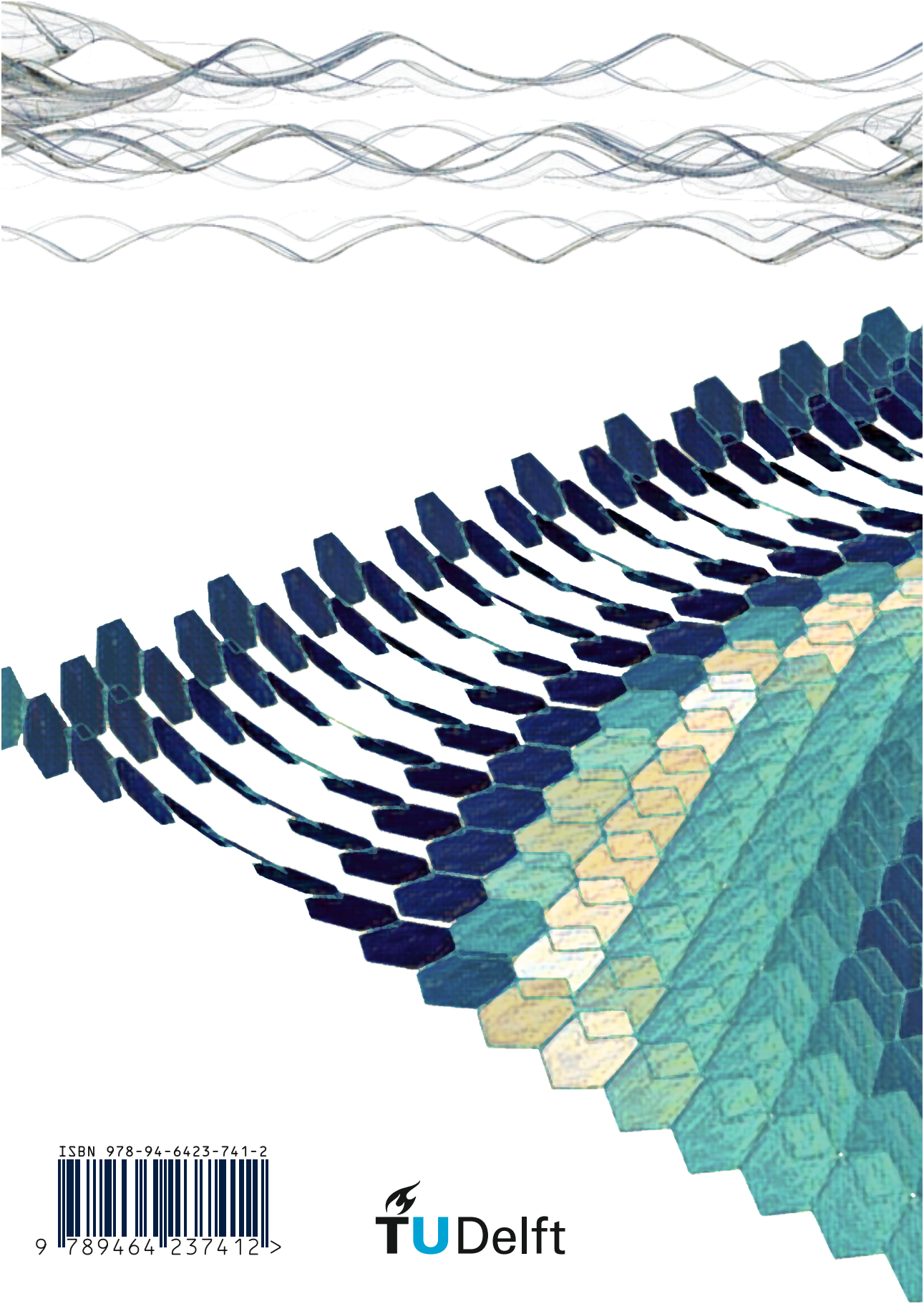

ISBN 978-94-6423-741-2

TU Delft